**Title**
Reconstruction of Cosmological Fields in Forward Model Framework



**Author**
Modi, Chirag

**Publication Date**
2020

Peer reviewed|Thesis/dissertation

Reconstruction of Cosmological Fields in Forward Model Framework

by

Chirag Modi

A dissertation submitted in partial satisfaction of the

requirements for the degree of

Doctor of Philosophy

in

Physics

in the

Graduate Division

of the

University of California, Berkeley

Committee in charge:

Professor Uroš Seljak, Chair
Professor Martin White
Professor Fernando Pérez

Summer 2020

Reconstruction of Cosmological Fields in Forward Model Framework

Abstract

Reconstruction of Cosmological Fields in Forward Model Framework

by

Chirag Modi

Doctor of Philosophy in Physics

University of California, Berkeley

Professor Uroš Seljak, Chair

The large scale structures (LSS) of the Universe contain a vast amount of information about the birth, evolution and composition of our Universe. To mine this information over the next decade, large scale imaging surveys such as the Dark Energy Spectroscopic Survey (DESI), Large Synoptic Survey Telescope (LSST), Euclid and WFIRST will probe the Universe with unprecedented precision, and on the largest scales. This provides an opportunity to shed light on the longstanding mysteries regarding the true nature of dark matter and dark energy, as well as to resolve tensions between different probes of the past decade. However to utilize the full potential these surveys which are no longer statistically limited, it is critical to develop analytic methods that extract the maximum amount of information across all scales. In this regard, the massive data volumes, the non-linearity, and non-Gaussianity of the signal in the regimes probed by these surveys will pose outstanding challenges.

The focus of this thesis is to tackle aforementioned challenges with a novel framework for the analysis of the large scale structures by reconstructing cosmological fields using forward models. These forward modeling approaches are the most promising way to jointly model different cosmological observations with requisite accuracy at all scales, while accounting for their individual systematic biases and noise. We approach reconstruction within a Bayesian formalism - by optimizing the likelihood of the observed data and maximizing the corresponding posterior of initial conditions. This requires solving optimization problems in multi-million dimensional space and we develop novel differentiable forward models as well as adiabatic optimization algorithms to assist with this.

We begin by using this approach to reconstruct the initial density field from a continuous dark matter field, as well as discrete observables like dark matter halos. We also construct a power spectrum estimator for this reconstructed Gaussian density field, which is the summary statistic for optimal analysis. With 21-cm intensity mapping, we show how this framework can instead be used for secondary analysis such as de-noising the observed data and recovering lost cosmological information. For this, we also introduce Hidden Valley Simulations

- a suite of high resolution N-Body simulations and develop models to simulate HI clustering. Having demonstrated the efficacy of this approach, we finally introduce FlowPM - a GPU-accelerated, distributed, and differentiable N-Body solver in TensorFlow that naturally interfaces with the most advanced machine learning tools. This will enable the community to efficiently solve large scale cosmological inference problems and develop differentiable forward models for the reconstruction of cosmological fields with the next generation of LSS surveys.

To my parents,

Ajay and Nisha Modi,

who with unconditional love, support, constant encouragement and sacrifices raised me to be the person I am today. You have always been an inspiration to me.

And to my grandfather Sanat Kumar Modi, who always believed in me. I miss you Ba.

# Contents

# List of Figures

# List of Tables

## Acknowledgments

First and foremost, my heartfelt thanks goes to my partner Noopur Bhandari, who has been my constant companion for over a decade. Despite the distances, you have always been my anchor and it is hard to imagine doing any of this without your love, support and patience. Thank you for always being there, you are awesome.

Then of course, I would like to thank my advisors, Uroš Seljak and Martin White, who have not only taught me so much about cosmology, but also different ways of pursuing scientific research and the qualities necessary to be a successful researcher. Over the course of my PhD, you have not only supported but also pushed my forays in other scientific domains, preventing me from pigeonholing myself and for that I am deeply grateful. I am thankful to Adrian Lee and Fernando Pérez for agreeing to serve on my qualifying and dissertation committee and providing timely suggestions to improve my research work and methodology. I also owe thanks to my previous mentors, Punit Parmananda, Thorsten Battefeld, Raghava Verma and Sanjay Gupta whose encouragement and guidance led me to Berkeley to pursue this research in the first place.

Throughout my PhD, postdocs in our Berkeley Center for Cosmological Physics have played crucial role in shaping my research as well as work-life outlook, beginning all the way with Florian Beutler, Nick Hand and Marcel Schmittfull who all trained me as a novice, to Chang Hoon Haan, Michael Wilson, Emnanuel Schaan, Sukhdeep Singh and Benjamin Horowitz; scientific discussions with whom broadened my scope an thought. I am thankful to my most frequent collaborator Emanuele Castorina who first trained me in theory, emphasized not working on the weekends, and left me with my first car, Bugg, to ensure the same. I owe my modest coding skills to the genius of Yu Feng who decided to choose me as a sounding board when planning codes and ended up inspiring me to code better. A very warm thank you to Yin Li for all the late nights, sharing snacks with Nuan, solving puzzles or going down internet rabbit holes when not discussing science. I cannot thank François Lanusse enough for guiding my forays into machine learning and brainstorming different paths to pursue in future research. The amplifier has served my home well. Simone Ferraro, thank you for always standing by this troublemaker, whether in deciding his next journey, planning hikes, ski trips or stock market takeovers. I owe you a couple projects. Finally, thank you Vanessa Böhm for sharing all those dinners, drinks and rides, helping me in giving back a little more, making me snow-shoe and dance, and simply being a friend. This is unfinished if I do not point out that my stay in Berkeley would have been significantly drier if not for Vanessa Böhm, François Lanusse, Michael Wilson, Simone Ferraro and Chang Hoon Haan leading to all the late nights at various watering holes around Berkeley.

In this foreign land, these close friends have played an irreplaceable role in supporting me and keeping me tethered to my ways of life. Niladri Chatterji, you I cannot thank enough for standing by as a singularly genuine friend through every thick and thin we have been over the past half decade. We both have come a long way since the first time you came for the open-house, and what a ride it has been. You have been the only one here to see it all. Thank you, friend. Prateek Shah and Archit Gupta, thank you for always letting your home be my home these past years, and literally for the fortnight I made myself homeless with genius planning. From countless dinners and rides to music nights, FIFA days, board games, camping, sailing and ALC ride with captain Nehal Bhandari, the three of you have been my support throughout, a family that I knew I could rely on. Ambrish Rawat, my old friend, always sitting in the distance but looking out for me, thank you for talking about anything and everything such that the time and distances didn't matter. Despite the years, with you I can still be myself. I will always cherish Iceland, and until next time. Rishabh Bhargava and Vidhi, with you I was back home in India, except the nights we ended up playing pool till sunlight. Thank you Ayush Saxena for being my getaway, from snowboarding, thanksgivings, camping, stargazing to obscure concerts. I could always count on you being ready. Fiiine!!! the sky is not freaking blue but every sunset is the best. Thank you Ballu for trusting me with your car, until you couldn't anymore. It has also been apt and wonderful to break away with Rohan, Ankit and Aman on thanksgivings. Ajay Uncle and Sharmila aunty, thank you for all the home cooked meals. On this journey, I have always been glad that my past has stayed with me and I am grateful for my friends from the previous life- Adwait, Aviral, Abhishek, Shruti, Abhijeet, Anil, Raj, Rishi, Harshveer, Swati and my oldest friend, Aditi, for maintaining my connection with my roots despite all these years.

Finally, I owe thanks to my housemates over the years who made me look forward to coming back home after a long day. Tom Darlington, for being my first friend in Berkeley and the gaming nights that followed. Evan Anderson, thank you for the refreshing late-night discussions and 90's kid dress-up. I cannot thank enough my current housemates who made the house a home in these last months during the pandemic. Zoe, for taking care of us with your amazing food and educating me on countless sociocultural references. Your Tiramisu will be missed. I will forever cherish your creativity and hold onto the precious colorful pictures you have painted for me with your words Nazia, your perseverance, gratitude and love for everything big and small is inspiring. Thank you for abetting in all the brainless decisions during this memorable chapter of life. gang-gang \m/. Kyla, thank you for bringing all the color, love and care (and plants) to make it a home, for your excitement and sense of wonder and truly changing my appreciation for so many things in ways that will stay with me throughout my life. I will honor our blood pact. I also thank you- Kyla, Naz and Zoe, for an unforgettable graduation ceremony to conclude this journey.

Lastly, since words fail me, thank you ma and papa for everything.

# Chapter 1

# Introduction

With the wealth of extra-galactic observations in the last two decades, cosmology has evolved into a precision science and there has emerged a concordance model for cosmology. It has been extremely successful at simultaneously describing disparate properties of the Universe ranging from the existence and structure of the cosmic microwave background, the large-scale structure in the distribution of galaxies to the observed abundances of light elements as well as the the accelerating expansion of the universe. In this model, the universe contains three major components: i) a dark energy component contributed by non-vanishing cosmological constant ($\Lambda$), ii) non-baryonic, dissipationless, collisionless cold dark matter (abbreviated CDM), and iii) ordinary baryonic matter. Consequently, this model is known as $\Lambda$CDM model and is often dubbed as standard model of cosmology.

According to this model, the Universe originated from an initial singularity at the Big Bang and was immediately followed by a very brief period of exponential expansion known as *inflation* that lasted about $10^{-32}$ seconds. This was followed by a long period of several hundred thousand years where the Universe expanded slowly and cooled progressively. During this period, it was a hot plasma (above 10,000 K) of constantly interacting of baryons, electrons and photons. Due to these interactions, photons had extremely short mean free paths and were in thermal equilibrium with electrons and baryons. This phase also coincides with the radiation dominated era i.e. when radiation was the dominant energy component of the Universe. As the Universe expanded and cooled to reach temperature of 3000K about 380,000 years after Big Bang, the energy of these photons dropped below the threshold required to excite electrons away from light nuclei, allowing protons and electrons to combine in an event called *recombination* and form neutral atoms. At this point, the photons decoupled from baryons and electrons to move freely and their mean free path increased to reach Hubble scale. The first light emitted from this time is visible to us in the form of *Cosmic Microwave Background Radiation* (CMB). A little prior to this decoupling, we also cross the matter-radiation equality, that is the time at which the evolution of the Universe starts to be dominated by the matter energy density while photons and relic neutrinos become less and less important. In this era, after CMB decoupling, the matter perturbations can start to grow under the gravitational attraction and evolve to give rise to the large scale structures

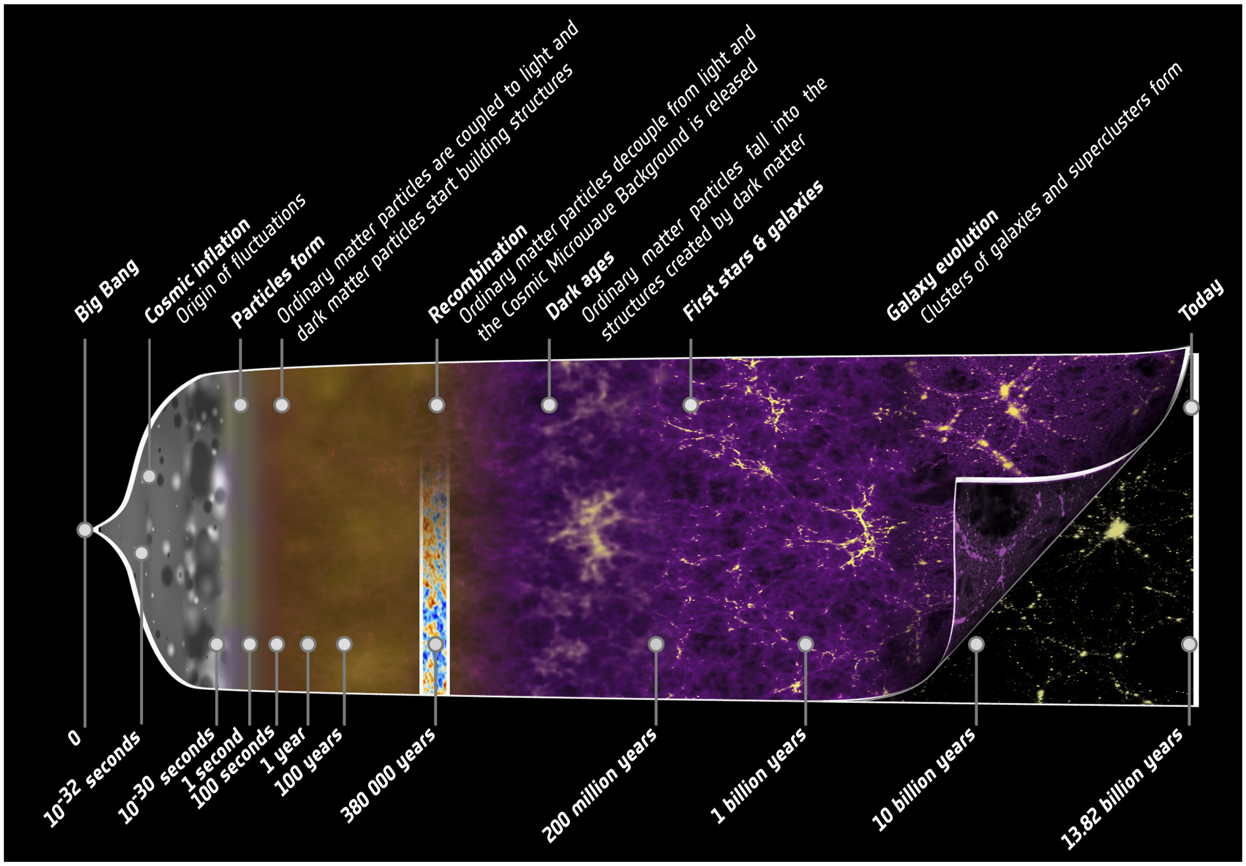


Figure 1.1: Cosmic history and evolution of the Universe from Big Bang to the present day. *Credits ESA*

that we observe today. The final stage in the evolution of Universe started around 4 billion years ago when the Universe is finally moved out from matter domination to enter a phase of the an accelerated expansion of the largest scales believed to be driven by dark energy, as discovered in the observation of the furthest supernovae. This history and evolution of the Universe is shown in

The success of ΛCDM model is altogether more impressive in that in the simplest standard model, it matches all the cosmological observations and describes the evolution of the Universe with only 6 physical parameters - physical baryon density parameter; physical dark matter density parameter; the age of the universe; scalar spectral index; curvature fluctuation amplitude; and reionization optical depth. The best fit value of these parameters in latest CMB analysis by Planck is given in 1.1.

| Parameter | Symbol | Value (68 % c.l.) | | |
|---|---|---|---|---|
| Baryon density | $\Omega_b h^2$ | 0.02242 | $\pm$ | 0.00014 |
| Dark Matter density | $\Omega_c h^2$ | 0.11933 | $\pm$ | 0.00091 |
| Angular Acoustic Scale | $100\theta_{MC}$ | 1.04101 | $\pm$ | 0.00029 |
| Optical Depth | $\tau$ | 0.0561 | $\pm$ | 0.0071 |
| Primordial Power Spectrum Amplitude | $\ln(10^{10}A_s)$ | 3.047 | $\pm$ | 0.014 |
| Scalar spectral index | $n_s$ | 0.9665 | $\pm$ | 0.0038 |
| Hubble Constant | $H_0[\mathrm{kms}^{-1}\mathrm{Mpc}^{-1}]$ | 67.66 | $\pm$ | 0.42 |
| Dark Energy Density | $\Omega_\Lambda$ | 0.6889 | $\pm$ | 0.0056 |
| Age of the Universe | Age[Gyr] | 13.787 | $\pm$ | 0.020 |

Table 1.1: The best-fit cosmological parameters from combined PlanckCMB power spectra, in combination with CMB lensing reconstruction and BAO (TT,TE,EE+lowE+lensing+BAO) [187]. The top group of six rows are the base parameters, which are sampled in the MCMC analysis with flat priors. The middle group lists derived parameters.

ΛCDM model was first established after the discovery of accelerated expansion of Universe [197, 185] and following Stage II cosmic microwave background (CMB) and large scale structure (LSS) surveys. While Stage III surveys such as SDSS BOSS [31], Planck [187], DES [61] have broadly validated ΛCDM model over other proposals and firmly entrenched it as standard model of cosmology, they have also pushed it to its limit. Most notably, there is a 4.4 $\sigma$ tension between the value of Hubble constant inferred from local Universe with supernovae experiments and that inferred from cosmological scales with Planck and BOSS [196]. Additionally, there is also a discrepancy in the amplitude of fluctuations as inferred from weak lensing and CMB experiments. In addition to these, ΛCDM model also faces some fundamental challenges regarding its key components. While we understand the phenomenological properties of dark matter and dark energy reasonably well, the components themselves remain elusive. Extensive searches for dark matter particles have so far shown no well-agreed detection and the dark energy may be almost impossible to detect in a laboratory. The energy density of the cosmological constant itself is unnaturally small as compared to naive theoretical predictions, by some 120 orders of magnitude.

The coming decade will see transformative dark energy science done by Stage IV surveys, based both on the ground such as (DESI [68], LSST [138]), CMB-S4 [2] and space-based missions (Euclid [10], WFIRST [70]). We expect that large swaths of the universe will be sampled to close to the sample variance limit on very large scales using galaxies as tracers of density field as well as sources used to measure the weak gravitational lensing shear, cosmic backlights illuminating the cosmic hydrogen for Lyman-$\alpha$ forest studies and cosmic microwave background radiation with its associated gravitational lensing. At the same time, these fields will offer a multitude of cross-correlation opportunities, through which more and more robust science will be derived. A number of upcoming (CHIME [19], HIRAX [165], Tianlai [50], SKA[4]) or planned (PUMA, the proposed Stage II experiment [55]) interferometric instruments will also use the 21-cm signal to probe this volume of the universe.

Given the unprecedented size and scales of these surveys, it is necessary to develop corresponding theoretical and analytic tools to optimally extract cosmological information from their noisy and incomplete data across all scales. Developing such tools for the analysis of large scale structures is the focus of thesis.

## 1.1 Large Scale Structures

It has been long established that the galaxies are not randomly distributed in the Universe and there is an underlying large scale structure (LSS) of nodes and filaments where galaxies cluster together with large void spaces between them. These provide a sensitive probe of the underlying cosmology and in this section we briefly summarize the basic tools to study these and will be referred to throughout this thesis.

## 1.2 Modeling Growth and Evolution of Dark Matter

The large scale structures are seeded by small inhomogenieties in the early Universe that grow under gravitational collapse. We will follow the standard model where these gravitational dynamics are primarily governed by cold dark matter in an isotropic, otherwise homogeneous expanding Universe. Thus we begin by writing the Friedmann equations which relate the dynamical evolution of the Universe to the total matter and energy content in the Universe.

$$\Big(\frac{\dot{a}}{a}\Big)^2 = \frac{8\pi G}{3}\rho - \frac{Kc^2}{a^2} \tag{1.1}$$

$$\frac{\ddot{a}}{a} = -\frac{4\pi G}{3}\Big(\rho + \frac{3p}{c^2}\Big) \tag{1.2}$$

$$\tag{1.3}$$

where $a$ is the scale-factor, K is the curvature of the Universe (=0 in the rest of this work), $\rho$ and $p$ are the total energy content and pressure of different components often related by an equation of state. We also introduce dimensionless Hubble parameter $H(t) = \dot{a}(t)/a(t)$ which measures the expansion rate of the Universe and its value today is the Hubble constant. The value of the energy density at which the curvature of the Universe vanishes is the critical density $\rho_c$. Its related to the Hubble parameter such that

$$\rho_c(a) = \frac{3H^2(a)}{8\pi G} \tag{1.4}$$

and it is common to rescale the density $\rho$ by the critical density to define dimensionless density parameter $\Omega(a) = \rho(a)/\rho_c(a)$. We will also use $\mathcal{H} = Ha$, which is the conformal expansion rate defined with respect to conformal time $\tau$ related to cosmic time $t$ with $dt = a(t)d\tau$. Similarly, we will use comoving coordinates $\mathbf{x}$ corresponding to physical coordinates $\mathbf{r} = a\mathbf{x}$.

Now, turning towards the evolution of the large scale structures, let us define the density contrast $\delta$

$$\rho(\mathbf{x}, a) \equiv \bar{\rho}(\mathbf{x}, a)[1 + \delta(\mathbf{x}, a)] \tag{1.5}$$

Let $\mathbf{v}(\mathbf{x}, a)$ be the peculiar velocity of matter with respect to the background expansion and the gravitational potential sourced by the density fluctuations with the Poisson equation as

$$\nabla^2 \mathbf{\Phi}(\mathbf{x}, a) = \frac{3}{2}\Omega_m(a)\mathcal{H}^2(a)\delta(\mathbf{x}, a) \tag{1.6}$$

## Eulerian Approach

To study the evolution, we first take the approach of Eulerian dynamics [25]. We write the Euler equations in the expanding Universe

$$\dot{\delta} + \nabla \cdot [(1 + \delta)\mathbf{v}] = 0 \tag{1.7}$$

$$\dot{\mathbf{v}} + (\mathbf{v} \cdot \nabla)\mathbf{v} = -\mathcal{H}\mathbf{v} - \nabla\mathbf{\Phi} \tag{1.8}$$

where the dots denote time derivative with respect to conformal time $\tau$. Henceforth, we assume that $\mathbf{v}$ is curl free, thus ignoring vorticity and instead focus on the divergence of velocity $\theta = \nabla \cdot \mathbf{v}$. Combining these with the Poisson and Friedmann equations results in the coupled integro-differential equations that can be solved to obtain the evolution of matter. However given the complex nature of these equations, they are typically solved perturbatively by Taylor expanding the density contrast. This gives rise to the Eulerian perturbation theory solutions for the large scale structures.

At first order, i.e. under the assumption of small density fluctuations and peculiar velocity, we obtain the linear perturbation theory solution for the evolution of density contrast

$$\ddot{\delta} + \mathcal{H}(\tau)\dot{\delta} + \frac{3}{2}\mathcal{H}^2(\tau)\Omega_m(\tau)\delta = 0 \tag{1.9}$$

This second order differential equation with a source and damping term allows for a general solution having a decaying ($D_-$) and growing mode ($D_+$), with decoupled spatial and temporal coordinates -

$$\delta(\mathbf{x}, \tau) = D_+(\tau)A(\mathbf{x}) + D_-(\tau)B(\mathbf{x}) \tag{1.10}$$

where $A(\mathbf{x})$, $B(\mathbf{x})$ are initial density perturbations. For the purpose of structure formation, the decaying mode is not important and we focus only on the growing mode for which the general solution is

$$D_+(a) = \frac{5\Omega_m}{2}\frac{H(a)}{H_0}\int_0^a \frac{da'}{(a'H(a')/H_0)^3} \tag{1.11}$$

Here we have used the normalizing convention that growing mode is equal to the scale factor in matter dominated epoch $D_+(a) = a$. We use the continuity equation at first order to calculate the velocity gradient -

$$\theta(\mathbf{x}, \tau) = -\dot{\delta}(\mathbf{x}, \tau) = f(\tau)\mathcal{H}(\tau)\delta(\mathbf{x}, \tau) \tag{1.12}$$

where

$$f(\tau) = \frac{d\,\mathrm{ln}D}{d\,\mathrm{ln}a} \tag{1.13}$$

is the logarithmic growth rate.

## Lagrangian Approach

While the Eulerian approach describes the density and velocity fields of matter in a fixed coordinate system, Lagrangian approach concentrates on the trajectory of individual particle. Let $\mathbf{q}$ denote the Lagrangian (comoving initial) coordinate of a particle. Then in Lagrangian approach, the dynamical variable is the Lagrangian displacement field $\mathbf{\Psi}(\mathbf{q}, \tau)$ defined by

$$\mathbf{x}(\tau) = \mathbf{q} + \Psi(\mathbf{q}, \tau) \tag{1.14}$$

From the previous section, the Newtonian equations of motion for the trajectory of the particle are -

$$\ddot{\mathbf{x}} + H(\tau)\dot{\mathbf{x}} = -\nabla\mathbf{\Phi} \tag{1.15}$$

Now, the particle density in the Largrangian coordinates is the same as the average density of the Universe. Therefore by mass conservation

$$\bar{\rho}(\tau)d^3q = \bar{\rho}[(1 + \delta(\mathbf{x}, \tau)]d^3x \tag{1.16}$$

Hence we can relate the Eulerian density contrast to the displacement vector

$$1 + \delta(\mathbf{x}, \tau) = \left|\frac{d^3q}{d^3x}\right| = \frac{1}{J(\mathbf{q}, \tau)} \tag{1.17}$$

where $J$ is the Jacobian matrix for the transformation from Lagrangian to Eulerian coordinates

$$J(\mathbf{q}, \tau) = \det(\delta_{ij} + \Psi_{i,j}(\mathbf{q}, \tau)) \tag{1.18}$$

Combining this with the equation of motion and Poisson equation, we obtain the non-linear equation to generate the solutions of Lagrangian perturbation theory

$$J(\mathbf{q}, \tau)[\delta_{ij} + \Psi_{i,j}(\mathbf{q}, \tau)]^{-1}\left[\ddot{\Psi}_{i,j}(\mathbf{q}, \tau) + \mathcal{H}(\tau)\dot{\Psi}_{i,j}(\mathbf{q}, \tau)\right] = \frac{3}{2}\mathcal{H}^2(\tau)\Omega_m(\tau)[J(\mathbf{q}, \tau) - 1] \tag{1.19}$$

This equation is again solved perturbatively by expanding the displacement to successive $n$-th powers

$$\mathbf{\Psi}(\mathbf{q}, \tau) = \mathbf{\Psi}^{(1)}(\mathbf{q}, \tau) + \mathbf{\Psi}^{(2)}(\mathbf{q}, \tau) + \ldots \tag{1.20}$$

At linear order, the solution for the Lagrangian displacements becomes

$$\nabla_q \mathbf{\Psi}^{(1)}(\mathbf{q},\tau) = -\nabla_q^2 \phi^{(1)}(\mathbf{q},\tau) = -\delta_1(\mathbf{x},\tau) \tag{1.21}$$

$\phi$ is the Lagrangian potential $\mathbf{\Psi}^{(1)}(\mathbf{q},\tau) = -\nabla_q \phi^{(1)}(\mathbf{q},\tau)$ using the the curl-free condition of the Lagrangian displacement. The time-evolution of $\delta_1(\mathbf{x},\tau)$ is governed by the same linear growth factor $D_+(\tau)$.

At second order, the LPT solution (often referred to as 2LPT solution in literature) is given by

$$\nabla_q \mathbf{\Psi}^{(2)} = \frac{1}{2} D_2(\tau) \sum_{i\neq j} \Psi^{(1)}_{i,i} \Psi^{(1)}_{j,j} - \Psi^{(1)}_{i,j} \Psi^{(1)}_{j,i} \tag{1.22}$$

and the time-evolution obeys

$$D_2(\tau) \sim -\frac{3}{7} D_1^2(\tau) \Omega_m^{-2/63} \tag{1.23}$$

Given these Lagrangian displacements, we can then solve for the position and velocity of the particles. *Zeldovich approximation* extrapolates the linear theory solution so obtained into non-linear regime [261]. This often leads to non-physical structures such as Zeldovich pancakes. 2LPT leads to remarkable improvements over these since takes into account the fact that gravitational instability is non-local. While we develop equations here summing upto second order, over years there has been a lot of work on summing to higher orders in Lagrangian perturbation theory [146, 148, 39, 46, 42].

## N-Body Simulations

Perturbation theories are able to model the growth and evolution of the large scale structures analytically. While they perform well on large scales, their accuracy deteriorates quickly as we go to increasingly non-linear scales. The performance also worsens as we move from dark matter to halos and observed galaxies, as well as from real space to redshift space. Modeling these non-linear scales is of critical importance since they have tremendous constraining power. This can be seen by a simple mode counting argument, with the number of independent LSS modes growing as $k_{\max}^3$ for 3-dimensional data.

To accurately model the large scale structures at small scales, we use N-body simulations. These simulations populate the Universe with component particles (here we focus on dark matter simulations only) to trace the matter field in the Universe. and evolve them computationally under the mutual self-gravitational interaction of these particles. On the largest scales, gravitational force of underlying cold-dark matter drives the evolution to a very good approximation. On small scales, it becomes increasingly important to account for other components such as baryons, neutrinos, photos and their non-gravitational interactions. However even then, dark matter only simulations significantly outperform perturbation theories on all scales, being almost exact up-to quasi-linear scales and we focus on them in this thesis.

For every particle in N-Body simulations, we integrate the equations of motion

$$\frac{d^2\mathbf{x}_i}{dt^2} + 2H\mathbf{v}_i = -\frac{1}{a^3}\sum_{j\neq i}^{N} Gm_j \frac{\mathbf{x}_i - \mathbf{x}_j}{|\mathbf{x}_i - \mathbf{x}_j|^3} \tag{1.24}$$

where $\mathbf{x}_i$ $\mathbf{v}_i$ are the comoving position and velocity of the particle $i$ and $m$ is the particle mass. Modern N-Body simulations regularly evolve billions of dark matter particles. Solving these coupled equations together naively for as many particles in computationally intractable since it will require evaluating gravitational force amongst all the $N(N-1)/2$ pair interactions. Instead, modern simulations use fast approximated numerical schemes such as Particle-Mesh (PM) solvers [153, 229, 251, 83, 115], $\mathrm{P}^3\mathrm{M}$, Trees [20] to estimate these forces efficiently.

In addition, to force estimation, we need an integration technique to evolve the particles forward in time. This is achieved with leapfrog symplectic integration which updates the positions and velocities at interleaved time points, achieving second-order accuracy with only one force evaluation.

Lastly, solving these differential equations also requires setting up initial conditions for the positions and velocities of the particles. This is achieved using the Lagrangian Perturbation Theory from the previous section. Simulations begin by generating standard Gaussian initial density field at $a = 0$ and scaling it with density power spectrum predicted by linear Boltzmann codes like CAMB [135] and CLASS [32] to match this linear power spectrum. Then LPT dynamics can be used to integrate the equations of motion from $a = 0$ to initial time $a_{init}$ and generate the initial positions and velocities of particles. If $a_{init} < 0.1$ (or 0.05 more conservatively), the density fluctuations are small enough that LPT is an excellent approximation for evolution.

Figure 1.2 shows the initial conditions, evolution of matter under Zeldovich approximation, second order Lagrangian perturbation theory and 20 step particle mesh simulation which is a form of approximate N-Body simulation.

We will focus in more detail on these computational methods in the next chapter.

## 1.3 Modeling Halos and Galaxy Distribution

Galaxies observed in LSS surveys do not perfectly trace the underlying matter density. Making a connection between them is a two step process- to realize that galaxies reside in dark matter halos following some statistical distribution- and that these halos themselves are biased tracers of matter distribution. Dark matter halos can be thought of as the basic unit in which matter collapses. These are collapsed, gravitationally bound structures that have decoupled from the Hubble expansion. In this section, we focus on the modeling of these two steps, both theoretically and computationally.

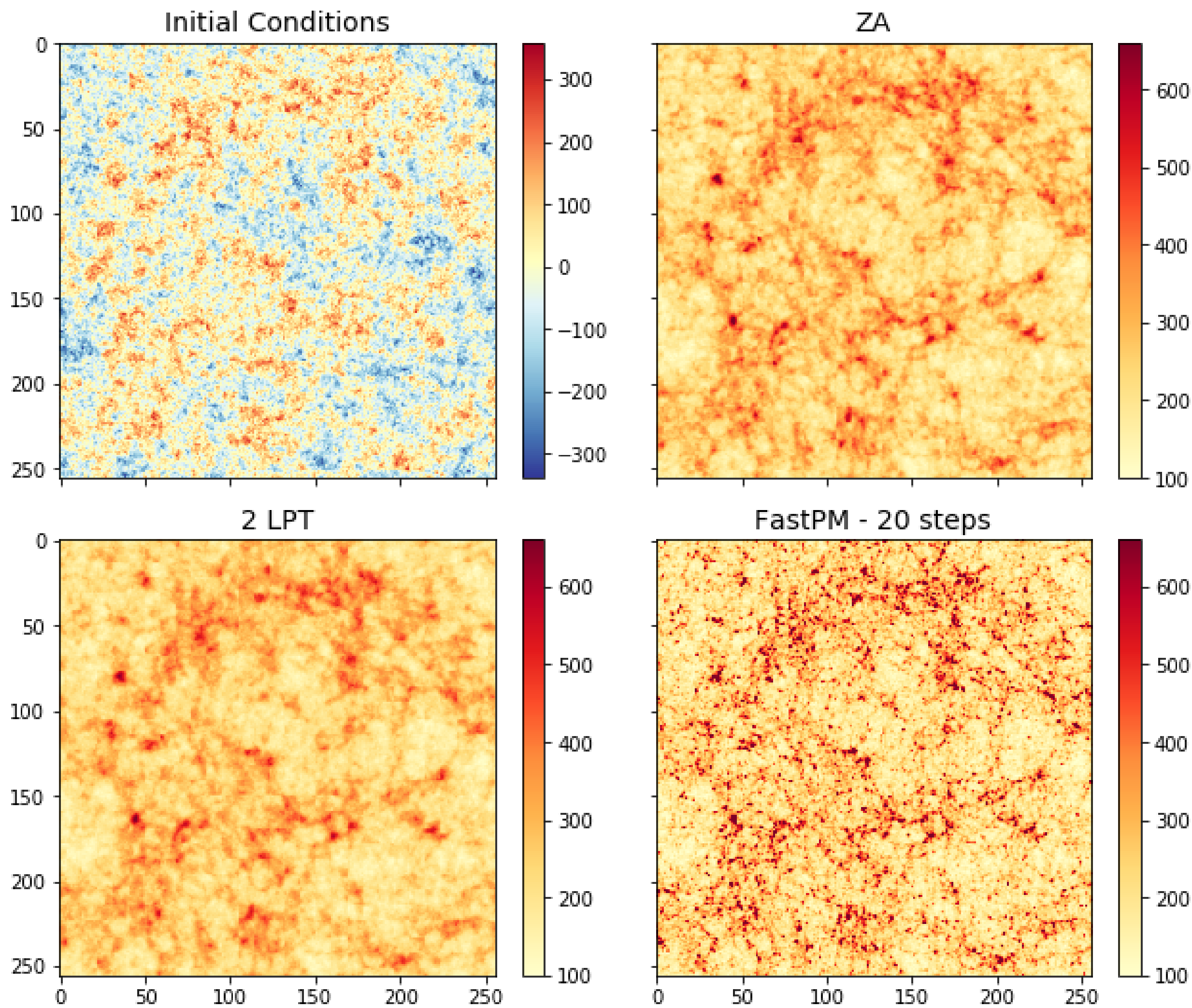


Figure 1.2: Evolution of dark matter field under gravity. We show (top left) the initial Gaussian field at $z = 9$, (top right) Zeldovich evolution, (bottom left) 2LPT evolution and (bottom right) FastPM [83] particle mesh evolution with 20 time steps to $z = 0$.

## Bias Model

In full generality the relation between the halo density field and the dark matter contains information about all processes relevant for the formation of halos, as well as stochastic contributions arising due to the fact that halos come in a finite number. However on large enough scales, we can hope to treat the problem perturbatively and characterize both, dark matter halos and galaxies as a biased tracer of the underlying matter field. The simplest way to get physical intuition of halo bias comes from the so-called Peak-Background split argument (PBS) [122, 123, 154, 222]. In the original formulation of PBS, halos are regions where the value of the dark matter density field exceeds some critical threshold. This threshold can be crossed more easily in presence of a positive large scale dark matter fluctuations, and conversely less easily for a negative one. This means that, on average, overdense regions host more halos than the mean. Linear bias, ($b_1$), can therefore be defined as the linear response of the halo overdensity field ($\delta_h$), to the presence of long wavelength perturbations ($\delta_m$),

$$\delta_h = b_1\delta_m \tag{1.25}$$

The above relation can be generalized to any order in the density field, leading to the well known result by [92],

$$1 + \delta_h(x) = \sum_{n=0}^{\infty} \frac{b_n}{n!}\delta_m^n(x)\,, \tag{1.26}$$

where however one must also enforce integral constraint by imposing that $\langle\delta_h\rangle = 0$.

Typically the bias expansion is written in two ways: either by relating the the halo field to the dark matter field at time the observations are made, *i.e.* at low redshift, or by identifying in the initial Gaussian field regions which are more likely to collapse into halos at a later time. The former is called a *Eulerian bias approach*, the latter a *Lagrangian bias approach*. While the two approaches can be shown to be mathematically equivalent, each method has its own pros and cons. In this thesis we will primarily use the latter since in Lagrangian Space non-linear evolution and the biasing scheme are decoupled from each other.

In addition to the dark matter density field, as in Eq. (1.26), it has been recently shown that the statistics of the halos also depends on spatial derivatives of the density field,[69, 162, 18] and on the tidal fields in Eulerian space [48, 16, 202] and [155, 133, 5] in Lagrangian space. These new terms, with abuse of notation, have been called non local bias coefficients, since they contain gradients of the the density field or of the gravitational potential. Additionally, works such as [69, 180, 29, 18, 46] show the presence of a scale dependent bias term at linear level and its measured value agrees fairly well with analytical models of structure formation [180, 46].

Recently [239] have shown that at 1-loop in Lagrangian Effective Perturbation theory, the measurements in redshift space of the halo multipoles are very well described if one adopts the bias expansion to second order and we will work to this order in this thesis.

$$\delta_h(\mathbf{x}) = b_1\delta_m(\mathbf{x}) + \frac{b_2}{2}[\delta_m^2(\mathbf{x}) - \langle\delta_m^2(\mathbf{x})\rangle] + b_{s^2}[s^2(\mathbf{x}) - \langle s^2(\mathbf{x})\rangle]\,, \tag{1.27}$$

where $s^2$ is the tidal tensor field

$$s^2(\mathbf{x}) \equiv \sum_{ij} s^2_{ij}(\mathbf{x}) \ , \ \ s^2_{ij}(\mathbf{x}) = \Big(\frac{\partial_i \partial_j}{\partial^2} - \frac{1}{3}\delta^K_{ij}\Big)\delta_m(\mathbf{x}) \ , \tag{1.28}$$

where the indices $i, j$ run over all the three directions.

## Halo Finding Algorithms

As with perturbation theory, while the bias model analytically describes the halo and galaxy distribution well enough on large scales, it breaks down on small scales. This modeling is further complicated in redshift space. There are also many recent works which suggest that the halo and galaxy bias depends on secondary properties such as halo environment, concentration and others in addition to the halo mass [143].

At the same time, bias model primarily models the ensemble clustering of these objects and does not identify individual properties of a single object. Thus we turn to N-Body simulations which accurately capture the evolution of underlying dark matter and provide a way of accurately modeling the halo and galaxy field computationally.

Halo finders mine the N-body data to find locally over-dense gravitationally bound systems and generate dark matter halo catalogs. They contain dark matter halos (or groups of dark matter particles) and their intrinsic properties, like position, velocity, mass and radius, amongst other things. While there are many variants of halo finding algorithms currently being used in cosmology, they are primarily built around one of the following two approaches [129].

The first approach is Friends of Friends approach [66]. This method connects and links together all the particles close together to each other i.e. if their distance lies below a certain threshold, called "linking length". This means that the distances of particles at the boundary of such a linked object (a "FOF group") are smaller or equal than the linking length, corresponding to a density threshold. These distances can be defined either in in a 3D configuration or in 6D phase-space. Once they exhaust linking all the particles in a particular group, they then determine the properties of the halo such as its center, velocity and mass as an aggregate of all the particles.

The other approach in based on Spherical Overdensity method [192]. This approach begins by identifying a local density peak in the matter field by whatever means/ Then about these centres, spherical shells are grown out to the point where the density profile drops below a certain pre-defined threshold, normally derived from a spherical top-hat collapse. Once the halo boundary is defined, subsequent properties of every halo can be determined.

## Halo Galaxy Connection

Dark matter forms the skeleton on which galaxies form, evolve, and merge. The growth, internal properties, and spatial distribution of galaxies are thus likely to be closely connected to the growth, internal properties, and spatial distribution of dark matter halos. This physical and statistical connection between them, the *galaxy–halo connection*, allows us to populate the halo catalogs of N-Body simulations with galaxies and match the observed large scale structures of the Universe. A recent review on various approaches in the literature can be found at [248].

This modeling can broadly be categorized in two basic approaches - empirical modeling, which models this relationship in a parametric form and constrains the parameters to match observed data; and physical modeling, which either directly simulates or parametrizes the physics of galaxy formation such as gas cooling, star formation, and feedback inside a halo. Incorporating physical modeling into a complete cosmological analysis is still computationally expensive since they either involve full hydrodynamical simulations or involve a large number of parameters to model these basic processes of galaxy formation by approximating various physical processes with analytic prescriptions.

The empirical models are primarily one of the two types -

i) *(Subhalo) Abundance Matching* - In its simplest forrm, this approach makes the most basic assumption that the more massive galaxies live in the more massive dark matter halos and subhalos [131, 235]. Alternatively, instead of matching mass directly, one can abundance match another halo property to a galaxy property with some scatter amongst the two. This scatter is determined to best match the observations. Properties of galaxies such as their positions and velocities are determined primarily based on the subhalos they occupy. Abundance matching is appealing since to a large extent, it is a non-parametric approach. However to be able to match subhalos, we require high-resolution simulations to be able to resolve substructures and accurate merger trees of the halos.

ii) *Halo Occupation Distribution (HOD)* - This approach specifies a probability distribution for the number of galaxies meeting some criteria (for example, a luminosity or stellar mass threshold) in a halo. While traditionally this has been conditioned on halo mass $P(N|M)$, recent works have suggested conditioning on secondary halo properties as well. Typically this PDF is quantified separately for the central galaxies of halos and the satellite galaxies, former with a Bernoulli distribution and latter with a a Poisson distribution [262]. Properties such as positions and velocities of the galaxies are also often modeled with parametric relations. To determine the luminosity and stellar masses of the galaxies, one can also parametrize the conditional luminosity function (CLF) of the centrals and satellites for a given halo mass [257]. Given these distributions, galaxy catalogs can be generated from halo catalogs using a Monte Carlo approach in a simulation. Alternatively, these distributions can be combined with an analytic halo model of dark matter clustering to make predictions for some observed statistics analytically.

To constrain the various parameters and validate different halo galaxy-halo connection, we match the models against various cosmological observations. Of these, the primary observations are [248]: i) galaxy abundances - the abundance of galaxies as a function of stellar mass or luminosity, i.e., the stellar mass function (SMF) or the luminosity function, ii) two point clustering of the galaxies iii) group and cluster catalogs i.e. finding individual dark matter halos observationally and measuring the galaxy content within them iv) weak gravitational lensing to measure the cross-correlation between galaxies and matter.

## 1.4 Analysis

### Two point clustering

The most obvious way to measure the underlying structure in large scale structures is to quantify how the entire distribution of galaxies differs from what would otherwise be expected of a random Poisson distribution. This makes two point clustering statistics are the most ubiquitous quantitative measure of large scale structures. (Auto) Correlation function ($\xi$) describes the excess probability of finding two galaxies separated by a distance (excess over and above the probability that would arise if the galaxies were simply scattered independently and with uniform probability). Thus it measures clumpiness of the Universe on different scales, and since the Universe is isotropic, it is a function of only length scale $r$.

$$\xi(r) = \langle \delta(\mathbf{x})\delta(\mathbf{x}+\mathbf{r}) \rangle \tag{1.29}$$

where $\delta$ is the matter overdensity. The fourier transform of correlation function is 3D matter power spectrum $P(k)$. Since the matter distribution in the Universe is stationary, isotropic and homogenous, its Fourier modes are uncorrelated. Thus if the autocorrelation function describes the probability of a galaxy at a distance $r$ from another galaxy, the matter power spectrum decomposes this probability into characteristic lengths, $k \approx 2\pi/L$, and its amplitude describes the degree to which each characteristic length contributes to the total over-probability. Power spectrum can equivalently be defined by averaging the Fourier modes $\delta(\mathbf{k})$

$$(2\pi)^3 P(k)\delta_D(\mathbf{k}-\mathbf{k}_0) = \langle \delta(\mathbf{k})\delta^*(\mathbf{k}_0) \rangle \tag{1.30}$$

where $\delta_D$ is the Dirac delta function.

Figure 1.3 shows the matter power spectrum (left), comparing theoretical prediction with measurements from different tracers of the large scale structure. The right panel shows the correlation function compared from N-Body simulations and fit to different perturbation theory models.

The overall shape of the matter power spectrum is best understood in terms of perturbation theory analysis of the growth of structure discussed in the previous section. At first order, the power spectrum simply grows as -

$$P(k,t) = D_+^2(t)P_0(k) \tag{1.31}$$

where $P_0$ is the primordial matter power spectrum which is related to the matter distribution at the end of inflation. Galaxies and halos are biased tracers of the underlying dark matter. At first order, their distribution is simply a linear response to underlying matter density field $\delta_h = b_1\delta_m$ and thus halo power spectrum is simply

$$P_{hh} = b_1^2 P_{mm} \tag{1.32}$$

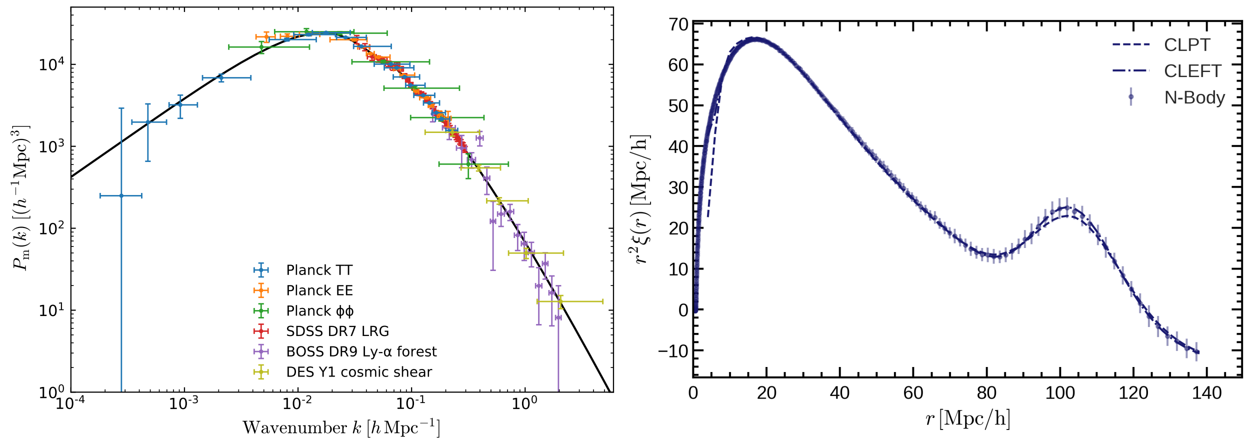


(a) 1a (b) 1b

Figure 1.3: (Left) Real space matter power spectrum. with measurements from various surveys probing LSS of the Universe. Figure taken from [6]. (Right) Matter correlation function in real space. Figure taken from [60]

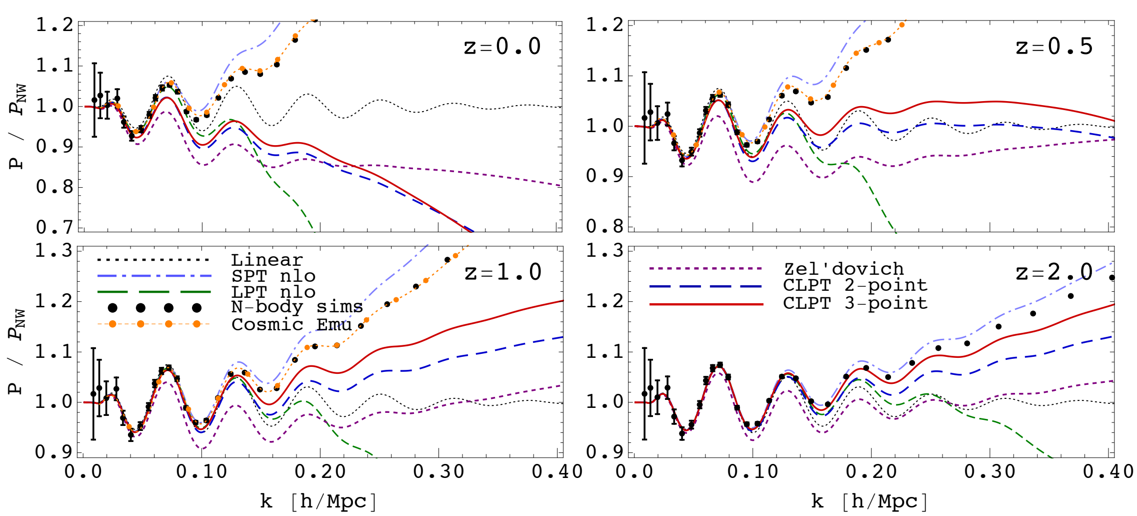


Figure 1.4: Modeling matter power spectrum in real space at different redshifts. We show results from N-Body simulation, along with linear theory, Eulerian and Lagrangian perturbation theories at different orders and Cosmic Emu emulator. Figure taken from [242]

and correspondingly for the correlation function.

The first order predictions are valid on large scales which evolve linearly and on to model the power spectrum on quasi-linear scales, one needs to go to higher orders in perturbation theory. For biased tracers i.e. halos and galaxies, one also needs to include higher order bias parameters such as $b_2, b_{s^2}$ etc. Even then, these analytic models are unable to fit the clustering on smaller, non-linear scales. This is shown in Figure 1.4 which compares the clustering of dark matter in real space in N-Body simulations with different perturbative models and emulator different epochs in real space. Even in this simplest scenario, models break down on quasi linear scales, with predictions degrading at lower redshifts when the evolution becomes increasingly non-linear. This failure of analytic models on modeling clustering in non-linear regime is one of the motivations for the work presented in this thesis.

## Redshift Space Distortions

It is important to realize that cosmological surveys do not observe radial distance to the objects, but their redshifts. In principle these are related by the Hubble expansion but the observed redshifts of objects is also affected by their peculiar velocities. This leads to *redshift space distortions* (RSD) and needs to be accounted with modeling the clustering of tracers [102].

On very large scales, objects fall in towards overdense regions. This makes the objects between us and the overdensity appear to be further away (closer to overdensity) and objects on the other side appear closer. The net effect here is to enhance the overdensity and this effect is called "Kaiser effect" [124]. On these scales, these effects can be modeled with linear theory of perturbations and the clustering is simply

$$P_{hh}(k,\mu) = b_1^2 P_{mm}(k)(1 + f\mu^2)^2 \tag{1.33}$$

where $f$ is the logarithmic growth rate (Eq. 1.13) and $\mu$ is the angle between the line-of-sight. Taking angular average, we see that the overall clustering has enhanced on the large scales where the linear theory approximation is valid. However since RSD effects make the observed clustering anisotropic, we also measure the multipoles of power spectrum or power spectrum in angular wedges. As in real space clustering, going to higher orders in perturbation theory and bias parameters is necessary to push to smaller scales in modeling redshift space clustering.

Due to its sensitivity to the logarithmic growth rate $f$, clustering in redshift space is sensitive to the growth of structures and hence will be critical in measuring dark energy as well as constraining modified gravity theories [249].

While clustering is enhanced on large scales due to RSD, a different effect takes place on small scales within a galaxy cluster. Random, virialized motion smears out the redshifts of different galaxies, making them appear stretched out along the line of sight and leads to the so called *Fingers-of-God* effect [116]. This smearing out washes away the clustering signal on these small scales and hence limits the usefulness of RSD. The situation is further

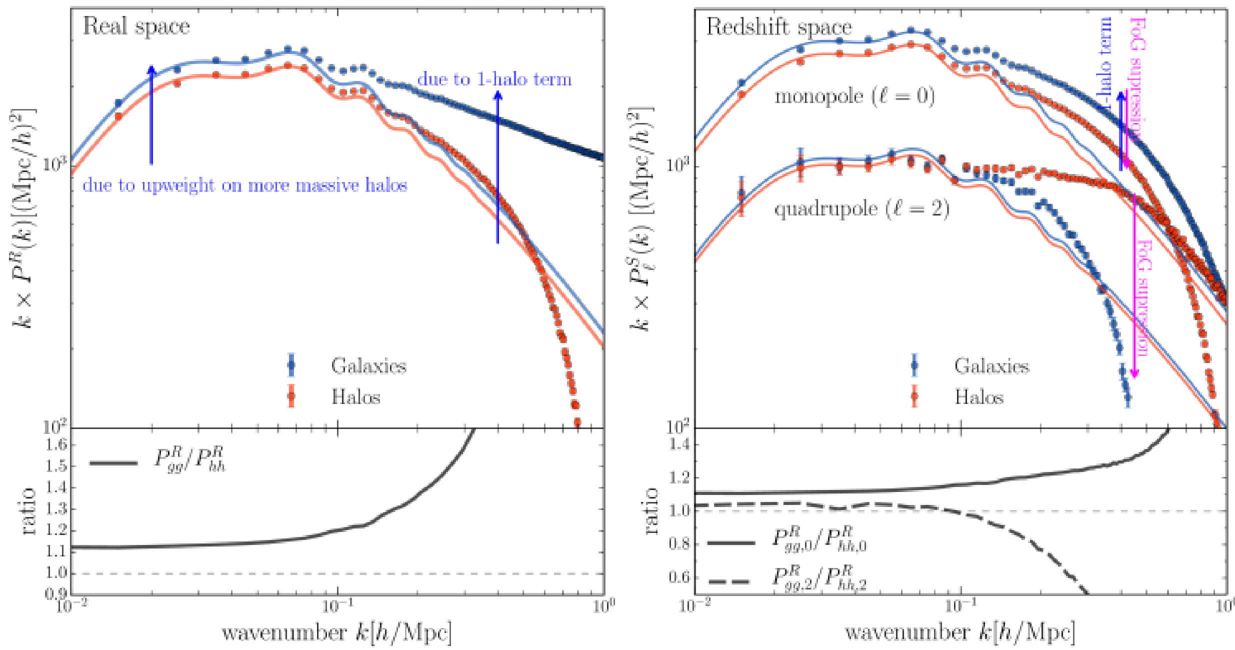


(a) 1a

(b) 1b

Figure 1.5: (Left) Halo (red) and galaxy (blue) power spectrum in real space. Solid lines are perturbation theory fits and points are N-Body simulations. (Right) Halo and galaxy power spectra, monopole and quadrapole, in redshift space. FOG suppression on small scales is clearly visible in case of galaxies. Figure taken from [175].

exacerbated by the highly non-linear nature of this effect which makes analytic modeling challenging. If we observe only dark matter halos, or central galaxies at halo centers, this effect will not be dominant. However since we also observe satellite galaxies which undergo virial motion, this effect becomes a nuisance on small scales. The impact of clustering due to redshift space distortions on dark matter halos and galaxies is shown in Fig. 1.5.

One of the goals of works presented in this thesis is to develop forward models for the observables of LSS. Thus these forward models need to promote the observables from real to redshift space correctly accounting for both these effects.

## Baryon Acoustic Oscillation

Baryon acoustic oscillations (BAO) are fluctuations in the density of the visible baryonic matter caused by acoustic density waves in the primordial plasma of the early universe [76]. These acoustic waves are created due to the counteracting forces of gravity and pressure in this primordial soup of dark matter, baryons and photons. While the region of overdensity gravitationally attracts matter towards it, the heat of photon-matter interactions creates a large amount of outward pressure. These spherical waves of baryons and photons propogate

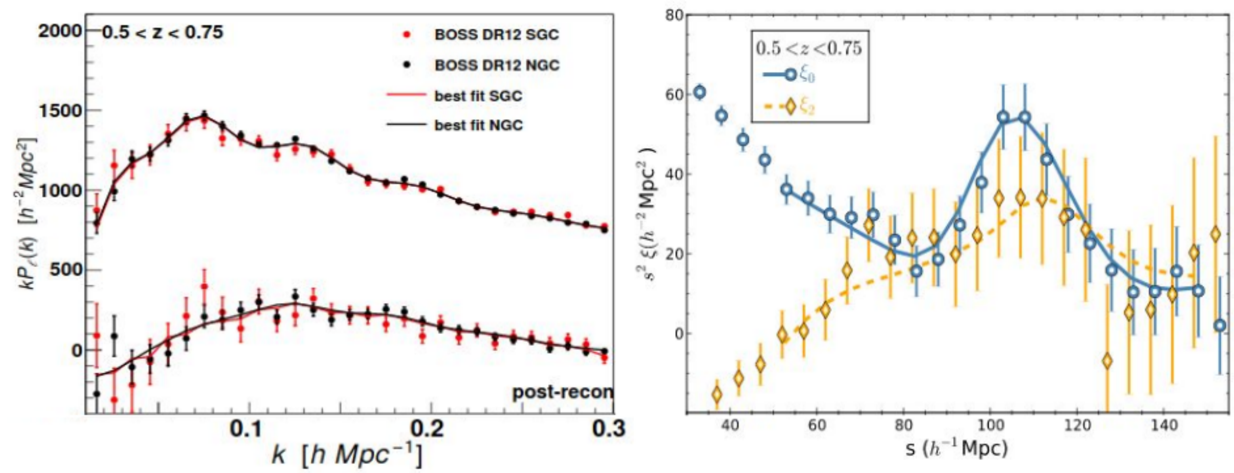


Figure 1.6: Baryon acoustic oscillations in SDSS-BOSS survey, data release 12, between redshift $0.5 < z < 0.7$. Lines are best fits and markers are observed data points. (Left) BAO in the power spectrum as wiggles in the monopole, and in quadrapole. We separately show SGC and NGC data. Figure taken from [27] (Right) BAO as the peak in correlation function monopole and quadrapole. Figure taken from [199].

outwards from the overdense regions while the dark matter interacts stays at the central overdensity since it interacts only gravitationally. This wave of photons and baryons travels together until decoupling, after which the photons diffuse away and leave behind a shell of baryonic matter. The distance traveled by the sound waves until decoupling, i.e. the radius of this shell, is referred to as 'sound horizon'. As structure formation proceeded under gravitational interaction of baryons and dark matter after decoupling, total matter pertrubations peaked at both the center (with dark matter) and the radius of these baryonic shells. Thus these anisotropies become preferential sites sites for galaxy formation, and we expect to see a greater number of galaxy pairs separated by the sound horizon distance scale than by other length scales.

Over the last decade, BAO has emerged as one of the dominant techniques for LSS analysis [27, 199]. One of the reasons for this is that the physics of the propagation of the baryon waves in the early universe is fairly simple and well understood. This prediction can be combined with CMB radiation which carries an imprint of these waves at the time of decoupling. As a result, the sound horizon scale can be determined to high accuracy and provides a 'standard ruler' for length scale in cosmology. In BAO analysis at lower redshifts, we compare the clustering observed in transverse and line of sight direction with this standard ruler to measure the angular diameter distance ($D_a(z)$) and Hubble parameter ($H(z)$) respectively.

Fig. 1.6 shows the Baryon acoustic oscillation as its observed in the clustering analysis. In correlation function monopole, it stands out as a peak centered at the sound horizon scale

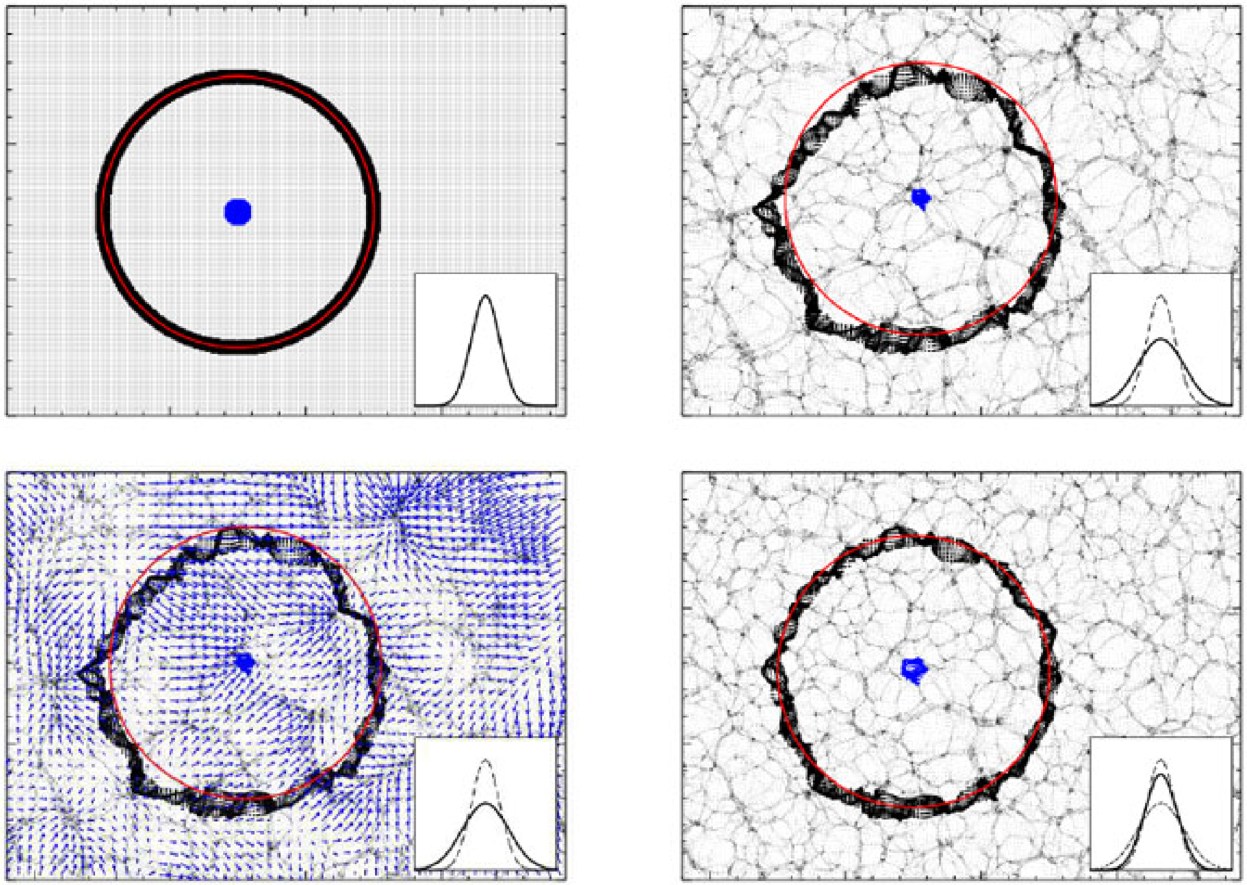

Figure 1.7: Damping and reconstruction of BAO (Top Left) Sharp BAO peak feature at the time of decoupling. (Top Right) Broadening of BAO peak due to displacement of galaxies under gravity. (Bottom Left) Estimated Zeldovich displacements to undo the non-linear evolution of the galaxies. (Bottom Right) Reconstructed density field and sharpened BAO peak. Figure taken from [179].

($\sim$ 100 Mpc/h). In power spectrum monopole, BAO results in oscillations over otherwise smooth power spectrum, as is expected by the Fourier transform of a peak in the correlation function.

Despite being a robust feature in the clustering of galaxies, BAO feature is damped at lower redshifts as compared to decoupling. This is due to the non-linear gravitational evolution resulting in displacement of galaxies that shifts and broadens the BAO peak in correlation function and correspondingly damps the oscillations as seen in power spectrum. This reduces the signal to noise of this measurement and loss of information that can be extracted. If we could estimate the displacement of these galaxies, one can imagine moving them backwards to their original positions to enhance BAO signal [73, 179]. This undoing of non-linear evolution and *reconstruction* of a more linear field has become a standard practice in BAO analysis. The standard reconstruction method estimates Zeldovich displacement of the galaxies based on their observed position and corresponding matter field to move back galaxies. Figure 1.7 illustrates this broadening and corresponding reconstruction of BAO peak. Even though this is not the the correct displacement, its reasonably accurate over large scales and increases significance of BAO measurement by a factor of few [**Seo16**, 215]. Since then, several other works have proposed modifications and alternate methods to do BAO reconstruction [211, 207, 263, 156, 30].

The main objective of this thesis work is develop a framework for reconstruction of cosmological fields in the similar spirit to enhance cosmological information, but not limited to only BAO analysis.

## 1.5 Other Probes of Large Scale Structures

Large scale structures probe the 3D distribution of matter at low redshifts and complement the early Universe cosmic microwave background radiation. So far we have focused only on galaxy surveys which measure the position of the nearest galaxies as perhaps the most obvious means for surveying the large-scale structure in the universe. In this section, we briefly touch upon other probes for LSS, especially those for which the formalism of forward modeling and reconstruction developed in this thesis can be extended to.

### Lyman Alpha Forest

The Lyman-alpha forest is a series of absorption lines in the spectra of distant galaxies and quasars [97]. These lines are thought to arise due to absorption of the quasar continuum by clouds along the line of sight which contain (sometimes trace amounts of) neutral hydrogen, leading to Lyman series transition of electron between ground state and higher energy levels. The most prominent of these is the Lyman-alpha line of rest wavelength 121.6 nm which corresponds to an electron transitioning between the ground state (n = 1) and the first excited state (n = 2).

Due to the expansion of the Universe, the quasar light redshifts as propagates through the Universe. Thus neutral hydrogen clouds in the intergalactic medium at different distances from Earth absorb different wavelengths in the observed spectrum. Each individual cloud leaves its fingerprint at the unique wavelength that corresponded to Lyman alpha wavelength at its redshift. Thus one can use the absorption map to plot the positions of region of intervening hydrogen between us and the quasar and construct a map of the Universe.

Lyman alpha systems are determined by three parameters; its position in redshift space, its hydrogen column density (number of neutral hydrogen atoms per area), and line width determined by gas temperature and turbulent pressure. These parameters determine the entire absorption profile, consisting of a convolution of a Lorentzian resonance curve and a Maxwell-Boltzmann velocity distribution, known jointly as the Voigt profile [65].

The Lyman Alpha forest is a powerful cosmological probe as, on small spatial scales ($\sim$ 1 Mpc/h) where the thermal pressure of the gas is not important. On these scales the intergalactic medium traces the underlying dark matter mass distribution much more closely than the stellar light of galaxies. Being able to agree with observations on these small scales is a point in favor of cold dark matter model and one cannot have too much hot dark matter since it erases structure on small scales [114]. Lyman alpha forests are also excellent probes for tracing LSS at high redshifts where observed galaxies are much more sparse and would likely be highly biased since only the brightest galaxies can be observed. Traditionally, most of this information is extracted by measuring one-dimensional flux power spectrum as a function of redshift $P_F(k, z)$ [59]. With recent surveys like DESI [68] and CLAMATO [134], as the number density of sight-lines is increasing, one can go beyond 1-D power spectrum to measure 3D correlations in nearby sight-lines [89].

## Weak Lensing

When observing galaxies and other distant objects, intervening matter along the line of sight gravitationally bends the light and distorts their shape and position via a phenomenon called gravitational lensing [141]. This distortion can be split into terms - the convergence term that magnifies the background objects by increasing their size, and the shear term that stretches them tangentially around the foreground mass. The amount of this shear and magnification depend on the integral of the gravitational potential along the line of sight and a geometric function which depends on the redshift of the source and peaks midway between the source and the observer. Since gravitational potential is not sensitive to the dynamical state of the intervening masses, lensing yields a direct measure of the total matter, dark plus luminous. Distortions in this regime are generally very small and cannot be detected on individual galaxies. Thus weak lensing is an intrinsically statistical measurement and these distortions are detected only statistically, by averaging over a large number of galaxies. At the same time, its plagued by various systematics such as shape noise, point spread function, photometric redshift errors to name a few, which make the analysis quite challenging [141].

Cosmic shear is the gravitational lensing by large-scale structure that produces an observable pattern of alignments in background galaxies [125]. This distortion is only 0.1%-1% - much more subtle than cluster or galaxy-galaxy lensing. To detect this, one computes shear correlation functions which measure the mean product of the shear at two points as a function of the distance between those points. Cosmic shear is a very versatile probe of the LSS since it measures the clustering of the LSS from the highly non-linear, non-Gaussian sub-Mpc regime, out to very large, linear scales. By measuring galaxy shape correlations between different redshifts, the evolution of the LSS can be traced, enabling us to detect the effect of dark energy on the growth of structure. Since it is also sensitive to the geometry of the Universe, cosmic shear can potentially distinguish between dark energy and modified gravity theories [113, 249].

In contrast to cosmic shear, galaxy-galaxy lensing (GGL) correlates shapes of high-redshift galaxies with positions of galaxies at lower redshift [189]. The resulting weak-lensing correlation singles out the mass associated with the foreground galaxy sample and probes the galaxy halo from several length scales. This probe is also particularly powerful when combined with other observations of properties of the foreground galaxy sample, such as galaxy correlations, cosmic shear and others [3]. This combination of observables allows for detailed and quasi-model-independent analyses of the relation between luminous and dark matter and tests of gravity. Repeating this analysis by dividing the survey into multiple redshift bins, with the low-redshift bins lensed by structures very near to us, while the high-redshift bins lensed by structures over a wide range of redshift allows us to map the 3D distribution of mass and is dubbed "cosmic tomography" [113, 108].

## 1.6 Outline of this Thesis

Due to the sheer number of modes that can be observed in the three-dimensional map of the Universe, there is a vast amount of statistical information in the large scale structures of the Universe. We are investing a large amount of resources as a community in collecting this information with current and upcoming large scale imaging surveys such as the Dark Energy Survey (DES[1]), Dark Energy Spectroscopic Survey (DESI[2]), Large Synoptic Survey Telescope (LSST[3]), Euclid[4] and WFIRST[5], to name a few. Developing novel analytic methods to maximize the information extracted from this unprecedented data is the focus of this thesis.

As seen by mode counting arguments, a large fraction of this information is present in the small scales. These are highly non-linear and current analytic methods are unable to describe these modes accurately, thus forcing us to rely on on computational forward models. Most of the focus so far has also been on using the two-point function of the nonlinear modes to extract information. However these statistics are not optimal since there is information in higher order statistics as well. Because of this the two point function analysis is sometimes supplemented with additional, likely complementary statistics such as three point function/bispectrum, various void statistics, topology statistics, counts of objects like clusters or other density peaks etc. Combining the different statistics creates a significant problem of modeling their joint error distribution.

The objective of this thesis is to develop a framework for the analysis of large scale structures with reconstruction of cosmological fields in a forward model framework. We have already seen the power of reconstruction in case of Baryon acoustic oscillations wherein undoing non-linear motion of galaxies improves the constraints by a factor of few. One of the primary, but not the only, goals of reconstruction in our approach is to reconstruct the complete initial, linear field. Since the initial density modes are assumed to be Gaussian, their power spectrum is a lossless summary statistic, which should contain all the information present in the data (with an exception of cosmological parameters that may be required to

[1] https://www.darkenergysurvey.org/
[2] http://desi.lbl.gov/
[3] https://www.lsst.org
[4] http://sci.esa.int/euclid
[5] https://wfirst.gsfc.nasa.gov

map from the initial modes into the final data). In addition, one can also reconstruct observed or unobserved underlying fields such as non-linear dark matter field, velocity field or de-noise the observed data field to enhance the signal to noise ratio.

We approach this reconstruction with a Bayesian formalism in a forward model framework. Our strategy will be to optimize the likelihood of the observed data (and maximize the corresponding posterior of initial conditions). This will require solving challenging optimization problems in mulit-million dimensional space and we develop novel differentiable forward models to assist with this. While computationally expensive, forward modeling frameworks are appealing since they allow us to mimic exactly how we connect theory to observed data and capture all the uncertainties and systematics directly as part of the analysis pipeline. Computational forward models also have the capacity to go beyond the analytic methods discussed in the previous sections. Lastly, they also make it possible to combine different cosmological observables organically while sharing the common underlying elements.

The outline of this thesis is as follows - In chapter 2, we will discuss some differentiable forward models that will be later used in subsequent chapters. In chapter 3, we will develop the our approach for Bayesian reconstruction of initial conditions as well as their power spectrum and demonstrate it on dark-matter data from N-Body simulations. We build upon this in chapter 4 by developing a differentiable neural network model to connect underlying dark matter with halos, which are proxies for galaxies observed in imaging survey, and use it to reconstruct the initial field. In chapter 5, we move away from initial density reconstruction and instead focus on reconstruction to de-noise the observed data in context of 21-cm intensity mapping. Here we also introduce a Hidden Valley Simulations, a suite of high resolution N-Body simulations and develop models to simulate HI clustering. Finally, in chapter 6, we introduce FlowPM, a GPU-accelerated, distributed, and differentiable N-Body solver in TensorFlow that naturally interfaces with the most advanced machine learning tools. This will enable the community to efficiently solve large scale cosmological inference problems, in particular differentiable forward models and the reconstruction of cosmological fields.

# Chapter 2

# Differentiable Forward Models in Cosmology

Sections of this chapter were originally published in

> Reconstructing large-scale structure with neutral hydrogen surveys
> *Modi C., White M., Slosar A., Castorina E. (arXiv:1907.02330)* JCAP 11(2019)023
>
> Cosmological Reconstruction From Galaxy Light: Neural Network Based Light-Matter Connection
> *Modi C., Feng Y., Seljak U. (arXiv:1805.02247)* JCAP10(2018)028
>
> Towards Optimal Extraction of Cosmological Information from Non-linear Data
> *Seljak U., Aslanyan G., Feng Y., Modi C. (arXiv:1706.06645)* JCAP 12(2017)009
>
> Halo Bias in Lagrangian Space: Estimators and Theoretical Predictions
> *Modi C., Castorina E., Seljak U. (arXiv:1612.01621)* MNRAS 472,3959 (2017)

The main goal of this thesis is to develop a framework for reconstruction of cosmological fields in the forward model framework. When approached in a Bayesian formalism, this requires optimizing the likelihood of the observed data given initial matter density field at the beginning of the Universe. Since its a high dimensional optimization problem, the forward model connecting the observed data and initial density field needs to differentiable. In this chapter, we discuss the differentiable forward models that will be used in the next chapters of this thesis. We will first discuss particle mesh simulations to evolve initial dark matter field under gravity and generate the non-linear, Eulerian dark matter field. Next we will discuss modeling dark matter halos and galaxies with bias models as well as neural network models.

## 2.1 Particle Mesh Simulations

We begin with N-Body simulations that evolve billions of dark matter particles under gravitational forces to model the large scale structures of the Universe at late times. While the full N-body simulations can provide very precise predictions, they are extremely slow and computationally expensive since in naive implementation, they will require computing gravitational force between $\sim N^2$ particle pairs. As a result they are usually complemented by fast approximated numerical schemes to estimate forces on the particles. such as Particle-Mesh (PM) solvers [153, 229, 251, 83, 115].

In particle mesh approach, simulation particles are interpolated on a regular 3D grid with some interpolation scheme, weighted with their mass. The gravitational forces experienced by dark matter particles can then be computed by Fast Fourier Transforms as a solution to the Poisson equation. This makes PM simulations very computationally efficient and scalable, at the cost of approximating the interactions on small scales close to the resolution of the grid and ignoring the force calculation on sub-resolution scales. This interpolation to-and-from PM grid and efficient FFTs to estimate gravitational forces form key elements of all PM algorithms as well as Lagrangian perturbation theory fields [229, 127, 224].

In this work, we will use FastPM scheme of [83] to evolve dark matter from the initial redshift to the final redshift. FastPM generates non linear dark matter and halo fields in a quick way, employing a number of approximations to reproduce the results of full N-body simulation. Despite its approximate nature, in [83] it was shown that the code performs extremely well on various benchmarks such as dark matter power spectrum, the halo mass function and halo power spectrum. For further technical details on the choices and accuracy of the implemented FastPM scheme, we refer the reader to the original paper of [83]. We will use high-resolution simulation with many time steps to to generate data as well as low-resolution, few time-step simulations for reconstruction.

### Generating Initial Conditions

Before doing any simulation, we need to generate the initial conditions for the positions and velocity of dark matter particles at initial redshift $z_i$. We do this by using Lagrangian perturbation theory as described in the previous chapter. Briefly, we follow the following steps on a cubic box of $N^3$ grid points which represent the Lagrangian coordinate $\mathbf{q}$. For any field $f$, $f(\mathbf{q})$ represents the field in configuration space, on this Lagrangian grid, and $f(\mathbf{k})$ is the corresponding field in Fourier space obtained with Fast Fourier transforms.

- Generate random initial Gaussian density field $\delta(\mathbf{q})$ such $\delta(\mathbf{k})$ is Hermitian field with $\delta(\mathbf{k}) = \delta_r(\mathbf{k}) + i\delta_i(\mathbf{k})$ and $\langle \delta_{i,r} \rangle = 0$, $\langle \delta_{i,r}^2 \rangle = \sqrt{VP/2}$ where $V$ is the volume of the box and $P(k) = P(k, z_i)$ is the linear power spectrum generated from CAMB at redshift $z_i$.

- At first order in LPT, Lagrangian displacement is $\nabla_q \mathbf{\Psi}^{(1)}(\mathbf{q}, z_i) = -\delta_1(\mathbf{x}, z_i)$. In Fourier space, this is easily estimated with

$$\mathbf{\Psi}^{(1)}(\mathbf{k}, z_i) = i\mathbf{k}\frac{\delta_1(\mathbf{k}, z_i)}{k^2} \tag{2.1}$$

Then we move particles at each grid point $\mathbf{q}$ by the displacement vector at that point

$$\mathbf{x} = \mathbf{q} + \mathbf{\Psi}^{(1)}(\mathbf{q}, z_i) \tag{2.2}$$

and assign velocity

$$\mathbf{v} = f_1(z_i)\mathcal{H}(z_i)\mathbf{\Psi}^{(1)}(\mathbf{q}, z_i) \tag{2.3}$$

- At second order in LPT, we need to estimate second order Lagrangian potential

$$\phi^{(1)}_{,ij}(\mathbf{k}) = -k_i k_j \phi^{(1)}(\mathbf{k}, z_i) = \frac{k_i k_j \delta_1(\mathbf{k}, z_i)}{k^2} \tag{2.4}$$

These are then Fourier transformed to configuration space to generate

$$F(\mathbf{q}) = \frac{1}{2}\sum_{i,j=1,2,3}\left[\phi^{(1)}_{,ii}(\mathbf{q})\phi^{(1)}_{,jj}(\mathbf{q}) - (\phi^{(1)}_{,ij}(\mathbf{q}))^2\right] \tag{2.5}$$

Then the second order displacement is

$$\mathbf{\Psi}^{(2)}(\mathbf{k}, z_i) = \frac{3}{7}[\Omega_m(z_i)]^{-1/143}\frac{i\mathbf{k}F(\mathbf{k}, z_i)}{k^2} \tag{2.6}$$

and this gives the position and velocity to second order as

$$\mathbf{x} = \mathbf{q} + \mathbf{\Psi}^{(1)}(\mathbf{q}, z_i) + \mathbf{\Psi}^{(2)}(\mathbf{q}, z_i) \tag{2.7}$$

$$\mathbf{v} = f_1(z_i)\mathcal{H}(z_i)\mathbf{\Psi}^{(1)}(\mathbf{q}, z_i) + f_2(z_i)\mathcal{H}(z_i)\mathbf{\Psi}^{(2)}(\mathbf{q}, z_i) \tag{2.8}$$

To generate initial conditions of the simulation, the initial redshift $z_i$ is set at earlier times, often $z_i > 10$. However we also consider ZA and 2LPT forward models for evolution of dark matter. In this case, these perturbative approximations are extrapolated to non-linear regimes and we set $z_i$ to late-time redshifts of the observables directly.

## The FastPM particle mesh N-body solver

Once the initial conditions of the positions and velocities of the particles are generated, we can integrate the equations of motion to do N-Body evolution. In FastPM, this time integration for gravitational evolution is implemented as a symplectic series of Kick-Drift-Kick operations [193] starting from the initial conditions to the observed large scale structures at the final time-step. In the *Kick* stage, we estimate the gravitational force on every particle and update their momentum $p$. Next, in the staggered *Drift* stage, we displace the particle to update their position ($x$) with the current velocity estimate. Thus, we can write the drift and kick operators as -

$$x(t_1) = x(t_0) + p(t_r)\mathcal{D}_{\mathrm{PM}} \tag{2.9}$$

$$p(t_1) = p(t_0) + f(t_r)\mathcal{K}_{\mathrm{PM}}, \tag{2.10}$$

where $\mathcal{D}_{\mathrm{PM}}$ and $\mathcal{K}_{\mathrm{PM}}$ are scalar drift and kick factors and $f(t_r)$ is the gravitational force. The vanilla PM scheme fails to reproduce linear theory growth on large scales for small number of time-steps [229, 115] and FastPM does some modifications to improve accuracy on large scales by modifying the scalar drift and kick operators.

Estimating the gravitational force is the most computationally intensive part of the simulation. In a PM solver, the gravitational force is calculated via 3D Fourier transforms. First, the particles are interpolated to a spatially uniform grid with a kernel $W(x)$ to estimate the mass density (and corresponding overdensity) field at every point in space. The most common choice for the kernel, and the one we implement, is a linear window of unity size corresponding to the cloud-in-cell interpolation scheme [111]. For a cell of size $\Delta x$ at the distnace $x$ from the particle, it assigns mass

$$W(x) = \frac{1}{\Delta x}\begin{cases} 1, & \text{if } |x| < \frac{1}{2}\Delta x \\ 0, & \text{otherwise} \end{cases} \tag{2.11}$$

We then apply a Fourier transform to obtain the over-density field $\delta(\mathbf{k})$ in Fourier space. This field is related to the force field via a transfer function ($\nabla\nabla^{-2}$).

$$f(\mathbf{k}) = \nabla\nabla^{-2}\delta(\mathbf{k}) \tag{2.12}$$

There are various ways to write down the transfer function in a discrete Fourier space, as explored in detail in [111]. The simplest way of doing this is with a naive Green's function kernels ($\nabla^{-2} = k^{-2}$) and differentiation kernels ($\nabla = i\mathbf{k}$). We use this in the previous section to generate initial conditions. Alternatively, FastPM implements a finite differentiation kernel with

$$\nabla^{-2} = \left(\sum_{d=x,y,z}\left(x_0\omega_0\,\mathrm{sinc}\frac{\omega_d}{2}\right)^2\right)^{-1} \tag{2.13}$$

$$\nabla = D_1(\omega) = \frac{1}{6}\Big(8\sin\omega - \sin 2\omega\Big) \tag{2.14}$$

where $x_0$ is the grid size and $\omega = kx_0$ is the circular frequency that goes from $(-\pi, \pi]$.

Once the force field is estimated on the spatial grid, it's interpolated back to the position of every particle with the same kernel $W$ as was used to generate the density field in the first place. This force then updates the velocity in the kick step and we iterate until we reach the observed redshift.

## Derivative of ZA Model

In this section we will show that the particle mesh simulations are differentiable with respect to the initial density field. To it tractable, we only derive the derivative of simple Zeldovich forward model since it captures all the underlying elements of interpolation and Fourier transform that form the basis of any PM simulation. For a multi-step PM simulation, the procedure here can be repeated at each time-step with the chain rule to obtain the derivative of total simulation. The derivatives at 1-LPT level have also been presented in [**Wang14**] and at 2-LPT level in [211] which is the original source of this section.

The density modes of interest are $\boldsymbol{\delta}_j(\mathbf{k})$ where the subscript $j$ is 0 or 1 for the real and complex parts of a Hermitian field respectively. Thus the derivative explicitly summed over all the positions is

$$\begin{aligned}
\boldsymbol{g}_j(\mathbf{k}) &= \sum_{\mathbf{x}} \frac{\partial \boldsymbol{f}_{\boldsymbol{\delta}}(\mathbf{x})}{\partial \boldsymbol{\delta}_j(\mathbf{k})} \rho_d(\mathbf{x}) &(2.15)\\
&= \sum_{\mathbf{k}_1} \frac{\partial \boldsymbol{f}_{\boldsymbol{\delta}}{}^*(\mathbf{k}_1)}{\partial \boldsymbol{\delta}(\mathbf{k})} \rho_d(\mathbf{k}_1), &(2.16)
\end{aligned}$$

where we use $\rho_d(\mathbf{k}_1) = \mathcal{F}\rho_d(\mathbf{x}$ as any generic function in the volume that is assumed to be constant with respect to $\delta(\mathbf{k})$ in this step of chain rule and $\mathcal{F}$ is the Fourier transform $(\sum_x e^{-i\mathbf{k}\cdot\mathbf{x}})$.

The forward model with CIC interpolation of particles from their Eulerian position $\mathbf{r}(\mathbf{q})$ is,

$$\boldsymbol{f}^*_{\boldsymbol{\delta}}(\mathbf{k}_1) = w(R_s k_1) \sum_{\mathbf{x}} e^{i\mathbf{k}_1\cdot\mathbf{x}} \sum_{\mathbf{q}} W(\mathbf{x} - \mathbf{r}(\mathbf{q})), \tag{2.17}$$

where $w(R_s k_1)$ is a smoothing kernel (independent of $\delta(\mathbf{k})$) and $\sum_{\mathbf{q}} W(\mathbf{x} - \mathbf{r}(\mathbf{q}))$ is the CIC kernel assignment.

The ZA forward model calculates the Eulerian positions of the particles to second order in Lagrangian displacement, $\mathbf{r}(\mathbf{q}) = \mathbf{q} + \boldsymbol{\Psi}^{(1)}(\mathbf{q})$. These displacements in Fourier domain are

$$\boldsymbol{\Psi}^{(1)}(\mathbf{k}) = \frac{i\mathbf{k}}{k^2}\delta(\mathbf{k}) \tag{2.18}$$

Thus, the complete derivative is

$$\begin{aligned}
g_j(\mathbf{k}) &= \sum_{\mathbf{k}_1} \rho_d(\mathbf{k}_1) w(R_s k_1) \sum_{\mathbf{x}} e^{i\mathbf{k}_1\cdot\mathbf{x}} \sum_{\mathbf{q}} \frac{\partial W(\mathbf{x} - \mathbf{r}(\mathbf{q}))}{\partial \delta_j(\mathbf{k})} &(2.19)\\
&= \sum_{\mathbf{q}} \frac{\partial \mathbf{r}(\mathbf{q})}{\partial \delta_j(\mathbf{k})} \cdot \sum_{\mathbf{x}} \frac{\partial W(\mathbf{x} - \mathbf{r}(\mathbf{q}))}{\partial \mathbf{r}(\mathbf{q})} \sum_{\mathbf{k}_1} \rho_d(\mathbf{k}_1) w(R_s k_1) e^{i\mathbf{k}_1\cdot\mathbf{x}} \\
&= \sum_{\mathbf{q}} \frac{\partial \boldsymbol{\Psi}^{(1)}(\mathbf{q})}{\partial \delta_j(\mathbf{k})} \cdot \Xi(\mathbf{q}) &(2.20)\\
&= g_j^{(1)}(\mathbf{k}) &(2.21)
\end{aligned}$$

where, we have defined

$$\Xi(\mathbf{q}) = \sum_{\mathbf{x}} \frac{\partial W(\mathbf{x} - \mathbf{r}(\mathbf{q}))}{\partial \mathbf{r}(\mathbf{q})} \sum_{\mathbf{k}_1} \rho_d(\mathbf{k}_1) w(R_s k_1) e^{i\mathbf{k}_1\cdot\mathbf{x}}, \tag{2.22}$$

which can be evaluated using simple Fourier transforms and re-griddings. Then, to first order (1-LPT), this leads to

$$\begin{aligned} g_j^{(1)}(\mathbf{k}) &= \sum_{\mathbf{q}} \frac{\partial \mathbf{\Psi}^{(1)}(\mathbf{q})}{\partial \delta_j(\mathbf{k})} \cdot \Xi(\mathbf{q}) \\ &= \sum_{\mathbf{k}_2} \frac{i\mathbf{k}_2}{k_2^2} \frac{\partial \delta(\mathbf{k}_2)}{\partial \delta_j(\mathbf{k})} \cdot \sum_{\mathbf{q}} e^{i\mathbf{k}_2\cdot\mathbf{q}} \Xi(\mathbf{q}) \\ &= \sum_{\mathbf{k}_2} \frac{i\mathbf{k}_2}{k_2^2} \frac{\partial \delta(\mathbf{k}_2)}{\partial \delta_j(\mathbf{k})} \cdot \Xi^*(\mathbf{k}_2) \end{aligned} \tag{2.23}$$

which leads to the final expression for the most modes

$$g_0^{(1)}(\mathbf{k}) = (2)\frac{\mathbf{k}}{k^2} \cdot \Xi_1(\mathbf{k}) \tag{2.24}$$

$$g_1^{(1)}(\mathbf{k}) = -(2)\frac{\mathbf{k}}{k^2} \cdot \Xi_0(\mathbf{k}). \tag{2.25}$$

while the factor of (2) drops out for the self-conjugating (zero and the nyquist) modes of the hermitian field.

This gives the gradient of ZA forward model with respect to the initial density field, demonstrating that the PM forward models for non-linear evolution of matter field are naturally differentiable.

## 2.2 Bias Model

In this section, will discuss in more detail the the traditional bias forward model to make connection between underlying dark matter and observed halos and galaxies with are discrete, biased tracers. We will work primarily with bias model in Lagrangian space up-to second order including tidal tensor bias

$$\delta_h(\mathbf{x}) = b_1\delta(\mathbf{x}) + \frac{b_2}{2}[\delta^2(\mathbf{x}) - \langle\delta^2(\mathbf{x})\rangle] + b_{s^2}[s^2(\mathbf{x}) - \langle s^2(\mathbf{x})\rangle] \,, \tag{2.26}$$

We first begin by estimating these bias parameters to match the clustering statistics of halos and develop some intuition on their magnitude and scale dependence. There are several ways of estimating these and here we reproduce the Fourier space method from [155] that found the first clear evidence of tidal shear in the bias expansions.

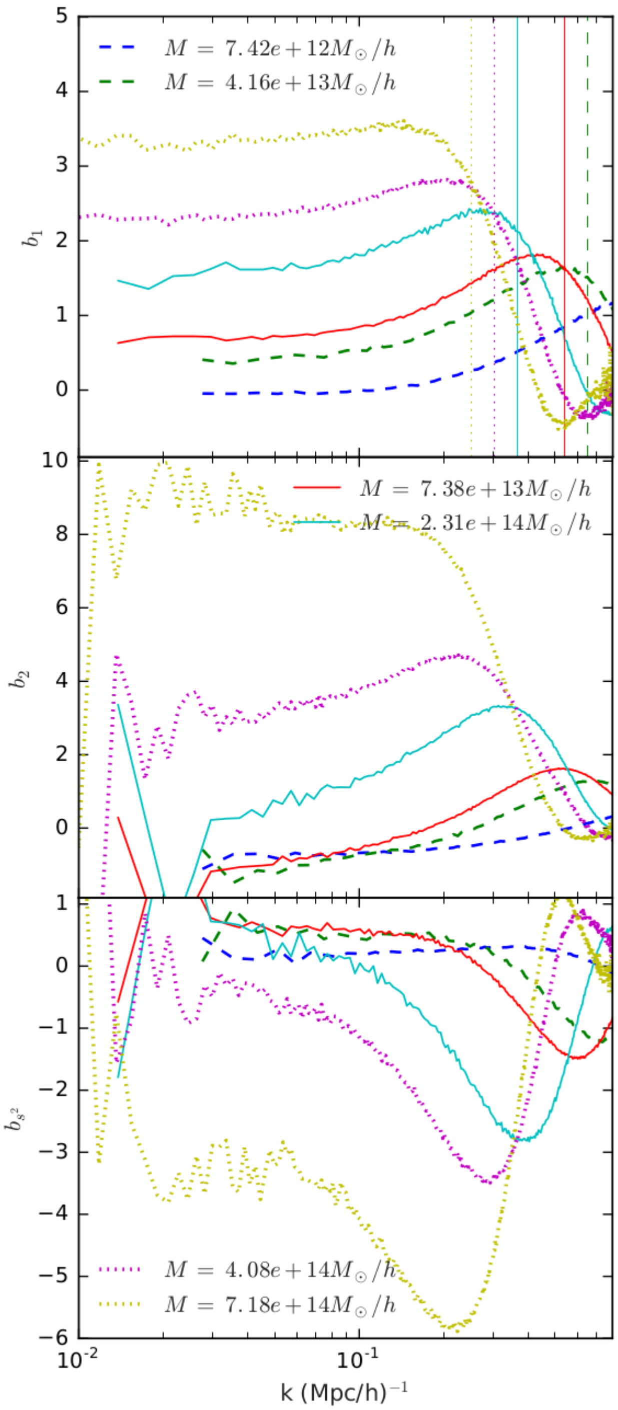


Figure 2.1: **Bias parameters as function of** $k$: We show $b_1$, $b_2$ and $b_{s^2}$ as measured from Fourier space estimator. For clarity, we only show 2 mass bins from every box and different line-styles (dashed, solid and dotted) correspond to different boxes (of size $L = 690, 1380, 3000$ $Mpc/h$ respectively), from which the corresponding mass bins (specified by color) are picked. The dependence on the wavenumber is the shared by all the parameters: constant piece on large scales followed by $k^2$-like piece on intermediate scales followed by a cutoff around the halo scale. This scale is shown with vertical lines in top-panel in corresponding colors for different masses.

## Bias estimation in Fourier space

In this section, and only here, we will refer to the proto-halos as dark matter halo *i.e.* we identify the collection of the particles in the simulation which forms the halo at the final redshift, and this collection of particles mapped to the initial redshift forms our (proto)halo in the Lagrangian space. This mapping is easily achieved by storing the particles ID at each snapshot. Then, to define the proto-halo field, we calculate the center-of-mass of these particles using their positions at the initial conditions and use them as (proto)halo positions.

The easiest thing to measure in Fourier Space is linear bias. One way to estimate it is simply taking the ratio of halo-matter cross spectrum with the matter-auto spectrum.

$$b_1 = \frac{P_{h\delta}}{P_{\delta\delta}} \tag{2.27}$$

where in our notation the power spectrum between the $X$ and $Y$ field reads $P_{XY}$. Throughout this section, we refer to the halo-field with subscript $(h)$ while $(\delta)$ will refer to the Lagrangian overdensity field scaled to z=0 using linear theory. In Figure 2.1, top panel, we show linear bias as measured from our FastPM runs for several halo mass bins. The common features shared by all the halos are: a constant piece on large scales, and then a $k^2$-like piece on intermediate scales followed by a cut off, approximately at the scale of the halo. Similar plots for linear bias can be found for instance in [18].

Next we extend this approach to higher order bias coefficients, and in particular $b_{s^2}$. First, we notice that since the bias relation in Eq. (2.26) is written in real space, any estimators of second order bias coefficients in Fourier space will make use of convolutions, for instance the squared density field is trivially

$$\delta^2(x) = \int \frac{\mathrm{d}^3 k}{(2\pi)^3}\, e^{-i\vec{k}\cdot\vec{x}} \int \mathrm{d}^3 q\, \delta(q)\delta(k-q) \tag{2.28}$$

and an analogous expression holds for $s^2$. We also recall that since the dark matter field is linear in Lagrangian space, cross correlations between the halos and a generic quadratic fields are very easy to write down, as any expectation value involving three fields vanishes. Within the model in Eq. (2.26) we arrive to

$$\begin{aligned} P_{h\delta^2}(k) &= \frac{b_2(k)}{2} P_{\delta^2\delta^2}(k) + b_{s^2}(k) P_{s^2\delta^2}(k) \\ P_{hs^2}(k) &= \frac{b_2(k)}{2} P_{s^2\delta^2}(k) + b_{s^2}(k) P_{s^2 s^2}(k) \end{aligned} \tag{2.29}$$

where for instance

$$\begin{aligned} P_{\delta^2\delta^2}(k) \;&=\; \frac{2k^3}{4\pi^2} \int_{r=0}^{\infty} dr \bigg( \; r^2 P_{\delta\delta}(kr) \times \\ & \int_{x=-1}^{1} dx \;\, P_{\delta\delta}(k\sqrt{1+r^2-2rx}) \bigg) \end{aligned} \tag{2.30}$$

and similar expression can be written for $P_{s^2\delta^2}(k)$ and $P_{s^2s^2}(k)$. However, to be consistent in our approach, we do not evaluate these integrals numerically to estimate bias but evaluate these power-spectra directly from the corresponding simulations we find the halos in.
The linear system of equations in Eq. (2.29) can be solved to obtain a value of $b_2$ and $b_{s^2}$ at each mode $k$ and for different halo populations. (To assist in solving, one can also re-write these equations in terms of $g^2 = s^2 - \frac{2}{3}\delta^2$ to decouple $s^2$ from $\delta^2$, though it is not necessary.) The solution is shown in the two bottom panels of Figure 2.1, which makes clear that the behavior as a function of $k$ we have seen for linear bias also applies to higher order bias coefficients. Scale dependence of non linear bias would have, for instance, to be taken into account for Lagrangian Perturbation theory calculations beyond 1-loop order.

The bottom panel clearly shows that tidal bias is non zero for a variety of halo populations. This has important consequences for cosmological analyses using Lagrangian perturbation theory plus Lagrangian bias ([145, 40, 247, 253, 239]). As already known, $b_2$ is negative for low mass halos and then becomes large and positive for very massive halos. The opposite trend is observed for $b_{s^2}$, which is negative at the high mass end. This is expected, since shear is acting against the formation of the halos, whereas density enhances it. We emphasize that had we started with simply a local bias expansion at second order, we would have gotten different values for $b_2(k)$, in contradiction with the results from other approaches in the literature. The scale independent bias coefficients, such as those in Eq. (2.26), need to be extracted from the large scale values of any bias parameter $b(k)$ in Figure 2.1. To do this, we fit for functional form $b(k) = b_0 + b_k k^2$ for some constant $b_k$ on large scales ($k < 0.2$ h/Mpc) weighted by inverse variance of individual $b(k)$ data points (variance is calculated from the 5 simulations we have for each box size). Then $b_0$ corresponds to the scale independent large scale bias we are interested in.

## Stochasticity

Next, we are interested in examining how well we reconstruct the halo field with the estimated bias parameters. Following [210, 98, 17], for any two fields $X$ and $Y$, where the field $Y$ is supposed to model field $X$, we measure the error in modeling in terms of the stochasticity, $S_{XY}$, defined as

$$S_{XY} = P_{XX} - \frac{P_{XY}^2}{P_{YY}} \tag{2.31}$$

Thus $X$ is the halo overdensity field and $Y$ is the corresponding field modeling the halo field and given by the right hand side of the Eq. (2.26). For the modeling field ($Y$), we successively add the higher order bias parameters, starting from $b_1$ to $b_2$ and $b_{s^2}$ so that we can identify the improvement contributed by every successive parameter. Then, $P_{XX}$ is the halo power spectrum ($P_{hh}$), while $P_{YY}$ is the auto-power spectra for the modeling (bias) field ($P_{bb}$, where $b$ will be the highest order (in terms of complexity) bias used). The explicit expression for $P_{bb}$ as well as cross-spectra $P_{XY}$ in terms of different bias parameters is

$$\begin{aligned}
P_{XY} \equiv P_{hb} &= b_1 P_{h\delta} + \frac{b_2}{2} P_{h\delta^2} + b_{s^2} P_{hs^2} \\
P_{YY} \equiv P_{bb} &= b_1^2 P_{\delta\delta} + \frac{b_2^2}{4} P_{\delta^2\delta^2} + b_{s^2}^2 P_{s^2s^2} + b_2 b_{s^2} P_{\delta^2 s^2}
\end{aligned} \tag{2.32}$$

If the modeled bias-field reconstructs the halo field perfectly, all the three power spectra in the definition of stochasticity should be the same resulting in $S_{hb} = 0$. However since the number of halos, $n$, is finite, the halo auto spectrum contains Poisson shot noise, $\frac{L^3}{n}$ (where $L$ is the box size), which is not captured by the continuous bias field.

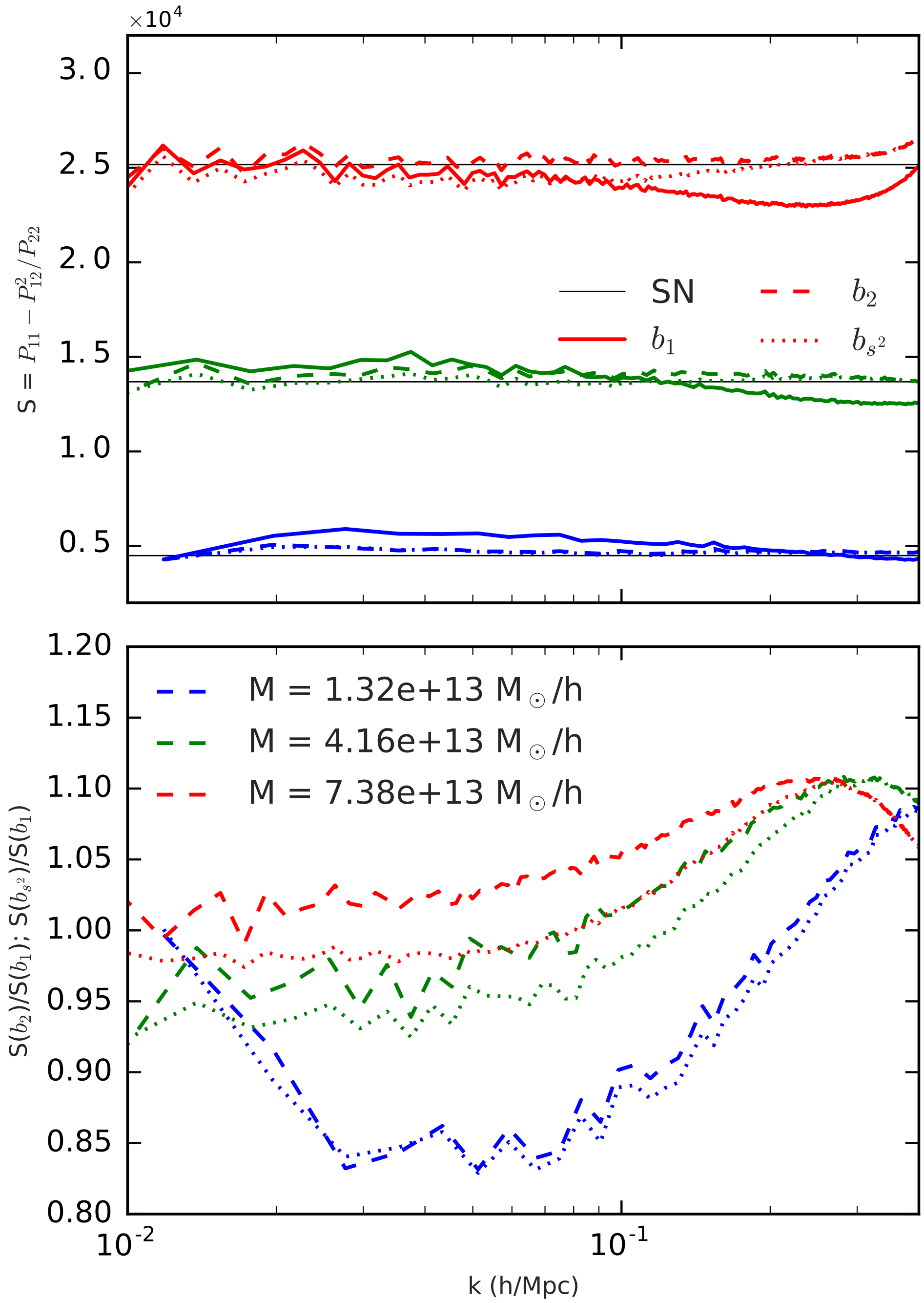


Figure 2.2: **Stochasticity of Halos:** The stochasticity in the upper panel is calculated using Eq. (2.31). The solid lines, dashed and dotted lines respectively correspond to measurements on successively including $b_1$, $b_2$ and $b_{s^2}$ in Eq. (2.32). For comparison, the black lines are shot noise for that mass bin. The lower panel shows the ratio of dashed and dotted lines of upper panel with the solid lines to emphasize that more complex bias models reduce stochasticity.

In Figure 2.2, we show measurement of stochasticity in for three different mass bins, one from each of the three simulation boxes. For each mass, we show how the stochasticity changes as we include higher order bias parameters over simple linear bias $b_1$ in Eq. (2.32). To estimate stochasticity, we first average the various power spectra for all 5 simulations of a given size to reduce noise and cosmic variance in individual measurements on large scales. These mean spectra are then used with the constant (large scale) Fourier space bias estimates in Eq. (2.31).

Overall, on large scales, the stochasticity is close to its Poisson shot noise value for intermediate and low mass bin, while its somewhat lower for heavier halos ([17] explains this as exclusion effects). However, especially for the low mass halos, simply using the linear bias for halo field does leave significant scale dependence in the stochasticity which is improved upon by including higher order bias parameters (upper panel). This is useful since this residual can still be modeled with a scalar, if not necessarily poisson, shot noise. In addition, including $b_2$ and especially $b_{s^2}$ does assist in reducing stochasticity further over linear bias models (lower panel).

## 2.3 Lagrangian Bias at Field Level

In the previous section, we outline a bias model for mapping from the underlying matter field to the observed tracers i.e. a bias model. However in fitting for this mapping, we relied only on matching the two-point functions of the model and data field. In this section, we discuss an alternate Lagrangian bias model (as for example in refs. [146, 148, 39, 251, 238, 155, 206]) that will match the model with the observations at the level of the field. We expect this to reduce the stochasticity further over including tidal tensor bias as was observed in the previous section. Furthermore, the previous model captured the clustering of proto-halos while imaging surveys observe halos in Eulerian space. Hence here we also combines the bias model with non-linear evolution under gravity by promoting the Lagrangian fields to Eulerian space (and redshift space if required).

Having established the evidence for tidal tensor bias in previous section, we again use a Lagrangian bias model including terms up to quadratic order. At this order, the Lagrangian fields are $\delta_L(\mathbf{q})$, $\delta_L^2(\mathbf{q})$ and $s_L^2(\mathbf{q}) \equiv \sum_{ij} s_{ij}^2(\mathbf{q})$ the scalar shear field where $s_{ij}^2(\mathbf{q}) = (\partial_i \partial_j \partial^{-2} - [1/3]\delta_{ij}^D)\delta_L(\mathbf{q})$. We use these fields from the ICs of the simulation itself but evolved to $z = 0$ using linear theory (due to this evolution, care must be taken in interpreting our bias parameters). Since $\delta_L^2(\mathbf{q})$ and $s^2(\mathbf{q})$ are correlated, we define a new field $g_L^2(\mathbf{q}) = \delta_L^2(\mathbf{q}) - s^2(\mathbf{q})$ which does not correlate with $\delta_L^2(\mathbf{q})$ on large scales and use this instead of shear field. In addition, we subtract the zero-lag terms to make these fields have zero mean.

Then, to generate our model field as a combination of these Lagrangian fields, we use the approach developed by ref. [206], which is itself an implementation of the ideas of ref. [148] (e.g. Eq. 8) and its extensions [238]. Each particle is 'shifted' to its Eulerian position, $\mathbf{x}$, with the non-linear dynamics of choice and then binned onto the grid with cloud-in-cell (CIC) interpolation and weight

$$weight = 1 + b_1\delta_L(\mathbf{q}) + b_2(\delta_L^2(\mathbf{q}) - \langle\delta_L^2(\mathbf{q})\rangle) + b_g\left(g_L(\mathbf{q}) - \langle g_L(\mathbf{q})\rangle\right) \tag{2.33}$$

Note the contributions of $\delta_L$, $\delta_L^2$ and $g_L^2$ assigned to each particle are based on its initial location ($\mathbf{q}$). This procedure is equivalent to building separate fields with each particle weighted by 1, $\delta_L$, $\delta_L^2$ and $g_L$ and then taking the linear combination of those fields after shifting, which is how the model was actually implemented. Thus our modeled tracer field is:

$$\delta^b_{\rm model}(\mathbf{x}) = \delta_{[1]}(\mathbf{x}) + b_1\delta_{[\delta_L]}(\mathbf{x}) + b_2\delta_{[\delta_L^2]}(\mathbf{x}) + b_g\delta_{[g_L]}(\mathbf{x}) \qquad . \tag{2.34}$$

where $\delta_{[W]}(\mathbf{x})$ refers to the field generated by shifting the particles weighted with '$W$' field.

To fit for the bias parameters, we minimize the mean square model error between the data and the model fields which is equivalent to minimizing the error power spectrum of the residuals, $\mathbf{r}(k) = \delta^b_{\rm model}(\mathbf{k}) - \delta_h(\mathbf{k})$, in Fourier space:

$$P_{err}(k) = \frac{1}{N_{modes}(k)} \sum_{\mathbf{k},|\mathbf{k}|\sim k} \left|\delta^b_{\rm model}(\mathbf{k}) - \delta_h(\mathbf{k})\right|^2 \tag{2.35}$$

where the sum is over half of the $\mathbf{k}$ plane since $\delta^\star(\mathbf{k}) = \delta(-\mathbf{k})$ for the Fourier transform of a real field, and the 'data' correspond to our 'clean' field with no noise at this stage.

In principle the bias parameters can be made scale dependent, $b(k)$, and treated as transfer functions [206]. To get these transfer functions, we simply minimize Eq. 5.16 for every $k$-bin independently. However if the the best-fit parameters turn out to be scale independent to a very good degree, we can minimize the number of fitted parameters by using scalar bias parameters and fit for them by minimizing the error power spectrum only on large scales. We will use this model for reconstruction in Chapter 5 and show below that the fit is quite insensitive to this $k$-range (chosen reasonably) used for fitting the bias parameters.

Traditionally, bias parameters are defined such that the bias model field matches the observations in real space. However the observations of done in redshift space, we can model to 'shift' the Lagrangian field directly into redshift space and minimize the error power spectrum (Eq. 5.16) directly in redshift space instead of real space.

## 2.4 Neural Network Model

Bias model approaches are unlikely to be accurate on an object by object basis since they ultimately model a discrete, point-wise halo (galaxy) field with weighted continuous matter field. An alternative approach proposed in [156] is to connect the halo positions and masses to the underlying matter density using Artificial neural networks (ANN/NN). These networks are fully differentiable, yet are able to model even very discrete distributions of near pointlike structures. This differentiability is of key importance since it ultimately allows us to use these

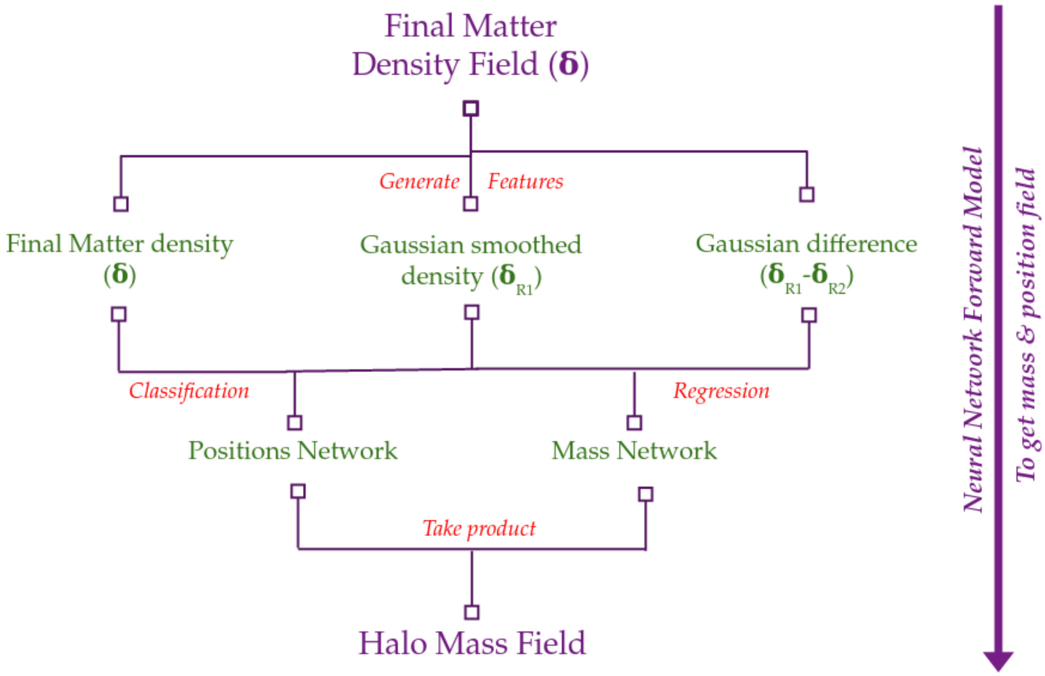


Figure 2.3: Flowchart summarizing the operations involved in second step of the forward model i.e. to predict halo mass field from the final matter field using two neural networks to identify the position and masses of halo.

forward models for the reconstruction of comoslogical fields. The schematic for this forward model step is shown in the right panel in Figure 4.1.

While neural networks come in various architectures and sizes, for our purpose here, we use a simple variant called fully-connected neural network. These are directed, weighted graphs where elements called neurons are arranged in layers and each neuron in a layer is connected to all those in the next layer (Figure 4.2a), with an associated bias factor ($\mathbf{b}$) and a weight ($W$) and activation function ($\phi$)(Figure 4.2b) to determine the output for every directed connection. Thus it recursively takes the input from ($\mathbf{x}$) from previous layers to produce output ($\mathbf{y}$) as

$$\mathbf{y} = \phi(W \cdot \mathbf{x} + \mathbf{b}) \tag{2.36}$$

Every neural network requires some underlying features as input to develop a meaningful relationship between these inputs and the data. Given an image, sophisticated convolutional networks (CNN) develop these features themselves by optimizing filters of a restricted size and we could have used them instead of a fully connected network. But in the view of simplicity and understanding, since we have some physical intuition of what information we are seeking and the importance of associated features, we will design the filters ourselves.

The schematic for our model is presented in the form of the flowchart in the Figure Figure 2.3. We use the underlying dark matter field and its transformations as input features to learn the mapping from matter to halos (discussed in detail below). Our model consists of two fully connected neural networks, one to predict the 'position' field for the observables and the other to predict the 'magnitude' of the corresponding observable, which in this case is halo mass. We break down the model into two separate networks for mass and position since it considerably simplifies the problem. Identifying the positions of the observables is now a classification problem which are inherently somewhat easier to solve than regression problems (which we would otherwise be solving to get an observed mass field directly). It is also independent of what the observed quantity corresponding to the mass label is and we can thus use the same trained position network to predict different observables. Identifying the mass after having identified the position of the halos also reduces the dynamic range of regression which makes the problem more amenable.

As mentioned, to make our model differentiable, we have to give up the concept of a pointlike halo and instead we predict the 'fields' of these observables. By 'fields', we imply that these quantities have been convolved on a grid of ones choosing using a suitable convolution scheme. While such a grid structure is not a fundamental feature of the observables themselves, it arises naturally in any image analysis. Using different grids or convolution schemes should only change the training of our model networks while keeping the conceptual approach unchanged. In this work, we consider only CIC convolution scheme, but any other interpolation or smoothing scheme should work as well. Furthermore, as a result of working with the grids, we are unable to distinguish between a single and multiple point like objects present in the same cell. Instead, at every point, the networks will predict cumulative, convolved values of the observable for all the objects associated with that point. Tracing back these predicted values to individual objects inside the grid cells should not be relevant to the application of the model in this work.

The first network (**NNp**) identifies the CIC convolved halo positions on the grid. Thus, NNp performs classification wherein it identifies if any of the 8 cells (due to the CIC convolution) associated with a grid point hosts a halo and assigns a value between 0 and 1, which is akin to the probability of there being a halo. The output of NNp is thus a discrete, position mask for the halo field (see Figure 4.3a). The second network (**NNm**) on the other hand performs a regression on the underlying features to predict the value of CIC convolved mass at a given grid point, assuming that there is a halo associated with that grid point. This leads to a continuous mass field (see Figure 4.3b).

Given these two networks, our model for the discrete halo mass field is simply the product of these two fields.

$$\mathrm{model} = \mathrm{NNp} \times \mathrm{NNm}$$

## Features

The neural network requires a set of underlying features (ideally physically motivated) as inputs. These features should provide meaningful information to learn their relationship

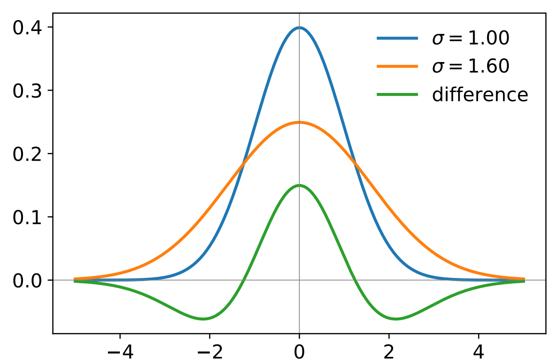


(a)

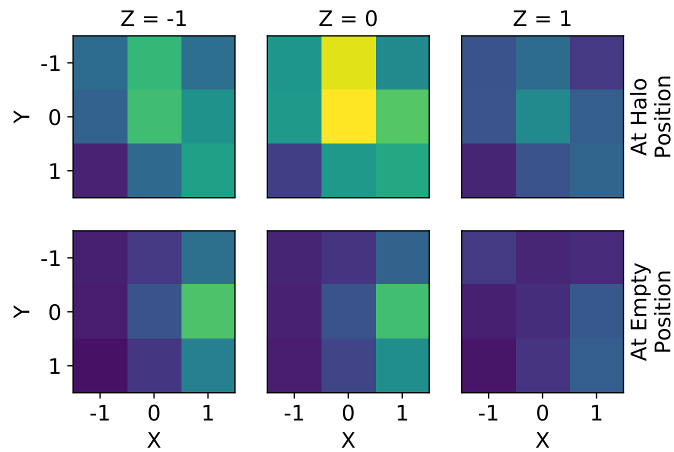


(b)

Figure 2.4: (a) Difference of two Gaussian smoothed fields (green) localizes the peaks better than either of the fields. (b) The density field at 27 nearest neighbor points of the central grid point (X=0, Y=0, Z=0; Z-coordinate in the title is increasing going from left to right) for 2 cases - (top row) when the central grid point corresponds to a halo position, (bottom row) central grid point is an empty grid point in the field. In the top row, local maxima is visible around the halo- along X axis (middle row in Z=0 square), Y axis (middle column in Z=0 square) and Z axis (central cells in the three squares). In comparison, the bottom panel looks more like a smooth gradient.

with the corresponding observed data and hence to be able to predict the latter from the former. Since we are interested in predicting the halo mass field, and all halo formation models predict that more halos form in regions of higher overdensity, the underlying final matter density field provides a natural candidate for these features. The simplest models such as Spherical collapse [96] simply predict that halos form where overdensity exceeds a certain threshold with the mass of the halos corresponding to the largest scale at which it does so [190, 34]. Other halo formation models such as Ellipsoidal collapse advocate the role of shear [221, 220] while assembly bias models suggest that other environmental features [103, 142] also play a role in halo formation. We also find some evidence of this with the detection of non-zero shear bias in the previous section.

In principle, one can use all these fields as underlying features and this should ideally improve the accuracy of predictions, albeit the gains gradually diminish [139]. The increasing complexity of the model will also lead to increased difficulty of training the neural networks. In [156], we find that for a simple fully connected neural network model and approximate simulations where quantities such as velocity fields are not resolved completely accurately, the following three transformations of density fields at different smoothing scales suffice as features suffice and can approximately capture environmental information supplementing local density information.

- CIC convolved matter density field ($\delta_0$)
- Density field smoothed with a finite Gaussian kernel on some scale ($\delta_{R1}$)
- Difference of finite Gaussian smoothed fields on two different scales ($\delta_{R1} - \delta_{R2}$)

Of these, Gaussian difference (GD) is an approximate blob detection technique used in computer vision [137] to identify peaks in this space. Since halos are more likely to form at peaks in density fields, we find that GD localizes the position of halos by identifying peaks in high density blobs which are likely to cross a simple density threshold over more than one grid points for a single halo (Figure 2.4a).

Another way to capture non-local and environmental information is to use the values of the three fields from all the 27 points in a $(3 \times 3 \times 3)$ cube around that point in the feature vectors. This is motivated by the fact that the preferred locations of halo formations are density peaks above some threshold and given three consecutive points in any dimension, it is easier to identify the positions of these density maximas (see the caption of Figure 2.4b for description). Indeed, this improves the performance significantly for the position network over using the values only at the grid point, as is done for the mass network. This is also similar to what a CNN does, wherein its every neuron identifies the filters by convolving spatial pixels to maximize the information. We do find improvements on using full CNN architecture with multiple filters upon the simple approach presented here, but for the purpose of reconstruction in this work, our approach suffices.

We discuss the technical details regarding the implementation and the performance of this model in Chapter 4 where we use it to reconstruct the initial conditions from halo mass field.

# Chapter 3

# Towards optimal extraction of cosmological information from nonlinear data

The contents of this chapter were originally published as

Towards Optimal Extraction of Cosmological Information from Non-linear Data
*Seljak U., Aslanyan G., Feng Y., Modi C. (arXiv:1706.06645)* JCAP 12(2017)009

In this chapter, we develop a hierarchical Bayesian formalism to optimally extract cosmological information in the nonlinear regime. Our approach is to relate the initial linear modes of the density field to the observed non-linear data with a differentiable forward model and then reconstruct the initial conditions by maximizing the posterior of these modes. We also construct an initial power spectrum estimator by integrating out the modes using perturbative expansion of the likelihood. For a fixed forward model, this contains all the cosmological information if the initial modes are Gaussian. We develop numerical methods that are computationally feasible and preserve the near optimality of the analysis. We apply the method in the simplified context of nonlinear structure formation, using either simplified 2-LPT dynamics or N-body simulations as the nonlinear mapping between linear and nonlinear density, and 2-LPT dynamics in the optimization steps used to reconstruct the initial density modes. We demonstrate that the method gives an unbiased estimator of the initial power spectrum, providing among other a near optimal reconstruction of linear baryonic acoustic oscillations.

## 3.1 Introduction

The issue of optimal map reconstruction and optimal power spectrum reconstruction from a set of noisy and sparsely sampled data has received a lot of attention in the field of large scale structure (LSS) and cosmic microwave background (CMB) anisotropies. Most of the work assumes the data are a linear transformation of the initial modes, as is the case with CMB

[100, 230, 33]. In this case the minimum variance map solution is the well-known Wiener filter map [200]. Computing Wiener filter can be expensive, since it requires an inverse noise weighting of the data, where in the cosmological context noise consists both of the actual measurement noise and the actual signal (the so called sampling or cosmic variance noise). Noise covariance matrix is typically sparse (often diagonal) in the configuration space, and given sparsely sampled data its Fourier space representation is not diagonal. Signal covariance matrix is diagonal in Fourier space, and its configuration space representation is not diagonal. The sum of the two is thus not sparse in any basis, and computing the inverse covariance matrix using brute-force methods is an $N^3$ process, which becomes prohibitively expensive for large $N$. Alternative methods must therefore be used to solve for the Wiener filter map [178, 77].

The reconstructed map typically has millions of data points and contains too much information to be useful on its own. What we want instead is the optimal power spectrum given the map. This is a typical hierarchical Bayesian setting, where there are many latent variables that need to be marginalized over, and only their priors remain. Here the latent variables are the modes and their prior is the power spectrum, which is a useful summary statistic, since for a Gaussian field of initial modes it contains all the information present in the data, and the data compression is lossless. In the linear regime it can be computed using the optimal quadratic estimator, which is quadratic in the data. This requires the data to be first inverse covariance matrix weighted [100, 230, 33], hence it is also computationally expensive. The two problems, optimal map making and optimal power spectrum, are connected: the optimal quadratic estimator can be built out of the Wiener field map reconstruction [208].

An alternative method to optimal quadratic estimator is to use sampling methods to determine the power spectrum probability distribution. For example, a Gibbs sampling approach consists of a two step sampling procedure [244]. In the first one a sample map consistent with the data is created by adding a generalized noise realization to the Wiener filter map. In the second, sampling of the power spectrum is created consistent with the given map realization. Creating a map sample also requires an expensive inversion of the covariance matrix, and as a consequence these sampling approaches are typically slower than the optimal quadratic estimator, and converge particularly slowly in the high noise regime.

These methods, while optimal in the linear regime, are often replaced with faster and less optimal methods due to their computational cost. Traditional power spectrum estimations of CMB and LSS use a linear transformation between the data and the model (Fourier transform, FT), and assume that the covariance matrix of the data is diagonal (which allows a fast evaluation of the corresponding curvature matrix of the modes). In LSS this is the so called FKP method [81], while in CMB it is called the pseudo-$C_l$ method [182, 243]. This solution is not optimal, because the correct weighting of the data is to multiply it with the inverse of the covariance matrix, an evaluation that scales as $N^3$ and is too costly to be performed on large data sets. FKP or pseudo-$C_l$ weighting is particularly poor if the noise is varying significantly across the survey, in which case it is optimized for a single value of the power spectrum (the one used in FKP weighting). It also fails if there is a complicated geometry of the survey. Moreover, the method does not handle optimally if there are modes that are contaminated and create large scale correlations that need to be marginalized over. Nevertheless, these methods have become standard, because for linear problems one can show that under certain assumptions (typically valid on scales small compared to the survey size) the amount of information is nearly the same [71].

So far the discussion above has been about a linear mapping between the modes and the data. While the primary CMB is linear to a very good approximation, in LSS this is only valid on the largest scales. Most of the LSS information is contained on smaller, nonlinear, scales: in a 3-d LSS survey the number of modes scales as $k^3$, where $k \sim 1/R$ is the typical wavevector and $R$ the typical scale. The question of optimal linear map given the nonlinear data has been addressed in recent work, and Hamiltonian Monte Carlo (HMC) sampling approach has been used to create the map [246], as well as create samples consistent with the data for a given power spectrum [117, 118]. Hamiltonian sampling has an advantage over regular (e.g. Metropolis-Hastings) sampling that it can propagate far from the current sample using dynamics rather than random walk, and still the acceptance rate can be very high, both of which are necessary conditions for a rapid convergence in large dimensions due to the curse of dimensionality. However, in the current implementations the samples are still highly correlated, with correlation length of order 100-200 being reported [118]. To create each sample one needs many Hamiltonian dynamics evaluation steps (of order 10), so the total cost of evaluation of a single independent realization can easily exceed 1000 calls, each being a full forward model. It also requires knowledge of a gradient of the data model with respect to initial modes, a feature shared with the methods developed in this chapter.

In contrast to the optimal linear power spectrum analyses, there has been very little work in terms of extracting the optimal summary statistics given a set of noisy and incomplete data in the nonlinear regime. For sampling methods this may be too difficult to solve, if HMC requires 1000 calls or more to create a single independent realization. In the high noise regime sampling converges very slowly onto the correct cosmological model, because most of the mode power comes from the assumed power spectrum at a previous step. As a consequence this approach may not be feasible. Most of the focus so far has instead been to extract information from the two-point function of the nonlinear modes. In this case the same quadratic estimator methods discussed above can be used [231], but they are not optimal since there is information in higher order statistics as well. Because of this the two point function analysis is sometimes supplemented with additional statistics that are most likely to be complementary. Among these are the higher order correlations, starting with the three point function/bispectrum, various void statistics, topology statistics, counts of objects like clusters or other density peaks, and reconstruction methods, primarily focused on baryonic acoustic oscillations (BAO) (see e.g. [249] for a review of different probes of LSS). These approaches share the property that they use statistical information in addition to the two point statistics of the final field, but beyond that they differ enormously in terms of their motivation and scope. Combining the different statistics creates a significant problem of modeling their joint error distribution, since their joint covariance matrix cannot be computed ab-initio, but must instead be obtained from the simulations, which are noisy and expensive. Moreover, there is no guarantee that even after combining several of these statistics one will exhaust the information content in the data: new statistics are continuously being proposed (and argued to be superior by their authors), suggesting that this question is unlikely to be settled by this ad-hoc approach. Ideally, what is needed is an ab-initio approach that is built with a guarantee to give a nearly optimal answer. This is an approach we attempt to develop in this chapter.

Since the initial density modes are assumed to be Gaussian, their power spectrum is a lossless summary statistic, which should contain all the information present in the data (with an exception of cosmological parameters that may be required to map from the initial modes into the final data). The lossless nature may however break down in the situations of shell crossings, where there can be more than one initial solution that maps to the same final data. In this chapter we derive an initial linear power spectrum estimation, given incomplete and noisy data and given a nonlinear model between the initial modes and the data. We will show that as an intermediate step we will also need to derive the optimal initial density reconstruction. For the linear case the optimal power spectrum from the optimal density reconstruction has been derived in [208], and here we generalize the expressions to the nonlinear model. We will show that it is possible to cast the solution into an optimization problem, and we develop methods to solve it efficiently. We then generalize the method to include forward model parameters as well. As a proof of principle we apply the derived expressions to extract the initial power spectrum from a final density field obtained either in an N-body simulation of dark matter or in a 2-LPT simulation models, and using a 2-LPT approximation (e.g. [25]) as a forward model.

## 3.2 Statistical approach and heuristic derivation

Following the notation of [208] let us assume that we measure some nonlinear observations $d(\boldsymbol{r}_i)$ at pixelized (2-d or 3-d) spatial positions $\boldsymbol{r}_i$. The data could be nonlinear dark matter density (although this is typically not directly observable), some projected dark matter density such as lensing shear or convergence, galaxy density or luminosity, Sunyaev-Zeldovich intensity etc. We arrange these into a vector $\boldsymbol{d} = \{d(\boldsymbol{r}_i)\}(i = 1, ..., N)$. Each measurement consists of a signal and a noise contribution, $\boldsymbol{d} = \boldsymbol{f(s,\lambda)} + \boldsymbol{d}_n$, where noise is assumed to be uncorrelated with the signal. Here $\boldsymbol{f(s,\lambda)}$ is a nonlinear mapping from the initial linear density modes to the final model prediction of the observation, and $\boldsymbol{s} = \{s_j\}(j = 1, ..., M)$ are the underlying initial density mode coefficients that we wish to estimate. In the statistical language $\boldsymbol{d}$ are the observed variables, $\boldsymbol{s}$ are the latent variables and $\lambda$ are the forward model parameters. While our primary motivation for these is linear matter over-density $\boldsymbol{\delta}$, the formalism we develop is also useful for other applications such as CMB anisotropies, hence we keep the notation more general. We will assume these coefficients to be in Fourier space, where their Gaussian prior can be written in a diagonal form. The modes are complex and obey $s^*(\boldsymbol{k}) = s(-\boldsymbol{k})$, where $\boldsymbol{k}$ is the wavevector, but in our labeling of modes we will treat real and imaginary component as two independent modes. If the mapping is linear we can write $\boldsymbol{f}(\boldsymbol{s}) = \boldsymbol{f'}\boldsymbol{s}$.

We will assume the nonlinear mapping $\boldsymbol{f(s, \lambda)}$ to be computable given the initial density field and given some forward model parameters $\boldsymbol{\lambda}$. Typically this mapping will be a full N-body simulation, with some additional processing to produce a realistic model prediction for the specific observations. The forward model parameters can be matter density, massive neutrinos or other parameters that affect the growth of structure, various astrophysical modeling parameters (related to how galaxies and baryons populate dark matter halos), and observational nuisance parameters (such as shear bias in weak lensing etc.). The mapping may also include smoothing (e.g. beam smoothing) or pixelization of the data. The true underlying field has an infinite number of Fourier modes, but only a finite number of these can be estimated. Typically we will embed a given LSS survey into a periodic box larger than the survey, with zero padding in regions without the data, but in this chapter we will simplify this to periodic box analysis.

The modes $\boldsymbol{s}$ are latent variables with a prior of their own. This prior is parametrized as a multivariate Gaussian, with covariance matrix $\boldsymbol{S} = \langle \boldsymbol{s}\boldsymbol{s}^{\dagger} \rangle$, which is assumed to be diagonal in Fourier space. We will assume the power spectrum depends on parameters $\boldsymbol{\Theta}$, which will typically be bandpowers, but this will later be generalized to any parameters that change the power spectrum. These bandpowers can also have a prior (a hyperprior in the language of hierarchical Bayesian models), but in this chapter we will assume their prior is flat, and we will not even impose positivity, since these are summary statistics expected to be used in a later analysis of cosmological parameters.

The noise vector $\boldsymbol{d}_n = \{d_{n,i}\}(i = 1, ..., N)$ is parametrized with the noise covariance matrix $\boldsymbol{N} = \langle \boldsymbol{d}_n \boldsymbol{d}_n^{\dagger} \rangle$.The i-th diagonal element $N_{ii}$ corresponds to the noise variance $N(\mathbf{r}_i$ at the spatial position $\mathbf{r}_i$. This noise matrix is assumed to be known, uncorrelated with the signal and diagonal (or sparse) in real space, so that any operations involving noise matrix scale as $O(N)$ rather than $O(N^2)$ or steeper. For simplicity we will also assume noise is Gaussian distributed, but this can be generalized to other probability distributions. It is reasonably appropriate for weak lensing, where by central limit theorem averaging over shape noise produces approximately Gaussian noise. Outside the survey mask (which can include holes inside the survey) we will assume $N(\boldsymbol{r}_i) = \infty$ and assign $d(\boldsymbol{r}_i) = 0$ (although assigning any other value would be just as good).

The goal of parameter inference is to derive the posterior distribution of parameters $\boldsymbol{\Theta}$ and $\boldsymbol{\lambda}$ given their prior and the data $\boldsymbol{d}$. In some cases, such as linear model, one can write analytic expression for the likelihood $L(\boldsymbol{d}|\boldsymbol{\Theta}, \boldsymbol{\lambda})$, but its explicit evaluation requires inversion and trace or determinant of a very large non-sparse matrix, both of which are $O(N^3)$ operations, which becomes too expensive when the size of the data becomes large. In the nonlinear case even writing down the posterior is a major challenge. We will argue that it is easier to solve the problem in a typical hierarchical Bayesian model approach, by working with the latent variables $\boldsymbol{s}$ and solving for these first, then marginalizing over them to obtain the likelihood and the posterior of parameters (which are the same if the priors are flat, as we will assume here). This approach perhaps seems counter-intuitive, since the dimension of the latent variables $M$ is comparable to the data $N$. However, the major simplification in the linear case is that there are no large matrix inversions required for the solution to be obtained. For the nonlinear case we will argue that finding a good solution at or close to the global minimum is achievable even in a large number of dimensions, and the problem cannot even be solved in the absence of latent variables. By writing a full probabilistic model in terms of conditional probabilities between individual variables, in this case latent variables $\boldsymbol{s}$ conditional on $\boldsymbol{\Theta}$, and data $\boldsymbol{d}$ conditional on $\boldsymbol{\lambda}$ and $\boldsymbol{s}$, we are able to solve for the posterior of $\boldsymbol{\Theta}$ and $\boldsymbol{\lambda}$ given the data $\boldsymbol{d}$ (combining with the (hyper)priors on $\boldsymbol{\Theta}$ and $\boldsymbol{\lambda}$).

One can write the joint probability of signal $\boldsymbol{s}$ and noise $\boldsymbol{d}_n$ as a product of individual probabilities, under the assumption that they are uncorrelated,

$$P(\boldsymbol{s},\boldsymbol{n}) = P_s(\boldsymbol{s})P_n(\boldsymbol{d}_n) = (2\pi)^{-(M+N)/2}\det(\boldsymbol{S}\boldsymbol{N})^{-1/2}\exp\left(-\frac{1}{2}\left[\boldsymbol{s}^\dagger\boldsymbol{S}^{-1}\boldsymbol{s}+\boldsymbol{d}_n^\dagger\boldsymbol{N}^{-1}\boldsymbol{d}_n\right]\right). \tag{3.1}$$

The Bayes theorem can be applied to $\boldsymbol{s}$, $\boldsymbol{\Theta}$ and $\boldsymbol{\lambda}$ to obtain their posterior

$$P(\boldsymbol{s},\boldsymbol{\Theta},\boldsymbol{\lambda}|\boldsymbol{d}) \propto P_n(\boldsymbol{d}-\boldsymbol{f}[\boldsymbol{s},\boldsymbol{\lambda}])P_s(\boldsymbol{s}|\boldsymbol{\Theta})P(\boldsymbol{\Theta},\boldsymbol{\lambda}). \tag{3.2}$$

The first term $P_n$ is the probability distribution of the noise for some set of observations $\boldsymbol{d}$, $\boldsymbol{d}_n = \boldsymbol{d}-\boldsymbol{f}(\boldsymbol{s},\boldsymbol{\lambda})$, while the second $P_s$ is the prior for $\boldsymbol{s}$ given $\boldsymbol{\Theta}$ (or, equivalently, $\boldsymbol{S}$). The last term $P(\boldsymbol{\Theta},\boldsymbol{\lambda})$ is the prior on the initial power spectrum parameters $\boldsymbol{\Theta}$ and on forward model parameters $\boldsymbol{\lambda}$. We will assume this prior is flat, so that we have no prior information on them. This is because we want the result of the analysis to summarize the information from the given data, without inclusion of external data. This is easy to modify at a later stage if combining different data sets. Similarly, we will not be concerned with the normalization of the posterior, so we simply use the proportionality symbol in equation 3.2. We will fix the normalization at the end using Gaussian approximation for the posterior.

Maximizing the posterior in terms of $\boldsymbol{s}$ at a fixed $\boldsymbol{\Theta}$ and $\boldsymbol{\lambda}$ gives $\hat{\boldsymbol{s}}$, the so called maximal a posterior (MAP), which is also the Wiener filter map in the linear case. We will use optimization methods with analytic gradient evaluation to perform this step. Gradient based optimization methods can be very efficient at finding the maximum, but typically do not provide a reliable curvature matrix (Hessian or its inverse). We will develop a method where the curvature matrix of $\boldsymbol{s}$ around $\hat{\boldsymbol{s}}$ is not needed in the construction of the final solution, so that any optimization method can be used.

Ultimately the optimal map is not what we really care about. What we want is the posterior of model parameters $\boldsymbol{\Theta}$ and $\boldsymbol{\lambda}$ independent of latent variables $\boldsymbol{s}$. One way to do this would be to use sampling of both $\boldsymbol{s}$, $\boldsymbol{\Theta}$ and $\boldsymbol{\lambda}$, but with $M \gg 10^6$ dimensions this can be extremely expensive. Another approach would be to maximize the posterior with respect to all the parameters at once. This approach is strictly not valid when the latent variables depend on the parameters we wish to determine: maximization is not the same as marginalization. In addition, this approach has technical difficulties related to the fact that for the parameters we care about we also need a very accurate curvature matrix and its log determinant, which is not provided by the optimizer. In this chapter we instead perform an analytic marginalization over the latent variables.

In our approach, we work with large dimensions of the modes, $M \gg 10^6$. We will assume that the same maximum is always found. To be more precise, we will argue that many posterior maxima can exist and do not change the nature of the solution as long as they are all similar to each other in a well defined sense discussed in section 3.4). This assumption can be explicitly proven in the linear regime where the loss function is convex [208]. In the nonlinear case it depends on the nature of the problem, but cannot be proven generally. For example, in the strongly nonlinear regime, inside virialized regions, satellites on orbits can yield several identical phase space configurations. While this degeneracy will be broken by the Gaussian prior on the modes, it still suggests local maxima in posterior (even if not of equal height). We will proceed not ignoring this issue, but assuming it can be calibrated out under the assumption that the maxima are always quantitatively similar.

We will thus analytically integrate over $\boldsymbol{s}$

$$P(\boldsymbol{\Theta}, \boldsymbol{\lambda}|\boldsymbol{d}) = \int d^M \boldsymbol{s} P(\boldsymbol{s}, \boldsymbol{\Theta}, \boldsymbol{\lambda}|\boldsymbol{d}), \tag{3.3}$$

performing this marginalization around the MAP solution $\hat{\boldsymbol{s}}$. We will perform a perturbative expansion of the posterior around MAP, which we can integrate over. This produces two terms, one is simply the value of the loss function in the exponent of equation 3.2 at the MAP position, and the second is the volume of posterior, roughly given by the determinant of the curvature matrix at that position (and further increased by the higher order moments). However, we will never explicitly perform this integral, and instead develop a method to determine the resulting volume element using simulations, so in this sense our approach does not rely on perturbative expansion.

Once we have $P(\boldsymbol{\Theta}, \boldsymbol{\lambda}|\boldsymbol{d})$ we can perform its maximization with respect to $\boldsymbol{\Theta}, \boldsymbol{\lambda}$ to find their peak posterior solution, i.e. the maximum likelihood (since we assume flat prior). By expanding the log posterior to second order we also obtain the curvature matrix under the Laplace approximation. We will use Newton's method to find the maximum likelihood solution and then construct an explicitly unbiased estimator out of it. In this chapter we focus primarily on bandpowers for $\boldsymbol{\Theta}$, and we argue that quadratic expansion of their log likelihood is likely to be sufficient, but we also develop the method for other parameters, such as forward model parameters.

In the past work on linear problem [178], the evaluation of the curvature matrix has proven to be the most expensive part of the problem. In this chapter we develop a novel method to evaluate an approximation to its ensemble average, the Fisher matrix. We use data simulation(s) and investigate their response to the change in parameters, taking advantage of the fact that in Newton's method the response matrix is also the curvature matrix. This enables us to evaluate this term much faster than otherwise possible. In the linear case this approach remains Bayesian, since the curvature matrix equals the Fisher matrix. In the nonlinear case this is no longer the case, but we will argue that the difference are likely to be small due to the large number of modes.

It is worth emphasizing that if the initial equations 3.1 and 3.2 are exact in a probabilistic sense, and if all the steps we described above are performed exactly, then the final solution is optimal, i.e. we obtain true posterior distribution of the parameters given the data. In this chapter we will discuss in detail which approximations we are invoking to solve these equations and what their impact may be on the optimality of the final result.

## Heuristic derivation

The simplest power spectrum estimate one can make out of MAP is to square the modes $\hat{\boldsymbol{s}}$ and average them within the bandpower bin. This does not lead to an unbiased estimator, but intuitively this must be the path to the correct procedure, since it is built from the minimum variance estimator of the initial modes, which in some sense is the best we can do. This procedure has indeed been formally proven in the linear case [208]. In the next sections we present a nonlinear version of this statement. Before proceeding we give a heuristic derivation of our procedure following the arguments in [208].

In general an optimal two point function (e.g. power spectrum) analysis for the linear case requires first inverse generalized noise weighting of the data, after which one adds up all pair products of these inverse noise processed data, weighted by the expected response of each pair product to the specific power spectrum parameter (e.g. bandpower). Inverse weighting by the generalized noise means weighting by the inverse of the full covariance matrix, which consists of noise variance and signal (sampling) variance, and is in general not diagonal in any basis. In the nonlinear case the generalized noise matrix cannot even be defined a priori since it depends on the solution. However, finding MAP of initial modes $\hat{\boldsymbol{s}}$ achieves this inverse generalized noise weighting. This may still not be sufficient for an optimal analysis, but going beyond it would require doing a full likelihood analysis in $M$ dimensional space, which we would like to avoid if possible. So our strategy will be to use this solution to construct the linear power spectrum.

While minimum variance mode reconstruction $\hat{\boldsymbol{s}}$ has been inverse generalized noise weighted, its square cannot give an unbiased estimator of the power spectrum, and needs to be corrected. First of all, $\hat{\boldsymbol{s}}$ contains noise contribution, and upon squaring it this will give a term that needs to be removed. Second, minimum variance modes $\hat{\boldsymbol{s}}$ only agree with truth in the absence of noise and for a complete coverage, but are otherwise reduced in amplitude and mixed with each other. So one needs a mixing matrix to correct for these effects.

Heuristically, we can write an estimator for power $S(k)$ at the single mode $k$ as

$$(\boldsymbol{F}\hat{\boldsymbol{S}})_k = \frac{|\hat{s}(k)|^2}{2S_{\text{fid}}(k)^2} - b_k, \tag{3.4}$$

where $\boldsymbol{F}$ is the mixing matrix between the modes and $b_k$ is the noise bias term. This term can be determined by requiring that the equation above is unbiased at some fiducial power spectrum $S_{\text{fid}}$. We have divided by the sampling variance of the power spectrum for a single mode $2S_{\text{fid}}(k)^2$ (to be evaluated at some fiducial power spectrum). In the limit where there is no noise the latter is the variance of that mode power (note that we are imagining one independent mode per each $\boldsymbol{k}$, while in practice these are complex modes with two independent mode realizations, but where the mode at $\boldsymbol{k}$ is a complex conjugate of the mode at $-\boldsymbol{k}$). So in this limit this gives the inverse variance weighting of the power spectrum, where the variance is given by the signal (sampling variance). Noise variance is accounted for by the reduced value of $\hat{s}_k$ relative to no noise case, an outcome of the minimum variance reconstruction of MAP $\hat{\boldsymbol{s}}$. As shown below, the above expression correctly weights by the inverse generalized noise of the power.

We will interpret $\boldsymbol{F}$ as the matrix that determines the mixing between the different power spectrum estimators (where in the expression above each mode leads to an independent power spectrum estimator). We will determine both $\boldsymbol{F}$ and $\boldsymbol{b}$ using simulations around some fiducial model, enforcing that equation 3.4 gives an on average unbiased estimation for any small power spectrum variations around some fiducial model. We will show that we can interpret $\boldsymbol{F}$ as the Fisher matrix, i.e. the ensemble averaged inverse covariance matrix for the estimators, as a consequence of Newton's method. Since equation 3.4 leads to an estimator for each mode it is customary to average them into bandpowers, by adding up estimators within a certain range of wavevectors.

The plan of the next sections is as follows. In section 3.3 we construct the minimum variance solution for $\boldsymbol{s}$. We will assume $\boldsymbol{\Theta}$ and $\boldsymbol{\lambda}$ are fixed and we will not carry their dependence. In section 3.4 we marginalize over $\boldsymbol{s}$ and construct maximum likelihood solution for $\boldsymbol{\Theta}$, assuming $\boldsymbol{\lambda}$ is fixed. In section 3.5 we apply the method to a simple but nontrivial nonlinear example, which is followed by conclusions in section 3.6.

## 3.3 Maximum a posteriori (MAP) initial mode estimator

In this section we work out the minimum variance modes $\boldsymbol{s}$ at fixed $\boldsymbol{\Theta}, \boldsymbol{\lambda}$ around some fiducial model, so we will not include their dependence in the expressions below. For simplicity we will use $\boldsymbol{S}$ for the fiducial model. The conditional posterior probability for $\boldsymbol{s}$ given the data and prior $P_s(\boldsymbol{s})$ is $P(\boldsymbol{s}|\boldsymbol{d}) \propto P_s(\boldsymbol{s})P_n(\boldsymbol{d}-\boldsymbol{f}(\boldsymbol{s}))$, which from equation 3.1 is

$$P(\boldsymbol{s}|\boldsymbol{d}) = (2\pi)^{-(M+N)/2}\det(\boldsymbol{S}\boldsymbol{N})^{-1/2}\exp\left(-\frac{1}{2}\left\{\boldsymbol{s}^{\dagger}\boldsymbol{S}^{-1}\boldsymbol{s} + \left[\boldsymbol{d}-\boldsymbol{f}(\boldsymbol{s})\right]^{\dagger}\boldsymbol{N}^{-1}\left[\boldsymbol{d}-\boldsymbol{f}(\boldsymbol{s})\right]\right\}\right). \tag{3.5}$$

The MAP solution of the initial modes can be obtained by maximizing the posterior of $\boldsymbol{s}$ at a fixed $\boldsymbol{S}$ and $\boldsymbol{N}$, which is equivalent to minimizing the loss function $\chi^2$,

$$\chi^2(\boldsymbol{s}) = \boldsymbol{s}^{\dagger}\boldsymbol{S}^{-1}\boldsymbol{s} + [\boldsymbol{d}-\boldsymbol{f}(\boldsymbol{s})]^{\dagger}\boldsymbol{N}^{-1}[\boldsymbol{d}-\boldsymbol{f}(\boldsymbol{s})], \tag{3.6}$$

with respect to all coefficients $\boldsymbol{s}$.

The problem of finding the minimum variance field $\boldsymbol{s}$ can thus be recast into solving a minimization problem of a nonlinear function $\chi^2$, which is an optimization problem. A generic class of optimization models is based on second order Newton's method, which expands the nonlinear function to a quadratic order around a point $\boldsymbol{s}_m$,

$$\chi^2(\boldsymbol{s}) = \chi_0^2 + 2\boldsymbol{g}^\dagger \Delta \boldsymbol{s} + \Delta \boldsymbol{s}^\dagger \boldsymbol{D} \Delta \boldsymbol{s}, \tag{3.7}$$

where $\Delta \boldsymbol{s} = \boldsymbol{s} - \boldsymbol{s}_m$. We can introduce the gradient matrix around $\boldsymbol{s_m}$ as

$$f'_{ij} = \frac{\partial f(\boldsymbol{s_m})_i}{\partial s_j}. \tag{3.8}$$

Response function depends on the position $\boldsymbol{s_m}$, but we will not keep that index explicitly in our expressions. For linear models the matrix $\boldsymbol{f'}$ is a constant independent of position. The gradient of the cost function is

$$\boldsymbol{g} = \frac{1}{2}\frac{\partial \chi^2}{\partial \boldsymbol{s}} = \boldsymbol{S}^{-1}\boldsymbol{s_m} - \boldsymbol{f'}^\dagger(\boldsymbol{s_m})\boldsymbol{N^{-1}}[\boldsymbol{d} - \boldsymbol{f}(\boldsymbol{s_m})]. \tag{3.9}$$

We want to find a solution where $\boldsymbol{g} = 0$, and we will denote the solution as $\hat{\boldsymbol{s}}$,

$$\boldsymbol{g} = \boldsymbol{S}^{-1}\hat{\boldsymbol{s}} - \boldsymbol{f'}^\dagger(\hat{\boldsymbol{s}})\boldsymbol{N}^{-1}[\boldsymbol{d} - \boldsymbol{f}(\hat{\boldsymbol{s}})] = 0. \tag{3.10}$$

Note that $\boldsymbol{f'}$ is the derivative of the forward model at every position with respect to every initial mode. This can be very expensive to compute for complicated nonlinear models since it requires back-propagation, and is typically not part of the standard N-body simulation codes.

The curvature matrix $\boldsymbol{D}$ equals one half of Hessian matrix and can be written as

$$\boldsymbol{D} = \frac{1}{2}\frac{\partial \chi^2}{\partial \boldsymbol{s} \partial \boldsymbol{s}} = \boldsymbol{S}^{-1} + \boldsymbol{f'}^\dagger \boldsymbol{N}^{-1}\boldsymbol{f'} + \boldsymbol{f''}\boldsymbol{N}^{-1}[\boldsymbol{d} - \boldsymbol{f}(\boldsymbol{s_m})]. \tag{3.11}$$

The last term above contains a second derivative of the $\chi^2$, $\boldsymbol{f''} = \partial^2 f / \partial \boldsymbol{s} \partial \boldsymbol{s}$, and is often neglected when performing optimization, because it fluctuates around zero uncorrelated with the model and hence tends to average to zero. It is also often small (or exactly zero for linear models), and its inclusion may make the optimization unstable [191]. We will also not keep it in our expressions below, and the procedure becomes the so called Gauss-Newton method. Keeping or dropping this term has no impact on the final solution of the optimization.

Minimizing $\chi^2$ equals setting its gradient with respect to $\Delta \boldsymbol{s}$ to zero,

$$\frac{\partial \chi^2(\boldsymbol{s})}{\partial \Delta \boldsymbol{s}} = 0, \tag{3.12}$$

which from equation 3.7 gives

$$\Delta \boldsymbol{s} = -\boldsymbol{D^{-1}}\boldsymbol{g}. \tag{3.13}$$

If we had a perfect inverse curvature matrix and the system was linear this would find the solution where $\boldsymbol{g} = 0$. In nonlinear Newton's method one takes this solution as a starting point, performing a line search in the direction of $\boldsymbol{\Delta s}$ to find a suitable new position $\boldsymbol{s}_{m+1}$, which reduces the cost function $\chi^2$ along the line,

$$\boldsymbol{s}_{m+1} - \boldsymbol{s}_m = -\alpha \boldsymbol{D^{-1}g}. \tag{3.14}$$

We start with $\alpha = 1$. If this reduces the cost function we accept it as the next iteration, otherwise we use bisection method to determine a new $\alpha$, repeating the procedure (if no solution is found we switch to regular steepest descent method). This line search does not require a new evaluation of the derivatives, but it does require a full forward model evaluation of $\boldsymbol{f(s_m + \Delta s)}$ for each $\alpha$, and hence can be expensive. The procedure is repeated until one converges to the minimum $\hat{\boldsymbol{s}}$.

As stated above in linear models one can perform this step only once, starting from $\boldsymbol{s}_0 = 0$, to give

$$\boldsymbol{\Delta s} = \hat{\boldsymbol{s}} = \boldsymbol{D^{-1} f'^{\dagger} N^{-1} d}. \tag{3.15}$$

This is the Wiener filter solution, which minimizes the variance [200]. Note that even though the solution is analytic, it requires inversion of a large matrix $\boldsymbol{D}$, which is an $M^3$ process and becomes prohibitively expensive for large $M$. Optimization methods discussed here can be the best choice even for linear models.

At the position of the minimum one can write the conditional probability of $\boldsymbol{s}$ given the data as

$$P(\boldsymbol{s}|\boldsymbol{d}) \propto \exp\left(-\frac{1}{2}[\boldsymbol{s} - \hat{\boldsymbol{s}}]^{\dagger} \boldsymbol{D} [\boldsymbol{s} - \hat{\boldsymbol{s}}]\right), \tag{3.16}$$

where $\hat{\boldsymbol{s}}$ is the value of $\boldsymbol{s}$ found at the minimum. The covariance matrix of residuals is given by the inverse of curvature matrix

$$\langle [\boldsymbol{s} - \hat{\boldsymbol{s}}]^{\dagger} [\boldsymbol{s} - \hat{\boldsymbol{s}}] \rangle = \boldsymbol{D}^{-1} = \left(\boldsymbol{S}^{-1} + \boldsymbol{f'}^{\dagger} \boldsymbol{N}^{-1} \boldsymbol{f'}\right)^{-1}, \tag{3.17}$$

where the gradient $\boldsymbol{f'}$ is computed at the MAP $\hat{\boldsymbol{s}}$ and we dropped $\boldsymbol{f''N}^{-1}(\boldsymbol{d} - \boldsymbol{f})$ term, which fluctuates around zero.

Function optimization (minimization/maximization) is a large field of research, and many different methods have been developed for a wide range of applications [168]. Here we will work in a large number of dimensions (with both $M$ and $N$ expected to be in millions or more), and a brute force Hessian inversion in equation 3.13 is not feasible. Two of the popular classes of optimization solvers are conjugate gradient methods (often coupled to a preconditioner), which do not require a construction of curvature matrix (or its inverse) at all, and quasi-Newton's methods, which approximate the inverse Hessian, of which limited memory BFGS (L-BFGS) is the most popular implementation [191]. We have used Gauss-Newton's approach in the derivation above to highlight the analogy with linear algebra derivation of [208], but ultimately the choice of optimization method will be determined by its effectiveness. In our tests we have found L-BFGS to be faster than conjugate gradient, but this could depend on the application and implementation. The derivation above does not include normalization, but in practical applications we have found to be useful to rescale (normalize) and work with the modes $\boldsymbol{u} = \boldsymbol{s}/\boldsymbol{S}^{1/2}$.

## 3.4 Minimum variance initial power spectrum estimator

While knowing the MAP solution $\hat{\boldsymbol{s}}$ is useful to create a map of the universe, this is still too much information for most applications. What we want to know is the statistical distribution of the linear modes, and since these are assumed to be Gaussian a suitable summary statistic is their power spectrum. Basically, we want to know the parameters $\boldsymbol{\Theta}$, which are priors for $\boldsymbol{s}$ and marginalize over $\boldsymbol{s}$. In this section we address the dependence on parameters $\boldsymbol{\Theta}$, while still keeping parameters $\boldsymbol{\lambda}$ fixed at their fiducial values (and we will not carry their dependence).

Formally we want to maximize the posterior probability of the data as a function of some power spectrum parameters $\Theta_l$ that determine the initial mode power spectrum $\boldsymbol{S}$, independent of the underlying field $\hat{\boldsymbol{s}}$. We can introduce a derivative matrix $\boldsymbol{\Pi}_l$ around some fiducial power spectrum $\boldsymbol{S}^{\text{fid}}$, defined as

$$\left[\frac{\partial \boldsymbol{S}}{\partial \Theta_l}\right]_{\boldsymbol{S}^{\text{fid}}} = \boldsymbol{\Pi}_l, \tag{3.18}$$

which is to be evaluated at the fiducial model. In terms of this we can write

$$\boldsymbol{S} = \boldsymbol{S}^{\text{fid}} + \sum_l \Delta\Theta_l \boldsymbol{\Pi}_l. \tag{3.19}$$

For linear dependence of $\boldsymbol{S}$ on $\boldsymbol{\Theta}$ and bandpowers we can use

$$\boldsymbol{\Pi}_l = \frac{\boldsymbol{S}_{\text{fid}}}{\Theta_l}, \tag{3.20}$$

i.e. $\langle s_{k_l} s^*_{k_l} \rangle = \Theta_l \Pi_l(k_l)$. In this case the derivative matrix takes us from $\Theta_l$, which is the power spectrum value representative over a bin, to $\boldsymbol{S}$ that is the power spectrum. For concreteness we will initially bin the power spectrum into bins, summing over all the $K_l$ modes $\{s_{k_l}\}(k_l = 1, ..., K_l)$. These are the modes that contribute to $l$ bandpower of the power spectrum parametrized with $\Theta_l$. For a narrow bin the derivative matrix $\boldsymbol{\Pi}_l$ consists of ones along the diagonal corresponding to the $K_l$ modes and zeros otherwise. For broader bandpower bins the derivative matrix can allow for any expected variation of the power within the bin. For example, if we only have a single bin which covers the entire range of modes then the corresponding $\Theta_1$ is a power spectrum amplitude chosen at some wavemode $k_f$ (or some integral over the modes, such as $\sigma_8^2$ normalization), while the derivative matrix has the shape of a fiducial power spectrum, i.e. $\boldsymbol{\Pi}_1 = \boldsymbol{S}_{\text{fid}}/\Theta_1$.

### Analytic marginalization with perturbative approach

In the case of power spectrum estimation one wants to marginalize the full posterior over the parameters $\hat{\boldsymbol{s}}$. Since a brute force approach with sampling is too expensive, we choose to approximate it as a multi-variate Gaussian as in equation 3.16. An implicit assumption in the procedure is that there is one global minimum, to which optimization converges regardless of the starting point. This is a major assumption and may not be valid, either because the global minimum is not reachable (because optimization is stuck in a local minimum), because the correct solution does not correspond to the global minimum, or because the posterior around the global minimum is not well described as a multi-variate Gaussian. Here we will assume this approach is justified but there are no guarantees and indeed on very small scales the methodology may need to be modified.

Under this assumption our strategy is to marginalize over the modes, by writing it as a multi-variate Gaussian around the maximum, and then complete the square. Note that the MAP $\hat{\boldsymbol{s}}$ and its covariance $\boldsymbol{D}$ is implicitly a function of the data, the forward model parameters and the power spectrum bandpower parameters $\boldsymbol{\Theta}$ we wish to estimate. In [109] the resulting expression was called a grand likelihood $L(\boldsymbol{d}|\boldsymbol{\Theta})$. The full problem can be solved if we linearize the response around the MAP initial mode estimator $\hat{\boldsymbol{s}}$ and perform analytic integration under Gaussian approximation. We begin with equation 3.5, expanding around $\boldsymbol{s} = \hat{\boldsymbol{s}} + \delta\boldsymbol{s}$,

$$P(\boldsymbol{s},\boldsymbol{d}|\boldsymbol{\Theta}) = (2\pi)^{-(M+N)/2}\det(\boldsymbol{S}\boldsymbol{N})^{-1/2}\times$$
$$\exp\left(-\frac{1}{2}\left\{(\hat{\boldsymbol{s}}+\delta\boldsymbol{s})^{\dagger}\boldsymbol{S}^{-1}(\hat{\boldsymbol{s}}+\delta\boldsymbol{s}) + \left[\boldsymbol{d}-\boldsymbol{f}(\hat{\boldsymbol{s}}+\delta\boldsymbol{s})\right]^{\dagger}\boldsymbol{N}^{-1}\left[\boldsymbol{d}-\boldsymbol{f}(\hat{\boldsymbol{s}}+\delta\boldsymbol{s})\right]\right\}\right). \quad (3.21)$$

If we collect all the terms that involve $\delta\boldsymbol{s}$ they will vanish by the requirement that the gradient is zero, equation 3.10, by definition of $\hat{\boldsymbol{s}}$: the posterior surface is quadratic at the minimum of the loss function. We are left with

$$\begin{aligned}
&P(\boldsymbol{s},\boldsymbol{d}|\boldsymbol{\Theta}) = (2\pi)^{-(M+N)/2}\det(\boldsymbol{S}\boldsymbol{N})^{-1/2}\times\\
&\exp\left(-\frac{1}{2}\left\{\hat{\boldsymbol{s}}^{\dagger}\boldsymbol{S}^{-1}\hat{\boldsymbol{s}} + \left[\boldsymbol{d}-\boldsymbol{f}(\hat{\boldsymbol{s}})\right]^{\dagger}\boldsymbol{N}^{-1}\left[\boldsymbol{d}-\boldsymbol{f}(\hat{\boldsymbol{s}})\right] + \delta\boldsymbol{s}^{\dagger}\boldsymbol{D}\delta\boldsymbol{s}\right\}\right)\times\\
&\exp\left[\boldsymbol{D}_3(\hat{\boldsymbol{s}})\delta\boldsymbol{s}\delta\boldsymbol{s}\delta\boldsymbol{s} + \boldsymbol{D}_4(\hat{\boldsymbol{s}})\delta\boldsymbol{s}\delta\boldsymbol{s}\delta\boldsymbol{s}\delta\boldsymbol{s} + ...\right],
\end{aligned} \quad (3.22)$$

where $\boldsymbol{D}$ is the curvature matrix of equation 3.11 and more generally we have defined

$$\boldsymbol{D}_n(\hat{\boldsymbol{s}}) = \frac{1}{2n!}\left[\frac{\partial^n\chi^2}{(\partial\boldsymbol{s})^n}\right]_{\boldsymbol{s}=\hat{\boldsymbol{s}}}. \quad (3.23)$$

We see that $\boldsymbol{D} = 2\boldsymbol{D}_2$. In terms of derivatives of $\boldsymbol{f}$ we have

$$\boldsymbol{D}_3 = \frac{1}{4}\boldsymbol{f}'^{\dagger}\boldsymbol{N}^{-1}\boldsymbol{f}'', \quad (3.24)$$

and

$$\boldsymbol{D}_4 = \frac{1}{48}\left[3\boldsymbol{f}''^{\dagger}\boldsymbol{N}^{-1}\boldsymbol{f}'' + 4\boldsymbol{f}'^{\dagger}\boldsymbol{N}^{-1}\boldsymbol{f}'''\right]. \quad (3.25)$$

We have consistently dropped the terms with $\boldsymbol{d}-\boldsymbol{f}(\hat{\boldsymbol{s}})$, which fluctuate around zero. All the terms in the last line of equation 3.22 are scalars.

Next we assume a perturbative expansion in terms of higher order derivatives and/or low noise (we will define the expansion parameter below), bringing the higher order terms $\boldsymbol{D}_n$ down from the exponential,

$$\exp\left[\boldsymbol{D}_3(\hat{\boldsymbol{s}})\delta\boldsymbol{s}\delta\boldsymbol{s}\delta\boldsymbol{s} + \boldsymbol{D}_4(\hat{\boldsymbol{s}})\delta\boldsymbol{s}\delta\boldsymbol{s}\delta\boldsymbol{s}\delta\boldsymbol{s} + ...\right] = 1 + \boldsymbol{D}_3(\hat{\boldsymbol{s}})\delta\boldsymbol{s}\delta\boldsymbol{s}\delta\boldsymbol{s} + \boldsymbol{D}_4(\hat{\boldsymbol{s}})\delta\boldsymbol{s}\delta\boldsymbol{s}\delta\boldsymbol{s}\delta\boldsymbol{s} + ... \quad (3.26)$$

We can now obtain the perturbative expansion of the marginalized likelihood function by integrating out $\delta\boldsymbol{s}$,

$$\begin{aligned}
&P(\boldsymbol{\Theta}|\boldsymbol{d}) \propto L(\boldsymbol{d}|\boldsymbol{\Theta}) = \int P(\boldsymbol{s},\boldsymbol{d}|\boldsymbol{\Theta}) d^M\delta\boldsymbol{s} \\
&= (2\pi)^{-(M+N)/2}\det(\boldsymbol{S}\boldsymbol{N})^{-1/2}\exp\left(-\frac{1}{2}\left[\hat{\boldsymbol{s}}^\dagger\boldsymbol{S}^{-1}\hat{\boldsymbol{s}} + (\boldsymbol{d}-\boldsymbol{f}(\hat{\boldsymbol{s}}))^\dagger\boldsymbol{N}^{-1}(\boldsymbol{d}-\boldsymbol{f}(\hat{\boldsymbol{s}}))\right]\right)\times \\
&\int \exp\left\{-\frac{1}{2}\delta\boldsymbol{s}^\dagger\boldsymbol{D}\delta\boldsymbol{s}\right\} d^M\boldsymbol{s}\left[1 + \boldsymbol{D}_3(\hat{\boldsymbol{s}})\delta\boldsymbol{s}\delta\boldsymbol{s}\delta\boldsymbol{s} + \boldsymbol{D}_4(\hat{\boldsymbol{s}})\delta\boldsymbol{s}\delta\boldsymbol{s}\delta\boldsymbol{s}\delta\boldsymbol{s}...\right] \\
&= (2\pi)^{-N/2}\det(\boldsymbol{S}\boldsymbol{N}\tilde{\boldsymbol{D}})^{-1/2}\exp\left(-\frac{1}{2}\left[\hat{\boldsymbol{s}}^\dagger\boldsymbol{S}^{-1}\hat{\boldsymbol{s}} + (\boldsymbol{d}-\boldsymbol{f}(\hat{\boldsymbol{s}}))^\dagger\boldsymbol{N}^{-1}(\boldsymbol{d}-\boldsymbol{f}(\hat{\boldsymbol{s}}))\right]\right). \quad (3.27)
\end{aligned}$$

We have defined

$$\det\tilde{\boldsymbol{D}}^{-1/2} = \det\boldsymbol{D}^{-1/2}\left[1 + 3\mathrm{tr}(\boldsymbol{D}^{-1}\boldsymbol{D}_4\boldsymbol{D}^{-1}) + ...\right]. \quad (3.28)$$

The lowest order term $\det\boldsymbol{D}$ is given by the Gaussian integral. The next order term is a 1-loop contribution consisting of $f''^2$ and $f'''f'$ inside $\boldsymbol{D}_4$, and we used Wick's theorem to perform the Gaussian integrals. We can also define

$$\tilde{\boldsymbol{C}} \equiv \boldsymbol{S}\boldsymbol{N}\tilde{\boldsymbol{D}} = \boldsymbol{N} + \boldsymbol{f}'\boldsymbol{S}\boldsymbol{f}'^\dagger + ..., \quad (3.29)$$

where ... denotes higher order terms in $\tilde{\boldsymbol{D}}$ and we used equation 3.17 for $\boldsymbol{D}$.

We see that to marginalize over a set of parameters $\boldsymbol{s}$ one has first to find their maximum posterior $\hat{\boldsymbol{s}}$, as derived in previous section via optimization, after which the integration over the parameters can be performed analytically assuming a perturbative expansion. This procedure implicitly assumes a single maximum posterior and a simple posterior around $\hat{\boldsymbol{s}}$. When this is not satisfied, for example in the presence of multiple peaked posterior, one must either perform the appropriate statistical average over these, if they are widely separated, or show that all the local peaks are close to each other and thus essentially giving the same solution. For now we will proceed assuming a single peaked posterior. Note that integration over $\boldsymbol{s}$ produced an additional factor of $\tilde{\boldsymbol{D}}^{-1/2}$ relative to doing the maximum likelihood over all parameters simulteneously.

Let us look at the structure of the resulting expression in equation 3.27. The main term that depends on the data is in the exponential, $\exp[-\chi^2(\hat{\boldsymbol{s}})/2]$. This term consists of the prior term and of the goodness of data fit, both evaluated at the MAP position $\hat{\boldsymbol{s}}$. The other term is $\det\boldsymbol{S}\boldsymbol{N}\tilde{\boldsymbol{D}}$. This term represents the volume of the priors and posteriors. We wish to explore its sensitivity to the parameters $\boldsymbol{\Theta}$ that determine $\boldsymbol{S}$, so we wish to take derivative of this term wrt $\boldsymbol{\Theta}$.

From equation 3.29 we obtain

$$\det(\tilde{\boldsymbol{C}}) \approx \det(\boldsymbol{N} + \boldsymbol{f'} \boldsymbol{S} \boldsymbol{f'}^{\dagger}). \tag{3.30}$$

In the low noise limit it gives $\det(\tilde{\boldsymbol{C}}) \approx \det(\boldsymbol{f'} \boldsymbol{S} \boldsymbol{f'}^{\dagger})$, which is highly sensitive to the parameters $\boldsymbol{\Theta}$ inside $\boldsymbol{S}$. In the high noise limit we have $\det(\boldsymbol{SND}) \approx \det \boldsymbol{N}$. In this limit we do not get any information about the parameters $\Theta$. This is reflected in the values of $\hat{\boldsymbol{s}}$, which are at the their full value in the low noise limit and become smaller and smaller as the noise increases.

Next we look at the data dependence of the curvature matrix $\tilde{\boldsymbol{D}}$. If the model is linear $\tilde{\boldsymbol{D}}$ does not depend on the data, because $\boldsymbol{f'}$ is a constant and $f^{(n)} = 0$ for $n > 1$. Thus this term can be evaluated using a method that is data independent, such as a simulation. For nonlinear models we have to account for the data dependence of $\tilde{\boldsymbol{D}}$. Let us first look at the leading term $\boldsymbol{D}$, given in equation 3.17. For nonlinear models the first derivative $\boldsymbol{f'}(\hat{\boldsymbol{s}})$ is data dependent. For example, suppose we Taylor expand the forward model in terms of $\boldsymbol{s}$,

$$\boldsymbol{f}(\boldsymbol{s}) = \boldsymbol{R}_1 \boldsymbol{s} + \frac{1}{2} \boldsymbol{R}_2 \boldsymbol{s}\boldsymbol{s}..., \tag{3.31}$$

we see that

$$\boldsymbol{f'}(\hat{\boldsymbol{s}}) = \boldsymbol{R}_1 + \boldsymbol{R}_2 \hat{\boldsymbol{s}} + ... \tag{3.32}$$

and hence the covariance $\boldsymbol{D}$ depends on $\hat{\boldsymbol{s}}$ through $\boldsymbol{R}_2 \hat{\boldsymbol{s}} + ....$ Depending on the realization value of $\hat{\boldsymbol{s}}$ the associated error can be larger or smaller than the first order term $\boldsymbol{R}_1$. We can see this from equation 3.10. The solution to this equation balances between the prior term $\boldsymbol{S}^{-1} \hat{\boldsymbol{s}}$, which on its own would give $\hat{\boldsymbol{s}} = 0$, and the data term $\boldsymbol{f'^{\dagger}}(\hat{\boldsymbol{s}}) \boldsymbol{N^{-1}} [\boldsymbol{d} - \boldsymbol{f}(\hat{\boldsymbol{s}})]$, which on its own would solve for $\boldsymbol{f}(\hat{\boldsymbol{s}}) = \boldsymbol{d}$. The balance between the two is determined by $\boldsymbol{S} \boldsymbol{f'^{\dagger}}(\hat{\boldsymbol{s}}) \boldsymbol{N^{-1}}$, which contains data realization dependence inside $\boldsymbol{f'}(\hat{\boldsymbol{s}})$. Thus the solution for $\hat{\boldsymbol{s}}$ automatically accounts for generalized noise weighting of the modes including realization dependence, at least at the lowest order.

Let us look next at the 1-loop term $\mathrm{tr}(\boldsymbol{D}^{-1} \boldsymbol{D}_4 \boldsymbol{D}^{-1})$. This term represents an increase in volume of posterior of $\delta \boldsymbol{s}$ around $\hat{\boldsymbol{s}}$ relative to the Gaussian approximation. Using equations 3.17 and 3.25 we find this term scales as, schematically,

$$\boldsymbol{D}^{-1} \boldsymbol{D}_4 \boldsymbol{D}^{-1} \propto [3 \boldsymbol{f''}^2 + 4 \boldsymbol{f'} \boldsymbol{f'''}] \boldsymbol{N}. \tag{3.33}$$

Thus the 1-loop term vanishes in the limit of either small noise or small nonlinearity. Both of these conditions are likely to be satisfied on large scales, where noise relative to power is small and modes are nearly linear. As we push the marginalization to smaller scales we get larger and larger corrections from this term. This term is also data dependent. This means that one may have a situation where Taylor expansion suggests the posterior is wide (narrow), because the variance of the mode $\boldsymbol{D}^{1/2}$ is large (small), but the full posterior may be narrower (wider) once we include higher order terms, such as curtosis computed here. At this order our procedure will cease to be optimal in terms of optimal mode weighting, but we will still make it unbiased, as described below. It is unclear however how suboptimal due to higher order corrections our method is. We will show below that our method is essentially giving equal weight to all reconstructed modes, and this may well be valid even beyond the formal applicability regime derived here.

Optimization methods in large number of dimensions do not provide $\det \boldsymbol{D}$, although approximations to it exist in certain methods (e.g. BFGS). It seems even less promising to be able to compute analytically $\det \tilde{\boldsymbol{D}}$. While this term is data realization dependent, it is computed independently of the $\exp[-\chi^2(\hat{\boldsymbol{s}})]$ term, and is essentially determined by the posterior volume of $\delta\boldsymbol{s}$ around $\hat{\boldsymbol{s}}$. In a large number of dimensions the average of this term will not be strongly data realization dependent: for any given realization we will have about the same level of mode to mode fluctuations that will on average have the same posterior volume and give the same value of $\det \tilde{\boldsymbol{D}}$ regardless of where $\hat{\boldsymbol{s}}$ is. This suggests we may evaluate this term average using Monte Carlo methods, with a realistic simulation of the data: even though the MAP values $\hat{\boldsymbol{s}}$ in a simulation will have no relation to the corresponding MAP of the data, the posterior volume of $\delta\boldsymbol{s}$ around it will be nearly the same as for the data, as long as the simulation is close enough to the data. We may give up some optimality by not properly weighting the modes by their full posterior volume, but our procedure is exact in the linear case and in the low noise case, and as argued above equal weighting of the modes may be the valid approach even beyond these two formal limits. In any case, we cannot evaluate the posterior volume properly using the methods developed here, which are perturbative anyways and so not valid in general. This will be the basis for our efficient method of evaluating the optimal estimator and its covariance matrix. Note that even though we use random simulations in this chapter to compute the volume term, we may also construct a simulation that is close to the actual data realization, further reducing the dependence of the volume term on the data realization.

## Maximizing the bandpower likelihood

Using the Bayes theorem and assuming a flat prior on $\boldsymbol{\Theta}$ we have interpreted the posterior $P(\boldsymbol{\Theta}|\boldsymbol{d})$ as proportional to the likelihood $L(\boldsymbol{d}|\boldsymbol{\Theta})$. We can justify using flat prior as the choice which gives unbiased estimators of cosmological parameters, when the summary statistics $\hat{\boldsymbol{\Theta}}$ are used to determine them. This interpretation is only valid when the noise bias and Fisher matrix are evaluated using a fiducial power spectrum not affected by the measurements. When the fiducial model is too far from the final solution one can repeat the procedure with a fiducial model that is closer to the actual solution. Note that we do not impose positivity of the bandpowers with the prior: this is justified if the bandpowers are viewed as summary statistics that are subsequently used to determine cosmological parameters (where physical priors can be imposed).

The next step is to maximize this likelihood with respect to the bandpowers $\boldsymbol{\Theta}$. Given a set of measurements $\boldsymbol{d}$ we wish to find the most probable set of bandpowers $\boldsymbol{\Theta}$ from equation

3.27, where $\boldsymbol{D}$, $\boldsymbol{S}$ and $\hat{\boldsymbol{s}}$ implicitly depend on the bandpowers $\boldsymbol{\Theta}$. To find the most probable set of parameters one needs to find the maximum of the likelihood function $L(\boldsymbol{\Theta})$.

We will find the maximum posterior using Newton's method. We wish to expand the log likelihood in terms of $\boldsymbol{\Theta}$ to a quadratic order around some fiducial values,

$$\ln L(\boldsymbol{\Theta}_{\text{fid}}+\Delta\boldsymbol{\Theta}) = \ln L(\boldsymbol{\Theta}_{\text{fid}}) + \sum_l \left[\frac{\partial \ln L(\boldsymbol{\Theta})}{\partial \Theta_l}\right]_{\boldsymbol{\Theta}_{\text{fid}}} \Delta\Theta_l + \frac{1}{2}\sum_{ll'} \left[\frac{\partial^2 \ln L(\boldsymbol{\Theta})}{\partial \Theta_l \partial \Theta_{l'}}\right]_{\boldsymbol{\Theta}_{\text{fid}}} \Delta\Theta_l \Delta\Theta_{l'}, \tag{3.34}$$

where the terms are evaluated at the fiducial model $\boldsymbol{\Theta}_{\text{fid}}$. We will seek a solution where the first derivative vanishes using Newton's method. The last term of equation 3.34 defines the curvature matrix as the second derivatives of log likelihood with respect to the parameters.

To get the first derivative we need to take a derivative of log likelihood in equation 3.27 with respect to $\Theta_l$. The dependence on $\Theta_l$ is in $\hat{\boldsymbol{s}}$, $\boldsymbol{S}$ and $\boldsymbol{f}(\hat{\boldsymbol{s}})$. We have

$$\frac{\partial \left[(\boldsymbol{d}-\boldsymbol{f}(\hat{\boldsymbol{s}}))^\dagger \boldsymbol{N}^{-1}(\boldsymbol{d}-\boldsymbol{f}(\hat{\boldsymbol{s}}))\right]}{\partial \Theta_l} = -2\left[\boldsymbol{R}\frac{\partial \hat{\boldsymbol{s}}}{\partial \Theta_l}\right]^\dagger \boldsymbol{N}^{-1}(\boldsymbol{d}-\boldsymbol{f}(\hat{\boldsymbol{s}})) = -2\left[\frac{\partial \hat{\boldsymbol{s}}}{\partial \Theta_l}\right]^\dagger \boldsymbol{S}_{\text{fid}}^{-1}\hat{\boldsymbol{s}}, \tag{3.35}$$

where the first relation follows from equation 3.8 and the last relation follows from equation 3.10. We also have

$$\frac{\partial \left[\hat{\boldsymbol{s}}^\dagger \boldsymbol{S}_{\text{fid}}^{-1}\hat{\boldsymbol{s}}\right]}{\partial \Theta_l} = 2\left[\frac{\partial \hat{\boldsymbol{s}}}{\partial \Theta_l}\right]^\dagger \boldsymbol{S}_{\text{fid}}^{-1}\hat{\boldsymbol{s}} - 2E_l(\boldsymbol{S}_{\text{fid}}, \hat{\boldsymbol{s}}), \tag{3.36}$$

defining

$$E_l(\boldsymbol{S}_{\text{fid}}, \hat{\boldsymbol{s}}) = \frac{1}{2}\hat{\boldsymbol{s}}^\dagger \boldsymbol{S}_{\text{fid}}^{-1}\boldsymbol{\Pi}_l \boldsymbol{S}_{\text{fid}}^{-1}\hat{\boldsymbol{s}}. \tag{3.37}$$

All the matrix operations involve diagonal matrices, so using equation 3.20 we get

$$E_l(\boldsymbol{S}_{\text{fid}}, \hat{\boldsymbol{s}}) = \frac{1}{2}\sum_{k_l} \frac{\hat{s}_{k_l}^2}{\Theta_{\text{fid,l}} S_{\text{fid},k_l}}, \tag{3.38}$$

where the sum is over all modes within the bandpower and $S_{\text{fid},k_l}$ is the fiducial power spectrum amplitude at mode $k_l$, which for narrow power spectrum bins is simply $\Theta_{\text{fid},l}$. We see that the terms with $d\hat{\boldsymbol{s}}/d\Theta_l$ cancel out, which gives us, using equation 3.27

$$\frac{\partial \ln L(\boldsymbol{\Theta})}{\partial \Theta_l} = E_l - b_l, \tag{3.39}$$

where we defined

$$b_l = \frac{1}{2}\text{tr}\left[\frac{\partial \ln(\boldsymbol{S}\boldsymbol{N}\tilde{\boldsymbol{D}})}{\partial \Theta_l}\right]_{\boldsymbol{S}_{\text{fid}}}. \tag{3.40}$$

Note that $\boldsymbol{N}$ has no dependence on $\boldsymbol{\Theta}$. This term is non-zero because squaring the MAP field (as done in first term of rhs in equation 3.39) creates a bias. In line with the linear analysis we will continue to call this term noise bias, but unlike the linear case this term may depend on both the noise and the signal. The first term in equation 3.39 states that for narrow bins the derivative is given by adding up all the squares of the modes. We can see that in this term the curvature matrix $\boldsymbol{D}$ (or its generalization $\tilde{\boldsymbol{D}}$) does not enter, and its evaluation is not required. Since we cannot compute the curvature matrix we also cannot take its derivative with respect to parameters, which is needed to compute the noise bias in equation 3.40. In this chapter we instead compute the noise bias by evaluating its ensemble average, using a method described further below. This will mean that we have given up on the information contained in this term. We expect this information to be subdominant, at least in the linear and low noise limits.

The maximum likelihood solution for $\hat{\boldsymbol{\Theta}}$ is given by

$$\left[\frac{\partial \ln L(\boldsymbol{\Theta})}{\partial \Theta_l}\right]_{\hat{\boldsymbol{\Theta}}} = E_l(\hat{\boldsymbol{\Theta}}) - b_l(\hat{\boldsymbol{\Theta}}) = 0. \tag{3.41}$$

To evaluate we would need to evaluate equation 3.40. This gives

$$b_l = \frac{1}{2}\mathrm{tr}\left[\frac{\partial \ln \tilde{\boldsymbol{C}}}{\partial \Theta_l}\right] = \frac{1}{2}\mathrm{tr}\left[\frac{\partial \tilde{\boldsymbol{C}}}{\partial \Theta_l}\tilde{\boldsymbol{C}}^{-1}\right]. \tag{3.42}$$

Using equation 3.29 and dropping higher order terms we obtain

$$b_l = \frac{1}{2}\mathrm{tr}\left[\boldsymbol{f'}\boldsymbol{\Pi}_l\boldsymbol{f'}^{\dagger}\tilde{\boldsymbol{C}}^{-1}\right]. \tag{3.43}$$

We wish to solve equation 3.41 to obtain ML estimate of $\hat{\Theta}_l$, which appears inside $\boldsymbol{S}$. This is a complicated nonlinear equation in terms of $\boldsymbol{S}$ and hence one cannot write the solution in a closed form.

Instead of solving this equation directly we will adopt Newton's method, where we use the quadratic expansion of log-likelihood in equation 3.34, evaluate all the elements at $\boldsymbol{\Theta}_{\text{fid}}$ where the log-likelihood derivative is not zero, and then use Newton's method to find the values $\hat{\boldsymbol{\Theta}}$ where the first derivative is zero. To do this we must therefore evaluate the curvature matrix. Instead of the actual curvature matrix for parameters we will often work with the Fisher matrix, defined as the ensemble average of the curvature around the maximum,

$$F_{ll'} = -\left\langle \frac{\partial^2 \ln L(\boldsymbol{\Theta})}{\partial \Theta_l \partial \Theta_{l'}} \right\rangle. \tag{3.44}$$

Brackets denote ensemble averaging. It may be possible to compute the actual curvature matrix for the data,but in this chapter we will not distinguish between the two and simply call it Fisher matrix, even though this is not exactly the same as the curvature matrix in the Bayesian analysis. For modes that are Gaussian distributed one can interpret the inverse of the Fisher matrix $\boldsymbol{F}^{-1}$ as an estimate of the covariance matrix of the parameters $\hat{\boldsymbol{\Theta}}$,

$$\langle \Delta\hat{\boldsymbol{\Theta}}\Delta\hat{\boldsymbol{\Theta}}^{\dagger}\rangle - \langle \Delta\hat{\boldsymbol{\Theta}}\rangle\langle \Delta\hat{\boldsymbol{\Theta}}\rangle^{\dagger} = \boldsymbol{F}^{-1}. \tag{3.45}$$

Note that for linear modes the likelihood function can be approximated as Gaussian around the maximum provided that sufficient number of independent modes contribute to each $\Theta_l$, by central limit theorem.

We are finally in position to use Newton's method to write the maximum likelihood estimator for $\Delta\boldsymbol{\Theta}$. The solution to the quadratic log likelihood at the peak can be obtained by setting the derivative of equation 3.34 with respect to $\boldsymbol{\Delta\Theta}$ to zero, which upon inserting equation 3.39 gives

$$(\boldsymbol{F}\Delta\hat{\boldsymbol{\Theta}})_l = E_l - b_l, \tag{3.46}$$

where $b_l$ is the noise bias contribution. To solve this equation one needs both $b_l$ and $F_{ll'}$. In principle we could get the latter by evaluating equation 3.44. This would give an expression in terms of a matrix multiplications and trace,

$$F_{ll'} = \frac{1}{2}\mathrm{tr}\left[\frac{\partial\tilde{\boldsymbol{C}}}{\partial\Theta_l}\tilde{\boldsymbol{C}}^{-1}\frac{\partial\tilde{\boldsymbol{C}}}{\partial\Theta_{l'}}\tilde{\boldsymbol{C}}^{-1}\right], \tag{3.47}$$

which is formally of order $N^3$, if we had the matrices. But we do not actually have the matrix $\tilde{\boldsymbol{C}}$ or $\tilde{\boldsymbol{D}}$, so we cannot evaluate this even if we wanted to. We will thus evaluate the Fisher matrix using a different approach using ensemble averaging of simulations. However, in the special case of no mode coupling the Fisher matrix is diagonal and we can combine equations 3.41, 3.42 and 3.47 to obtain

$$F_{ll'} = \frac{2E_l^2}{K_l}\delta_{ll'}. \tag{3.48}$$

In this case we get the actual curvature matrix from the data itself. We will test the accuracy of this approximation in section 3.5 for the specific case of periodic boundary conditions, which is the only case where the assumption of uncorrelated modes may be valid.

From equation 3.46 we see that the raw power spectrum $E_l$ of the reconstructed field requires noise bias subtraction. We also see that after noise bias subtraction we obtain the bandpower estimates convolved with the Fisher matrix $\boldsymbol{F}\Delta\hat{\boldsymbol{\Theta}}$. Fisher matrix thus describes both the covariance matrix and the bandpower mixing. It is the latter interpretation that will be the basis for our fast Fisher matrix evaluation method. As promised, equation 3.38 agrees with our heuristic derivation in equation 3.4. The procedure is implied to be iterative: if the chosen fiducial model is not sufficiently close to the final answer one should choose a new fiducial model and repeat the procedure. The fiducial model should not be simply chosen to be the observed one given by $\boldsymbol{\Theta}_{\mathrm{fid}} + \Delta\hat{\boldsymbol{\Theta}}$, since that contains noise and sampling variance fluctuations. Instead, it should be a smooth model that is sufficiently close to it. Equation 3.46 suggests that all the information from the data is inside $E(\boldsymbol{S}_{\mathrm{fid}}, \hat{\boldsymbol{s}})$. In reality, $\boldsymbol{b}$ and $\boldsymbol{F}$ may also be data dependent (although this is explicitly not the case for the linear model). This is discussed further below.

The form given in equation 3.46 is not the only possibility, and may not be the most practical. More generally, one can write

$$\Delta\hat{\Theta}'_k = \sum_l M_{kl}\left[E_l - b_l\right], \text{ or in matrix form, } \Delta\hat{\boldsymbol{\Theta}}' = \boldsymbol{M}(\boldsymbol{E} - \boldsymbol{b}), \tag{3.49}$$

where $\boldsymbol{M}$ is a matrix that can be chosen depending on the form in which we wish to provide the estimator $\Delta\boldsymbol{\Theta}$', which can be viewed as a window convolved version of $\Delta\boldsymbol{\Theta}$. There are three natural choices [178] that we discuss next.

First choice is $\boldsymbol{M} = \boldsymbol{F}^{-1}$, which corresponds to the fully deconvolved estimator ($\Delta\boldsymbol{\Theta}' = \Delta\boldsymbol{\Theta}$ from equation 3.46), with anti-correlated errorbars (which can explode if the sampling of modes is too fine compared to the width of the window).

A second choice is

$$M_{kl} = \frac{\delta_{kl}}{\sum_i F_{ki}}, \tag{3.50}$$

which corresponds to the minimum variance errors on $\Delta\hat{\Theta}'_k$, but which are all convolved with a window given by $\boldsymbol{MF}$. We will use this choice in this chapter because it does not require a matrix inversion. Division by $\sum_i F_{ki}$ ensures the estimator is centered around the true value. However, this can cause problems if the matrix $\boldsymbol{M}$ is singular, which can happen if there is no information about a given bandpower in the data. In this case it is better not to divide by this factor and simply use $M_{kl} = \delta_{kl}$.

A third choice is to decorrelate the estimators (within the disconnected covariance matrix approximation) [101],

$$M_{kl} = \frac{F_{kl}^{-1/2}}{\sum_i F_{ki}^{1/2}}. \tag{3.51}$$

With any of these definitions we can write the expectation value and variance of the estimator as

$$\langle \Delta\hat{\boldsymbol{\Theta}}' \rangle = \boldsymbol{MF}\Delta\boldsymbol{\Theta} \equiv \boldsymbol{W}\Delta\boldsymbol{\Theta}, \tag{3.52}$$

$$\langle \Delta\hat{\boldsymbol{\Theta}}'\Delta\hat{\boldsymbol{\Theta}}'^{\dagger} \rangle - \langle \Delta\hat{\boldsymbol{\Theta}}' \rangle \langle \Delta\hat{\boldsymbol{\Theta}}'^{\dagger} \rangle = \boldsymbol{MFM} \equiv \boldsymbol{C}, \tag{3.53}$$

where the latter contains only the connected part of covariance matrix and we defined the window matrix $\boldsymbol{W} = \boldsymbol{MF}$ and the covariance matrix $\boldsymbol{C} = \boldsymbol{MFM}$. All of these choices are equivalent in terms of their information content: there is no gain or loss of information in choosing one over the other. All the data compression has been done in equation 3.49. The first choice corresponds to identity window matrix, the second is minimum variance and does not require any matrix inversion (equation 3.52) and is thus the easiest to compute, while the third choice provides a diagonal covariance matrix of the estimator, so bandpowers are easy to combine.

The estimator is unbiased as long as the Fisher matrix is computed using a fiducial power spectrum, not affected by the data. If the chosen fiducial power spectrum is very different from the one preferred by the data the procedure is still unbiased, but the estimator may not be optimal and the Fisher matrix may not be accurately interpreted as a covariance matrix. In these situations one may repeat the analysis with a chosen fiducial power spectrum closer to the one preferred by the data. In the case of high precision cosmology where the deviations between the true and fiducial power spectrum are small, the corresponding error induced on the covariance matrix also becomes small.

The estimator presented here (quadratic in MAP) approximates the posterior for bandpowers as a multi-variate Gaussian. This allows us to normalize the posterior, and assuming $L$ bandpowers we have

$$P(\Delta\boldsymbol{\Theta}|\boldsymbol{d}) = [(2\pi)^L \det \boldsymbol{C}]^{-1/2} \exp\left(-\frac{1}{2}\left[\boldsymbol{W}\Delta\boldsymbol{\Theta} - \Delta\hat{\boldsymbol{\Theta}}^{\prime}\right]^{\dagger} \boldsymbol{C}^{-1}\left[\boldsymbol{W}\Delta\boldsymbol{\Theta} - \Delta\hat{\boldsymbol{\Theta}}^{\prime}\right]\right). \quad (3.54)$$

In the linear case this is valid in the limit of large number of modes by central limit theorem. Typically one combines different bandpowers to determine a small number of cosmological paramaters, which makes central limit theorem even more valid. However, in special cases, such as clustering on very large scales with few measured modes, the small number of modes requires one to use a more accurate posterior probability distribution. The connected part of the covariance matrix is not given by the Fisher matrix construction presented above. However, since we are estimating the linear power spectrum, which is assumed to be Gaussian, it is likely that there is no significant connected part, at least for low noise. To address this properly one needs to compare the disconnected covariance matrix to the one from a large number of mocks where the whole procedure has been simulated, and we will not investigate this in any detail in this chapter.

## An efficient evaluation of noise bias and Fisher matrix

What is left is to evaluate the noise bias and Fisher matrix. This is often the most expensive part of the calculation, even for the linear model [178]. Here we are solving the nonlinear problem in which the minimization cannot be solved with linear algebra anyways, so we have to devise a new scheme to evaluate these terms.

Before proceeding it is useful to clarify the nature of the whole procedure. We began by estimating the modes that minimize the variance of the data given the noise and the prior. In doing so we have chosen a fiducial power spectrum $\boldsymbol{S}_{\rm fid}$ for the prior. We then square these modes and add them up within the bandpower $l$. We want to make this estimator unbiased, and with the correct window function describing correlations between the bandpowers. Our primary task is to have the estimator that is unbiased for any choice of the fiducial power spectrum $\boldsymbol{\Theta}_{\rm fid}$. In practice, we expect the estimator will be almost as good as minimum variance even if the fiducial power spectrum chosen in the minimization procedure is not exactly the true power spectrum. Fisher matrix plays two distinct roles in the parameter estimation, as a window function (equation 3.52) and as a covariance matrix (equation 3.53). Here we will use its interpretation as the window function to derive it, quantifying the sensitivity of one bandpower to another. This only involves two point functions, and does not rely on the assumption of Gaussianity. But Newton's method guarantees that the resuting answer is also the covariance matrix.

Since a direct evaluation is not computationally feasible, we will be evaluating Fisher matrix and noise bias terms using simulations. The first question is whether these terms depend on the actual realization. For example, the noise bias is given by the derivative of the log determinant of the curvature matrix with respect to the bandpowers (equation 3.40) and this can depend on the actual realization. This is however not the case in the linear limit [208]. It is also not very important in the low noise limit, where most of the information is in the reconstructed modes and the noise bias is small. More generally, we have argued in the beginning of this section that the volume element $\det \tilde{\boldsymbol{D}}$ of $\delta \boldsymbol{s}$ around $\hat{\boldsymbol{s}}$ can be determined from a simulation in the limit of large number of modes even if the values of $\hat{\boldsymbol{s}}$ differ between a simulation and the data. We will thus proceed by assuming that there is no realization dependence of Fisher matrix and noise bias, and we will determine them using simulations that are unrelated to the actual realization given by the data. Should this assumption turn out to be violated one could explore realization dependence of these terms, for example by using realizations that are conditioned on the data (such as Gibbs sampling), but we do not pursue this further in this chapter. We emphasize that our estimator will still be unbiased at the fiducial model and small variations around it, but it may not be minimum variance.

For the simulations we thus first generate a Gaussian random realization of the signal in Fourier space $\boldsymbol{s}_s$ at the fiducial model, such that

$$\langle |\boldsymbol{s}_s|^2 \rangle = \boldsymbol{S}_{\text{fid}}. \tag{3.55}$$

We have explored both a Gaussian realization, which contains sampling variance fluctuations, and the fixed norm of the mode, where only the phase of the mode is random, while the mode square is exactly given by the fiducial power. The latter does not suffer from sampling variance and converges faster if no sampling variance correction is used, although we will also give prescriptions how to handle sampling variance for the former case. Suppression of sampling variance is crucial and guarantees faster convergence, so the procedure here should not be viewed simply as a Monte Carlo simulation approach.

Next, we map it into the observational space using a forward model,

$$\boldsymbol{d}_s = f(\boldsymbol{s}_s). \tag{3.56}$$

We also generate a noise sample. Similar to the signal, we have explored both a Gaussian realization with unit variance, and the real stochastic $Z_2$ estimator, where for each real space point $\boldsymbol{r}_i$ we generate a random number consisting of 1's and -1's. The latter has a fixed amount of power and is expected to converge faster. In both cases we multiply with $\sigma(\boldsymbol{r}_i)$, the square root of the noise variance at that point $N(\boldsymbol{r}_i) = \sigma^2(\boldsymbol{r}_i)$, to create a random noise data vector $\boldsymbol{d}_n$ with the correct variance. We use this noise realizations $\boldsymbol{d}_n$ added to the signal data $\boldsymbol{d}_{\boldsymbol{s}}$ to create

$$\boldsymbol{d}_{s+n} = \boldsymbol{d}_s + \boldsymbol{d}_n. \tag{3.57}$$

Now that we have a data simulation we pass this through the same sequence of optimization steps as the real data. This leads us to the simulated realizations of the mode estimator $\hat{\boldsymbol{s}}_{s+n}$ for the fiducial model. The cost for performing a single realization is comparable to the cost of analyzing the data.

We want to ensure that the final estimates are unbiased. From equation 3.46 the noise bias is

$$b_l = E_l(\boldsymbol{\Theta}_{\text{fid}}, \hat{\boldsymbol{s}}_{s+n}). \tag{3.58}$$

This equation is simply stating that for a fiducial simulation the estimate of bandpower relative to fiducial power has to vanish. If needed, this needs to be averaged over several realizations.

The window function interpretation of the Fisher matrix is a response of a bandpower $l$ to another bandpower at $l'$, as in equation 3.46. A way to evaluate it is to inject power into one bandpower and measure the estimator response in all the bandpowers (in statistics this is called a sensitivity analysis). Specifically, we take the fiducial power spectrum realization from equation 3.57. We create another Gaussian realization as a small perturbation to it, by injecting a small amount of power into the modes at a single bandpower $l'$. For each of the modes $s_s(k_{l'})$ within the bandpower $l'$ we have a choice to generate either a random realization of the phase, or one given by $s_s(k_{l'})$. We add it to fiducial realization $\boldsymbol{s}_s$

$$\boldsymbol{s}_{l',s} = \boldsymbol{s}_s + \Delta\boldsymbol{s}_{l'}. \tag{3.59}$$

We want the injected power to be $\Delta\Theta_{l'}\boldsymbol{\Pi}_{l'}$ (where $\Delta\Theta_{l'}$ should be small so that linearization of the Fisher matrix is valid, but not too small to be susceptible to roundoff errors), so we choose $\Delta\boldsymbol{s}_{l'}$ to satisfy

$$\langle|\Delta\boldsymbol{s}_{l',s}|^2\rangle - \langle|\Delta\boldsymbol{s}_s|^2\rangle = \Delta\Theta_{l'}\boldsymbol{\Pi}_{l'}. \tag{3.60}$$

We have found that the injected power with modes in phase with $\boldsymbol{s}_s$ works better in terms of the noise in the Fisher matrix.

We then run a forward model to generate $\boldsymbol{d}_{l',s} = f(\boldsymbol{s}_{l',s})$, to which we add exactly the same noise realization as the one in equation 3.57, $\boldsymbol{d}_{l',s+n} = \boldsymbol{d}_{l',s} + \boldsymbol{d}_n$. We pass it through the same sequence of optimization steps as the fiducial model simulation. Since we already have the optimization solution for the fiducial model simulation at $\boldsymbol{d}_s + \boldsymbol{d}_n$, and the injected modes $\Delta\boldsymbol{s}_{l'}$ are a small perturbation in a single bandpower, we can start the optimization at $\hat{s}_{s+n}$. This requires very few steps to converge, giving $\hat{\boldsymbol{s}}_{l',s+n}$. We compute for each bandpower

$$\Delta\hat{\boldsymbol{s}}_{l',s+n} = \hat{\boldsymbol{s}}_{l',s+n} - \hat{\boldsymbol{s}}_{s+n}. \tag{3.61}$$

We can apply equation 3.46 to $\Theta_{l'}$ and $\Theta_{l'} + \Delta\Theta_{l'}$, but still performing the optimization around the fiducial model,

$$\begin{aligned}
(\boldsymbol{F}\boldsymbol{\Theta}_{\rm fid})_l &= E_l(\boldsymbol{\Theta}_{\rm fid}, \hat{\boldsymbol{s}}_{s+n}) - b_l(\boldsymbol{\Theta}_{\rm fid}, \hat{\boldsymbol{s}}_{s+n}), \\
(\boldsymbol{F}[\boldsymbol{\Theta}_{\rm fid} + \Delta\boldsymbol{\Theta}_{l'}])_l &= E_l(\boldsymbol{\Theta}_{\rm fid}, \hat{\boldsymbol{s}}_{l',s+n}) - b_l(\boldsymbol{\Theta}_{\rm fid}, \hat{\boldsymbol{s}}_{l',s+n}).
\end{aligned} \tag{3.62}$$

We are assuming that the Fisher matrix changes are at higher order, so that $\boldsymbol{F}$ is the same at the fiducial model and small perturbation away from it. In general, the noise bias depends on the signal and we cannot assume $b_l(\boldsymbol{\Theta}_{\rm fid}, \hat{\boldsymbol{s}}_{s+n}) = b_l(\boldsymbol{\Theta}_{\rm fid}, \hat{\boldsymbol{s}}_{l',s+n})$. However, in the linear regime this condition is satisfied, and even when it is not we still obtain an estimator that is unbiased, but whose covariance may not be given by the resulting $\boldsymbol{F}$.

Taking the difference between the two terms in equation 3.62 we obtain

$$\left[F_{ll'} + \frac{\partial b_l}{\partial\hat{\boldsymbol{s}}}\frac{\partial\hat{\boldsymbol{s}}}{\partial\Theta_{l'}}\right]\Delta\Theta_{l'} \equiv \tilde{F}_{ll'}\Delta\Theta_{l'} = E_l(\boldsymbol{\Theta}_{\rm fid}, \hat{\boldsymbol{s}}_{l',s+n}) - E_l(\boldsymbol{\Theta}_{\rm fid}, \hat{\boldsymbol{s}}_{s+n}) = E_l(\boldsymbol{\Theta}_{\rm fid}, \Delta\hat{\boldsymbol{s}}_{l',s+n}), \tag{3.63}$$

where the last equality follows if the additional injected modes are uncorrelated with fiducial modes. We have defined a new matrix $\tilde{\boldsymbol{F}}$ as the sum of the true Fisher matrix and the matrix of derivatives of noise bias, which will only approximate the true Fisher matrix (although the relation is exact in linear case where the noise bias derivative term vanishes). In the remainder of this chapter we will ignore this distinction between $\boldsymbol{F}$ and $\tilde{\boldsymbol{F}}$, although we will verify the quality of resulting covariance matrix in our tests. The Fisher matrix is then obtained from equation 3.63, averaged over several realizations if needed. It is important to recognize that our final expressions do not explicitly evaluate the curvature matrix $\boldsymbol{D}$, hence any optimization method can be used to find MAP.

The Fisher matrix is rapidly changing with the bandpower $l$, mostly because typically both the number of modes $K_l$ and the fiducial power $\Theta_l$ are rapidly changing with $l$. However, we can also define normalized version

$$\langle T^2 \rangle_{ll'} = 2\Theta_l \Theta_{l'} F_{ll'} / (K_l K_{l'})^{1/2}, \tag{3.64}$$

which can be viewed as an average squared transfer function. This has the advantage of being a slowly changing function of $l$. As a consequence, one does not need to evaluate it at every $l$, especially for narrow bandpower bins. This allows one to determine the Fisher matrix by injecting the power into sparsely separated bandpowers, and then interpolate between averaged squared transfer function to get the full Fisher matrix.

Sometimes we can adopt a simple approximation of equation 3.48 (see [109]), which follows from the covariance interpretation of the Fisher matrix, together with the Gaussian variance approximation. We will show below this works remarkably well in simple periodic box test cases.

## 3.5 Application to dark matter simulations

We have tested the bandpower method described in section 3.4 on both 2-LPT simulations and on N-body simulations. For the latter we use a cubic box of size 750 Mpc/$h$ with a $128^3$ grid, using the publicly available code FastPM [87] for simulating the nonlinear structure formation and the public code Cosmo++ [15] for optimization. We have used both the full N-body simulation and a simplified second order Lagrangian perturbation theory (2-LPT) for our truth, but below we only show results for the 2-LPT, since the results were almost indistinguishable. We use standard Planck cosmology for all cosmological parameters and the outputs are evaluated at $z = 0$.

Generating a single realization of a full simulation using FastPM is fast. However, for the reconstruction one also needs a gradient with respect to all initial modes (equation 3.8). This can be done using backward propagation [247], but is expensive, both because FastPM is slower than 2-LPT, and because gradient calculation is expensive and memory intensive. Moreover, as we show below, the optimization requires hundreds of calls to compute the gradient, making the full gradient considerably more expensive to compute.

For the purpose of reconstruction in this chapter we thus use a simpler method - we simply use 2-LPT multiplied with an appropriate transfer function. Specifically, we first compute a transfer function by simulating the density fields using PM and 2-LPT and taking the square root of the ratio of the power spectra. Then the gradients are performed using 2-LPT multiplied by the transfer function. If the cross-correlation coefficient between full N-body and 2-LPT is close to unity then there is no loss of information in this process. In practice, at $k = 0.3$h/Mpc the cross-correlation coefficient is 0.98 [228], and this approximation is extremely accurate over the range of $k$ we are interested in here.

In this work we fix the transfer function, under the assumption that it does not vary with the input power spectrum. A full gradient implementation would remove this transfer function step. The simulated fields are smoothed with a Gaussian kernel of size 6 Mpc/$h$, which roughly corresponds to the pixel size. We add white noise to the truth simulation in real space. While smoothing was required to achieve convergence in our tests, with more accurate gradients one should be able to remove this step, and this is something we plan to pursue in the future. Smoothing can often be justified as a way to implement finite resolution of the experiment, although here it should be viewed simply as a tool to improve the convergence.

Note that since we use a full N-body simulation for the truth, but we only use 2-LPT times the transfer function for the optimization, we cannot claim that the procedure extracts all the information optimally. For this reason we also performed the same analysis using 2-LPT as the truth: in this case no transfer function is needed, and within the context of 2-LPT dynamics this procedure is guaranteed to give the optimal power spectrum reconstruction. However, we observe almost no difference between the two cases, a consequence of smoothing, which eliminates signal relative to noise at high $k$, where the cross-correlation coefficient drops below unity. We only present results from the 2-LPT simulation as the truth.

The forward model depends not only on the initial modes, but also on the assumed cosmology. Specifically, in the context of ΛCDM one needs to assume matter density $\Omega_m$, which determines the growth rate as a function of redshift. In this chapter we simplify the analysis by ignoring this dependence, and we assume $\Omega_m$ is known. A more general analysis would explore the likelihood surface as a function of $\Omega_m$ as well, and we plan to explore this in the future.

We show a slice of our truth simulation, with and without noise, in Fig. 3.1. The nonlinear power spectrum of the truth simulation is shown in Fig. 3.2. As a consequence of smoothing the data becomes noise dominated for $k \sim 0.3\, h\, \mathrm{Mpc}^{-1}$.

Let us first discuss the reconstruction of the initial density field. Our optimizer starts at the initial field of zero, and converges in 236 iterations, and at each iteration we evaluate one or two line search steps, with a total of about 300 function evaluations. A slice through the original and the reconstructed initial density fields are shown in Fig. 3.3. For comparison, we also show the reconstruction after 10 and 100 iterations. The corresponding nonlinear density fields are shown in Fig. 3.4. As we can see, the reconstruction works very well on large scales. However, the reconstruction is missing the small scale structure, which is expected, since the data is noise dominated on small scales and the prior, the first term in Eq. 3.6,

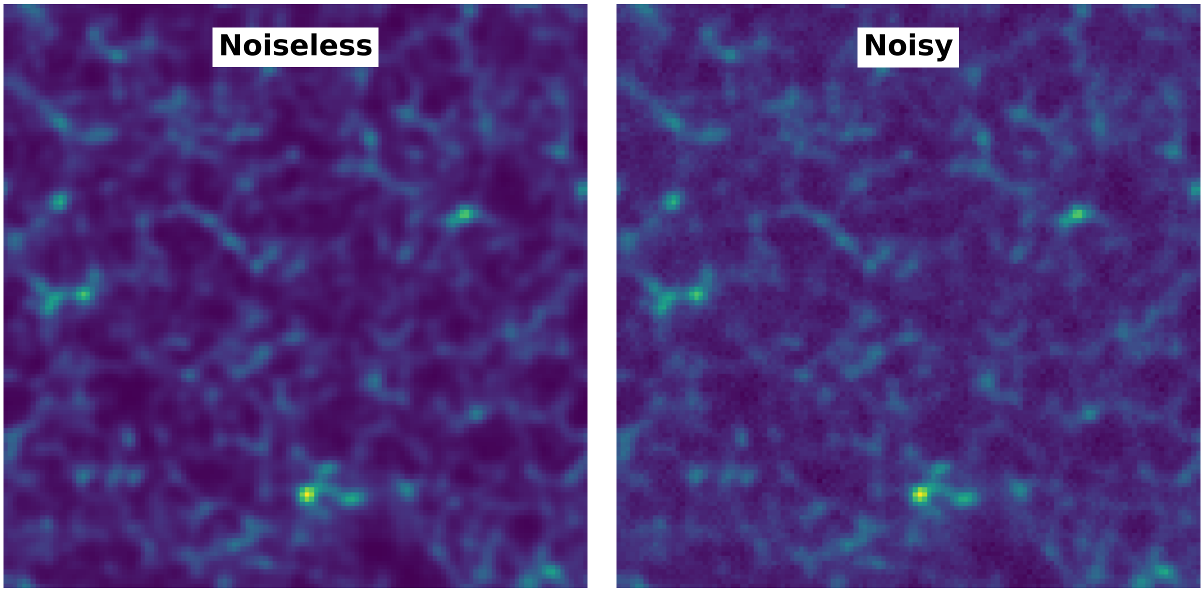


Figure 3.1: The truth simulations without (left) and with (right) noise. The projection uses a slab with a thickness of 24 Mpc/h.

drives the small scale modes to zero. The prior thus acts as a regularizer: in the absence of any real information in the MAP it sets the modes to zero. Lack of small scale modes is much more evident in the initial linear density field of Fig. 3.3. However, it can also be noticed in the nonlinear field in Fig. 3.4. So far we have not encountered any problems with local minima: the procedure always converges to the same solution irrespective of the initial starting point. It remains to be seen whether that will remain the case when we have to deal with strongly nonlinear regime.

Note that even after 10 iterations the structures on large scales are already reconstructed fairly well. For this reason we would expect baryonic acoustic oscillations (BAO) to be reconstructed well after a few iterations only, similar to the BAO reconstruction methods [74, 263, 204]. After 100 iterations the reconstructed field is indistinguishable by eye from the final iteration.

To show the convergence rate of the optimizer we have plotted $\chi^2 - \chi^2_{\rm min}$ as a function of number of iterations in Fig. 3.5. The convergence, here defined as a change of $\chi^2$ less than 1, is achieved after 236 steps. After 150 steps the $\chi^2$ is about 1000 above the minimum. While this may sound a lot, the number of modes is $128^3 \sim 2 \times 10^6$, so per degree of freedom this is a small change, and explains why visually the maps do not significantly change from 100 iterations to the final reconstructed map. We discuss this issue further below.

To compare the reconstructed density field with the original truth field quantitatively, we plot the cross correlation and the transfer function between these two fields in Fig. 3.6. The

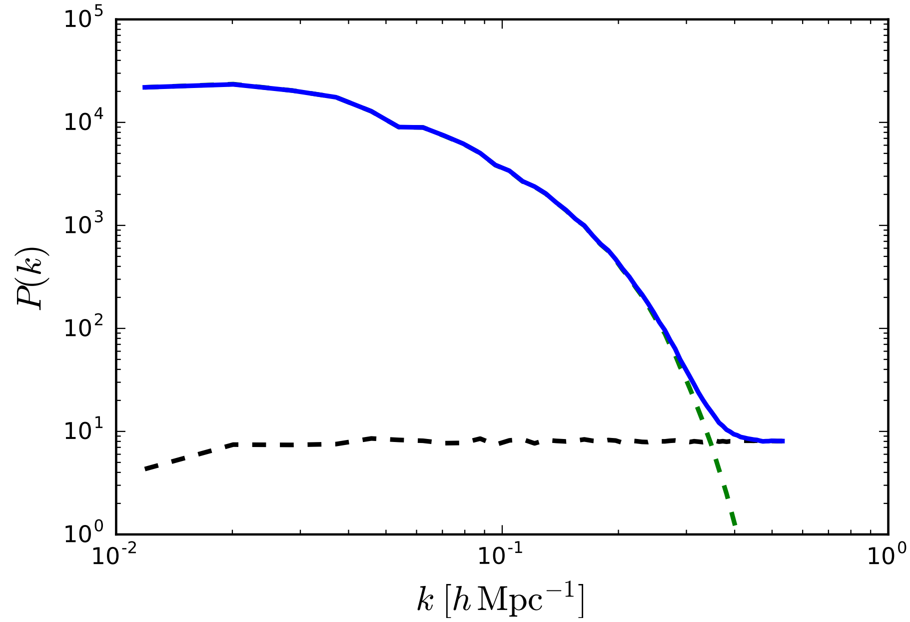


Figure 3.2: The non-linear power spectrum of the truth simulation. The green dashed curve shows the simulation without noise, the black dashed curve is the noise power spectrum, and the blue solid curve is the total power spectrum.

transfer function is defined as the square root of the ratio of the power spectra, while the cross correlation is the ratio of the cross-power to the square root of the product of the individual power spectra. As expected, both the transfer function and the cross-correlation are very close to unity for large scale modes, and gradually drop down to 0 for $k > 0.2\,h\,\mathrm{Mpc}^{-1}$. This is expected, since the data becomes noise dominated beyond $k \sim 0.3\,h\,\mathrm{Mpc}^{-1}$. The effect of noise is more pronounced for initial density field. This is because high $k$ nonlinear density field is still significantly determined by low $k$ linear density, as a consequence of nonlinear mode coupling and power transfer.

Let us now discuss the power spectrum reconstruction. We use 64 equal width bins in $k$. For the reconstruction we use a fiducial power spectrum which is a no-wiggle version of the power spectrum for the truth simulation. This means that the BAO wiggles have been removed. One of the goals of the initial power spectrum reconstruction is to reconstruct the BAO wiggles without putting them into the fiducial model, and to show that the reconstruction completely removes nonlinear smoothing it is best if the fiducial power spectrum has no wiggles at all.

We use equations 3.63 and 3.58 to compute the Fisher matrix and noise bias. Specifically, we first create a fiducial power spectrum mock simulation as in equation 3.57, and perform exactly the same optimization steps as for the "truth" simulation. We next inject small

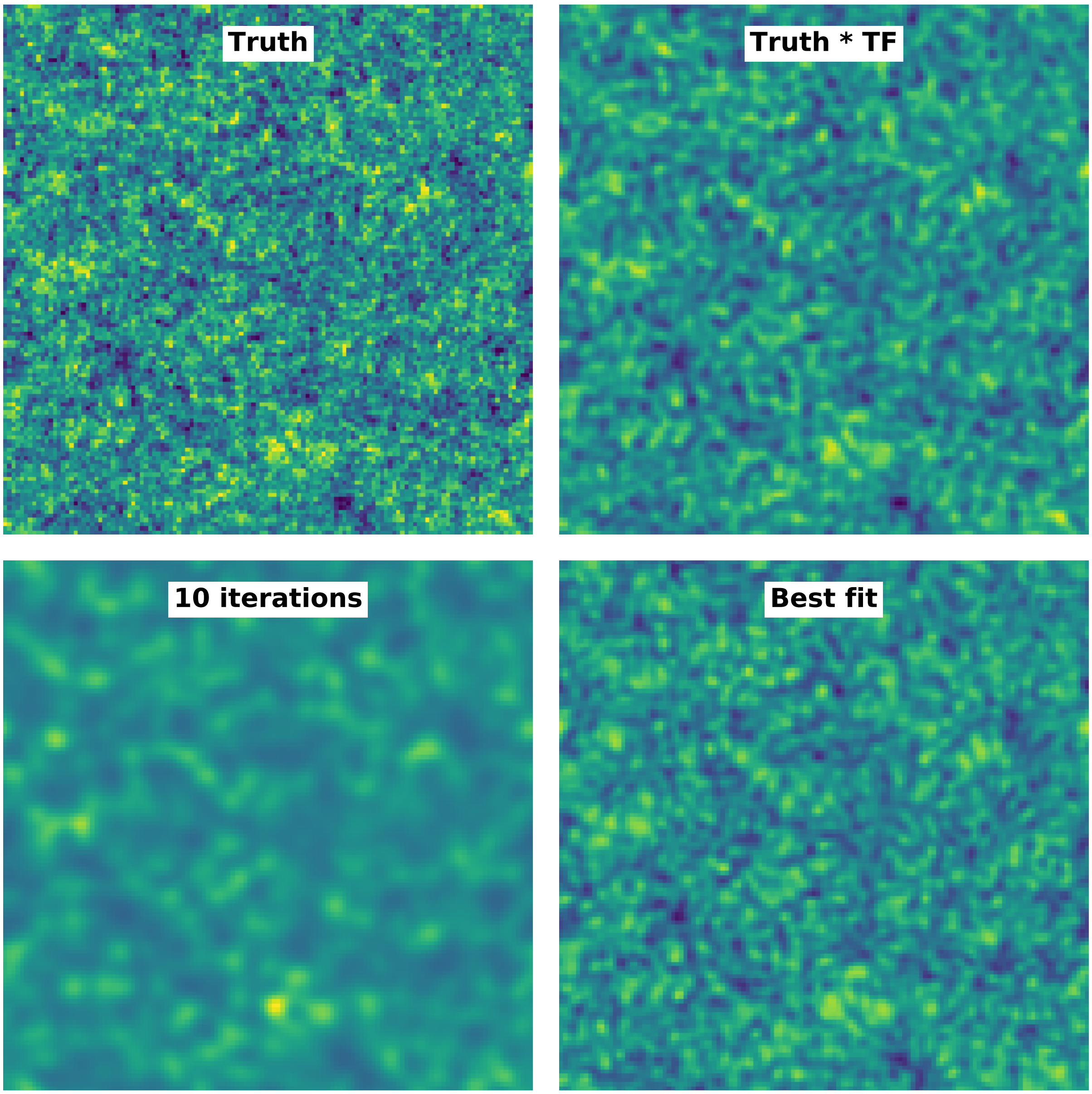


Figure 3.3: The reconstructed initial linear density field (Best fit, lower right) compared to the truth simulation (Truth, upper left). Noise and smoothing prevent us having a perfect reconstruction, and small scale details are lost. We apply the transfer function on the truth simulation to demonstrate this (Truth*TF, upper right). Also shown are the reconstructed field at iteration 10 (10 iterations, lower left). The projection use a slab with a thickness of 24 Mpc/h.

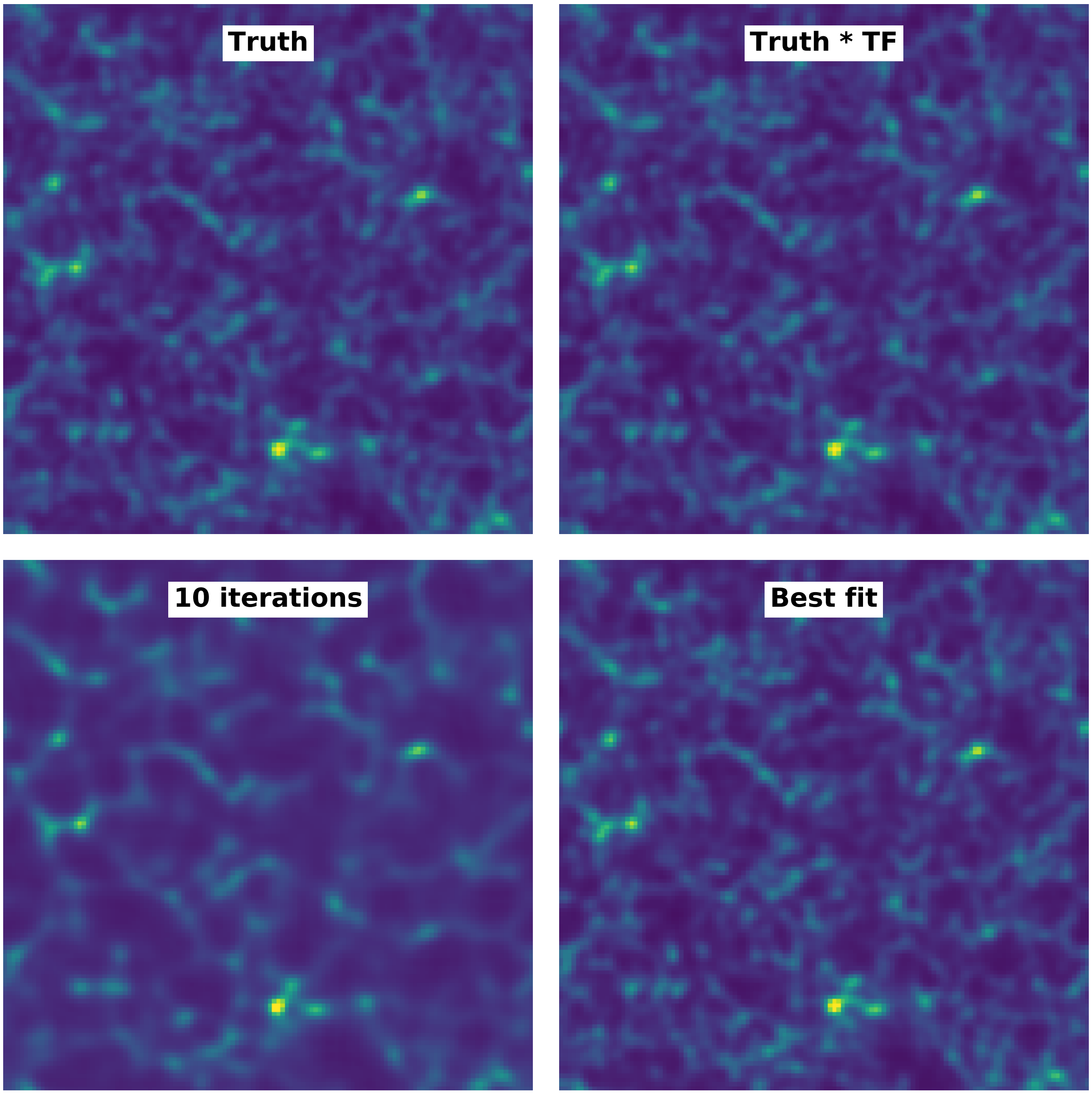


Figure 3.4: Same as Fig. 3.3 but for nonlinear density field. Note that reconstructed and original fields appear much closer to each other. The projection use a slab with a thickness of 24 Mpc/h.

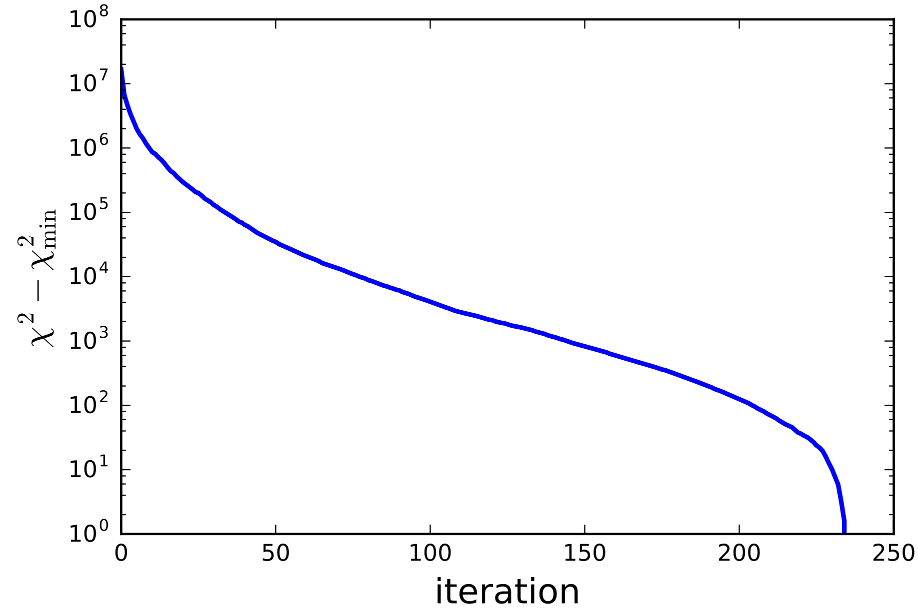


Figure 3.5: $\chi^2 - \chi^2_{\rm min}$ as a function of iterations.

amount of power into a single bandpower and measure the response as given by all the other bandpowers. Here we start the optimization at the values given by the fiducial model simulation, and as a consequence we only need about 50 calls to converge. To make the procedure even faster we could do this for every N-th bandpower (e.g. N=5), since the mean transfer function squared of equation 3.64 is a smooth function of bandpower and can be interpolated across them. Once we have computed the Fisher matrix we also compute the noise bias using equation 3.58.

We plot the normalized Fisher matrix (equation 3.64) in figure 3.7. As we can see, the window functions are peaked at the diagonal, and no significant mixing of modes occurs. This is expected when noise is low, since in that case we are reconstructing true modes. Note that we use periodic box, so there is no window function associated with the survey geometry itself: the nonlinear modes are orthogonal, so any window function deviation from a delta function would be due to the nonlinear mode coupling to noise, creating off-diagonal elements. However, we observe no such mode coupling and no off-diagonal window function even for high noise. This result is intriguing and suggests that nonlinear evolution coupled to noise does not create much off-diagonal coupling. Our test case had a very low level of noise, and it remains to be seen if the same result is confirmed with higher levels of noise. Survey mask and other effects will create a window, which will be localized to the width of the bin of order $2\pi/R$, where $R$ is the size of the survey. It may thus be possible to separate geometry effects from the nonlinear noise coupling effects, and develop rapid methods for

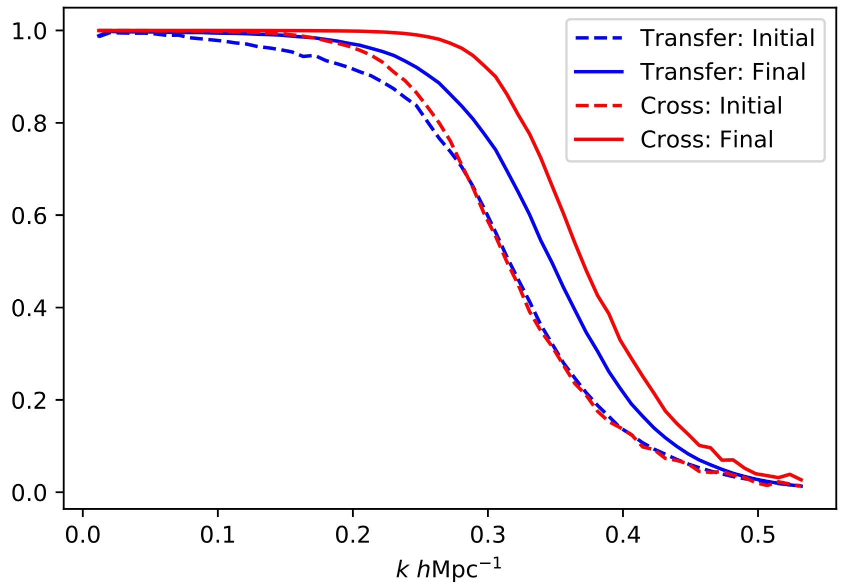


Figure 3.6: The transfer function and the cross correlation coefficient between the reconstructed and the true density fields, as a function of $k$. The blue curves show the initial field, and the red curves show the final field. The dashed curves show the transfer function, and the solid curves show the cross-correlation coefficient. We see that the final density is reconstructed better than the initial density at the same $k$, a consequence of nonlinear power transfer from low $k$ to high $k$.

the estimation of the covariance matrix. Clearly this needs more detailed investigation, as it could greatly simplify the calculation of the window function and covariance matrix.

Finally, we plot the original and the reconstructed power spectra in Fig. 3.8, all relative to no wiggle fiducial power spectrum. We show the original truth power spectrum (red solid curve), the power spectrum of the reconstructed MAP initial density field (grey dashed curve), and our reconstructed power spectrum with error bars (black points). We can see that our reconstructed "best fit" MAP density field has a power spectrum that matches very well the "truth" power spectrum on large scales, but starts to decrease at small scales. As we discussed above, this is due to noise: in the presence of noise the optimal reconstruction sends the modes to zero. However, our reconstructed power spectrum (black solid curve) is able to determine the amount of lost power, and make the estimator unbiased. Indeed, it matches very well the model power spectrum on small scales, which is an artifact of the fact that we used the no wiggle version of the same power spectrum for bias term as for the truth. In reality we would not have this luxury so the results will be biased at high $k$, however not more than the computed errors, which properly account for this effect: we see that the errors get very large for $k > 0.35$h/Mpc, since the transfer function of initial modes

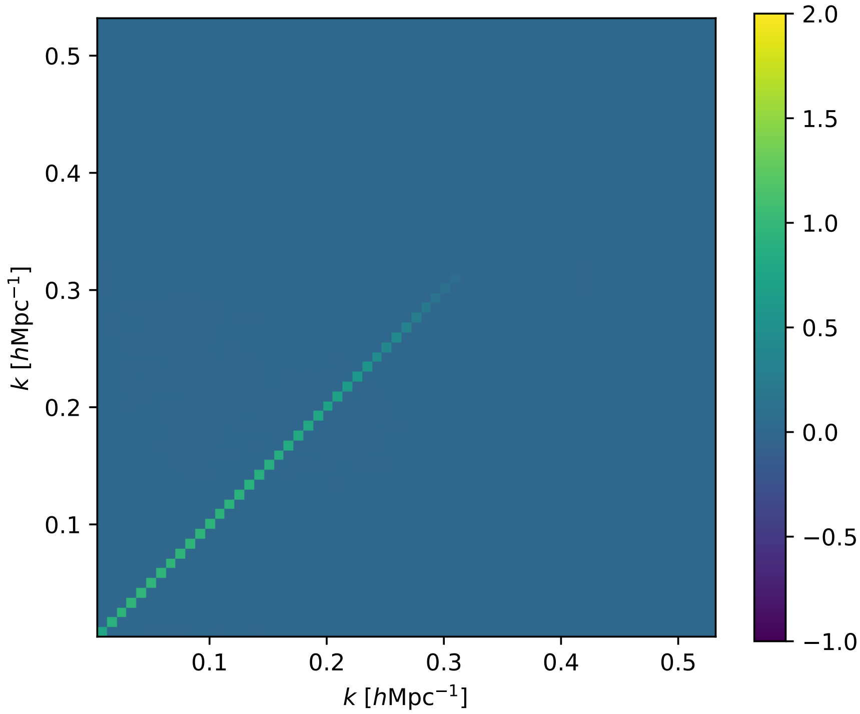


Figure 3.7: The normalized Fisher matrix, defined as in equation 3.64, computed from responses of the estimator to injection of power into a single bandpower bin. We observe no off-diagonal responses. At high k the responses vanish due to the noise.

becomes very close to 0 and the MAP reconstruction is very close to zero.

As we can see clearly from Fig. 3.8, our reconstruction does reproduce the linear BAO wiggles, which match very well the wiggles in the truth power spectrum. For the nonlinear power spectrum the BAO wiggles are damped, as shown in the plot with the blue dashed curve. We can see from the plot that we are reconstructing the BAO wiggles of linear power spectrum, and not of the nonlinear power spectrum, achieving very good reconstruction. The last two wiggle with $k > 0.35$h/Mpc are not reconstructed, because there the noise and smoothing already completely destroy the signal, and since we did not have BAO wiggles in our fiducial model they are not reproduced. The size of the errors reflects this, and the last BAO wiggle that is detectable is around $k > 0.3$h/Mpc.

As discussed earlier, it is not guaranteed that our procedure gives a reliable Fisher matrix that can be used as the covariance matrix, although this is guaranteed in the linear regime and in the low noise regime. We have computed goodness of fit value of the estimators relative to the truth $\Delta\mathbf{\Theta}^{\mathrm{truth}}$ (which is not 0 because our assumed fiducial model is not the

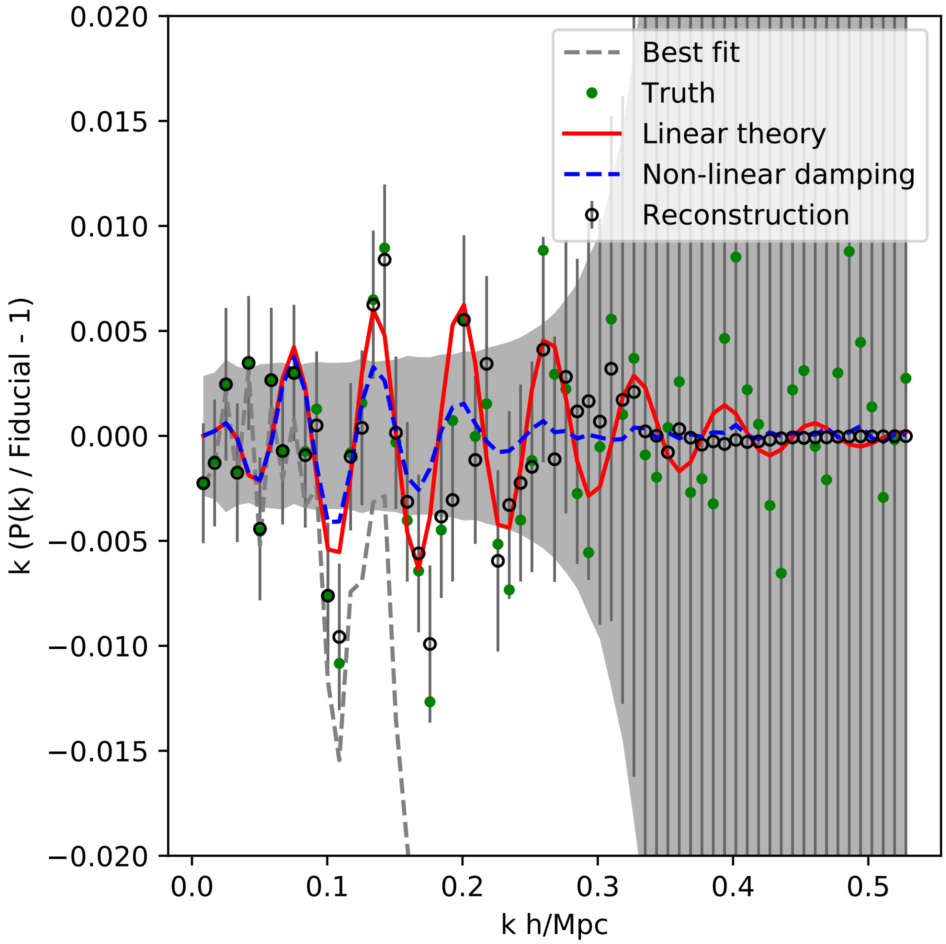


Figure 3.8: The original and reconstructed linear power spectra, divided by no wiggle fiducial model. The red solid curve shows the original linear power spectrum which was used to simulate the truth. The gray dashed curve is the power spectrum at the best fit MAP mode reconstruction, which shows loss of power at high $k$ due to noise, and the black circles with error bars is our final power spectrum reconstruction corrected by the noise bias. The green points shows the actual realization of the linear power spectrum (simulation truth). The power spectrum is shown as the relative difference of all of the power spectra to the no wiggle power spectrum, enhanced by a factor of $k$ for better presentation. Also shown is the ratio of the nonlinear model power spectrum to the no wiggle one (blue dashed curve). While nonlinear wiggles are completely damped for $k > 0.2$h/Mpc, linear ones are still visible, and our reconstruction agrees with linear realization (simulation truth). The gray band shows size of the error bars shifted to the center. The errors include sampling variance. The reconstruction appears perfect at high $k$ because we are using the same model for bias as for the truth, so for high $k$ where reconstructed MAP is zero this returns the fiducial model. In general the fiducial model would not be exactly the same as the truth, which is reflected by the size of the errors, becoming large at high $k$.

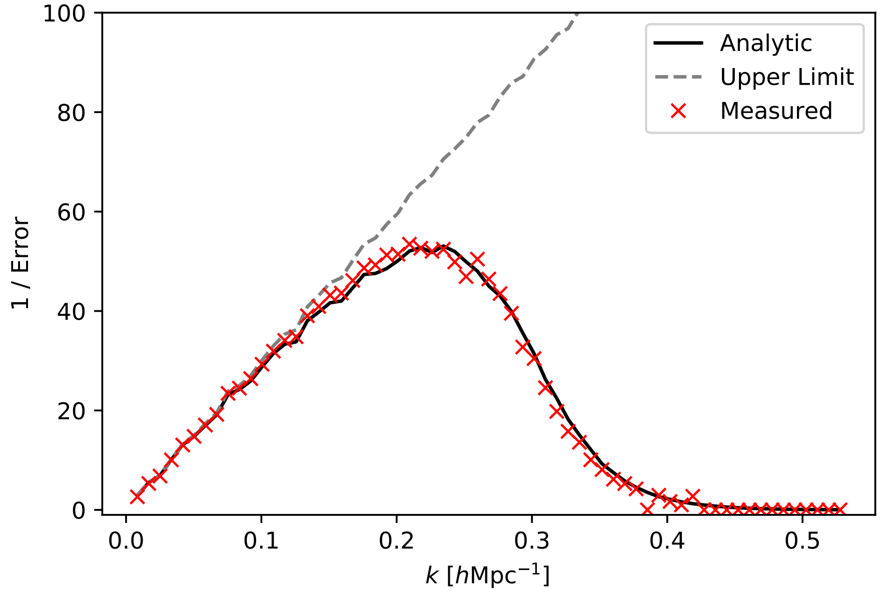


Figure 3.9: The square root of the diagonal terms of the Fisher matrix for normalized parameters, which is the signal to noise for the bandpower. We compare our main method (red crosses) to analytic prediction from equation 3.48 (solid black line), finding a good agreement between the two. We also plot the maximal inverse error in the case of perfect reconstruction (dashed line).

truth model)

$$\left[\boldsymbol{W}\Delta\boldsymbol{\Theta}^{\text{truth}} - \Delta\hat{\boldsymbol{\Theta}}\text{'}\right]^{\dagger}\boldsymbol{C}^{-1}\left[\boldsymbol{W}\Delta\boldsymbol{\Theta}^{\text{truth}} - \Delta\hat{\boldsymbol{\Theta}}\text{'}\right] \sim 38, \tag{3.65}$$

using 40 bandpowers up to $k_{\max} = 0.4\text{h/Mpc}$. The reduced $\chi^2$ of 0.94 suggests the covariance matrix is reliable.

We have also compared the diagonal terms of the Fisher matrix to the simple approximation of equation 3.48, finding good agreement between the two methods (figure 3.9). This, and the nearly diagonal window (figure 3.7) suggests that one may be able to estimate a reliable covariance matrix even without doing any simulations (more precisely, with a single simulation to compute $\boldsymbol{b}_l$, making sure the estimator is unbiased). This clearly deserves a more detailed investigation, in particular in the presence of a survey mask and other complications, but is beyond the goal of this chapter.

## Convergence and computational cost

Let us look at the computational costs of our method. As mentioned above the cost of a single optimization procedure is about 230 forward model calls, each being a few FFTs (to compute 2-LPT) of the $128^3$ mesh. On the data this is done once. For the simulations we have to do the same for the fiducial simulation realizations, and then for each of the Fisher matrix rows, where we inject a small amount of power into a single bandpower on top of the fiducial power. The latter would thus appear to dominate the computational cost, but because the Fisher matrix can be interpolated across the bandpowers (we only evaluate every fifth row), and because we can start the optimization from the fiducial model solution, which reduces significantly the number of iterations, in practice this entire operation is comparable in cost to the optimization of fiducial model simulation, or of the data. To achieve required precision one also needs to repeat the procedure until required precision is achieved. In our tests we have not found the need to average over many realizations.

Another possible acceleration is to extract the results without reaching the global minimum. As figure 3.3 shows the solutions between 100 iterations and final convergence are almost indistinguishable, since the optimizer is changing a large number of modes by a small amount that cannot change the solution significantly. This result is confirmed by the actual value of $E_l$ as a function of iteration number, which hardly changes at higher iterations even when the loss function is still changing significantly. In general, if we have $M$ modes $\boldsymbol{s}$ and the optimizer has determined each to within $\epsilon\sigma$, where $\sigma$ is the error for individual mode, then for $\epsilon \ll 1$ there is no loss relative to perfect optimization solution, in the sense that the total error is given by $(1+\epsilon^2)^{1/2}\sigma$. As long as the error is stochastic the same will be true for the bandpower error, where we average several modes. But this additional noise adds $\epsilon^2 M$ to the overall loss function, and for large $M$ this can be a large number even if $\epsilon$ is small. For example $\epsilon = 0.1$ only increases the overall error by 0.5%, suggesting that even the optimization solutions which are away from the global minimum by a large number may still be good enough. Another way to understand this argument is through the sampling perspective: when sampling each mode is on average $1\sigma$ away from MAP, and most of the sampling is done in a narrow range of loss function being $M \pm \sqrt{M}$ above the global minimum. The sampler never descends down to the minimum, and its exact position is irrelevant for the posterior distribution of the modes, which is ultimately what determines the solution. Figure 3.5 suggests that we could stop the optimization after 50-100 steps and still satisfy the condition that $\epsilon^2 \ll 1$. In practice we observe strong correlations in the modes of a single bandpower along the optimization path, so the argument above is too naive and one must develop a more robust criterion when to stop. We also observe this argument to fail when computing Fisher matrix elements, where small differences between solutions are relatively more important.

A related issue is the question of convergence to the global minimum. The loss function is only convex for the linear problem. For the nonlinear problem it becomes non-convex, meaning that there can be multiple local minima. In the mildly nonlinear regime this will not happen, but in deeply nonlinear regime this is very likely to happen. Changing the starting point of optimization, or using a stochastic descent which tries different paths down the hill are typical approaches to this problem, but a general solution is difficult. However, as argued above a local minimum is only problematic if it is very far from the global minimum. A situation where there are many high quality local minima at the bottom of the loss function is not of much concern, since all those solutions are in some sense equivalent, specially if they all give the same transfer function.

Another numerical issue are saddle points. These are numerically problematic, since they are attractors for Newton's method optimizers: they may give an impression that convergence has been reached, only for the optimizer to suddenly start reducing its loss function again once it has evolved past the saddle point. We have observed this in the configurations with high noise. Adding noise or momentum to the gradient, taking absolute value of the Hessian eigenvalues or some other way to change the Hessian make these issues less problematic [63]. More work is needed to develop optimal optimization methods for our problem.

In any case, the large number of forward model evaluations, in the hundreds to thousands, and the need to compute the gradients puts a high demand on its computational cost, and approximate methods like 2-LPT or fast simulations like FastPM [87] are crucial for the success of this program. We note that FastPM with 10 time steps is 7 times slower than 2-LPT, while its transfer function with full N- body simulations at $k = 0.3$h/Mpc is 1.02, relative to 1.2 for 2-LPT, so its computational cost is not prohibitive, while dramatically improving the accuracy. However, one also needs to demonstrate that its gradients can be implemented accurately and can be evaluated. In practice the choice of forward model will depend on the level of noise and resolution in the data, with low resolution/high noise data requiring only 2-LPT and high resolution/low noise data requiring N-body simulations with low number of time steps. It remains to be seen whether this will change with a more realistic survey geometry, where window functions will be less compact. It may be possible to reduce this number further if the convergence of the optimizer is accelerated. We note that in our tests a simple conjugate gradient optimizer was a factor of 2-3 times slower than L-BFGS, which is the reason we only present the latter in these tests. We plan to investigate some of these acceleration issues further in the future.

## 3.6 Conclusions

The purpose of this chapter is to develop a formalism to optimally extract cosmological information in the nonlinear regime, and to develop numerical methods that are computationally feasible and preserve the near optimality of the analysis, and allow an implementation of this formalism both in the linear and nonlinear regime. Traditional CMB/LSS analyses start with the power spectrum or correlation function of the observed field (such as CMB temperature and polarization, weak lensing shear or galaxy positions), and often end there. Even in this case the two-point function analysis is typically not optimal, because the data are not inverse covariance matrix weighted.

In the nonlinear regime the LSS evolution creates non-Gaussian signatures. This is a generic term that contains a lot of different manifestations: they range from the higher order correlations such as bispectrum, to existence of special objects like the density peaks (e.g. clusters), to non-trivial topologies such as sheets, filaments and voids. The problem with these descriptions is that they are not exhaustive, i.e. it is not possible to prove that any specific combination extracts all the information. Indeed, often it is not even clear that these additional statistics increase the amount of information relative to the power spectrum at all. When combining different statistics one must also obtain their joint covariance matrix, which is a challenge in itself, since it typically requires a large number of mock data realizations (parametric bootstraps).

In this chapter we present an (approximately) Bayesian analysis that attempts to nearly optimally extract the information contained in the data given a nonlinear structure formation models of LSS. By writing down an exact probabilistic model the optimality of the analysis is guaranteed as long as all the steps are solved exactly. In our approach we do not attempt to produce an exact solution, which is prohibitively expensive, but instead we develop a series of controlled approximations that we argue approximately preserve the optimality of the solution. Should these approximations turn out to be insufficient one can attempt to generalize the approach used here.

Specifically, our approach is to expand the likelihood around the maximum a posterior (MAP) solution for the initial modes, and integrate out the modes around this solution. In our specific implementation we assume existence of a single global MAP solution. This assumption is guaranteed in the linear model, and we argue that it is likely to be the valid at least in the mildly nonlinear regime, which is our primary focus. We do not analytically compute the integration volumes, which correspond to the product of all variances of the modes, but instead rely on simulations to compute their derivative with respect to the parameters. We do this using simulations, and the realization dependence of the variance is lost. We have argued that at the linear level this is a valid and lossless approach. We also expect any corrections to be small in the low noise limit, and in general we expect this to be a very good approximation. In this context it should be stated that in the presence of multiple local minima the solutions should not be expanded around the global MAP, but around the one that maximizes the loss function times the log of posterior volume (equation 3.27), which differs from what MAP maximizes by $\det \tilde{\boldsymbol{D}}^{-1/2}$. While we have argued that it is likely that one does not need to average over multiple local maxima, this does not imply that finding the one that maximizes MAP (or volume corrected MAP) is easy. A proliferation of lower quality (higher loss function) saddle points can still make convergence slow, and there is no guarantee that the optimization will find a global minimum, as opposed to a local minimum far from the best solution. We have argued that if these local maxima are close to the global MAP and all have the same transfer function it does not affect the unbiasedness of the solution.

Similarly, the optimality of the method is only guaranteed if the forward model is exact, even if it is unknown (exact in the sense that the nuisance parameters always cover the truth). Formally one adds more and more forward model parameters, and marginalizes over them. While it is easy to achieve this on large scales, it becomes increasingly more difficult to do so on small scales where many uncertain physical processes can affect the data, and one needs to include all possible variations consistent with the allowed physical processes, including physical priors on these parameters.

We argue that the bandpowers of optimally reconstructed initial power spectrum are lossless summary statistics, at least for the simplified case where the forward model connecting initial modes to the data is unique. We provide a derivation of the bandpower estimators, the corresponding Fisher matrix and noise bias, which fully quantify the information content of LSS data. Note that our approach does not involve any sampling of the modes, and we believe that current implementations of sampling procedure to be too slow to be of practical use in these applications.

This method can be generalized to the analysis allowing also for parameters that control the mapping from the initial modes to the final data, both cosmology parameters such as matter density or massive neutrinos, and astrophysical modeling parameters such as galaxy bias, shear bias etc. We expect that these parameters in general are not degenerate with the power spectrum amplitude parameters, even if they may be at the linear level: in the nonlinear regime this degeneracy can be broken, since nonlinear gravitational effects cannot be exactly mimicked by the nuisance parameters. This allows for possibility of marginalizing over the nuisance parameters internally, without the need for external constraints. We show that one can treat primordial non-Gaussianity as a forward model parameter and present an optimal analysis method to extract it. Our method involves only a single sum over the data, multiplied by a response function numerically derived at each data point. The details can be found in the original work, [211].

For linear models, such as the CMB or the LSS on large scales, where the relation between the data and the modes is a simple Fourier transform, the MAP is guaranteed to be at the global maximum with a Gaussian posterior and this guarantees optimality [208]. Even in this case we expect the numerical methods developed here, optimization and fast Fisher and noise matrix evaluations, to be useful in applying these estimators to the real data. We will present our results of applying these methods to weak lensing and CMB applications elsewhere.

This chapter focuses on the theoretical formalism, deriving the summary statistics in the context of nonlinear structure formation models. We implement the procedure on a simplified, yet nontrivial test case, where we use 2-LPT or N-body simulations as a forward model to generate a nonlinear density field, while we use simplified 2-LPT times the transfer function for gradient evaluations during the optimization. We show that the resulting solution recovers the linear baryonic acoustic oscillations, achieving a near optimal BAO reconstruction. Since our gradients are not exact we do not claim that the reconstruction is optimal, although this is very likely to be the case for BAO (since 2-LPT is expected to fully model nonlinear BAO evolution). Our reconstructed power spectrum is unbiased and comes with the bandpower window matrix and the (disconnected) covariance matrix that describes well the solution.

Some of the more realistic effects that remain to be included are incomplete data coverage, nuisance parameters such as the biasing of galaxies, and baryonic effects on the matter distribution. Equally importantly, while for the weak lensing the noise model is simple, for galaxy data noise probability distribution needs to be understood better, and sub Poisson noise should be achievable [209]. When applying to weak lensing one additional complication is the elongated radial projection window, which does not allow for a full 3-d reconstruction even when tomographic reconstruction is used, and will lead to significant degeneracies in the radial direction.

Ultimately we expect the methods developed here to superseed the traditional data analysis methods in cosmology. When this will be achieved depends mostly on the remaining technical and computational challenges that need to be addressed. Among these are fast evaluations of derivatives of N-body simulations, where we expect FastPM code [87], which achieves percent level agreement of halo clustering against high resolution simulations with as few as five time steps, to be particularly suitable for this purpose. Another challenge is the ability to perform gradients of galaxy density field, as well as gradients of forward model parameters evaluated on MAP. We plan to investigate some of these issues in the future. Given the higher computational cost of this approach, and various numerical challenges in the nonlinear regime, there may still be a long road ahead before we achieve this goal, but the payoff will be an increased precision of cosmological constraints and (near) optimality of the analysis.

# Chapter 4

# Cosmological Reconstruction From Galaxy Light: Neural Network Based Light-Matter Connection

The contents of this chapter were originally published in

Cosmological Reconstruction From Galaxy Light: Neural Network Based Light-Matter Connection
*Modi C., Feng Y., Seljak U. (arXiv:1805.02247)* JCAP10(2018)028

In this chapter, we build upon the framework of reconstructing the initial conditions of the Universe with a forward modeling approach as developed in the previous chapter. We apply this method to the large scale imaging surveys where the observed data is galaxies (we use dark matter halos as proxies), which are discrete, biased tracers of the underlying matter field. Since the standard way to identify halos and galaxies is non-differentiable, we propose a framework to model the halo position and mass field starting from the non-linear matter field using Neural Networks (NN), which are differentiable, yet can produce very pointlike maps. We evaluate the performance of our model on different metrics, quantify the modeling error and develop a likelihood model for the data. We use the framework from the previous chapter to then reconstruct the initial density field and show that it improves over the standard reconstruction practices. Additionally, to speed up and improve the convergence, we develop an annealing procedure for several parameters in the loss function.

## 4.1 Introduction

Studies of the large scale structure (LSS) of the Universe have played a very important role in establishing the standard model of cosmology. As a community, we are also investing a large amount of resources into the current and upcoming large scale imaging surveys such as the Dark Energy Survey (DES[1]), Dark Energy Spectroscopic Survey (DESI[2]), Large Synoptic Survey Telescope (LSST[3]), Euclid[4] and WFIRST[5]. Due to the sheer number of modes that can be observed in the three-dimensional map of the Universe, there is a vast amount of statistical information about the initial conditions of the Universe and the cosmological parameters available to be extracted from these surveys. Furthermore, most of this information is present on smaller scales, since the number of modes scales as $k_{max}^3$, where $k_{max}$ is the smallest wavevector.

However, the statistics of small scales in the late time Universe are complicated to model due to the highly nonlinear gravitational evolution. A large portion of the cosmological information is at best encoded into the higher order statistics, or at worst lost due to noise, and hence these scales are generally excluded from the cosmological analysis. In an effort to recover more of this information, the issue of 'reconstruction' of initial conditions has received a lot of attention over the last decade. The hope is to partly undo non-linear evolution of the Universe and recover the initial conditions, which are thought to be Gaussian and hence can then be described using a power spectrum statistics alone which contains all the information (apart from parameters which control the gravitational evolution).

As a result, different flavors of reconstruction have been proposed over the years. One of the most successful methods, now referred to as standard reconstruction, was proposed in [73] wherein one estimates the linear density field by reversing the Zeldovich displacement in the clustered (galaxy) and random catalog, as estimated from filtered non-linear density. Recently, similar methods with improved estimates of non-linear displacement have been developed [263, 205]. A conceptually different approach to reconstruction involves sampling initial density modes with Hamiltonian Monte Carlo (HMC), which are then evolved using a forward model of choice (N-body, PM, 2LPT) and compared against the true non-linear density field [119, 128, 247].

As presented in the previous chapter, an alternate approach is to instead reconstruct the initial density field by optimizing the posterior of initial density modes, followed by analytic marginalization over these modes to reconstruct the summary statistics that optimally contain the desired information [211]. A common feature of the latter two (sampling and optimization) approaches is that they require knowledge of the gradient of the forward data model with respect to the initial modes to perform efficiently. The data probed by these LSS imaging surveys is the positions of the galaxies as well as an estimate of their stellar mass and bolometric luminosity. This means that they do not map the dark matter field directly but instead observe a biased tracer (galaxies), along with the derived properties (stellar mass or luminosity) associated with the dark matter mass that may be prone to statistical and systematic noise. To be able to reconstruct initial density field from these observables, one needs to be able to forward model to these quantities directly.

[1] https://www.darkenergysurvey.org/
[2] http://desi.lbl.gov/
[3] https://www.lsst.org
[4] http://sci.esa.int/euclid
[5] https://wfirst.gsfc.nasa.gov

In traditional cosmological analysis, this is achieved in N-Body and Particle Mesh (PM) simulations by first identifying dark matter groups (halos) using algorithms such as Friends of friends (FOF) or Spherical Overdensity halo finders. These are then populated with galaxies using techniques such as Halo Occupation Distribution (HOD) [24] and assigned luminosity and stellar mass based on some relationship with the parent halo's mass. For the purpose of reconstruction, this approach has proven to be a complication, especially for the methods that rely on being able to take the gradient of the forward model: the derivatives of FOF and other halo finding or galaxy painting algorithms such as HOD with respect to the initial modes can not be easily evaluated. Moreover, the halo field is discrete and for discrete fields, it is difficult to write a suitable loss function.

Several ways have been proposed to overcome this problem. The simplest way to relate matter field to galaxy field is to use a bias model, as is done in standard reconstruction [73]. Linear bias model is also used in [119] to relate matter to the halo field, but they treat galaxies as a Poisson sampling of this biased field and develop the likelihood function to take this sampling into account. On an object by object basis this approach is unlikely to be very accurate since it does not reduce stochasticity over the Poisson shot noise. Another approach involves backward modeling from the galaxy catalogs to 'reconstruct' a nonlinear matter field first, and then using this field to do a reconstruction of initial conditions. For example, [245] has proposed a method to assign matter profiles to halos which have been constructed from simulations and [246] has used this matter field to perform initial condition reconstruction. Alternatively, [259] performs a Delaunay tessellation [47] of dark matter halos to reconstruct the continuous nonlinear matter field. Since these are backward modeling approaches it is difficult to insert modeling uncertainties into the process, and it is also difficult to develop a reliable noise model: typically noise is only uncorrelated in the data space (where it is simply detector noise or equivalent), and any backward modeling correlates the latent space of variables (such as the nonlinear dark matter density) in a way that would need to be modeled, but becomes very expensive to do so. Moreover, nonlinear dark matter is not our ultimate goal: what we want is to map higher order information (e.g. bispectrum and higher order statistics, various peak, filament and void statistics etc.) into two point function statistic, since this leads to an optimal extraction of information from the data [211].

In this work, we develop a forward model approach to go from the linear to the nonlinear matter field and then to the halos, galaxies and their corresponding observable properties in a *differentiable* fashion, such that its gradient can be evaluated and used for reconstruction. To make it differentiable we have to give up the concept of a pointlike galaxy or halo. However, forward models are preferable to backward models since the loss function can be written in the data space, where the noise is diagonal. This also makes it easier to incorporate some of the most prominent uncertainties and systematics in LSS analysis such as survey geometry and selection effects, incompleteness due to fiber collisions etc. Finally, the forward models can easily incorporate modeling uncertainties, such as relation between galaxy luminosity and halo mass, various satellite statistics etc. In the forward model, one parametrizes the effect of these nuisance variables on the data and then performs statistical analysis of these parameters together with the cosmological parameters.

The first part of our forward model consists of evolution from linear to nonlinear matter field using FastPM algorithm and reconstruction for this model has already been presented in earlier chapter ([211, 85]). As the next step towards reconstruction from observables, in this work we develop a forward model from the nonlinear matter field to the galaxy observable such as galaxy light or stellar mass. We will do so under the simplifying assumption that we have a mean relation between the halo mass and the galaxy luminosity (or stellar mass) calibrated using observations such as weak lensing [140]. This means we can work with the halo mass as a proxy for the galaxy luminosity, at least within a model with a known scatter between the two. To connect the halo masses to the underlying matter density, we propose using Artificial neural networks (ANN/NN), which are fully differentiable, yet are able to model even very discrete distributions of near pointlike structures. The schematic for this forward model step is shown in the right panel in Figure 4.1 and it was discussed in Chapter 2

Given our proposed forward model, we are able to develop a likelihood function to relate the initial modes and the observed data. This is then combined with the Gaussian prior of the initial modes to construct a loss function that we optimize over to generate a maximum a posteriori (MAP) estimate of the reconstructed initial density field. The schematic for this optimization cycle is presented in the left panel of Figure 4.1.

The motivation of any reconstruction exercise is to be able to extract cosmological information from a tractable statistic. A MAP estimate still leaves us with too many degrees of freedom to extract information in a meaningful way. One needs to be able to estimate the linear power spectrum from these modes because the initial modes are Gaussian and for Gaussian fields, the two point function is the natural summary statistic that captures all of the information. A framework to do so was developed in the previous chapter [211], where one uses simulations to estimate the bias and the mixing of bandpowers in the process of reconstruction and then obtain the correct band powers. However, for our data, there are other associated forward model and nuisance parameters, such as scatter in the halo mass-luminosity relation. One needs to handle these consistently to be able to marginalize over them and extract the correct underlying cosmological parameters. This is the ultimate goal of our reconstruction, but we will leave this band power reconstruction for future work. Instead, in this work we focus on the reconstruction of the initial field using our forward model and quantify information of reconstruction using various two point function statistics.

The structure of the chapter is as follows. In Section 4.2, we describe our model with respect to the architecture and training of the neural networks as well as the features from the non-linear matter field that are used. Then in Section 4.3, we describe our simulations and data on which we test our model and reconstruction. In Section 4.4 we evaluate the performance of our model in modeling the halo mass and position field using different metrics. Next, in Section 4.5, we use our model for reconstruction of initial density modes starting from halos as our data. We develop a loss function, discuss our strategy for optimization and evaluate the performance as well its dependence on the said loss function. To compare with other methods of reconstruction, we choose standard reconstruction and discuss linear information reconstructed in section 4.6. Finally, we conclude in Section 6.8 along with a

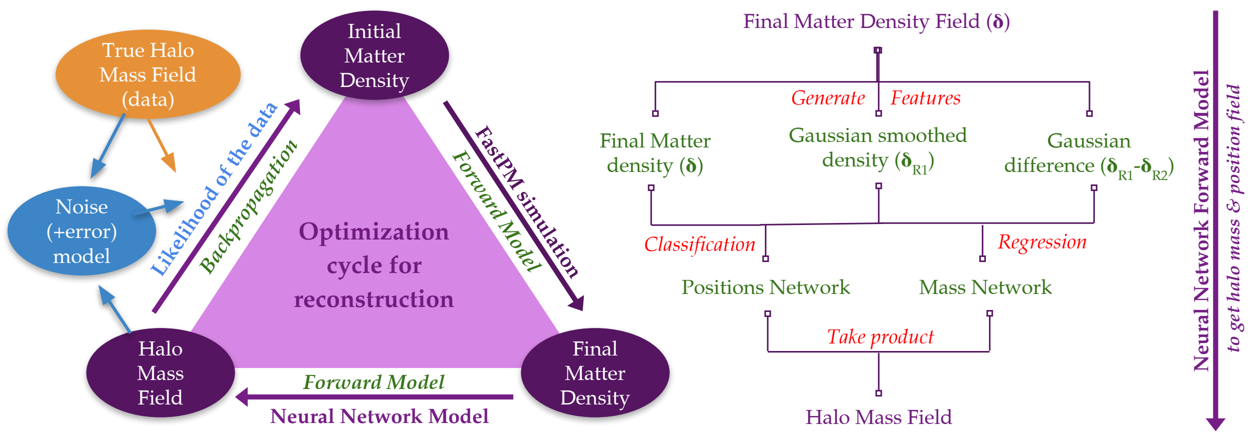


Figure 4.1: Left: Schematic showing the procedure for reconstruction. Every iteration starts from the initial field, which is evolved to the final matter field and this is then passed through the neural networks to predict the halo mass field. This field is used to estimate the likelihood of the data (Eq. 4.13) using a noise model (constructed beforehand from simulations using the trained network, see Section 4.4). Corresponding loss function (Eq. 4.14) is then minimized by estimating the gradients with respect to the initial modes and updating them accordingly. Right: Flowchart summarizing the operations involved in second step of the forward model i.e. to predict halo mass field from the final matter field. See Section 4.2 for details.

discussion of the future work.

## 4.2 Neural Network Model

We introduced the neural network model in Chapter 2. The schematic for our model is presented in the form of the flowchart in the right panel of Figure 4.1. Briefly, our model consists of two fully connected neural networks, one to predict the 'position' field for the observables and the other to predict the 'magnitude' of the corresponding observable. The true observables are the galaxies and their luminosity or stellar mass, but for this first work, we will instead use dark matter halos and halo mass as proxy and model them. Since both the halo mass and galaxy light are continuous properties directly related to the underlying matter content and proportional to each other with some scatter, we expect that it should be straightforward to adapt our model to predict these observables instead of dark matter halo mass. With this in mind, we will henceforth use the term 'mass' freely throughout

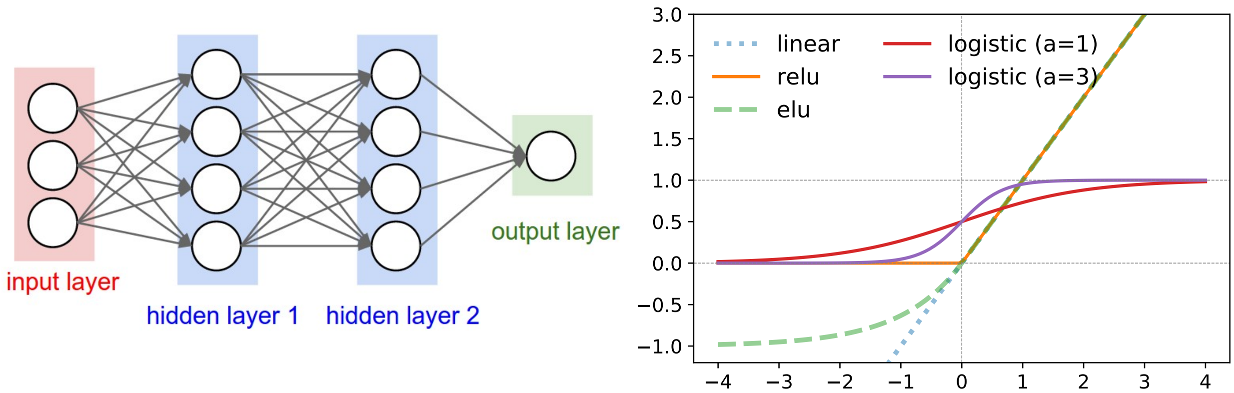


(a)

(b)

Figure 4.2: (a) A fully connected neural network with 2 hidden layers. Image taken from http://cs231n.github.io/neural-networks-1/. (b) Different activation functions used in the model

the text to imply dark matter halo mass (for this particular work) and magnitude of any associated observable (in a more general framework). On a similar note, imaging surveys observe galaxies in redshift space. However in this first work as a proof of principle, we work only with halos in real space.

Then, as discussed, the first network (**NNp**) identifies the CIC convolved halo positions on the grid. Thus, NNp performs classification wherein it identifies if the cell hosts a halo and assigns a value between 0 and 1 as a probability of there being a halo. The output of NNp is thus a discrete, position mask for the halo field (see Figure 4.3a). The second network (**NNm**) performs a regression on the underlying features to predict the value of CIC convolved mass at a given grid . This leads to a continuous mass field (see Figure 4.3b).

Given these two networks, our model for the discrete halo mass field is simply the product of these two fields.

$$\text{model} = \text{NNp} \times \text{NNm}$$

For the sake of brevity and to avoid repetition, henceforth we will say that neural network predict the halo position and the halo mass when we actually mean that it predicts the CIC convolved position field and CIC convolved mass field. We will also use NNp and NNm to refer to both, the networks as well as their outputs when it will not lead to any confusion.

For the input features to the neural network, we develop physically motivated features with transformations of underlying non-linear dark matter field. This is motivated by the fact that all halo formation models predict that more halos form in regions of higher overdensity. While in addition to density field, other environmental factors such as shear [221, 220], concentration, velocity fields etc. [103, 142] may also play a role in halo formation, the gains gradually diminish [139] with increasing features. The increasing complexity of the model will also lead to increased difficulty of training the neural networks. Given the simplicity of our neural network and the approximate nature of our simulations, we use only the following three combinations of density fields smoothed at different scales to capture environmental information and generate the feature vector - i) CIC convolved matter density field ($\delta_0$), ii) Density field smoothed with a finite Gaussian kernel on some scale ($\delta_{R1}$), iii) Difference of finite Gaussian smoothed fields on two different scales ($\delta_{R1} - \delta_{R2}$). The feature vector corresponding to a grid point in the position network (NNp), we use the values of the three fields from all the 27 points in a $(3 \times 3 \times 3)$ cube around that point, as discussed in Section 2.4. On the other hand, the feature vector for the mass network (NNm) consists of the values of aforementioned three fields at the grid point of interest and has dimension 3 since we did not find corresponding gains on using neighboring points for it.

## Architecture

As described above, fully connected neural networks consist of neurons arranged in layers with different activation functions to introduce non-linearities in the model. The choice for the number of layers, number of neurons in every layer and the activation functions are the hyperparameters that need to be tuned. We have explored different values of these hyperparameters and settled on the following architecture for the two networks:

- Position network (NNp): This network consists of 2 hidden layers with 50 and 30 neurons in the hidden layers, followed by an output layer of size 1. The activation functions used for the neurons in the hidden layers is ReLu (Eq. 4.1) and the output layer neuron is followed with a logistic function to squash the output value between 0 and 1. We also sharpen the logistic function by multiplying the exponent with ad-hoc factor of $a = 3$ (Eq. 4.3) to increase the discreteness of the output.

- Mass network (NNm): This network consists of 2 layers with 20 and 10 neurons in the hidden layers with ELU activation functions and a linear activation function followed by the final layer which is one neuron in size. We find that using ReLu activation instead of ELU (Eq. 4.2) also works well and but the latter is easier to train. Moreover, it turns out that a simple quadratic regression performed over the same underlying features (features described in the next subsection) also performs comparably to the neural network for some grid resolutions and halo number densities. However overall, the networks give more robust performance across different configurations.

$$\mathrm{ReLu}(x) = \begin{cases} x & \text{if } x > 0 \\ 0 & \text{if } x \leq 0 \end{cases} \tag{4.1}$$

$$\mathrm{ELU}(x) = \begin{cases} x & \text{if } x > 0 \\ e^x - 1 & \text{if } x \leq 0 \end{cases} \tag{4.2}$$

$$\mathrm{logistic}(x, a) = \frac{1}{1 + e^{-ax}} \tag{4.3}$$

In general, the performance of the models seems to be somewhat insensitive to the number of neurons beyond a given size. For example, we find that NNp gives similar performance with (30, 20) neurons in the hidden layers, but we choose (50, 30) architecture to be more conservative. The performance of networks, especially NNp, improves significantly on going from single hidden layer to 2 hidden layers, while a third hidden layer improves things marginally. Traditionally, practitioners of fully connected networks avoid going deeper than two or three layers since deeper networks are harder to train (this changes for deep CNN type networks where a third dimension of filter shapes is added). For our purpose, we settle with a 2 layer fully connected architecture in this work because we find satisfactory performance with this simplistic architecture. We also anticipate that more complex architectures will introduce difficulties taking gradients of forward model due to the possibility of vanishing gradients (due to activation functions saturating intermediate outputs). It is still likely that sophisticated architectures such as convolutional neural networks (CNNs) will improve the performance of our models and open doors to further applications such as generating mock catalogs of halos from density fields. We leave such forays for the future.

## Hyperparameters

Hyperparameters are parameters that are not learned during the training of the neural networks. Model parameters such as weights and bias are optimized during training, while other parameters like number of hidden layers, number of neutrons etc. are in practice set by hand and then configured for best performance by simply exploring the parameter space. For both networks, we fix the architecture after a couple of trials and hence do not change the associated hyperparameters such as number of hidden layers, number of neurons, activation function etc. Amongst parameters associated with training, we find that the performance is most impacted by varying batch size (the number of data points used in training at every iteration before updating weights with back-propagation) and regularization strength (penalty imposed on the norm of weights and biases to avoid over-fitting) and hence we have performed a grid search over these to get optimal values.

In addition, we also introduce other heuristic parameters to generate the training data set and to assist in training. The straightforward way to generate a training data set would be to simply use the full simulation. However, since the halos occupy a small fraction ($\sim 5\%$) of the grid points, using the whole simulation leads to severely imbalanced class ratio and it becomes much harder to train the networks. We also do not use the traditional ways of re-weighting and oversampling [106] to address this imbalance since most, *but not all*, high density regions host halos and using both these methods skews the ratio of halo to non-halo positions in these regimes. We find that training this way indeed leads to overly connected structures in the regions of high overdensity.

Thus, we introduce other parameters to leverage our knowledge of halo formation and construct better representative samples to balance the classes by reducing noise and redundancy in data. For training the position network to perform classification, instead of using the whole simulation, our training dataset consists of all the positions with halos to create one class (1) and then we sub-select certain number of empty, non-halo positions to fill the other class (0). Based on our domain knowledge, we divide these empty positions into 4 types and keep the number (fraction) of each type as a heuristic parameter. These different kinds of empty positions are - i) grid points that have a smaller halo below the abundance threshold of halos, ii) grid points above a heuristically chosen matter overdensity threshold, iii) grid points below the density threshold (we find that this is quite degenerate with the grid points having smaller halos in (i) and hence we end up not varying the number of these points as a parameter). In addition, we iv) keep a limiting value parameter to limit the CIC convolved value on the grid above which we accept the presence of halo. Therefore we do not choose all the 8 grid points to which CIC scheme interpolates over. Similarly for NNm, instead of using the full simulation, we use a parameter which selects only the points assigned a value above a threshold by the position network (NNp). This latter parameter is to guard against bad fits driven by points which are not going to be selected by the position network anyways. Thus upon including the batch size and regularization strength, we have 5 hyperparameters for NNp and 3 for NNm.

## Training

We use *Adam* [126] as our optimization algorithm during training. We gauge the performance of our networks by using L1 loss function for the position network (generally it is recommended to use cross-entropy loss function for classification but we find that L1 performs better in our case) and L2 loss function for the mass network, which is also the recommended loss function for regression. To prevent over-fitting, we use L2 (ridge norm) for regularization instead of L1 in both networks, primarily because we are not interested in the sparsity of the networks, given their small size. In addition, we use dropout of neurons during training, wherein some neurons are artifically excluded in each iteration with some probability $p_{drop}$. We find that $p_{drop} = 0.3$ works suitably well for us. We perform training on NERSC using *Keras*[6] with *Tensorflow*[7] backend [52, 1]. To generate the training data set, we combine data from three different simulations using the hyperparameters described in the last subsection and use a fourth simulation as validation set. The validation set is not used for training but we monitor the accuracy (loss) on this validation set over iterations and use it as the early stopping criterion, i.e. when the change in accuracy (loss) falls below a certain threshold value consecutively for a given number of epochs, we stop training further. Depending on the batch size, it took between 1-5 minutes to train a network on a single core, 2.3 GHz Intel Xeon Processor with 512 GB memory, on Cori supercomputer at NERSC. To tune hyperparameters, we perform a simple grid search over different parameters, and it takes 8-15 hours get a network trained for all the parameter combinations. We finally choose the networks that performed the best at the level of the two point functions (cross-correlation and transfer function, as described in Section 4.4) as our model for reconstruction. For the

[6] https://github.com/keras-team/keras
[7] https://github.com/tensorflow/tensorflow

purpose of this work, we trained a different network for every spatial resolution and number density of halos, but in principle one can train across different resolutions. We will explore this in the future.

## 4.3 Simulations

We use the halo catalog and density fields simulated using `FastPM`[8] code [83]. `FastPM` is a PM simulation to generate non-linear dark matter and halo fields in a fast manner, employing much fewer time steps and enforcing linear Zeldovich displacement on large scales to reproduce the results of full N-body simulation. Despite its approximate nature, in [83] it was shown that the code performs extremely well on various benchmarks such as the dark matter power spectrum, the halo mass function and the halo power spectrum.

The simulations have a flat $\Lambda$CDM cosmology model with the Hubble parameter $h = 0.6711$, matter density $\Omega_M = 0.3175$, baryon density $\Omega_b = 0.049$ and spectral index $n_s = 0.9624$. The linear power spectrum used was generated with `CAMB`. The initial conditions of particle displacement and velocity were computed at second order in Lagrangian Perturbation Theory at redshift $z = 9$. The underlying density fields which are used as features for the neural networks are generated using 5 step `FastPM` simulations since this is also the forward model that is used during the optimization. To generate the data, the halos are identified in a 4x higher resolution `FastPM` simulations with 40 time steps, starting from the matched initial conditions. Halos are identified using FOF halo finder in `NbodyKit`[9] [104] with the optimization presented in [84] using a linking length of 0.2. We use smaller number of timesteps for the features and optimization to reduce the cost of reconstruction which scales linearly with the number of timesteps. Unless otherwise specified, all the results are presented for periodic cubic box of size $L = 400$ Mpc/h with $N = 128^3$ mesh used to generate the underlying features for the neural network and $N = 512^3$ mesh used to identify the corresponding FOF halos for the data. The fiducial number density of halos is $\bar{n} = 10^{-3}(\,h\,\mathrm{Mpc}^{-1})^3$ unless otherwise specified, but we also show results for $\bar{n} = 5 \times 10^{-4}(\,h\,\mathrm{Mpc}^{-1})^3$. We have verified that results are similar in terms of the model performance at the truth (Section 4.4) and cross-correlations of the reconstructed initial conditions with the truth (Section 4.5) for other box sizes and resolutions $((L(\mathrm{M}pc/h), N) = (200, 64), (300, 128), (500, 128), (600, 128), (1000, 256)\ )$.

## 4.4 Model Performance

In this section, before using our NN model for reconstruction, we evaluate the performance of the model in modeling the halo position and mass fields of FOF halos for a new test simulation i.e. different from the realizations used in training and validating. In section 4.4, we present the visual output of the two networks and qualitatively compare this with

[8] https://github.com/rainwoodman/fastpm

[9] https://github.com/bccp/nbodykit

true halo fields as well as quantitatively discuss the performance in predicting the position of halos. In section 4.4, we estimate the error made in predicting the halo masses and this forms the basis of our loss function which will be optimized over in Section 4.5. Lastly, in section 4.4, we gauge our model at the level of two-point functions of interest.

## Visual Comparison

We compare the output of the neural networks, NNp and NNm, with the FOF halos in Figure 4.3. We show a local snapshot of single slice for all the four grids. Since the halos have been CIC interpolated to the nearest 8 grid cells, they are squares in the 2D projection. In the FOF slice in Figure 4.3a, the red points correspond to halos identified in the low-resolution simulation ($128^3$), from which the underlying features are generated, while the blue squares are smaller halos identified in a 4x higher resolution simulation ($512^3$) to reach the requisite abundance of $\bar{n} = 10^{-3}(\,h\,\mathrm{Mpc}^{-1})^3$ in 400 Mpc/h box. Thus Figure 4.3a shows that our neural network is able to identify the halos going much lower in mass ($\sim$ 8x in this configuration, see also Figure 4.5) than the FOF threshold of the simulation, set by the particle mass. This motivates the application of neural networks to generate halo catalogs for future surveys using coarse PM simulations.

The output of the mass network, NNm, is shown in Figure 4.3b. Since this network performs a simple regression, there are huge connected areas in regions of high density. To convert this to a discrete field corresponding to the halo mass field, this is multiplied with NNp. This is shown in Figure 4.6a, which has some more non-zero grid points than Figure 4.3a. This is because the position mask of NNp, is not a binary mask of 0s and 1s but rather a continuous output of logistic function (Eq. 4.3) and hence some high density (and correspondingly high mass) positions of NNm are only suppressed while not being quite set to zero. This continuity of logistic function is needed so we can take the gradients: in the limit of very high resolution the halo positions can be very precise, but if the field is discretized into Dirac delta functions with the use of a binary step function, the gradient will not be able to tell the field which way to move to reconstruct these delta functions. In the opposite limit of a very high smoothing (width of logistic function, set by the ad-hoc parameter '$a'$ in Eq. 4.3) one looses small scale information in the presence of the noise. The choice of width scale, $a = 3$ (Figure 4.2b), is thus a compromise between these different requirements. We note that for the choices of voxel scale and number density of halos made here most of the voxels are empty (Figure 4.3), which indicates that we have a high spatial resolution and we should be more concerned about singular gradients than loss of information due to smoothing.

To quantify how well we do in predicting positions of halos i.e. the accuracy of classification, one can look at the Receiver Operating Characteristic (ROC) of the network. This quantifies the trade-off between the true positives rate (TPR) and false positive rate (FPR) classified by the algorithm as one moves the threshold of probability for classification from 0 to 1. For the network NNp, this quantifies the halos that are detected correctly vs the the extra points identified as halos which are not present on the FOF grid. For the grids, these

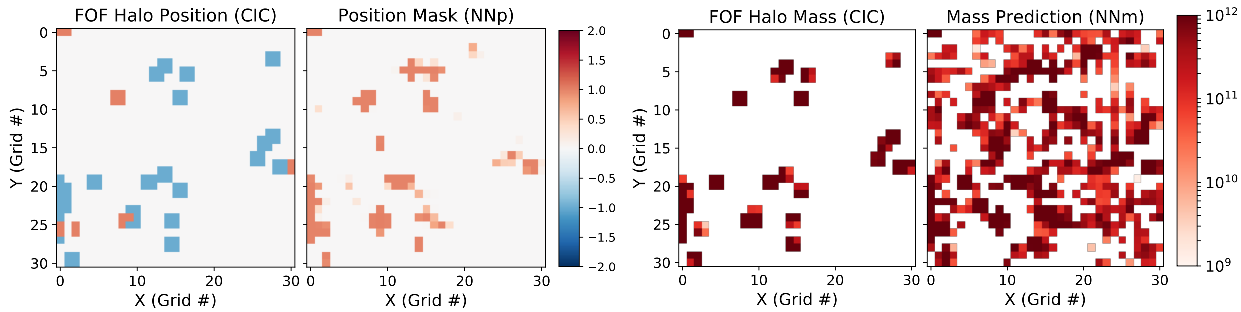


(a) (b)

Figure 4.3: We show a randomly selected subregion (30×30 grid cells ($\sim 90\,\mathrm{Mpc/h}$) in X-Y direction and 1 grid cell thick along Z-direction) of different fields. (a) Comparing output of NNp, position mask with the FOF halos. Since halos are convolved with CIC, they appear as squares in the projection. In the FOF halo position (left figure), we have distinguished between the massive halos found in $128^3$ simulation (which provides all the density field features for the neural network) in red, and the smaller halos supplemented from $512^3$, shown in blue (by artificially multiplying the latter with $-1$ to distinguish them, the sign of the values on the colorbar is irrelevant), to reach the requisite number density. (b) Comparison of regression output of NNm with FOF halos, without imposing the NNp mask on the prediction of NNm

rates are defined as

$$\mathrm{TPR} = \frac{\#(\mathrm{NNp}_{>0.5} \ \cap \ \mathrm{Dconv}_{>0})}{\#\mathrm{Dconv}_{>0}} \tag{4.4}$$

$$\mathrm{FPR} = \frac{\#(\mathrm{NNp}_{>0.5} \ \cap \ \mathrm{Dconv}_{=0})}{\#\mathrm{Dconv}_{=0}} \tag{4.5}$$

where NNp are the values at the grid points on the NNp; Dconv are the values of the data grid where FOF halos have been convolved on the grid with a convolution scheme (CIC or NN) and the subscript in $\mathrm{NNp}_{>0.5}$ for e.g. means only the points where the value on the said grid is greater than 0.5. We show the ROC curves in different mass bins in Fig. 4.4 for nearest neighbor convolution of the data ($\mathrm{D}_{NN}$). As expected, the accuracy of the network decreases as we go to halos of lower masses. The steepness of the curves also indicates that the halos are predicted (especially for higher masses) with high confidence i.e. halo prediction is insensitive to the probability threshold. This is suitable for us since this allows us to multiply with the NNm grid directly to model the halo mass field without passing the NNp grid through a probability threshold.

However, TPR and FRP do not tell the full story in our case since most of the points in the cosmological simulations at our resolution and number density have low overdensity and are empty i.e. do not have a halo ($> 95\%$ points are empty for $\bar{n} = 10^{-3}(\,h\,\mathrm{Mpc}^{-1})^3)$ . This makes them very easy to be classified, artificially boosting the FPR while not evaluating the performance of classification in more interesting regions.

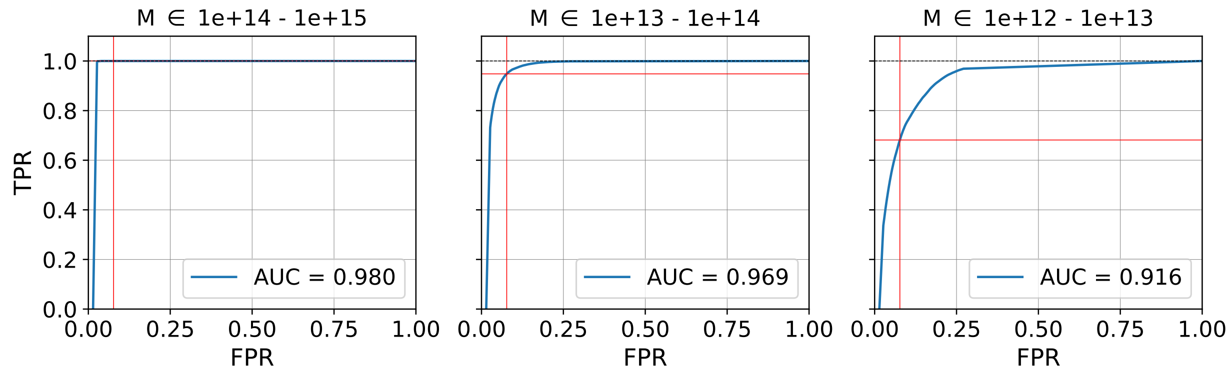


Figure 4.4: Receiver operating characteristic curve for NNp network for halos in different mass bins. The legends give the area under the curve. The thin red lines correspond to the true and false positive rates for $p = 0.5$ where the $p$ is the probability threshold used for classification.

Thus, we look at other kinds of errors that the position network makes. We would like to quantify the halos that are missed as a function of the mass. To quantify these errors, we define 'Missed fraction' and 'Empty Fraction'.

$$\text{Missed Fraction} = \frac{\#(\text{NNp}_{<0.5} \ \cap \ \text{Dconv}_{>0})}{\#\text{Dconv}_{>0}} \tag{4.6}$$

$$\text{Empty Fraction} = \frac{\#(\text{NNp}_{>0.5} \ \cap \ \text{Dconv}_{=0})}{\#\text{Dconv}_{>0}} \tag{4.7}$$

Missed fraction quantifies the number of halo locations that the neural network does not detect with the probability threshold of 0.5. For the number density of $\bar{n} = 10^{-3}$ $(5 \times 10^{-4})(\,h\,\text{Mpc}^{-1})^3$, when compared to CIC positions of halos ($\text{D}_{CIC}$; thus assigning 8 grid points to individual halo), missed fraction is around $\sim$ 25% (15%) while it drops to $\sim$ 15% (7%) when compared to the nearest neighbor gridding ($\text{D}_{NN}$) of halos. Since the latter assigns a single point per halo, it quantifies the actual number of halos missed completely by the model. Mass distribution of the missed halos as a fraction of the total number of halos (halo mass function) is shown in Figure 4.5. As expected, we find that the model accurately detects high mass halos and the missed halos are primarily of lower mass. We note that at these masses, finding the correct halos is hard, since most of the halos are close to the mass threshold, and whether or not a halo should be above or below the set threshold will thus depend on small details. This problem is somewhat alleviated if one is looking at the halo field weighted by the halos mass. This is explored further below.

Empty fraction is related to false positives and again quantifies the extra points that the network predicts as halo positions and which are not in the FOF catalog, but as a ratio of the total number of positions occupied instead. For CIC gridding, this is $\sim$ 10% (30%)

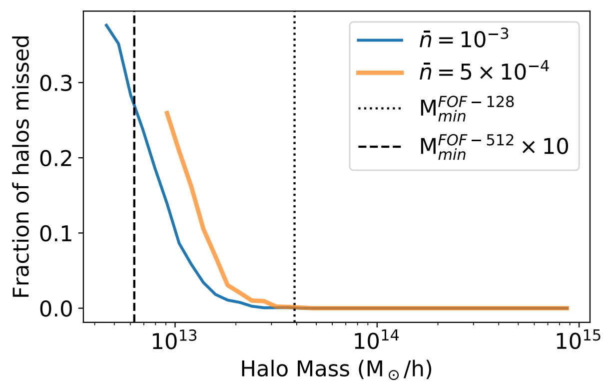


Figure 4.5: Fraction of halos (Nearest-neighbor points) missed by the position mask created by NNp network as a function of mass. For reference, the dashed and the dotted lines show the mass of the smallest halo with 12 particles identified in the simulation when run with $128^3$ grid- which generates the density features; and $512^3$ grid- which generates the data. Neural networks are able to identify the halos with mass upto $\sim 8$ times below the FOF threshold.

for the two number densities. For the nearest neighbor gridding, these numbers are higher. However, most of these positions are still adjacent to halos, and for triangular shaped cloud (TSC) convolution of the halos ($D_{TSC}$) the empty fraction drops to $\sim 1\%$ (5%). This is one motivation for smoothing of the fields when studying the error model of the mass network as explored below. The false positive grid points are primarily of 2 types - locations where center of FOF halos and density peaks positions are widely separated from each other, and locations which have lower mass halos and hence are below the abundance cut imposed on the catalog.

## Error Histograms

Having a forward model that predicts the halo mass or some other property is not all that is needed: to do reconstruction via optimization, one also needs a likelihood model for the data, i.e. an error/noise model which can be combined with the prior to construct a loss function. This error model should be sparse, so that it can be efficiently evaluated even on large grids. We are thus interested in estimating the error made by the model (NNp×NNm) in predicting mass over all points on the grid to create our noise model. However from the previous section, we know that NNp and hence the model has false positives, most of which lie close to a halo. If we directly calculate the error at the level of the two fields as is, we will be ignoring this information that we are in the correct neighborhood, if not at the exact position. This information has the potential of helping with the convergence of the optimizer during the reconstruction. To make use of this local information, we calculate the error in mass estimation on a smoothed model and data field instead i.e. we convolve both the

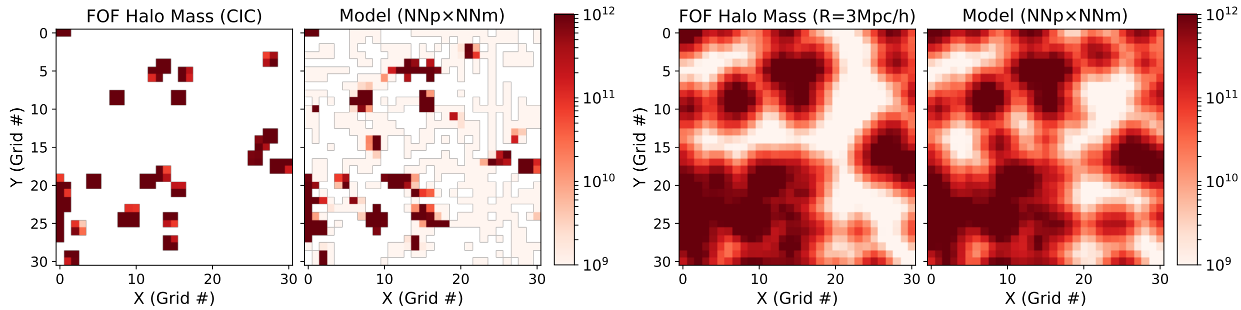


(a) (b)

Figure 4.6: We show the same subregion (30×30 grid cells ($\sim 90\,\mathrm{Mpc/h}$) in X-Y direction and 1 grid cell thick along Z-direction) of different fields as Fig. 4.3. (a) FOF halo mass field and the model prediction (NNp $\times$ NNm) (b) Same as (a) but smoothed with a Gaussian kernel of $3\,\mathrm{Mpc/h}$. The beefed up size of the halos is an artifact of log-color scaling which is used to show good agreement over orders of magnitude in mass.

predicted model field and the mass weighted halo field with a smoothing kernel. This creates a smoothly varying non-zero valued field in region around the position of the halos and in the model predictions. Thus, if the predicted and the true halos are offset by only a couple grid cell, a smooth field will have non-zero values at all the grid points between the two, leading to smoother variations in the noise(error) and non-zero gradients. This smoothing will hence tells the gradients which way to move to construct the peaks corresponding to the halos. We smooth both the modeled and the halo mass field by convolving with Gaussian smoothing kernel of $3\,\mathrm{Mpc/h}$ (since that was also the minimum scale used to generate the input features for the neural networks). These smoothed fields are shown in Figure 4.6b and they are in better visual agreement than the discrete fields (Figure 4.6a).

We then compare these two smooth fields at point by point basis to ascertain the error in our model. This is shown in Figure 4.7, where we show the histogram of the error made by the model in predicting logarithm of the mass at different points binned as a function of the true mass at those points (different panels). We also want an analytic form for the error PDF. We find that displaced log-normal model is effective for this purpose, so we calculate the difference in $\log(M_R + M_0)$ with $M_R$ being the value of the smoothed mass fields and $M_0$ a nuisance parameter, its value being $10^8 M_\odot/\mathrm{h}$ in Figure 4.7. We bin grid points based on the value of $M_R$ for the FOF halo mass fields in different panels as specified by the title and plot the corresponding error histogram.

The black points in Figure 4.7 are the modeling error data points, measured against true FOF halo masses convolved on the grid which were also used for training NNm network. The red dashed plots are the log-normal fits to the error histogram which fit the peak well but underestimate the tails. There is a non-zero offset for all mass bins, and it is taken out by our model. The error (standard deviation) increases as we go lower in mass until $M_0$

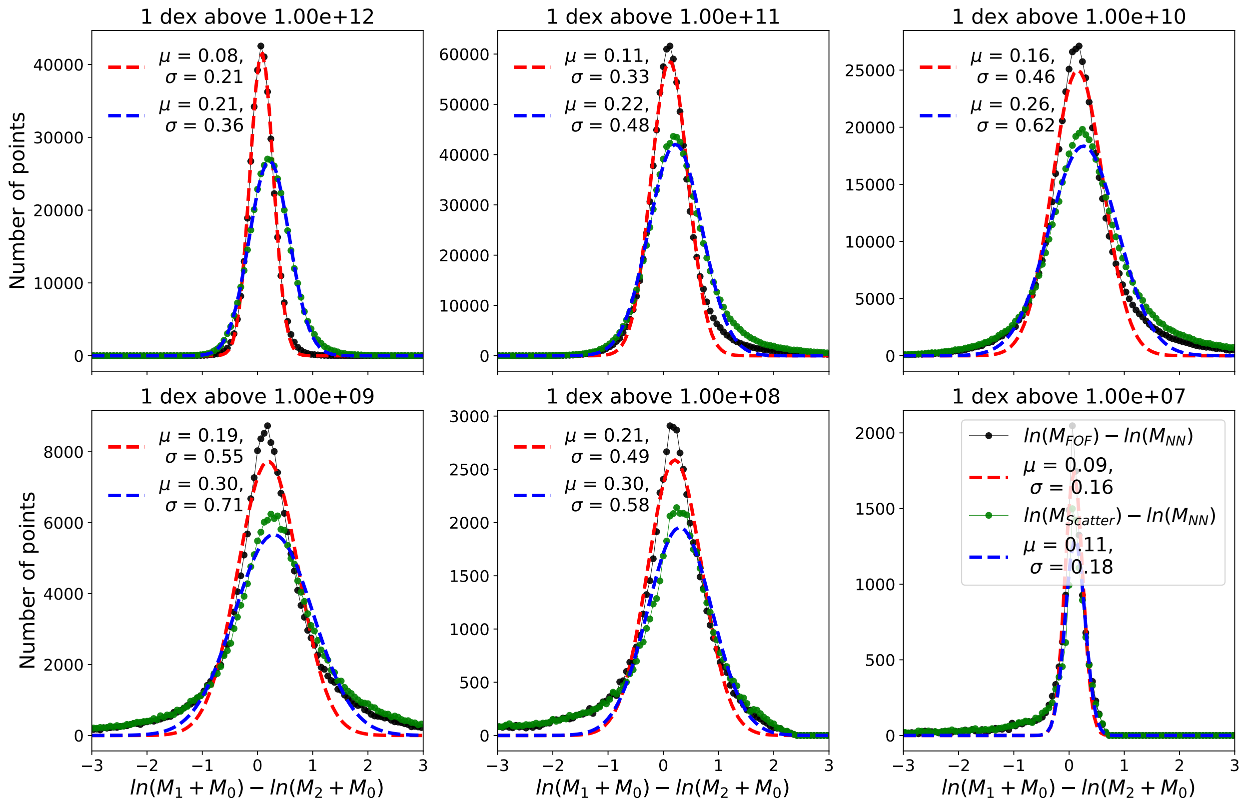


Figure 4.7: Modeling error histograms. Error is the difference between the smoothed mass fields of the data (FOF halos) and neural network predictions. It is estimated in terms of $\log(M_R + M_0)$ where $M_R$ is the value of the smoothed halo mass fields and $M_0$ is a constant nuisance parameter, here $M_0 = 10^8 M_\odot$/h. Every panel corresponds to different positions (bins) on the data grid where the data (mass) value at those points is in the range given by the titles of the panels. Black points are the data points from the simulation assuming the correct mass of the halos ($M_1 = M_{\rm FOF}, M_2 = M_{\rm NN}$), green points are with log-normal scatter of 0.2 dex in halo masses for the data ($M_1 = M_{\rm scatter}, M_2 = M_{\rm NN}$). The dashed lines are the log-normal best fits with mean and standard deviation specified in legend.

starts to dominate. Thus, as in position (Figure 4.5), our model predicts masses of heavier halos better than lower mass halos.

So far, we have assumed that we know the true masses of the dark matter halos. However this is not true in actual surveys. LSS surveys observe galaxies and there is an intrinsic log-normal scatter associated with stellar mass, luminosity or other observables and the corresponding halo mass [198]. If we constrain the halo masses by weak lensing, there is still an error associated with this calibration. To estimate our modeling error in the case of noisy halo masses, we add a log-normal scatter of 0.2 dex before matching abundance of halos and make the error histograms for our model against these noisy halo masses. These are the green points in Figure 4.7. The blue plot is the log-normal fit to this modeling error. The error (standard deviation) for the scattered data is larger than for the unscattered data i.e. when we assume we know the correct halo mass. Further, the offset has also increased over the true cases. However we are still able to fit the error histograms with a displaced log-normal and this motivates the choice of our noise model (loss function) in Section 4.5.

## Two point functions

Finally, we also compare the performance of the model in predicting CIC convolved halo mass and halo position fields at the level of 2 point functions in Fourier space. When comparing the position weighted fields, we take Fourier modes of the neural network field ($\delta_N$) corresponding to overdensity in the NNp field and compare them to the true modes of position weighted true halo field ($\delta_h$); and when comparing the mass weighted fields, we compare Fourier modes of the neural network model (NNp $\times$ NNm)($\delta_N$) and compare them to the modes of mass weighted halo mass field($\delta_h$).

To this end, we consider three different metrics for both, the position and mass weighted fields -

- cross correlation coefficient ($r_c$)

$$r_c = \frac{P_{hN}}{\sqrt{P_{hh} P_{NN}}} \tag{4.8}$$

- stochasticity ($s$)

$$s = P_{hh}(1 - r_c^2) \tag{4.9}$$

- and transfer function ($TF$)

$$TF = \sqrt{\frac{P_{NN}}{P_{hh}}} \tag{4.10}$$

where $P_{hh}$ is the auto-power spectrum of FOF halo mass (or position) field, $P_{NN}$ is the auto spectra for the model (or NNp) and $P_{hN}$ is cross spectrum. Figure 4.8 shows the scale dependence of these statistics for different resolutions and number densities, after taking mean of 5 independent realizations to reduce the noise. The dashed lines are position weighted FOF halos compared with output of NNp. The mass weighted halo fields and the modeled field are compared in solid lines. In dotted lines, we show the comparison between smoothed-mass weighted fields where smoothing is done at 3 Mpc/h with a Gaussian kernel, which is the same field that is used to estimate the error histograms in the previous section. Poison shot noise is shown as horizontal lines in the middle panel for the two number densities.

The cross correlation coefficient for position of halos on large scales is $\sim 0.98$ and drops to $\sim$ 0.9 at $k = 0.2,\ 0.3\, h\,\mathrm{Mpc}^{-1}$ for $\bar{n} = 5 \times 10^{-4},\ 10^{-3}(\,h\,\mathrm{Mpc}^{-1})^3$ respectively. The mass weighted fields are more than 95% correlated upto $k \sim 0.7\, h\,\mathrm{Mpc}^{-1}$ with $r_c$ being impressively close to one upto $k \sim 0.1$ (Mpc/h)$^{-1}$. The cross correlation coefficient is much

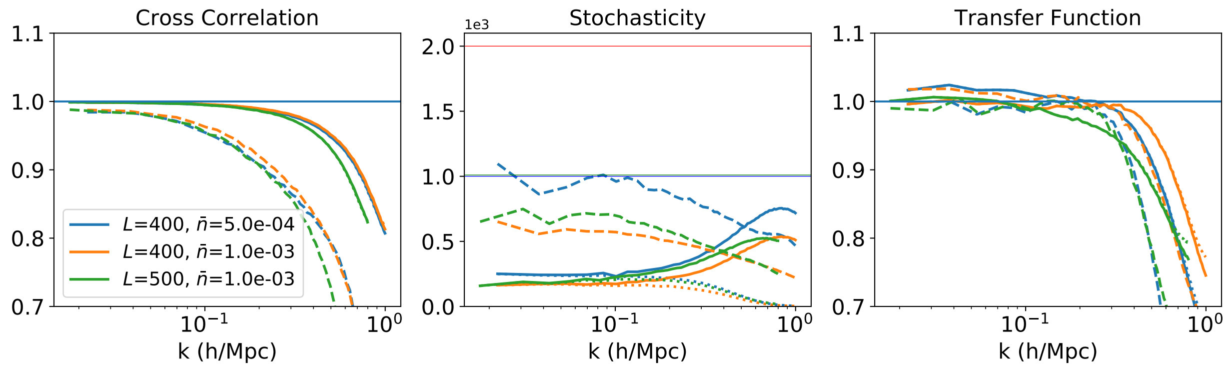


Figure 4.8: Cross correlation coefficient, stochasticity and transfer function for position (dashed) and mass (solids) weighted model field and FOF halos, as well as for the smoothed mass field (dotted). The horizontal lines in the middle panel are the Poisson shot-noise levels for the two number densities.

higher for mass weighted fields than the position fields because the former up-weights the heavy halos by orders of magnitude and the model is more accurate in detecting these halos (Figure 4.5 and 4.7).

At the level of stochasticity (against the FOF halo field), the model improves by a factor of 2 over of Poisson shot noise for the position fields. It is a significantly higher reduction as compared to simplistic bias models often used to model halo fields [155]. This is primarily driven by the fact that NNp is able to correctly identify the neighborhood of halos as discussed in the previous sections. For the mass weighted fields, the stochasticity is much lower than the position field, which is again because its dominated by heavier halos. The stochasticity for the mass weighted field is also flat on large scales and then rises up on small scales. For the smoothed mass field shown in dotted lines however, this increase in stochasticity on smaller scales is suppressed and now stochasticity is white on all the scales that it is non-zero.

The transfer function of our modeled field with respect to the halo mass field is noisier than either cross-correlation or stochasticity. Further, its close to but not unity on large scales for neither the position nor the mass weighted fields. This likely directly affects the transfer function of our reconstructed field (section 5.7) that will need to be calibrated out when reconstructing band powers for linear power spectrum.

## 4.5 Reconstruction

In the previous section, we have developed a forward model $\boldsymbol{f}(\boldsymbol{s})$ which does the non-linear mapping to go from the initial linear density modes ($\boldsymbol{s}$) to the final halo mass field ($\boldsymbol{d}$). This forward model consists of 5 step `FastPM` simulation followed by two neural networks performing non-linear transformations on the evolved density fields to generate our modeled halo mass field. Given this observation, $\boldsymbol{d}$=$\{d(r_{i(=1...N)})\}$, we are interested in recovering the initial density linear modes $\boldsymbol{s}$=$\{s_{j(=1...M)}\}$. In this section we explore this problem, closely following the formalism developed in [211]. An overview of our approach is shown in the left panel of Figure 4.1. In section 4.5, we use the modeling error discussed in section 4.4 to develop a loss function that we will optimize over to do the reconstruction. Then in section 4.5, we describe the optimization procedure and discuss methods to speed up and improve the convergence. In section 5.7, we finally present the results for our reconstruction for different number densities. In the next section 4.5, we discuss how these results depend on our choice of loss function.

## Loss Function

We write the observed halo mass field as a combination of signal term ($\boldsymbol{f(s)}$) and a noise term ($\boldsymbol{n}$) as $\boldsymbol{d = f(s) + n}$ where the noise, $\boldsymbol{n}$, has contributions from both, noise in the data as well as the errors in our model. One can thus write the joint probability of the signal and the noise as a product of individual probabilities, under the assumption that they are uncorrelated, as $P(\boldsymbol{s, n}) = P(\boldsymbol{s})P(\boldsymbol{n})$.

The initial modes are Gaussian and we assume them to be in Fourier space, where their Gaussian prior can be written in a diagonal form.

$$P(\boldsymbol{s}) = (2\pi)^{-M/2}\det(\boldsymbol{S})^{-1}\exp\left(-\frac{1}{2}\boldsymbol{s}\boldsymbol{S}^{-1}\boldsymbol{s}^\dagger\right) \tag{4.11}$$

with covariance $\boldsymbol{S} = \langle \boldsymbol{s}\boldsymbol{s}^\dagger \rangle$, which is also the power spectrum. We will assume that this power spectrum can be written in terms of parameters $\boldsymbol{\Theta}$ which are typically the bandpowers. The modes are complex and obey $\boldsymbol{s}^*(\boldsymbol{k}) = \boldsymbol{s}(-\boldsymbol{k})$, where $\boldsymbol{k}$ is the wavevector, but in our labeling of modes we treat real and imaginary component as two independent modes.

The noise vector $\boldsymbol{n}$ is parameterized with the noise covariance matrix $\boldsymbol{N} = \langle \boldsymbol{n}\boldsymbol{n}^\dagger \rangle$. This noise matrix is made up of 2 contributions - i) measurement noise that is assumed to be known, uncorrelated with the signal and diagonal (or sparse) in configuration space; ii) modeling noise that may be signal dependent but is still diagonal or sparse in configuration space. This consists primarily of the modeling uncertainty caused by our using a substitute Neural Net model for halo mass and position field in place of actual FOF halo masses and positions. Contributions to the measurement noise, that we do not include in this work, come from the fact that we do not know the dark matter halo masses accurately. These masses are often calibrated using weak lensing observations and there is noise associated with this calibration. In addition, we only observe the halos that host a galaxy and there is an intrinsic scatter associated with the halo mass and galaxy occupancy, as well as relationships between the halo masses and galaxy observables such as stellar mass and luminosity[198].

Our noise model for the modeling error caused by using NN model is based on the error histograms presented in section 4.4. Our working variable constructed out of our data (and model) for which we estimate error is

$$x = \log(M_R + M_0) \tag{4.12}$$

We estimate error at the level of smoothed halo mass fields for the reasons explained in that section. We work with the logarithm of the the mass rather than the mass directly so as to decrease the dynamic range over different halo masses and also make it comparable to the dynamic range of the prior on the initial Gaussian field. Furthermore, we add a constant nuisance parameter $M_0$ to the smoothed halo mass field. This suppresses the points which have mass assigned less than that value. For instance, by assigning a high value to $M_0$, we can suppress the lower mass halos and only compare the fields at the position of big halos. We can thus tune the value of $M_0$ such that we are affected only by the halos above the requisite abundance in our model and exploit this to assist in convergence when minimizing the loss function during reconstruction.

In Figure 4.7 we have seen that the probability distribution of the noise, both with and without the scatter in halo masses, is described well with the displaced log-normal distribution, albeit with different values of the parameters (standard deviation and the offset). With this noise model, one can then write the probability distribution of noise as

$$P(\boldsymbol{n}) = (2\pi)^{-N/2}\det(\boldsymbol{N})^{-1}\Pi_i \exp\Bigg[-\Bigg(\frac{\mu_N + log(M_{R,i}^{NN} + M_0) - log(M_{R,i}^{FOF} + M_0)}{2\sigma_N}\Bigg)^2\Bigg], \tag{4.13}$$

where the product is over all grid cells. This is equivalent to the likelihood of the data.

Combining this with the prior term (Eq. 4.11) and under the assumption that these are uncorrelated, one can write the joint probability for the signal and noise as a product of the two. This is also the conditional posterior probability of the signal, given the data, up to a constant evidence. Then, following [211], we can maximize the posterior of the signal to obtain the MAP estimate of initial modes. This can be achieved by instead minimizing the negative log-posterior which is equivalent to minimizing the corresponding $\chi^2$ in the exponent. Thus our loss-function to be minimized is,

$$\mathcal{L}(\boldsymbol{s}) = \frac{1}{2}\boldsymbol{s}\boldsymbol{S}^{-1}\boldsymbol{s}^{\dagger} + \sum_i \Bigg(\frac{\mathrm{\mu_N + log(M_{R,i}^{NN} + M_0) - log(M_{R,i}^{FOF} + M_0)}}{2\sigma_\mathrm{N}}\Bigg)^2 \times \mathrm{f}_{eff} \tag{4.14}$$

where the first term in the prior term and the second is the noise, or the residual term. $\mathrm{f}_{eff}$ is the compensating factor which is fraction of effective number of points as discussed below. $\mu_N$ and $\sigma_N$ are the offsets and standard deviations of the displaced log-normal fits to the noise model (Figure 4.7) and depend on $\mathrm{M}_R^{FOF}$ at the grid point.

The prior term is diagonal in Fourier space. We expect the noise term to be sparse in data (configuration) space and have correlations only on small scales. This is expected because we have smoothed the field to better exploit the information that we are in the correct neighborhood of the halos and hence improve on the gradient directions. Even otherwise, density and hence the mass prediction is correlated in regions around halos, which can lead to correlations in the modeling error. Using a covariance with non-zero diagonal entires for the noise makes the evaluation of the loss function computationally expensive, which can pose a serious problem for the optimization.

While a detailed investigation of the sparsity and correlations of the noise covariance matrix is certainly needed in the future, an alternate strategy to handle such covariances is to reduce the effective number of points in the data set that contribute to the meaningful information. If we ignore these correlations, we overestimate the information content of the residual term. This reduction can be achieved by simply changing the relative weighing of the prior and the residual term in the loss function. This simplifies our loss function significantly and leads to the compensating factor $f_{eff}$, which is the fraction of effective number of points on the grid after taking noise correlations into account. In practice, we have set $f_{eff}$ to 1 and instead used a constant $\sigma_N$ at a level higher than the one estimated by the error histograms (Figure 4.7). This is motivated by the observation that even though the modeling error is smaller for high mass halos (i.e. lower $\sigma_n$), the points in this neighborhood are expected to be correlated to larger scales and to a higher degree than the intermediate mass halos (i.e. leading to lower $f_{eff}$). The simplest way to capture this trade-off is to use the constant noise model and we find that it works very well in practice. This is further discussed in the section 4.5.

## Optimization Algorithm with Annealing

We do reconstruction of the initial density modes by minimizing the loss function (Eq. 4.14). This is an optimization problem in a high dimensional space, with both the number of underlying features (initial modes) and the number of data points (grid cells) being in millions or more. A brute force optimization scheme thus has no real hope of converging. At the same time, while second order methods such as Newton's method may perform better than simple gradient descent, Hessian inversion is not feasible. Instead, we balance the trade-offs between the two approaches by using limited memory BFGS (L-BFGS: Broyden–Fletcher–Goldfarb–Shanno) algorithm which is a quasi-Newton's method, where one approximates the inverse Hessian using low rank matrix approximation constructed from gradients of previous iterations.

L-BFGS algorithm requires gradients of the loss function with respect to all of the initial modes. This involves evaluating the gradient of the forward model, which in our case consists of a 5 step `FastPM` evolution followed by transformation of the final density field with Neural networks. The latter involves a series of matrix multiplication with the weights of different layers followed by analytic activation functions and hence estimating its derivatives is straightforward. The derivatives of `FastPM` evolution can be evaluated along the lines of PM derivatives as presented in [247, 85]. We implement these gradients using the automated differentiation package, `ABOPT`[10], developed with this application in mind.

[10] https://github.com/bccp/abopt

Since we are aware of physics driving our model as well as its performance, we can use our domain knowledge to assist the convergence by modifying the loss function over the iterations rather than simply brute-forcing the optimization with the vanilla loss function. With respect to the dynamics of our model, we know that the large scales are linear and posterior surface is convex and thus easy to converge, albeit low in number of modes. In terms of the model performance, we know that our model works better for larger mass halos than the smaller ones. Also, optimizing over a discrete field is harder as compared to a smoother, more continuous field. Based on these intuitions, we do the following optimizations.

- *Annealing of multigrid smoothing ($N_{sm}$)* [85]: We smooth the residual term of the loss function on small scales with a Gaussian kernel. Thus on these scales, the prior term pulls the small scale power to zero and we force the optimizer to get the large scales correct first. Instead of picking a physical scale, we set the smoothing scale in terms of mesh scale by choosing $N_{sm}$ = number of grid cells over which to smooth the residual and gradually decrease $N_{sm}$ to 0 (annealing). Since the smoothing scale is defined in terms of the grid scale, we are effectively using multiple coarser grids over iterations at the level of the residual term, even though the forward modeling is always done on the same fiducial grid. Without this kind of multigrid smoothing, we find that the small scale modes overwhelm the optimizer with their sheer number since the number of modes scales as $k^3$. Moreover, since they are more non-linear and more noise contaminated than the large scales which are linear, the optimizer spends most iterations tweaking these small scales without getting the large scales correct.

- *Annealing of $M_0$*: We start with a high value of $M_0$ and then decrease it over the course of optimization. Since our working variable in the loss function is $\log(M + M_0)$, this suppresses all the points on the grid where FOF halo mass is less than $M_0$. Hence we effectively force the optimizer to first get the large halos correct and then go down in halo mass. This helps in converging to the truth faster for two reasons: it prevents the optimizer from getting overwhelmed with small halos which are more numerous but where our model is slightly worse than it is for more massive halos. Also, the large scale power is driven by the bigger halos due to the mass weighing of the halos and identifying them correctly helps in converging to the correct large scales quicker.

- *Annealing of discreteness parameter $a$*: The last activation function in the NNp network that gives the position mask is the logistic function, Eq. 4.3, with $a = 3$, and this is responsible for the discreteness of the model field. However, discrete fields are harder to optimize over and hence we begin with $a = 1$ and then increase its value to 2 and 3 over the iterations. The logistic function saturates gradients when the values are much larger or smaller than the threshold (which is why its no longer favored in the hidden layers of neural networks) and this is more severe with sharper functions ($a = 3$). Thus starting with a 'broader' ($a = 1$) logistic function saturates the gradients less, thus assisting in convergence. Physically, it can be understood as an additional smoothing or decreasing the discreteness of the modeled field. Since the gradients are non-zero over more grid points, they have a better spatial information in which direction to move initially when we are far from the truth.

## Results

In this work, we show the results for reconstruction of initial density field using our forward model in a 400 Mpc/h box over $128^3$ grid for different number densities of halos which were identified in a $512^3$ simulation with 40 time steps. Our optimizer starts with random phases for the initial conditions. The amplitude of the initial conditions is 10% of the fiducial power for high number densities ($\bar{n} = 10^{-3}(\,h\,\mathrm{Mpc}^{-1})^3$ and $5 \times 10^{-4}(\,h\,\mathrm{Mpc}^{-1})^3$) and 50% power for the lower number densities ($\bar{n} = 2.5 \times 10^{-4}(\,h\,\mathrm{Mpc}^{-1})^3$ and $10^{-4}(\,h\,\mathrm{Mpc}^{-1})^3$). The correlations in the noise are addressed by changing the relative weighting of the residual and the noise term in the loss function. Instead of using an explicit $\mathrm{f}_{eff}$, we do so by using a higher $\sigma_N$ than the mass-dependent noise estimated from the displaced log-normal fits to the error histogram similar to Figure 4.7. For this subsection, the amplitude (variance) of the noise used is $\sigma_N^2 = 0.25$. We also keep the non-zero offset ($\mu$) in the means of the error histograms. In the next subsection, we will discuss how these choices in the loss function affect our results.

To assist the convergence of our optimization, we tweak the loss function over iterations in various ways. We have tried to change the parameters in different order and to multiple values to find an optimal balance between run-time and performance, where to quantify performance, we are monitoring the cross-correlation coefficient of the reconstructed initial density field with the truth on large scales as the quantity of primary interest. For the number densities under consideration, the following algorithm provides the optimal balance-

- For $M_0 = 10^{12} M_\odot/\mathrm{h}$
  - For $N_{sm} \in \{4, 2, 1, 0.5, 0\}$
    - For $a \in \{1, 2, 3\}$
      - do optimization using L-BFGS algorithm until $\mathcal{L}$ (loss function) per degree of freedom stops decreasing by 0.1% over successive iterations
- For $M_0 = 10^{11} M_\odot/\mathrm{h}$ & $a = 3$
  - For $N_{sm} \in \{1, 0.5, 0\}$
    - do optimization using L-BFGS algorithm until $\mathcal{L}$ (loss function) per degree of freedom stops decreasing by 0.1% over successive iterations

The values of $M_0$ roughly correspond to halo masses above which lie $\sim 25\%$ and $\sim 50\%$ of the points on the smooth halo mass grid. Further, the smallest halo for $\bar{n} = 10^{-3}(\,h\,\mathrm{Mpc}^{-1})^3$ has mass $\sim 5 \times 10^{12} M_\odot/\mathrm{h}$ and using these values of $M_0$ ensures that we have picked the neighborhood of most halos while suppressing most of the empty regions. This is useful since once we have converged for $M_0 = 10^{12} M_\odot/\mathrm{h}$, we do not need to start again with large smoothing of four grid cells as we have practically converged on the large scales. Also, we do not need to work with a smoother model ($a = 1,\ 2$) and can directly use the correct model ($a = 3$) for the discrete field. This is because spatially, we have already converged close to the truth. Decreasing $M_0$ to less than $10^{11} M_\odot/\mathrm{h}$ does not improve cross-correlations significantly, likely due to inaccuracies in our model at these small masses and decreasing signal to noise as we go down in mass and scales.

For all the number densities, the optimizer takes $\sim 100$ iterations to converge to the best-fit initial field for $M_0 = 10^{12} M_\odot/\mathrm{h}$ and $\sim 80$ iterations to converge for $M_0 = 10^{11} M_\odot/\mathrm{h}$, given our tolerance of $10^{-3}$ i.e. 0.1% decrease in the loss function before declaring convergence. Thus in all, we converge in $\sim$ 200 iterations. The number of iterations increases and the performance worsens if we do not assist the optimizer as outlined above. For instance, when starting with $M_0 = 10^{11} M_\odot/\mathrm{h}$ for number density $\bar{n} = 5\times10^{-4}(\,h\,\mathrm{Mpc}^{-1})^3$, the reconstruction takes $\sim 250$ iterations and converges to a worse solution with the cross correlation coefficient for the initial field not approaching 95% even on large scales. Similarly the cross-correlation coefficient does not increase beyond 90% when starting directly with $M_0 = 10^{10} M_\odot/\mathrm{h}$. In comparison, the optimization converges to the minimum where initial fields are more than 95% cross correlated upto $k = 0.16\,h\,\mathrm{Mpc}^{-1}$ for the annealing scheme described above.

We first gauge our reconstruction visually in Figure 4.9 which shows the reconstructed field in the bottom row along with the true field in the top row for the number density of $\bar{n} = 10^{-3}(\,h\,\mathrm{Mpc}^{-1})^3$. The three columns are the initial matter field that we are interested in, final (5 step evolved `FastPM`) dark matter field, and the halo mass field. For the reconstruction, this halo mass field is the output of the neural networks at convergence while for the data, it is the FOF halo mass field. At the level of the initial field, we are able to reconstruct the large scale modes quite well while the field is smoothed out on smaller scales. The small scale suppression is much less severe for the reconstructed Eulerian matter field due to non-linear coupling which transfers power from large scales to small scales. Thus we are able to reconstruct the cosmic web including the filaments, voids and halos remarkably well. The same holds true for the halo mass field. The reconstructed halo mass field underestimates some of the heaviest peaks while no such difference is visible in the final matter field. This is due to the non-zero offset $\mu$ in the loss function (see Eq. 4.14 and Figure 4.7) which accounts for the difference between the two halo mass fields.

In Figure 4.10, we show the reconstructed initial field at the various stages of the annealing procedure used in the optimization. For comparison, we also show the true initial field and its Gaussian smoothed version with smoothing scale of $R_G = 2.5\,h\,\mathrm{Mpc}^{-1}$. Changing the width of the logistic function ($a$) makes the boundaries of various overdense and underdense regions sharper by increasing the density contrast between them. Then reducing the smoothing scale $N_{sm}$ matches the reconstructed field to the data on increasingly smaller scales. Since $N_{sm}$ suppresses the residual term, the cross-correlation coefficient between the reconstructed field and the truth is zero on scales smaller than set by it. Lastly, at $M_0 = 10^{12} M_\odot/\mathrm{h}$, only $\sim$ 25% points effectively contribute to loss function and reducing it to $M_0 = 10^{11} M_\odot/\mathrm{h}$ optimizes over more ($\sim$ 50%) points. This gets contribution from smaller halos and halo environments which start getting reconstructed and it generates smaller scale features in the

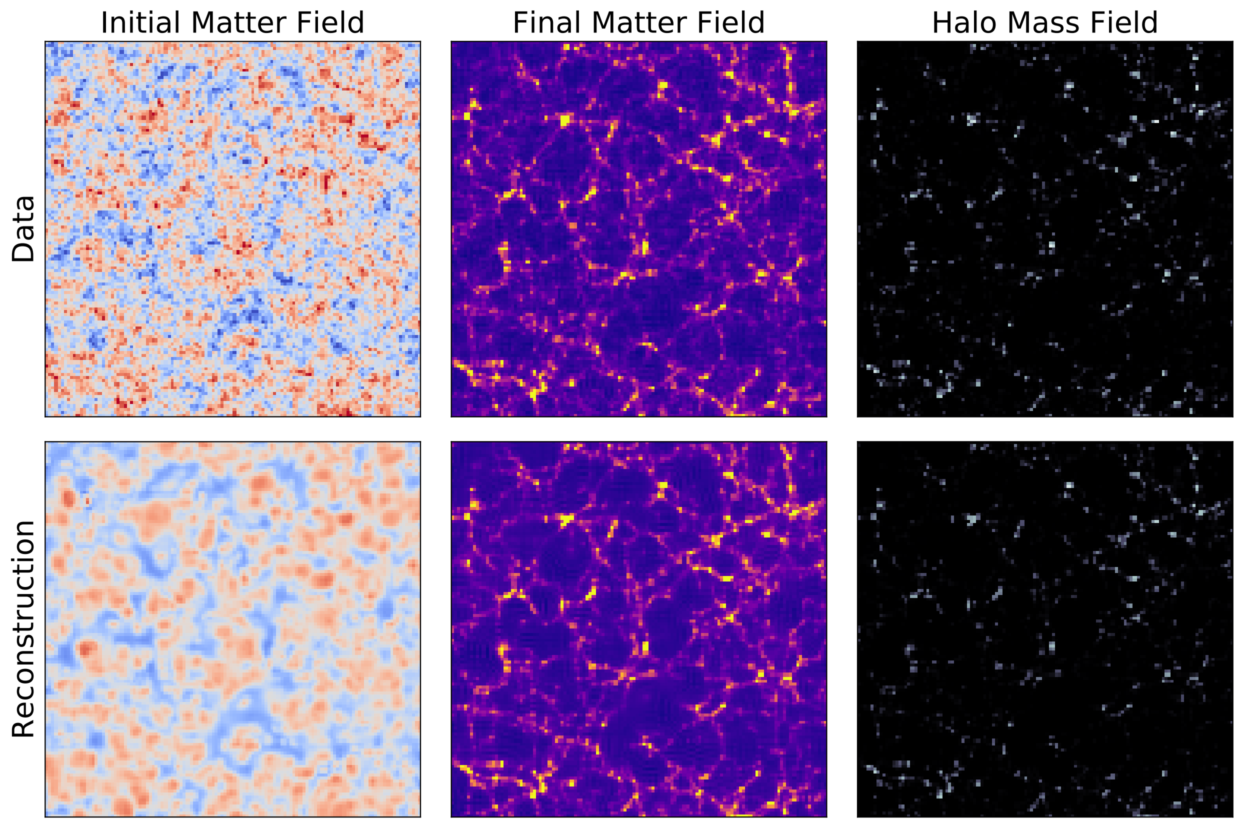


Figure 4.9: Reconstructed fields for 400 Mpc/h box, $128^3$ grid and $\bar{n} = 10^{-3}(\,h\,\mathrm{Mpc}^{-1})^3$ number density at the best-fit (converged) iteration with $M_0 = 10^{11} M_\odot/\mathrm{h}$. The color scheme is consistent in every column but different across the columns. The projection is over a slab of thickness 25 Mpc/h

reconstructed field.

To compare these fields quantitatively, we show the transfer function and the cross-correlation coefficient as function of scale for the reconstructed field in Figure 4.11. We compare the reconstruction for different number densities of halos. Except for the highest noise case ($\bar{n} = 10^{-4}(\,h\,\mathrm{Mpc}^{-1})^3$), in all cases the cross-correlation for all the three (initial, final and halo) reconstructed fields is very close to unity on large scales. With increasing number densities, we are able to push the reconstruction to smaller scales. The cross-correlation for the reconstructed initial field with the truth falls to less than 95% at $k = 0.12,\ 0.16,\ 0.18\ \,h\,\mathrm{Mpc}^{-1}$ for $\bar{n} = 2.5 \times 10^{-4},\ 5 \times 10^{-4}\ \&\ 10^{-3}(\,h\,\mathrm{Mpc}^{-1})^3$, respectively. For the final matter field, $r_c$ drops to 0.95 at $k = 0.23,\ 0.32,\ 0.42\ \,h\,\mathrm{Mpc}^{-1}$. The cross correlation coefficient of the final matter field is much higher than the initial field on the smaller scales, as also evident from the slices in Figure 4.9.

To gauge the cosmology dependence of the neural network model and the reconstruction procedure, we also do reconstruction by changing cosmology. Significant changes such as

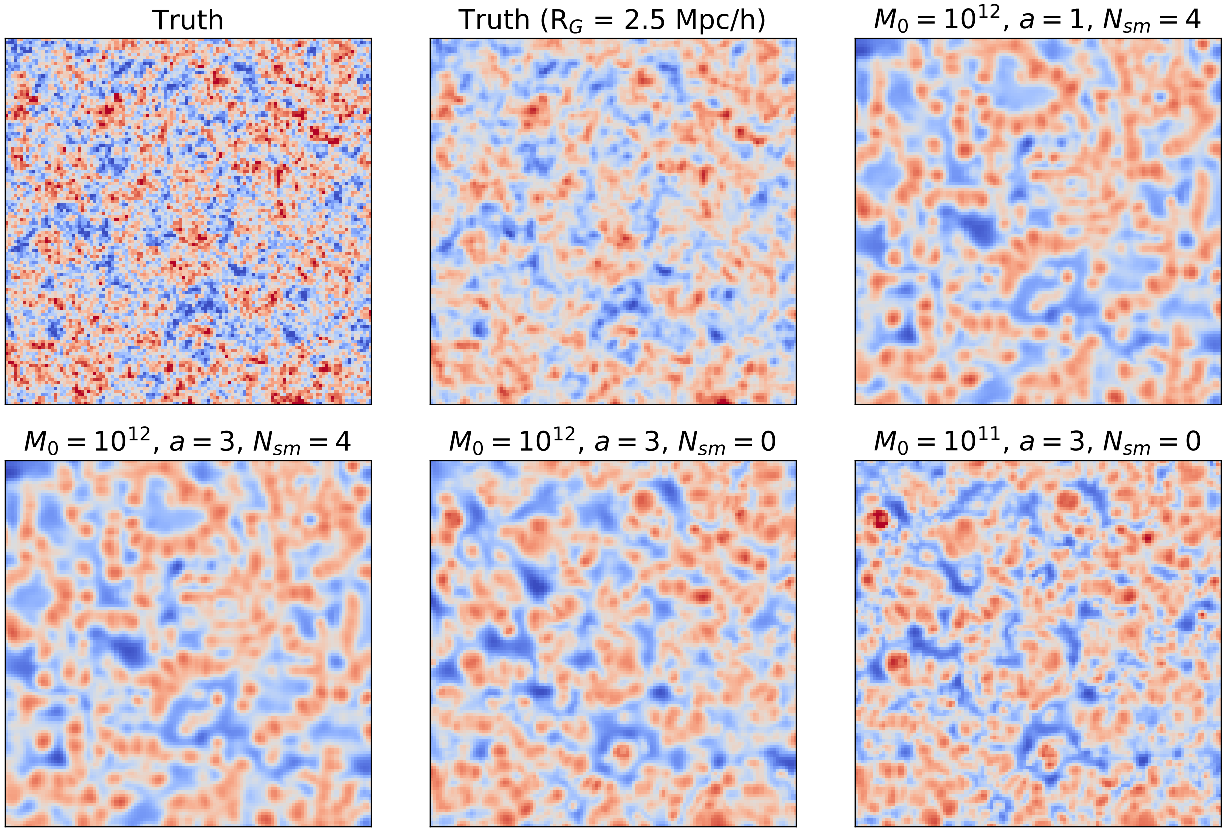


Figure 4.10: Reconstructed initial field at the various stages of the annealing procedure compared with the truth and its smoothed version with Gaussian kernel of $R = 2.5\,\mathrm{Mpc/h}$. The projection is over a slab of thickness $25\,\mathrm{Mpc/h}$.

warm dark matter model, exotic dark energy models or extreme changes in cosmological parameters will likely change the underlying relation between the matter density field and halo formation and mass. In this case we expect the procedure with a neural network trained on different cosmology to perform suboptimally. However in this work, we are primarily interested in the changes allowed within the currently validated cosmological framework. Thus we focus on two parameters, $\sigma_8$, which changes the overall amplitude of the power spectrum and $\Omega_m$, which changes the shape/slope of power spectrum. We increase them by 10% and 5% respectively, one at a time, while keeping other parameters same. We produce two new datasets i.e. the halo mass fields from new initial conditions generated with the same phases but the power spectrum with new values of these parameters. For reconstruction, we still use the fiducial power spectrum in the forward model for simulation and for the prior term in the loss function. The results, only for the initial field since it is that we are primarily interested in, are shown in Fig. 4.12. We find that the cross correlation coefficient is insensitive to the change in either of the cosmological parameters. Changing $\sigma_8$ does not

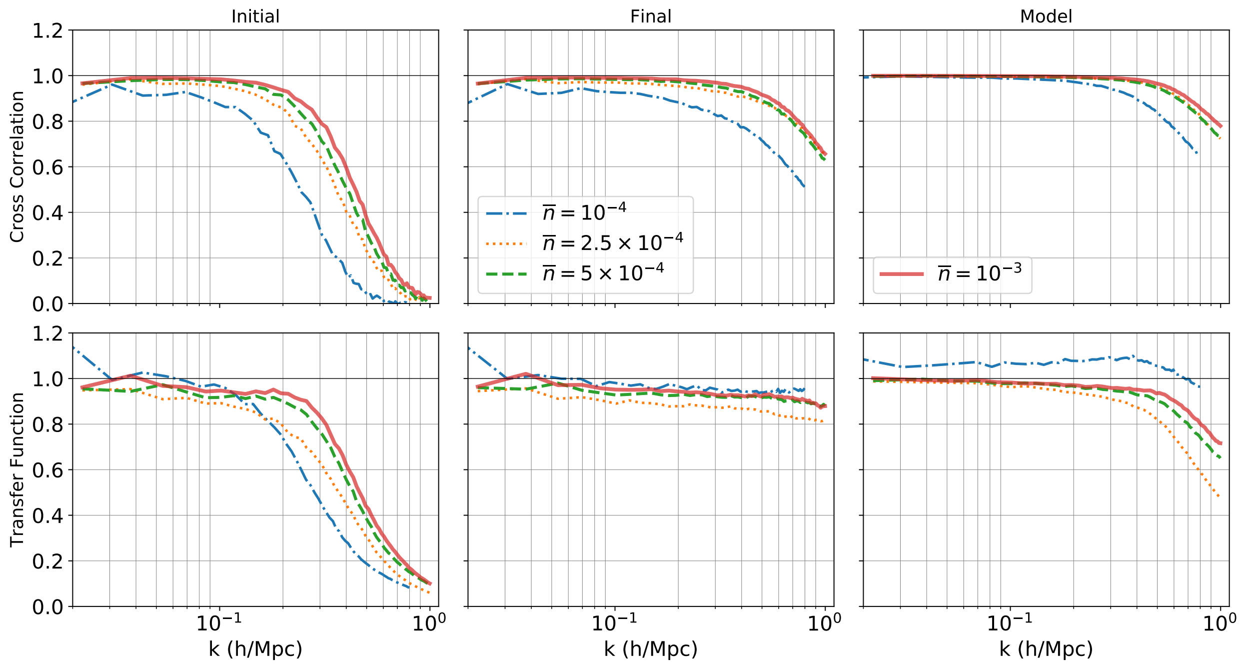


Figure 4.11: Transfer function and cross-correlation between the reconstructed fields and the truth for different number densities. Reconstruction for every number density is performed with a different neural network model, trained for that specific number density. From left to right, we show the result for initial linear field, the final evolved matter fields and the network predicted vs FOF halo mass field at the best fit of the reconstruction.

change the transfer function but changing $\Omega_m$ changes the transfer function on intermediate scales. We plan to investigate this further when doing bandpower reconstruction. We also verified that the reconstruction is independent of the realization by doing it for different initial conditions within the same cosmology by changing the seed that changes the phases (and the amplitude within cosmic variance). This is crucial since this will likely form the basis of our bandpower reconstruction which will enable us to extract the cosmological parameters from this exercise.

One can also estimate the error in the reconstruction by estimating the power of the residual fields, where the residuals are simply the difference of the true and the reconstructed fields. This is shown in the left panel of Figure 4.13 for the reconstruction with number density $\bar{n} = 10^{-3}(\,h\,\mathrm{Mpc}^{-1})^3$. We compare this with the relative noise level in the data (halo mass and halo position fields) by estimating $\sigma/b^2$ where $\sigma$ is the shot noise and $b$ is the bias of the data field. This corresponds to the noise level one would expect if the problem were a linear problem and reconstruction were done with a Weiner filter. We find that in our case, the noise in reconstructed initial field is reduced by a factor of 2 over this noise level. Another estimate of error in the phases is the quantity $1 - r_c^2$, where $r_c$ is the cross-

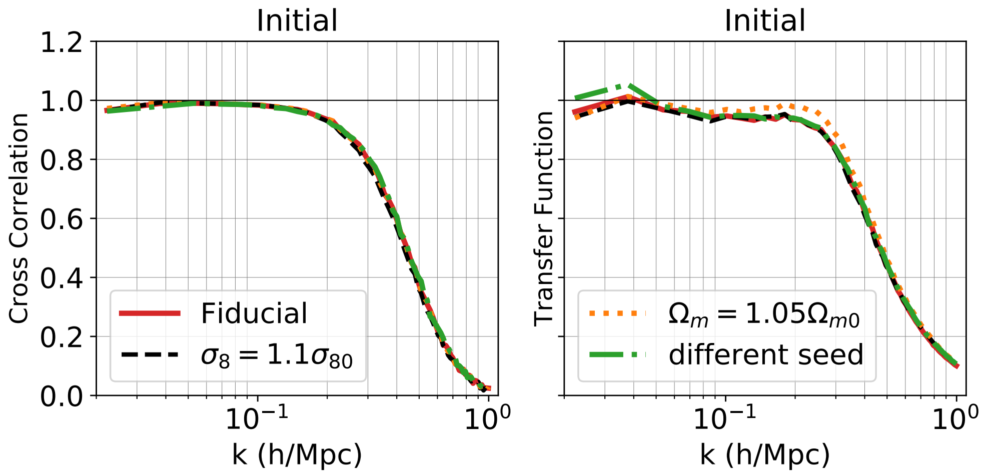


Figure 4.12: Transfer function and cross-correlation for the initial reconstructed field and the true initial field at the best fit of the reconstruction. We show results for different cosmologies i.e. by changing $\sigma_8$ and $\Omega_m$ as well as a different realizations i.e. different phases for the initial condition. The number density is $\bar{n} = 10^{-3}(\,h\,\mathrm{Mpc}^{-1})^3$ in each case.

correlation coefficient of the reconstructed field with the true field. This makes it easier to gauge the performance on large scales. We show this in the right panel of Figure 4.13 for $\bar{n} = 10^{-3}(\,h\,\mathrm{Mpc}^{-1})^3$. Note that unlike Figure 4. of [205], we do not rescale the reconstructed fields here to have the correct transfer function.

Unlike the cross-correlation coefficient, the transfer function of the different fields is less well behaved and not unity (Figure 4.11). While one would expect to reconstruct all the power, at least for the halo mass field since that directly enters the loss function, it is not the case. One reason for this is that the field being optimized over in the loss function is a non-linear transformation of the halo mass field which is presented in Figure 4.11. This is to say, we optimize over $x = \log(M_R + M_0)$ as a working variable, not the halo mass field itself, and the Fourier modes do not commute across such transformations. Another reason is the inaccuracy of the NN model itself: we have observed that the transfer function was not unity even at the truth, as shown when gauging the performance of the model in Figure 4.8. In the next subsection, we will show that the transfer function is also more sensitive to the choices we make for the different parameters in the loss function.

This implies that to reconstruct the linear power spectrum, one cannot simply estimate the power spectrum of the reconstructed initial field. This is well known in the linear case, for instance in Wiener filter reconstruction the reconstructed power is suppressed on noise dominated scales. This calibration and reconstruction of the linear band powers is non-trivial because in addition to marginalizing over all the latent initial modes, it also requires handling various forward model and nuisance parameters that affect the band powers. For example, here we have assumed that we can estimate the halo masses accurately but if that is not the

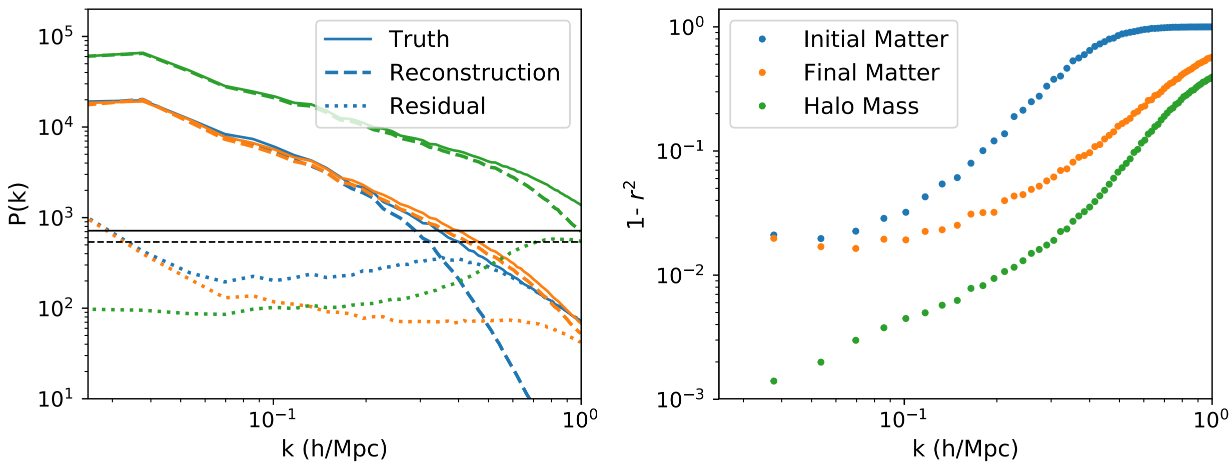


Figure 4.13: Left: Power spectrum of the true (t), reconstructed (r) and the residual (t-r) initial, final and halo mass fields for number density $\bar{n} = 10^{-3}(h\,\mathrm{Mpc}^{-1})^3$. The solid horizontal line is noise level in the position field ($\sigma_n/b_n^2$, where $b_n \sim 1.2$ is the bias of the halo position field and $\sigma_n = 1/\bar{n}$) and the dashed line is the noise level in the mass field ($\sigma_m/b_m^2$ where $b_m \sim 1.85$ is the bias of the mass-weighted ($w_i$) field and $\sigma_m = V \times (\sum w_i^2)/(\sum w_i)^2$) with $V$ being the volume. Right: Error power ($1 - r^2$, where $r$ is the cross-correlation coefficient of the reconstructed field with the truth) for the three fields.

case this uncertainty needs to be marginalized over. The noise in the observables and the scatter between the halo mass and galaxy light is another nuisance parameter that needs to be marginalized over: we know it is to some extent degenerate with the amplitude of the power spectrum since it changes the bias of the sample [258]. Moreover, the surveys live in redshift space and hence one needs to account for the redshift space distortions. An approach to reconstruct the band powers is proposed in [211] by performing analytic marginalization of the modes around the MAP. Handling this in full detail is beyond the scope of this work and we will pursue it in the future.

## Impact of the loss function

It is important to understand how the various assumptions that we have made regarding the loss function affect our reconstruction of the MAP. Specifically, we wish to estimate how sensitive we are to the choices we have made regarding the noise covariance $\sigma_N$, the offset $\mu$ and the free parameter $M_0$ in the loss function. For this purpose, we will focus on the reconstruction with number density of $\bar{n} = 10^{-3}(h\,\mathrm{Mpc}^{-1})^3$ in the $400\,\mathrm{Mpc/h}$ box. Our fiducial loss function, for which we presented results in the previous section has the parameters $\mu(M)$ (mass dependent offset), constant noise $\sigma_N^2 = 0.25$ and $M_0 = 10^{11} M_\odot/\mathrm{h}$ at the considered final iteration.

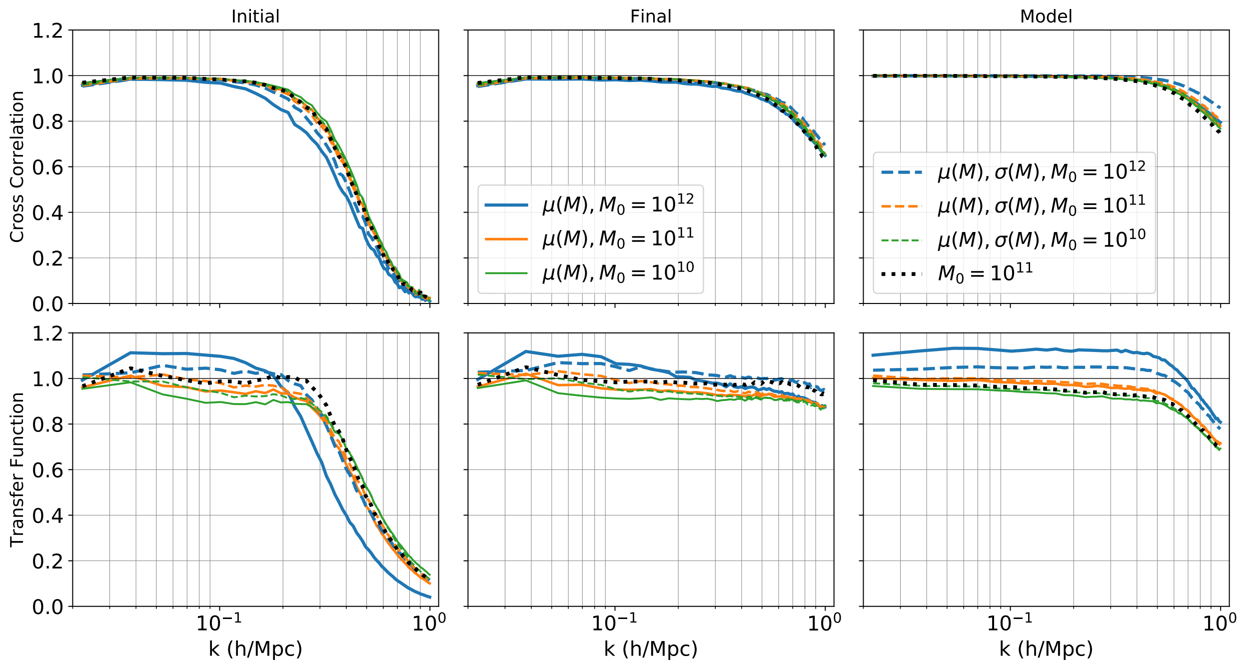


Figure 4.14: Transfer function and cross-correlation between the reconstructed fields and the truth for different parameter choices in the loss function, Eq. 4.14. $\mu(M)$ corresponds to the non-zero offset in the loss-function as estimated from error histograms. $\sigma(M)$ implies use of mass-dependent noise instead of the constant noise as estimated from error histograms. The dotted black line corresponds to the loss function without the offset and constant noise.

Figure 4.14 shows the cross-correlation and transfer function for different choices of the parameters in the loss function. The most direct difference in the performance comes due to the parameter $M_0$. In the previous section, we have advocated beginning with $M_0 = 10^{12} M_\odot/\mathrm{h}$ and reducing it to $M_0 = 10^{11} M_\odot/\mathrm{h}$. For the constant noise model used there, the improvement in cross-correlation of initial fields is significant upon reducing $M_0$ from $10^{12} M_\odot/\mathrm{h}$ to $10^{11} M_\odot/\mathrm{h}$, with the fields correlated to more than 95% upto $k = 0.13,\ 0.18\, h\,\mathrm{Mpc}^{-1}$ respectively. Lowering $M_0$ to $10^{10} M_\odot/\mathrm{h}$ improves this to $k = 0.196\, h\,\mathrm{Mpc}^{-1}$ but at a greater computational cost. Interestingly, at the level of the transfer functions, while we lose power on intermediate scales upon decreasing $M_0$ to $10^{10} M_\odot/\mathrm{h}$, we gain marginal power on small scales. This is likely due to an increased contribution to the loss function from the small mass halos which drive the small scale power and reduce the overall bias. This increased response might become more important when calibrating band-powers allowing us to push to smaller scales, and we plan to investigate this in the future.

To handle the correlations in the noise, we have chosen a higher constant noise of $\sigma_N^2 = 0.25$ at all points. Using this noise in comparison to that predicted by the noise histogram reduces the effective number of points contributing to the loss function residual and up-weighs prior. The amount of this down-weighting depends on the value of $M_0$. For $M_0 = 10^{12}, 10^{11}, 10^{10} M_{\odot}/\mathrm{h}$, using this amplitude of the constant noise, reduces the effective number of points by a factor of $\sim 16, 6, 3$, respectively. As compared to constant noise case, upon using the mass-dependent noise, the cross correlation improves significantly for $M_0 = 10^{12} M_{\odot}/\mathrm{h}$ but stays the same for $M_0 = 10^{11} M_{\odot}/\mathrm{h}$, while for $M_0 = 10^{10} M_{\odot}/\mathrm{h}$, it does not improve over $M_0 = 10^{11} M_{\odot}/\mathrm{h}$ i.e. 95% correlation is at the same $k = 0.18\, h\,\mathrm{Mpc}^{-1}$ (unlike $k = 0.196\, h\,\mathrm{Mpc}^{-1}$ for constant noise). Moreover, the higher constant noise case converged to the chosen tolerance in $\sim 200$ iterations, while the mass dependent noise took around $\sim 600$ iterations. Thus it seems like we have over-penalized the $M_0 = 10^{12} M_{\odot}/\mathrm{h}$ case with our noise amplitude, but we are adequately handling the $M_0 = 10^{11}$ & $10^{10} M_{\odot}/\mathrm{h}$ loss functions. At this level, we also seem to be somewhat insensitive to the actual value of the error at the position of the halos. One explanation for this is that the noise due to the discreteness of the tracers dominates over the error made in predicting mass. On the same note, changing the amplitude of the noise does not degrade the performance at the level of the cross-correlation as long as we do not over-penalize by reducing the effective number of points by a lot (more than a factor of $\sim 10$). Increasing $\sigma_N$ does slightly decreases the transfer function since it effectively up-weighs the prior, but this still needs to be calibrated out in all cases.

Lastly, to compare the effect of the offset, we perform a reconstruction without it and using the same constant noise as the fiducial case. This reconstruction is shown in the dotted-black line in Figure 4.14. The inclusion or exclusion of the offset does not seem to affect cross-correlation. It might seem like removing offset gives transfer function of unity on large scales, but this case here is a coincidence. Repeating the exercise for other number densities confirms that not including the offset generally gives higher transfer function than when including it, but not necessarily unity. However we prefer to include non-zero offset since preliminary results show that it will become more important when we add signal noise to the halo masses of the data.

Overall, we find that our reconstruction is most sensitive to $M_0$ with most of the information being reconstructed by $M_0 = 10^{11} M_{\odot}/\mathrm{h}$ for the number densities studied in this paper, and marginal improvements on small scales after that. Cross-correlation seems to be quite robust against the choice of various other parameters of the loss function. The transfer function is more sensitive to this choice since the parameters mainly serve to change the balance between the residual and the prior, or the amplitude of the matter density fields that is regressed over to give the halo mass (via offset). However note that these things generally shift the transfer function up or down as a whole, with almost no change in the scale dependence. As discussed, since none of these cases result in a response that is unity, we need to calibrate band-powers anyways. Thus we expect that this sensitivity of the transfer function on the parameters of the loss function will automatically be handled during the band-power calibration.

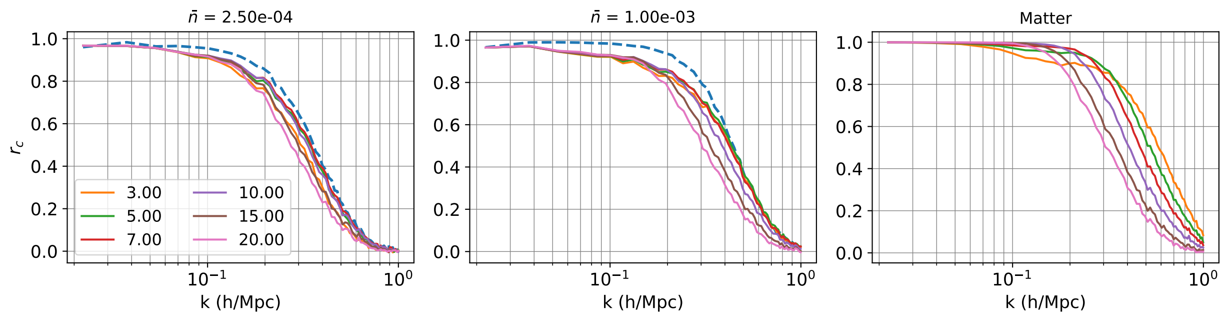


Figure 4.15: Performance of standard reconstruction when done with matter and halos of different number densities for different smoothing scales

## 4.6 BAO Information

In this section, we compare our reconstruction against standard reconstruction [73]. However before doing so, it is important to note that the objective of standard reconstruction is to maximize signal to noise for baryon acoustic oscillations (BAO) and it does not focus on the reconstructing the initial density field map or broadband power. On the other hand, our goal is to reconstruct the linear density map and via that, reconstruct the linear power spectrum to extract cosmological parameters. Nevertheless, at this stage we choose to compare against the standard reconstruction since it is the most widely used method of reconstruction and we leave the band power reconstruction for future work. Given the differences in the goal of standard and our reconstruction, we will compare the two reconstructions using metrics of the former. We are interested in estimating and comparing the linear BAO information reconstructed in the fields and then using to estimate the fractional error in identifying the location of the baryonic peak using both the methods. We use Fisher formalism for this estimation since our box size is insufficient to recover BAO signal due to the cosmic variance.

To recall, we work in a box of L $= 400\,\mathrm{Mpc/h}$ on a $128^3$ grid and use the halo catalogs with number density $2.5 \times 10^{-4}(\,h\,\mathrm{Mpc}^{-1})^3$ and $10^{-3}(\,h\,\mathrm{Mpc}^{-1})^3$ as our data. Standard reconstruction involves estimating the displacement field using the halo overdensity field. To suppress small-scale non-linearities where linear theory is not valid, we smooth the halo overdensity field with a Gaussian smoothing kernel $S(k) = e^{-k^2\Sigma_{sm}^2/4}$. The performance of standard reconstruction depends on the choice of the smoothing scale. Larger smoothing scales are more optimal for lower number densities which are noise dominated on smaller scales (Figure 4.15), but smaller smoothing scales reconstruct more information. We choose $\Sigma_{sm} = 10\,\mathrm{Mpc/h}$ for $\bar{n} = 2.5 \times 10^{-4}(\,h\,\mathrm{Mpc}^{-1})^3$ and $\Sigma_{sm} = 7\,\mathrm{Mpc/h}$ for $\bar{n} = 1 \times 10^{-3}(\,h\,\mathrm{Mpc}^{-1})^3$. We show the cross-correlation coefficient for both, our NN reconstruction and the standard reconstruction with the true linear density field in the left panel of Figure 4.16. Our reconstruction outperforms the standard reconstruction on all scales, with the two fields being 90% correlated respectively up to $k = 0.25\,h\,\mathrm{Mpc}^{-1}$ and $0.12\,h\,\mathrm{Mpc}^{-1}$,

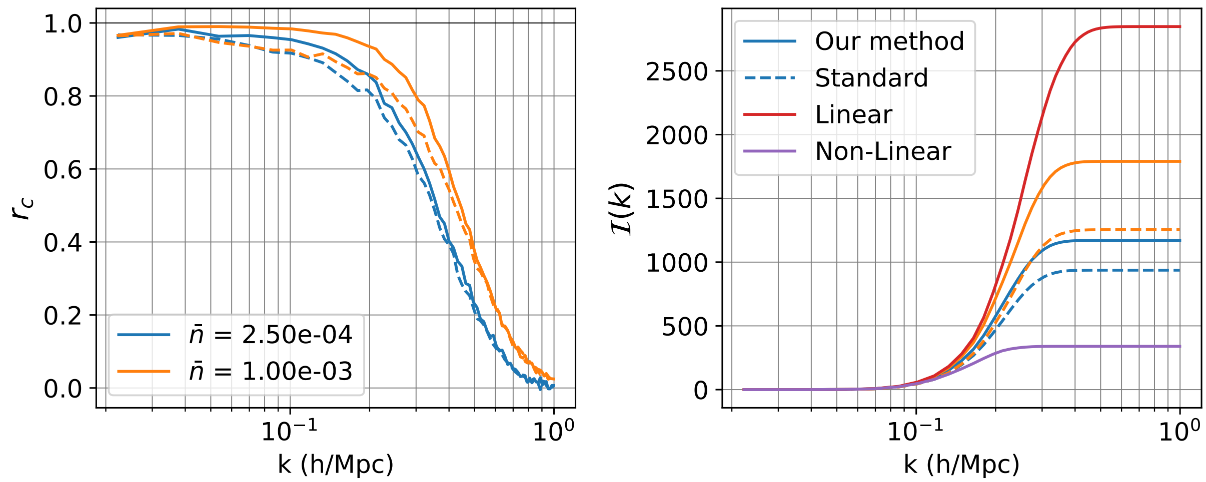


Figure 4.16: Left: Cross correlation coefficient of reconstructed fields from standard reconstruction (dashed) and our reconstruction (solids) with the true initial field when done from data with two different number densities. Right: Cumulative Fisher information to estimate the BAO peak as a function of scale for each case as calculated with Eq. 4.19. For comparison, we also show the same Fisher information for linear matter field (theoretical maximum) and the non-linear matter field.

for number density $\bar{n} = 1 \times 10^{-3}(\,h\,\mathrm{Mpc}^{-1})^3$ and $k = 0.16\,h\,\mathrm{Mpc}^{-1}$ and $0.11\,h\,\mathrm{Mpc}^{-1}$ for $\bar{n} = 2.5 \times 10^{-4}(\,h\,\mathrm{Mpc}^{-1})^3$.

In BAO community, the linear signal to noise in the reconstructed field is measured in terms of propagator [216, 214, 259], defined as

$$G(k) = \frac{\langle \delta_f \delta_{\rm lin} \rangle}{b\,\langle \delta_{\rm lin} \delta_{\rm lin} \rangle} \tag{4.15}$$

where $\delta_f$ is any field whose propagator we wish to evaluate (so it is the reconstructed fields in our case); $b$ is the linear bias of the tracer field (we set $b = 1$ for the NN reconstructed field since the bias is effectively modeled by our model of halo field i.e. the neural networks) and $\delta_{\rm lin}$ is the initial (linear) field. The propagator effectively estimates the projection of the field ($\delta_f$) on the linear density field $\delta_{\rm lin}$ [216]. Then, the linear signal power in the reconstructed field is simply $b^2 G^2(k) P_{\rm lin}$. The residual power not captured in the linear signal constitutes the noise term, otherwise referred to as the mode coupling term. Thus this mode-coupling term $P_{\rm MC}$ is such that

$$P_{\delta_f} = b^2 G^2(k) P_{\rm lin} + P_{\rm MC} \tag{4.16}$$

Therefore, assuming a log-normal error, the signal to noise ratio for the linear information in the reconstructed field relative to the linear density field is

$$\frac{S}{N} = \frac{b^2 G^2(k) P_{\rm lin}}{b^2 G^2(k) P_{\rm lin} + P_{\rm MC}} = r_c^2 \tag{4.17}$$

where $r_c$ is the cross correlation coefficient of the field with the linear field.

Given the propagator, we can also estimate the error in locating the BAO peak in the reconstructed signal by doing a simple Fisher analysis. For this, we follow the procedure presented in [212]. Briefly, assuming Gaussian likelihood for band powers of power spectrum, the Fisher matrix is approximately [232],

$$F_{ij} = V_{\rm eff} \int_{k_{min}}^{k_{max}} \frac{\partial \ln P(k)}{\partial p_i} \frac{\partial \ln P(k)}{\partial p_j} \frac{4\pi k^2}{2(2\pi)^3} dk \tag{4.18}$$

where we have integrated over the angles assuming isotropy, $p_i, p_j$ are the parameters of interest and $V_{eff}$ is the effective survey volume. The parameter of interest is the location of the centroid of the BAO peak and it corresponds to the sound horizon '$s_0$' at the drag epoch. This is only sensitive to the baryonic component of the power spectrum. BAO peak is damped due to the Silk damping and non-linear evolution and the information lost in the latter damping is modeled well with a Gaussian damping model ([170]) in theory and the propagator defined above in practice. Reconstruction aims at undoing this non-linear damping and its success is measured by using the propagator estimated for the reconstructed field. Modeling the sensitivity of the power spectrum to sound horizon in this way leads to the Fisher error given by (for full derivation, see [212, 214])

$$F_{\ln s_0} = V_{\rm survey} A_0^2 \int_{k_{min}}^{k_{max}} \frac{e^{-2(k\Sigma_s)^{1.4}} G^4(k)}{(P(k)/P_{0.2})^2} k^2 dk = \left(\frac{s_0}{\sigma_{s_0}}\right)^2 \tag{4.19}$$

where $A_0 = 0.4529$ for WMAP1 cosmology, $\Sigma_s \sim 7.76\, h\,{\rm Mpc}^{-1}$ is the Silk damping scale and $P_{0.2}$ is the linear power spectrum at $k = 0.2\, h\,{\rm Mpc}^{-1}$. While WMAP1 is not the cosmology of our simulations, our goal here is simply to broadly compare our reconstruction with the standard reconstruction and not to do an accurate Fisher forecast, hence any reasonable value of these parameters should suffice.

We show this Fisher information as the function of scale in right panel of Figure 4.16 for the standard reconstruction, and our method for two number densities. For comparison, we also show the Fisher information in the linear and the non-linear matter field which roughly correspond to the maximum and minimum (for matter) information bounds. As expected, at increasing number densities, the standard reconstruction becomes increasingly sub-optimal and we gain 33% and 45% more information at $\bar{n} = 2.5 \times 10^{-4} (\, h\,{\rm Mpc}^{-1})^3$ and $\bar{n} = 10^{-3} (\, h\,{\rm Mpc}^{-1})^3$ number densities. In effect, we gain as much by using an optimal reconstruction as we do by increasing the number density from $\bar{n} = 2.5 \times 10^{-4} (\, h\,{\rm Mpc}^{-1})^3$ by a factor of 4. We find that for this volume the fractional error in locating the peak of the BAO from non-linear field (i.e. estimated using the propagator for the final matter field) is $\sigma_{s_0}/s_0 \sim 5.4\%$. By undoing the non-linear evolution, this is reduced to $\sigma_{s_0}/s_0 \sim 3.4\%$ (standard) and $\sigma_{s_0}/s_0 \sim 2.9\%$ (our method) for $\bar{n} = 2.5 \times 10^{-4} (\, h\,{\rm Mpc}^{-1})^3$ and $\sigma_{s_0}/s_0 \sim 2.9\%$

(standard) and $\sigma_{s_0}/s_0 \sim 2.3\%$ (our method) for $\bar{n} = 10^{-3}(h\,\mathrm{Mpc}^{-1})^3$, respectively. Thus our reconstruction method shrinks the error on the location of the peak of BAO by about $\sim 15-20\%$ over the standard reconstruction. However for completeness, it should be noted that this only a Fisher prediction for halos in real space, at $z = 0$, and we have assumed that we have the information of halo masses accurately. Thus while the improvement is quite encouraging, we plan to address a more realistic case of galaxies in redshift space in the future.

## 4.7 Conclusions and Discussion

In this paper we address the question of how to model a discrete set of measured galaxy positions and their masses and represent them in a form that is suitable to be used for reconstruction of the initial density field using gradient based optimization methods. We simplify the problem and look at the dark matter halo centers as a proxy for the galaxy position and dark matter halo mass as a proxy for the galaxy stellar mass or luminosity. We also work in real space instead of redshift space where the actual survey data lives. Discrete objects are problematic for gradient based methods and halos are typically defined in an N-body simulation using non-differentiable methods such as Friends-of-Friends. Since our goal is to find a suitable differentiable forward model, we propose a neural network solution that represents halo properties (position and mass) with a set of NN coefficients and activation functions that take in dark matter properties as the input and output quantities such as the probability of finding a halo at a given position and the halo mass (Figure 4.1). Since NN are explicitly differentiable, once they are trained they can be used as part of the forward model of LSS that starts from the linear density modes, evolves them using nonlinear N-body simulation (in our case `FastPM` [83]) and ends with the predicted galaxy positions and masses.

We gauge the performance of our forward model of two neural networks in modeling the halo mass and position field on various metrics (section 4.4). We are able to reduce the stochasticity in halo positions over the Poisson shot noise by at least a factor of two and find good cross correlation coefficient up to small scales (Figure 4.8). This suggests that the forward model can be used to generate mock galaxy catalogs, but in this paper we are more interested in using it to reconstruct the initial density field given the data and leave investigating other applications for the future. To do the reconstruction, one must also define a loss function which takes into account the error probability distribution of the data given the model. For this, we adopt a simple displaced log-normal model, which seems to reproduce the error PDF well (Figure 4.7). Since our model localizes the neighborhood of halos quite well, estimating this error on smoothed mass fields results in white noise spectrum for error. Even though we expect our noise to be correlated on small scales, especially around halo positions, we assume diagonal noise in configuration space and address these correlations by changing the effective number of points contributing to the likelihood, thus altering the relative weighting of the residual and the prior term in the noise model.

Using this data noise model (Eq. 4.13) and Gaussian prior for the modes we are able to do reconstruction of initial density field starting from halo mass field by optimizing the loss function of Eq. 4.14 using L-BFGS algorithm. Due to the discrete nature of the data we develop several annealing methods where we typically gradually change the loss function with number of iterations to increase the resolution from coarse to fine, which help nudge the solution towards its final result. These are motivated by the domain knowledge of the distribution of our data, performance of our model as well as non-linearities generated by the cosmological evolution. This results in a significant speed up and improves the convergence of our optimizer. Specifically, we force the optimizer to fit for the large scales and the massive halos before gradually reducing the scale to fit for smaller scales and smaller halos. We also change the discreteness of the halo field to get better gradients when far from the truth, gradually making it sharper and sharper. With about $\sim 200$ iterations we reconstruct the initial density field that is more than 95% correlated to the true field up to $k = 0.12,\ 0.16,\ 0.18\ h\,\mathrm{Mpc}^{-1}$ for $\bar{n} = 2.5 \times 10^{-4},\ 5 \times 10^{-4}\ \&\ 10^{-3}(h\,\mathrm{Mpc}^{-1})^3$, respectively. (Figure 4.11). Due to the non-linear mode coupling introduced by gravitational evolution, the reconstructed final matter field has better cross-correlation on smaller scales with $r_c$ dropping to 0.95 at $k = 0.23,\ 0.32,\ 0.42\ h\,\mathrm{Mpc}^{-1}$ for the three number densities, respectively. As a result of the reconstruction of small scale power, we are able to identify cosmic web along with all the structures like nodes, voids and filaments in this field (Figure 4.9).

Using simulations with different initial conditions (phases) and different cosmology ($\sigma_8$), we also verify that our model and procedure is independent of realization and cosmology. We do a case-study to establish how our reconstruction depends on the choice of each parameter that enters the loss function (Figure 4.14). We reconstruct most of the scales by $M_0 = 10^{11} M_\odot/\mathrm{h}$ and decreasing $M_0$ further changes small scales only slightly. The cross-correlation coefficient of the reconstructed initial field is fairly robust against the values of the offset ($\mu$) and the noise ($\sigma_N$). Moreover, for $M_0 = 10^{11} M_\odot/\mathrm{h}$ and lower, using a constant, but higher value of noise, handles the noise covariances adequately. The transfer function seems to be more sensitive to the choices of these parameters, but only in amplitude and not in the scale dependence. Thus we expect to be able to marginalize over these dependencies when calibrating the transfer function to reconstruct the band powers and extracting cosmological parameters, but we leave this for the future. Using our fiducial loss function for reconstruction, we also show that we are able to improve upon standard reconstructions in terms of linear information and localization of BAO peak (Figure 4.16). We expect our method should be close to the optimal BAO reconstruction for finite number density of tracers.

The ultimate goal of our exercise is to construct a tractable summary statistic from which all of the cosmological information can be extracted. For linear modes such statistic is the band powers of the power spectrum, and by linearizing the mode evolution we expect we can achieve the same by using the reconstructed initial density modes to reconstruct the linear band powers. This is not trivial given that the transfer function for reconstructed field is not unity on all scales. We leave this calibration for the upcoming work. In addition to marginalizing over the latent initial modes, reconstructing band powers also requires that the nuisance parameters of our forward model and data are marginalized over. For instance, noise in the halo mass calibration and scatter in the halo mass-luminosity relation are both known to be correlated with the amplitude of the power spectrum $\sigma_8$ [258]. Thus, a full analysis to obtain cosmological parameters must also include a proper marginalization over the nuisance parameters of galaxy formation models.

This paper shows that one can build a realistic and differentiable halo field from the dark matter density alone, and that loss functions can be defined that give realistic penalty loss when applying such models to the data. To make our modeling more realistic and applicable to the real LSS survey data we must do several additional steps. First, we must include additional nuisance parameters such as the satellite distribution inside the halos etc., similar to the traditional HOD models [24]. Furthermore, we must also include the redshift space distortions by adding velocity to the halo position and map it to the redshift space. This will require deriving the gradient of the final velocity with respect to the initial modes. Redshift space distortions will not only modify the forward model but will also change the loss function: in particular, the velocity dispersion of the satellites will need to be modeled as an additional noise term in the radial direction, since it is unlikely that we can forward model it. Finally, we must also include survey mask effects and various galaxy selection effects for a complete forward model. We plan to pursue these issues in the future. The hope is that when a complete forward model is available, with a sufficient number of nuisance parameters to describe all the complications not included in the noise, then the inverse problem will be completely determined and an optimal analysis of cosmological parameters from the redshift space distortions data will be possible.

## Acknowledgments

CM would like to thank Vanessa Böhm, Yin Li, Patrick McDonald, Ambrish Rawat and Michael Wilson for useful discussions. We would also like to thank Vanessa Böhm, Yin Li, Matias Zaldarriaga and Hong-Ming Zhu for comments on the manuscript. This research used resources of the National Energy Research Scientific Computing Center, a DOE Office of Science User Facility supported by the Office of Science of the U.S. Department of Energy under Contract No. DE-AC02-05CH11231. We acknowledge support of NASA grant NNX15AL17G.

# Chapter 5

# Reconstructing large-scale structure with neutral hydrogen surveys

The contents of this chapter were originally published in

Reconstructing large-scale structure with neutral hydrogen surveys
*Modi C., White M., Slosar A., Castorina E. (arXiv:1907.02330)* JCAP 11(2019)023

Intensity mapping with neutral hydrogen and the Hidden Valley simulations
*Modi C., Feng Y., White M., Castorina E. (arXiv:1904.11923)* JCAP 09(2019)024

In this chapter, we turn towards 21-cm intensity mapping to adopt a different perspective on the reconstruction of cosmological fields. Upcoming 21-cm intensity surveys will use the hyperfine transition in emission to map out neutral hydrogen in large volumes of the universe. Unfortunately, large spatial scales of these maps are completely contaminated with spectrally smooth astrophysical foregrounds which are orders of magnitude brighter than the signal. This contamination also leaks into smaller radial and angular modes to form a foreground wedge, further limiting the usefulness of 21-cm observations for different science cases, especially cross-correlations with tracers that have wide kernels in the radial direction. Here we use the reconstruction framework built upon in the previous chapters to solve a denoising problem that reconstructs these lost modes in the observed data and study its implications on the cosmology with 21-cm. In developing this, we also address another challenge to 21-cm cosmology - that of simulating this signal in the largest possible volume while simultaneously maintaining high enough mass resolution to resolve 21-cm signal hosted in low-mass dark matter halos completely. To this end we present Hidden Valley Simulations, which is a series of large N-body simulations evolving $10240^3$ particles in a $1\,h^{-1}$Gpc volume to model the signals relevant to intensity mapping surveys.

## 5.1 Introduction

The coming decade will see transformative dark energy science done by both ground-based surveys (DESI [68], LSST [138]) and space-based missions (Euclid [10], WFIRST [70]). We expect that large swaths of the universe will be sampled to close to the sample variance limit on very large scales using galaxies as tracers of density field as well as sources used to measure the weak gravitational lensing shear or cosmic backlights illuminating the cosmic hydrogen for Lyman-$\alpha$ forest studies. At the same time, these fields will offer a multitude of cross-correlation opportunities, through which more and more robust science will be derived.

Looking beyond the current decade, several experimental options are being considered that will allow us to continue on the path of mapping ever increasing volume of the Universe. Photometric experiments, such as LSST, will likely be systematics limited by the quality of the photometric redshifts. Spectroscopic instruments are more attractive, especially using LSST as the targetting survey, but will require major investments in a dedicated new telescope and more aggressive spectrograph multiplexing to be truly interesting when compared to DESI. Going at higher redshift, traditional galaxy spectroscopy in optical becomes ever more difficult, since the sources are sparser, fainter and further redshifted. On the other hand, turning to radio and relying on the 21-cm signal from neutral hydrogen could offer a cost-effective way of reaching deep sampling of the universe, especially in the redshifts range $2 \lesssim z \lesssim 6$, which remains largely unexplored on cosmological scales.

A number of upcoming (CHIME [19], HIRAX [165], Tianlai [50], SKA[4]) or planned (PUMA, the proposed Stage II experiment [55]) interferometric instruments will use the 21-cm signal to probe this volume of the universe. In the post-reionization era most of the hydrogen in the Universe is ionized, and the 21-cm signal comes from self-shielded regions largely within halos. Such 'intensity mapping' surveys therefore measure the unresolved emission from halos tracing the cosmic web in redshift space.

### Challenges in simulations

State-of-the art cosmological analyses of large-scale structure rely on high fidelity numerical simulations and on accurate analytical modeling of the expected signal, the former frequently being used to test the latter. The goal of sampling the largest possible volume while simultaneously maintaining high enough mass resolution to resolve the low-mass dark matter halos which host the majority of the neutral hydrogen makes simulating 21-cm signal quite challenging. At the same time the very large survey volumes and low noise levels expected in 21-cm measurements will require characterization of the theory to unprecedented levels.

In this chapter, we discuss a series of large, N-body simulations designed to model the signals relevant to intensity mapping surveys. Each simulation evolves $10240^3$ particles in a $1\,h^{-1}$Gpc volume, simultaneously providing large volumes for precise measurements while resolving the halos most relevant for intensity mapping surveys. This makes it possible to address several modeling issues with higher precision than has been possible to date and at the same time analyze the response of the observed signal to these modeling choices.

Our initial focus will be on modeling the 21-cm signal over the range $2 < z < 6$, using a halo model formalism. The halo model combines a large degree of astrophysical realism while maintaining a flexibility which is highly desirable in our current state of ignorance about the high-$z$, 21-cm signal. We will present several different models motivated by existing theoretical ideas and simulations and assess their commonalities and differences, with the expectation that these models will need to be revised as further observational information becomes available.

## Challenges in Analysis

The 21-cm observations also suffer from another fundamental problem, namely that it is completely insensitive to modes which vary slowly along the line of sight (that is low $k_{\parallel}$ modes), because these are perfectly degenerate with foregrounds which are orders of magnitude brighter that the signal [217, 218, 188, 38]. This effect alone severely limits the usefulness of 21-cm observations for cross-correlations with tracers that have wide kernels in the radial directions. This is in particular true for cross-correlations with the cosmic microwave background (CMB) lensing reconstructions and shear field measured by the photometric galaxy surveys, such as that coming from LSST. Cross-correlations with CMB would allow us to use the 21-cm observations and CMB observations in conjunction to put the strongest limits on modified gravity by measuring growth. Cross-correlations with spectroscopic galaxies would allow us to characterize the source redshift of galaxy samples used for weak-lensing measurements, one of the main optical weak lensing systematics. Moreover, the foreground wedge (discussed below) can render further regions of the $k$-space impotent for cosmological analysis [62, 160, 181, 217, 218, 136, 188, 213, 54, 38]. The foreground wedge is not as fundamental as the low $k_{\parallel}$ foreground contamination, because it only results as a consequence of an imperfect instrument calibration rather than being a fundamental astrophysical bane. Nevertheless, it is a data cut that will likely be necessary at least in the first iterations of data analysis from the upcoming surveys.

Can this lost information be recovered? The answer is yes, although the extend to which this is possible depends on both the resolution and noise properties of the instrument. Imagine the following thought experiment. At infinite resolution in real space (and ignoring the thermal broadening of the signal for the moment), the underlying radio intensity is composed of individual objects, that appear as distinct peaks. A high pass filter in $k$ space will not fundamentally alter one's ability to count these objects. While the filtering might introduce 'wings' in individual profiles, the peaks in the density fields are still there. In this case, we can recover the lost large-scale modes perfectly. A somewhat different way to look at the same physics is to realize that the non-linear mode coupling propagates information from large-scale to small-scale modes, while the initial conditions of the small-scale modes are forgotten. Since the total number of modes scales as $k^2\,\delta k$, there are always many more small-scale modes than large-scale modes and in a sense the system is over-constrained if one wants to recover large-scale modes for which there is no direct measurements. Non-linear evolution erases the primordial phase information on small scales and encodes the primoridal large-scale field over the entire $k$-space volume. So it is clear that the process of backing out the large-scale information from the small scale is possible, at least in the limit of sufficiently low noise and sufficiently high resolution.

In this chapter, we approach this problem by means of forward modelling the final density field as developed in the previous chapters. Starting with an initial density field and a suitable bias parameterization, we reformulate the problem of recovering the large scales as a problem of non-linear inversion. In the past few years, several reconstruction methods have been developed to solve this [120, 211, 207, 156, 203, 206]. The solution of this non-linear problem is the linear, 3D field that evolves under the given forward model to result in observed final field. Thus one not only recovers the linear large scales where the information was gone, but also automatically performs an optimal reconstruction of the linear field *on scales where we had non-linear information to start with*. This is often the product that one ultimately desires. It allows not only optimal BAO measurement for the 21-cm survey, but also increases the scale over which one can model cross-correlations with other tracers, thus enabling cross-correlations with CMB lensing reconstruction and photometric galaxy samples.

The full implications of this reconstruction exceed the scope of this chapter. Instead we focus on the basic questions: i) Does the forward modeling approach to reconstruction work at all in the case where we loose linear modes to foregrounds? ii) What is the complexity of forward model required? iii) How does the result depend on the noise and angular resolution of the experiment? iv) How does the performance vary with scale, direction, redshift and real vs. redshift space data? v) What are the gains one expects for different science objectives such as BAO reconstruction, cross-correlations with CMB and cross-correlations with different LSS surveys such as LSST.

The outline of the chapter is as follows. We begin by discussing the simualtion requirements and observational constraints we are likely to face in Section 5.2. Then we discuss the Hidden Valley Simulation suite in Section 5.3 and different semi-analytic and halo based models we use to populate the simulated halos with HI as well as their calibration in Section 5.4. We then use these models to look at the clustering of HI in real- and redshift space in Section 5.5, with separate focus on redshift space distortions to the clustering and baryon acoustic oscillations. This section also presents a preliminary comparison with perturbative, analytic models. With this simulation suite at hand, we finally turn to the problem of reconstruction of large scale modes. We review our forward model and the method we use to reconstruct the field from the observations in Section 5.6 (building upon previous two chapters and refs. [211, 156]). In Section 5.7 we show the results for our forward model on the 'observed' 21-cm data, as well as gauge the performance of our reconstruction algorithm on different metrics for multiple experimental setups. In Section 5.8 we show the improvements expected by using our reconstructed field for different science objectives such as BAO reconstruction, photometric redshift estimation and CMB cross correlations. We conclude in Section 5.9.

## 5.2 Setting the Stage

We begin by discussing the physical and observational constraints that drive the requirements on the numerical simulation suite and reconstruction analysis. We start with a discussion of the required mass resolution (set by ideas about how HI inhabits dark matter halos) and then turn to the epochs and length scales that will be probed by proposed experiments as well as the relevant signal to noise on those scales that can be exploited for reconstruction.

### Mass resolution: the HI-halo connection

In the post-reionization era most of the hydrogen in the Universe is ionized, and the 21-cm signal comes from self-shielded regions such as galaxies (between the outskirts of disks until where the gas becomes molecular within star-forming regions). Unfortunately, there are not many observational constraints on the manner in which HI traces galaxies and halos in the high-$z$ Universe, so we are forced to rely on numerical simulations [64, 194, 237] and inferences from other observations [177, 42].

Both physical intuition and numerical simulations suggest that there is a minimum halo mass ($M_{\rm cut}$) below which neutral hydrogen will not be self-shielded from UV photons. Above this mass the amount of HI should increase as the halo mass increases, though not necessarily linearly. A reasonable model of the distribution of HI in halos is thus [176, 42]

$$M_{HI}(M_h; z) = A(z)(M_h/M_{\rm cut})^{\alpha(z)} e^{-M_{\rm cut}(z)/M_h} \tag{5.1}$$

where we have explicitly written the redshift dependence of the model parameters. The normalization constant can be fixed by matching the global HI abundance (see below). Simulations suggest $\alpha \approx 1$ at $z > 2$. The characteristic halo mass scale ($M_{\rm cut}$) is determined by the clustering of HI. At $z \simeq 0$ the HOD parameters are known from a joint analysis of HI-selected galaxies and groups in the Sloan Digital Sky Survey [174]. At $z \simeq 1$ this number is known approximately from cross-correlation with optical galaxies [144, 226, 12], however at higher $z$ there are no direct measurements. The clustering of Damped Lyman$\alpha$ systems (DLAs) has been measured at $z \simeq 2-3$ by ref. [184], and since the DLAs contain the majority of the HI at those redshifts this can be used as a proxy for the HI clustering amplitude. For the model in Eq. (5.1) the DLA measurement implies $M_{\rm cut} = \text{few} \times 10^9\, h^{-1} M_\odot$ if $\alpha \simeq 1$ [42]. These numbers agree with an analysis of the most recent hydrodynamical simulations (see Table 6 of ref. [237]). This requirement sets a particle mass resolution of about $10^8\, h^{-1} M_\odot$ or better in order to be able to resolve the majority of the HI.

### Observational constrains and relevant scales

The scope for the simulations, model and analysis has been set by considering the Stage II 21-cm experiment suggested by ref. [55], i.e. a compact, square array of $256 \times 256$, fully illuminated 6 m dishes observing half the sky with frequencies corresponding to $2 < z < 6$. We shall use this strawman proposal in order to motivate the range of scales our simulations

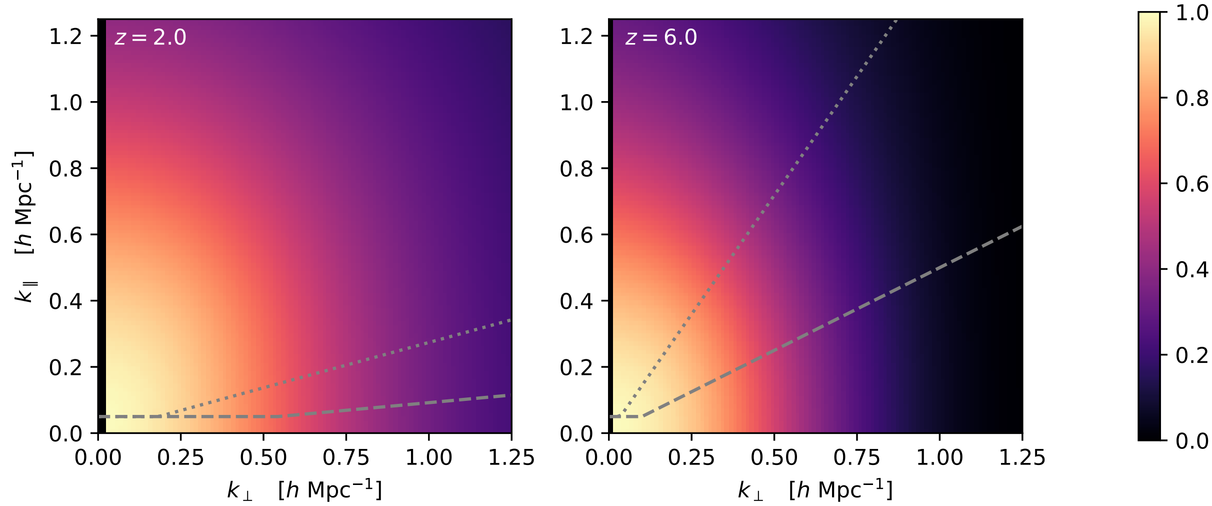


Figure 5.1: The region of $k_\perp - k_\parallel$ space well probed by the Stage II 21-cm experiment described in ref. [55]. The color scale shows $P_{\rm sig}/P_{\rm tot}$ at $z = 2$ (left) and $z = 6$ (right), including thermal noise and shot-noise appropriate to our fiducial model. Modes at very low $k_\perp$ are lost because dishes cannot be closer together than their diameters, imposing a minimum baseline length. Dashed lines show the foreground wedge assuming $k_\parallel^{\rm min} = 0.05\,h\,{\rm Mpc}^{-1}$ and the 'primary beam wedge' while the dotted line shows the equivalent cut for $3\times$ the primary beam (see ref. [49] for more information). Modes below and to the right of those lines become increasingly contaminated by foregrounds (see text).

should aim to resolve and the level of accuracy desired. At $z < 2.5$ the simulations could also be useful for CHIME and HIRAX, and at $z > 2$ for experiments targeting CO and/or C-II lines.

The Stage II experiment is an interferometer and as such it makes measurements directly in the Fourier domain. The correlation between every pair of feeds, $i$ and $j$, measures the Fourier transform of the sky emission times the primary beam at a wavenumber, $k_\perp = 2\pi\vec{u}_{ij}/\chi(z)$, set by the spacing of the two feeds in units of the observing wavelength ($\vec{u}_{ij}$) [233]. The visibility noise is inversely proportional to the number (density) of such baselines [260, 150, 216, 36, 213, 256, 8, 252, 172]. Where necessary, we take the noise parameters from Refs. [55, 49]. A defining feature of the Stage II experiment is that the total noise is dominated by shot noise at low $k$, in contrast with previous surveys that were thermal-noise dominated [54, 172, 19, 165, 50].

While the Stage II experiment has very low thermal noise, and as we shall see below the HI signal has intrinsically low shot-noise, it must still contend with bright foregrounds: primarily free-free and synchrotron emission from the Galaxy and unresolved point sources [93, 217, 188, 213, 54]. Radio foregrounds, primarily free-free and synchrotron emission from the Galaxy and unresolved point sources, are several orders of magnitude brighter than the signal of interest and present a major problem for 21-cm measurements [93, 217, 188]. However, due to their emission mechanisms, they are intrinsically very spectrally smooth and this is the property that allows them to be separated from the signal of interest which varies along the line of sight due to variation in underlying cosmic density field along the line of sight. This separation naturally becomes increasingly difficult as we seek to recover very low $k_\parallel$ modes, i.e. modes close to transverse to the line of sight. The precise value below which recovery becomes impossible is currently unknown (see Refs. [217, 218, 188, 38] for a range of opinions). To be conservative, for reconstruction, we will assume that we lose all the modes below $k_\parallel = 0.03\,h\,\mathrm{Mpc}^{-1}$, however we will also study how sensitive are our results to this cut-off value.

In addition to low $k_\parallel$, non-idealities in the instrument lead to leakage of foreground information into higher $k_\parallel$ modes. This arises because, for a single baseline, a monochromatic source (i.e. a bright foreground) at non-zero path-length difference is perfectly degenerate with signal at zero path-length difference (i.e. zenith for transiting arrays) but appropriately non-flat spectrum, such as that arising from 21-cm fluctuations. This is usually phrased in terms of a foreground "wedge" which renders modes with low $k_\parallel/k_\perp$ unusable [62, 160, 181, 217, 218, 136, 188, 213, 54, 38].

$$\mathcal{R} \equiv \frac{\chi(z)\,H(z)}{c(1+z)} = \frac{E(z)}{1+z}\int_0^z \frac{dz'}{E(z')} \qquad \text{(spatially flat)} \tag{5.2}$$

where $\theta \approx \theta_{FOV}$.

Due to the variation of Hubble parameter with redshift the wedge becomes progressively larger at higher redshift. Information in this wedge is not irretrievably lost, because using multiple baselines can break the degeneracy, but it requires progressively better phase calibration the deeper into the wedge one pushes. The better the instrument can be calibrated and characterized the smaller the impact of the wedge. The most pessimistic wedge assumption is that all sources to the horizon contribute to the contamination – will we not consider this case as it makes a 21-cm survey largely ineffective for large-scale structure. The most optimistic assumption is that the wedge has been subtracted perfectly. We regard this as unrealistic. A middle-of-the-road assumption is that the wedge matters to an angle measured by primary field of view. We take our 'optimistic' choice to be the 'primary beam' wedge defined as $\theta_w = 1.22\lambda/2D_e$, where $D_e$ is the effective diameter of the dish after factoring in the aperture efficiency ($\eta_\alpha = 0.7$) and the factor of two in the denominator gives an approximate conversion between the first null of the Airy disk and its full Width at half maximum (FWHM). We shall contrast this with the 'pessimistic' case $\theta_w = 3 \times 1.22\lambda/2D_e$.

Fig. 5.1 shows this information in graphical form. The color scale shows the fraction of the total power which is signal, as a function of $k_\perp$ and $k_\parallel$. The modes lost to foregrounds are illustrated by the gray dashed and dotted lines assuming a fiducial $k_\parallel^{\min} = 0.05\,h\,\mathrm{Mpc}^{-1}$ and $\theta$ equal to the primary beam (i.e. field of view) or $3\times$ the primary beam. At $z = 2$ and low $k$ the signal dominates, at intermediate $k$ the shot-noise starts to become important and at high $k_\parallel$ the thermal noise from the instrument dominates. At $z = 6$ the thermal noise

| Run | $\Omega_M$ | $h$ | $\sigma_8$ | $\Omega_B$ | $n_s$ | Amplitude |
|---|---|---|---|---|---|---|
| HV10240/F | 0.309167 | 0.677 | 0.8222 | 0.04903 | 0.96824 | Fixed |
| HV10240/F+ | – | – | 0.8633 | – | – | Fixed |
| HV10240/F- | – | – | 0.7811 | – | – | Fixed |
| HV10240/R | – | – | 0.8222 | – | – | Rayleigh |
| HV2560/F | 0.309167 | 0.677 | 0.8222 | 0.04903 | 0.96824 | Fixed |
| HV2560/F+ | – | – | 0.8633 | – | – | Fixed |
| HV2560/F- | – | – | 0.7811 | – | – | Fixed |
| HV2560/R | – | – | 0.8222 | – | – | Rayleigh |

Table 5.1: The cosmological parameters used in the simulations. The number in the name of each simulation represents $N_{\rm part}^{1/3}$ and the box size, in $0.1\,h^{-1}$Mpc (comoving).

is a larger fraction of the total for all $k$, but the fraction of the total which is signal is also increased by the higher bias of the HI at high $z$.

To benefit from the wide range of linear and quasi-linear scales that will be probed with high fidelity, we need to simulate a large cosmological volume. Resolving $k \simeq 0.01 - 0.05\,h\,\text{Mpc}^{-1}$ well requires a box size of $1\,h^{-1}$Gpc or larger. However, in the spirit of intensity mapping, the inteferometer will not resolve individual dark matter halos or galaxies. This suggests that the detailed profiles and subhalo properties of dark matter halos are less likely to be important than their relation to the evolving cosmic web. For this reason we choose to set our force resolution by the requirement that halos be properly formed, not that their internal properties be resolved or that we can track substructures within them.

## 5.3 Hidden Valley simulation suite

As outlined above, the simulation requirements for this project are quite demanding, since we need to simultaneously resolve the small-mass halos in which the majority of the neutral hydrogen signal lives while covering a large cosmological volume to make precise predictions for the clustering statistics that will be exquisitely measured by future surveys. To meet this challenge we employed the FastPM code [86] to evolve $10240^3$ particles in a periodic, cubic volume of $1024\,h^{-1}$Mpc resulting in a mean inter-particle separation of $100\,h^{-1}$kpc (comoving) and a mass resolution of $8.58 \times 10^7\,h^{-1}M_\odot$. The code used a $20480^3$ mesh (i.e. force resolution factor $B = 2$) for the gravity calculation and took 35 time steps from $z = 99$ to $z = 2$. We simulated $\Lambda$CDM cosmologies with parameters close to the latest Planck results, as given in Table 5.1. The linear power spectrum[1] was computed using CAMB [135] at $z = 2$ and initial conditions were generated from this using second-order Lagrangian perturbation theory at $z = 99$. We saved halo catalogs and a 4% subset of the dark matter

[1]We provide the CAMB parameter file and matter power spectrum as part of the public data release.

particles at $z = 6$ to 2 every 0.5 in $z$. The subsampling ensures the shotnoise level in the particles is less than 1% of the non-linear power spectrum at $k = 1\,h\,\mathrm{Mpc}^{-1}$ at redshift $z \leq 6$. In addition to the large volume we also ran a smaller, $256h^{-1}$Mpc simulation with the same spatial resolution as the larger box. The smaller volume is used for development of the numerical model and software tools.

We ran several realizations which differed only in the construction of the initial conditions. The realizations have identical phases, but the amplitudes are drawn differently. Our primary focus in this work is the 'F' simulations, which we ran with initial conditions chosen such that $|\delta_k| = \sqrt{P(k)}$ with no scatter in order to reduce sampling variance (i.e. Fixed amplitude). This technique has been shown to produce unbiased estimates of a large variety of 2 point and 3 point statistics [13, 53]. The Hidden Valley simulation suite also contains three other amplitude settings: 'R', where the amplitude is sampled from a Rayleigh distribution, corresponding to Gaussian initial conditions, and two additional fixed amplitude simulations, 'F+' and 'F-' where the power spectrum amplitude is changed by $\pm 5\%$, corresponding to a change in the $\sigma_8$ parameter which we can use to assess sensitivity of our results to $\sigma_8$.

The majority of the HI in a halo lies in the central galaxy, however a fraction can be distributed to larger radii. If a non-negligible fraction of the HI moves with close to virial velocity within the halo, this can impact the observed redshift-space clustering through a finger-of-god effect. Unfortunately, the observational constraints on this distribution are almost non-existent and so we are forced to model the satellites with simple prescriptions (described below).

Fig. 5.2 shows the real-space distribution of dark matter and HI in the simulation at our central redshift, $z = 4$. Each panel in the first column shows a $10\,h^{-1}$Mpc thick slice of the matter or HI field. Moving from left to right the panels show successive zooms by a factor of 10, which highlights the high dynamic range of the simulation in mass and force resolution. The cosmic web is clearly visible in the left and middle panels, while the complex environment around massive halos at high $z$ is obvious in the right-most panels. Due to the paucity of HI in low mass halos, and the sub-linear scaling at higher mass, the low density regions are more empty in the HI than in the matter and the highest density regions have lower contrast. Overall the structure is more pronounced in the HI than in the matter, as the former has a high bias.

## 5.4 The HI model

There[2] is lot of uncertainty in how hot and cold gas inhabit halos at high $z$. This is further complicated by the lack of any direct observational evidence on the mass scales of relevance.

[2]This section differs from the published version in that the HI content in Model A and Model C is scaled up with $(1+z)^3$ and Model B with $(1+3)^3$. This does not change the clustering of HI or S/N of any signal evaluated in the later sections due to consistent change in definition on signal and noise. It only changes the amount of HI in a given halo and hence $\Omega_{HI}$. The corresponding figures (Fig. 5.3 and Fig. 5.5) and tables (Table 5.2) have been updated.

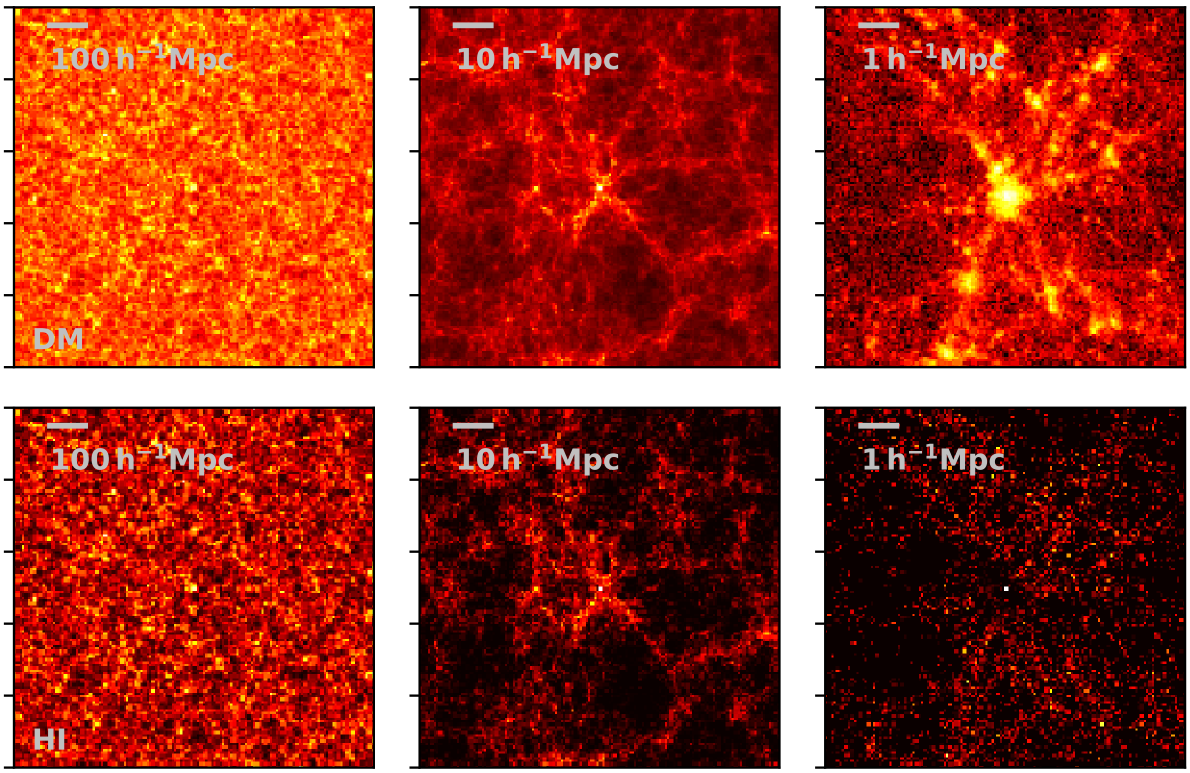


Figure 5.2: Slices through the simulation showing the projected dark matter (top) and HI (bottom) densities at our middle output, $z = 4$. The left panels show a $100\,h^{-1}$Mpc thick slice through the full simulation box, while the middle and right panels show successive zooms by a factor of 10, centered around the $5^{\text{th}}$ most massive halo in the simulation. The solid line in each panel indicates the linear scale while the color scale is log of the density. The HI clearly traces the large-scale structure seen in the matter.

Thus the flexibility of being able to alter the prescription for assigning HI to the halos as we build our mock catalog upon a dark matter simulation is highly desirable. In what follows we shall consider three methods for assigning HI to our halos and subhalos (generated by Monte Carlo as described as described below). Given the dearth of high redshift clustering observations, we will use the following two pieces of data to calibrate these models.

Our first calibration will be to the amount of neutral hydrogen at high $z$. We follow standard convention[3] and write the neutral hydrogen density as a fraction of critical at redshift $z$ as $\Omega_{HI}(z) = \rho_{HI}(z)/\rho_c(z)$. Existing constraints on $\Omega_{HI}$ are obtained by integrating the HI

[3] Some previous work (e.g. ref. [57, 42, 237]) introduced a related quantity where the density at $z$ is instead normalized by the present day critical density, $\Omega_{HI,0} \equiv \rho_{HI}(z)/\rho_{c,0}$. This differs by a factor of $\rho_c(z)/\rho_c(0) = E^2(z)/(1+z)^3$ from our definition.

column density distribution function inferred from QSO spectra. We take the compilation of $\Omega_{HI}$ from Table 5 of ref. [57], as shown in Fig. 5.3.

In order to fit for the characteristic mass scale and relative occupancy (e.g. $M_{\rm cut}$ and $\alpha$ in Eq. 5.1) we need some information about the clustering of the HI. Lacking such measurements in the redshift window of interest ($2 < z < 6$), we will use the clustering of Damped Lyman-$\alpha$ systems, which contain more than 90% of the neutral hydrogen in the Universe, as a proxy for the HI distribution. If the HI column density distribution is only weakly dependent on $M_h$, then $b_{DLA} \approx b_{HI}$ and we shall assume this is true for $z \simeq 2-3$ (there is support for this from the hydrodynamics simulation of ref. [237] and data [184]). The BOSS collaboration has measured $b_{\rm DLA} = 2.0 \pm 0.1$ in a broad bin centered at $z = 2.3$ [184]. As the clustering of DLAs is measured only at one redshift with sufficient accuracy, extrapolating the model in Eq. (5.1) requires some assumptions. We detail our fiducial model, and possible variants, below. Future data from high redshift QSOs in DESI [68], or direct measurement of the 21-cm signal, will be required to more accurately model $M_{HI}(M_h)$.

## Satellite model

We allow some of the HI in our halos to be hosted by satellites, in addition to centrals. As there is no observational data set with which to constrain the manner in which HI traces mass in satellite galaxies as a function of host halo mass and redshift, we shall opt for a simple model. Our simulation does not resolve halo substructure directly, so we add satellites in post-processing. We assume that the number of satellites is self-similar with [195, 14, 35]

$$N_{\rm sat}(> M_{\rm sat}) = \left(\frac{M_1}{M_{\rm sat}}\right)^{0.8} \qquad \text{with} \qquad 0.1\, M_{\rm cut} < M_{\rm sat} < 0.1\, M_h \tag{5.3}$$

where $M_1 = 0.03\, M_h$ corresponds roughly to the mass of the heaviest subhalo [14]. The slope of the HI-hosting subhalo mass function is not well known, but we have assumed it to be 0.8, slightly shallower than that of all satellites which is $\sim 0.9$ [14]. The lower mass limit of $0.1\, M_{\rm cut}$ is purely for convenience as lower mass subhalos are essentially free of HI. Since the rate of HI mass loss within subhalos is not well constrained, we opt to use an instantaneous assigned subhalo mass rather than attempting to correct for differential matter-HI mass loss.

Eq. 5.3 implies that the total number of subhalos more massive than $0.1\, M_{\rm cut}$ is $(M_1/0.1\, M_{\rm cut})^{0.8}$. We take this number of to be fixed and introduce stochasticity by randomly assigning masses to these satellites following Eq. 5.3. Each satellite is distributed within the halo following an NFW [164] profile with a concentration of 7 and given an additional line-of-sight velocity drawn from a Gaussian whose width equals the halo velocity disperion, $\sigma_h$. We use two velocity dispersions, one corresponding to matter (from [80]) and one with $\sigma_h$ reduced by two-thirds. The latter is motivated by Table 4 of [237] who find that the dispersion of HI is lower than that of matter. The details of the spatial distribution of subhalos significantly affects the clustering only on scales smaller than are of interest for proposed interferometric 21-cm experiments. The line-of-sight velocity affects the redshift-space power spectrum, leading to an additional damping of power at high $k_\parallel$.

| Model | Redshift | $10^3\Omega_{HI}$ | $b_1$ | $P_{sn}$ | $f_{\rm sat}$ |
|---|---|---|---|---|---|
| A | $z=2$ | 2.01 | 1.91 | 53.29 | 0.07 |
| | $z=3$ | 3.07 | 2.15 | 15.81 | 0.07 |
| | $z=4$ | 3.31 | 2.58 | 10.1 | 0.06 |
| | $z=5$ | 3.28 | 3.12 | 9.00 | 0.04 |
| | $z=6$ | 3.12 | 3.72 | 9.24 | 0.03 |
| B | $z=2$ | 5.17 | 1.79 | 40.42 | 0.03 |
| | $z=3$ | 3.20 | 2.45 | 42.44 | 0.02 |
| | $z=4$ | 1.83 | 3.10 | 42.93 | 0.02 |
| | $z=5$ | 0.96 | 3.72 | 43.62 | 0.01 |
| | $z=6$ | 0.51 | 4.33 | 43.6 | 0.01 |
| C | $z=2$ | 2.02 | 1.81 | 73.70 | – |
| | $z=3$ | 2.98 | 2.30 | 39.74 | – |
| | $z=4$ | 3.42 | 2.89 | 29.35 | – |
| | $z=5$ | 3.17 | 3.54 | 27.44 | – |
| | $z=6$ | 2.67 | 4.27 | 29.63 | – |

Table 5.2: Properties of the HI distribution in different models. The bias ($b_1$) is estimated from the (real-space) HI-matter cross-spectrum at low $k$. The shot noise $P_{\rm SN}$ is in $(h^{-1}{\rm Mpc})^3$. $f_{\rm sat}$ is the fraction of total HI that is in the satellites.

## Model A

Our first model, which we shall also use as a fiducial model for most of our plots, assigns HI to the halos using the $M_{HI} - M_h$ relation of Eq. (5.1). This HI is then distributed between the central and the satellite galaxies such that the total HI in galaxies adds up to that in the halo. Our primary motivation for this split is to include Finger of God (FOG) effects in the redshift-space power spectrum. To that end, assuming that all the HI in halos is associated with either centrals or satellites and ignoring the free HI content inside the halo not associated with any galaxy is a fair assumption [237].

The $M_{HI} - M_h$ relation we choose is motivated by the desire that the total HI content of a halo be given (at least approximately) by Eq. (5.1), as this has some support from recent numerical simulations. To calibrate this model, we are guided by Table 6 of ref. [237] and the data shown in Fig. 5.3. We take the parameters for this model to be

$$\alpha(z) = \frac{1+2z}{2+2z} \quad \text{and} \quad M_{\rm cut}(z) = 3\times 10^9\,h^{-1}M_\odot\,\left[1+10\left(\frac{3}{1+z}\right)^8\right] \tag{5.4}$$

valid only over the range $2 \le z \le 6$. The steep drop of $M_{\rm cut}$ with $z$ is required in order to flatten the increasing bias with $z$ at lower redshifts to better match the DLA data. To fit

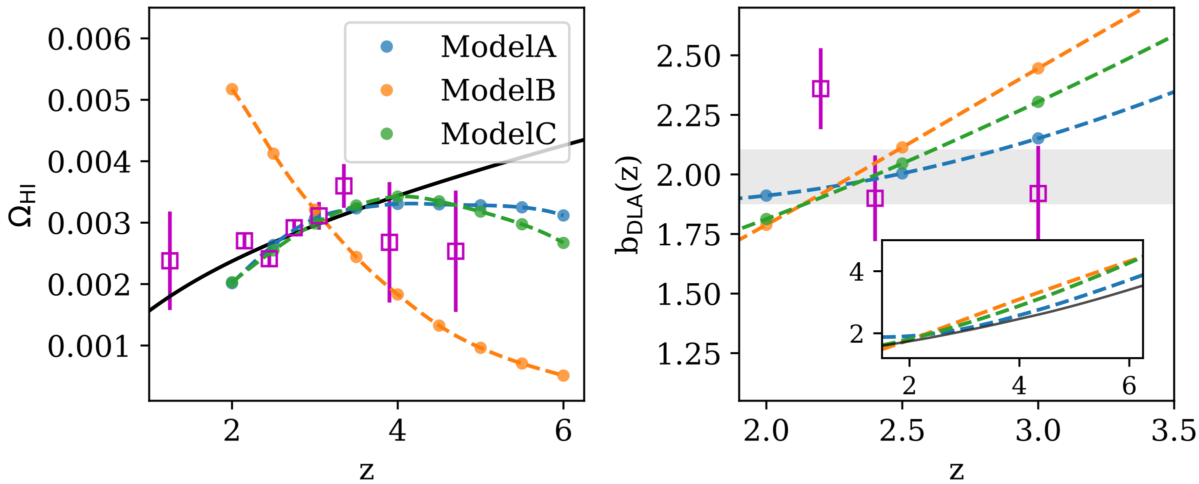


Figure 5.3: (Left) The neutral hydrogen density, in units of the critical density, as a function of $z$. The squares with error bars are from the compilation of ref. [57] (Table 5) and the line is their best fit. The circles show the results from our models. (Right) The bias of DLAs, which contain most of the HI in the high-$z$ Universe, at $z \simeq 2-3$. Squares with error bars are the measurements from ref. [184] while the circles and line show the predictions from our models. The horizontal grey band is the redshift-average value from ref. [184]. The inset shows the same bias prediction from our models up to $z = 6$. For comparison, we also show the bias for mass-weighted halo field with gray line in the inset.

the abundance of HI we set

$$A_h(z) = 8 \times 10^5 \, h^{-1} M_\odot \left[1 + \left(\frac{3.5}{z}\right)^6\right] \times (1+z)^3 \tag{5.5}$$

This leads to the predictions shown in Fig. 5.3 and Table 5.2, where we see relatively good agreement with the available data at high $z$. The parameters in Eq. 5.4 are slightly different than those in ref. [237]. The reason is that the hydrodynamical simulations in ref. [237], despite being in better agreement with the HI data than their predecessors, still underestimate both the measured $b_{DLA}$ (by $2\,\sigma$) and $\Omega_{\rm HI}$. In a halo based approach we have enough freedom to tune our parameters to better match the data.

Next we want to split this HI between centrals and satellites. We use the same relation for the satellites as for halos, albeit with a different normalization where we put more HI in satellites at the same (sub)halo mass and increasingly so with increasing redshift.

$$A_s(z) = A_h(z) \times (1.75 + 0.25\, z) \tag{5.6}$$

The centrals then take up the residual HI from the halos that is not assigned to satellites.

With our simple prescription, we are able to match the HI fraction in satellites observed by [237] in Illustris simulations.

We show the distribution of the HI for our model in halos of different mass and at different redshifts in Fig. 5.5. The top row shows the $M_{HI} - M_h$ relation as given by Eq. 5.1 for this model. The middle row shows the fraction of total HI that resides in the halos of a given mass. Towards highest halo masses the contribution decreases because of the exponential drop in the halo mass function, while at the lower end the HI hosted in the individual halos drops due to the cutoff (Eq. 5.4). Hence most of the signal contribution comes from halos of intermediate masses: $\sim 10^{11}\, h^{-1} M_\odot$ at $z = 2$ and decreasing to $\sim 10^{10}\, h^{-1} M_\odot$ at $z = 6$. This also illustrates the convergence of our simulations with respect to the HI signal i.e. for this model our simulations have enough resolution to capture essentially all the expected HI signal across all the redshifts of interest.

The last row of Fig. 5.5 show the fraction of total HI inside a halo that is embedded in the satellites as a function of halo mass. This fraction increases with the halo mass, with as much as $\sim 50\%$ HI residing in satellites for $\sim 10^{14}\, h^{-1} M_\odot$ halos. As described above, the remaining HI of the halos is assigned to centrals. This is in qualitative agreement with satellite HI fraction seen in the Illustris simulations in ref. [237].

While it would be straightforward to include a random scatter in HI at fixed $M_h$, we have no observational constraints on the form or evolution of the scatter. Thus we choose to neglect it, noting where this impacts our results.

## Model B

Inspired by ref. [64], our second model assumes that the HI content of galaxies depends upon stellar mass. We use the fit of ref. [161] to assign stellar masses ($M_\star$) to our central and satellite halos. The corresponding stellar mass function is shown in Figure 5.4 which agrees fairly well with the data [23]. We could likely improve the fit by adjusting the parameters in the stellar-mass halo-mass relation, but this is sufficient for our purposes so we keep the fiducial parameters of ref. [161]. Then we assign an HI mass to each of these galaxies based on the same 'HI richness' ($M_{HI}/M_\star$) relation. Ref. [64] find that $M_{HI}/M_\star$ evolves relatively little with redshift (e.g. see their Fig. 4) implying that the redshift evolution of $M_h - M_{HI}$ is due to the evolution of $M_\star$. We take

$$\frac{M_{HI}}{M_\star} = f\left(\frac{M_1}{M_1 + M_\star}\right)^\alpha \tag{5.7}$$

where by calibrating the against the observations we get $f = 11.52$, $\alpha = 0.4$, and $M_1 = 3 \times 10^8 M_\odot$. Similar to the $M_\star - M_h$ relation, it would be straightforward to include a random scatter in HI at fixed $M_h$, however we have no observational constraints on the form or evolution of the scatter. Thus we choose to neglect it.

[4]https://www.peterbehroozi.com/data.html

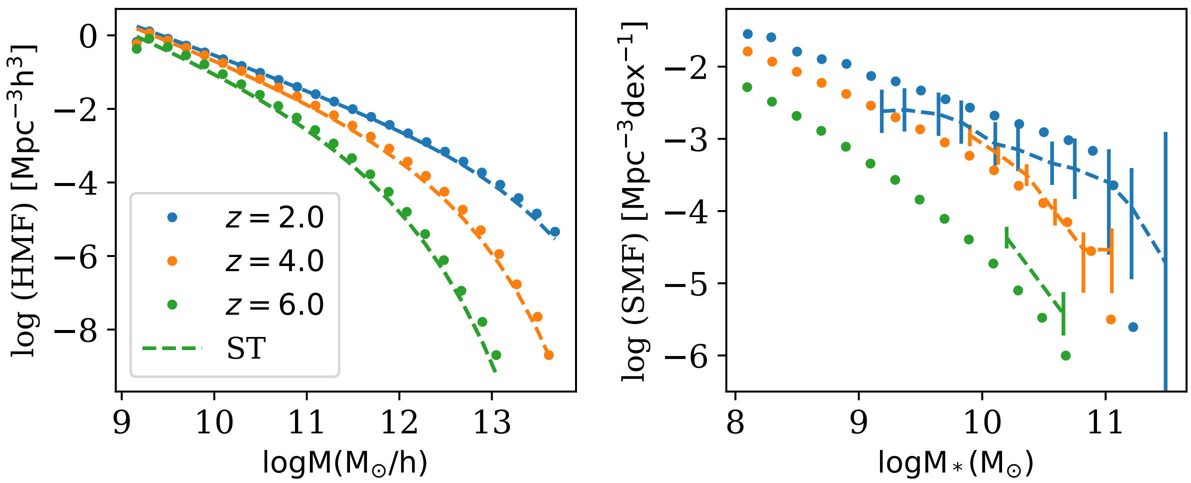


Figure 5.4: (left) The halo mass function from our simulations at $z = 2$, 4 and 6. The dashed lines are the Sheth-Tormen mass function prediction [221]. (right) Stellar mass function from our simulations (points) at the same redshifts. The data (dashed line with error bars) are taken from the compilation of ref. [23][4].

Unlike our fiducial model, this model does not have an explicit lower mass cut-off. Instead the HI distribution in small halos is implicitly suppressed (but not exponentially) by the stellar-mass halo-mass relation. Due to this lack of flexibility, it performs slightly worse in matching the DLA bias at low redshifts (Fig. 5.3). Similarly, due to its lack of explicit redshift dependence beyond the evolution of stellar mass, it also has very different evolution of $\Omega_{HI}$ across redshifts. This model also puts relatively more HI in the intermediate mass halos and less in the highest mass halos than our fiducial Model A (Fig. 5.5, top row) due to the flattening of the $M_\star - M_h$ relation at high mass. Hence the peak of the signal contribution as a function of halo masses (middle row) is shifted to slightly higher mass, and is lower compared to that of Model A. Since we use the same relation (Eq. 5.7) for both centrals and satellites, we lack the flexibility of Model A in distributing HI inside halos. As a result, we find that the satellite HI fraction for this model declines sharply with redshift and is in qualitative disagreement with ref. [237] at higher redshifts.

One advantage of this model is that the redshift dependence of the $M_h - M_{HI}$ distribution is entirely determined by the stellar mass evolution, which is fairly well constrained. Thus we have effectively only two free parameters, $M_1$ and $\alpha$, that impact the impact the shape of $b(z)$ and $\Omega_{\rm HI}(z)$ with $f$ impacting the overall amplitude. However in its current implementation, this lack of explicit redshift dependence leads to a different evolution in total HI content despite having similar clustering to Model A. Thus precise observations at high redshift in the future will serve to test the validity of this model.

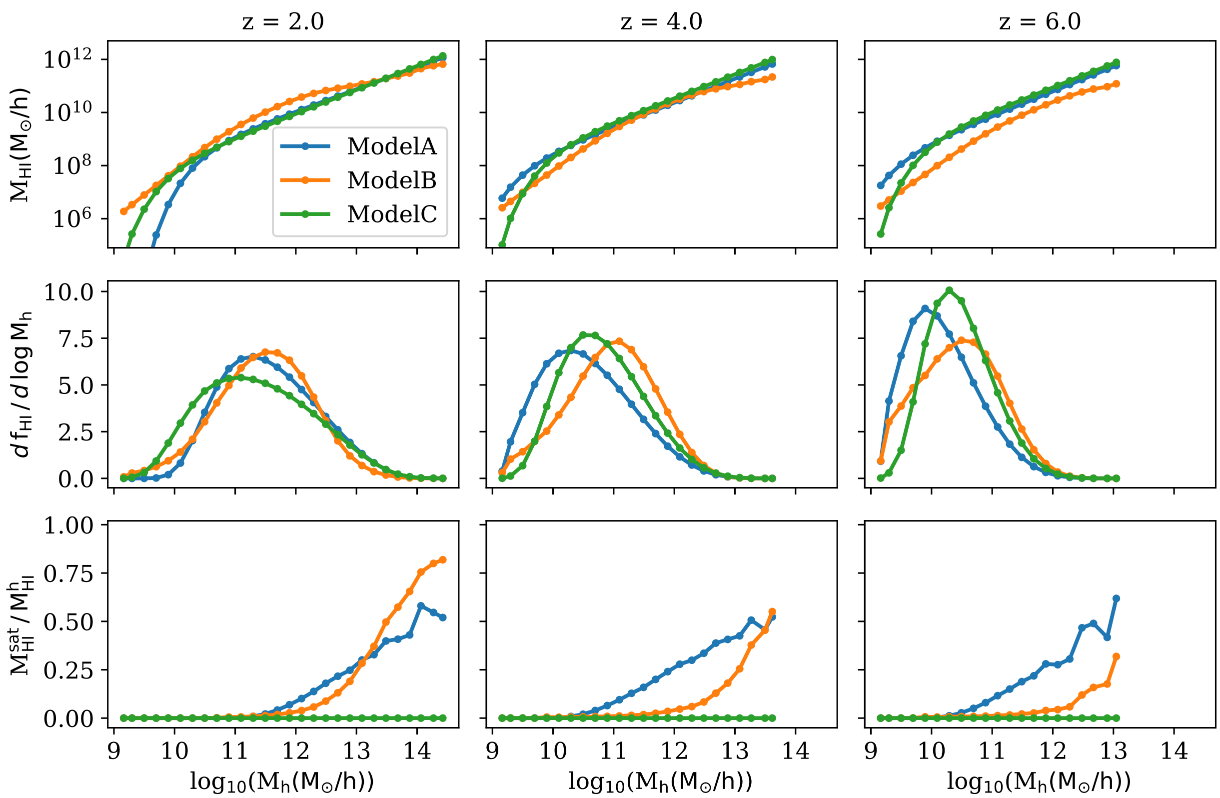


Figure 5.5: Distribution of HI for different models (colors) at different redshifts (columns): i) The top row shows the halo HI mass function i.e. the average HI mass inside halos as a function of halo mass. ii) The middle row shows the fraction of the total HI that resides in halos of a given mass. This illustrates the convergence of our simulations with respect to HI signal on the low halo mass end. iii) The bottom row shows the fraction of HI mass inside the halos that resides in the satellites (this is zero for Model C by assumption).

## Model C

As our last model, we use a simplistic alternative which assumes a constant $M_{\rm cut}$ and $\alpha$ at all redshifts to assign HI to halos. This has been used in the literature in refs. [42, 49]. We set $\alpha = 0.9$ (which is roughly the average of the values at the extreme redshifts used in Model A) and $M_{\rm cut} = 10^{10}\,h^{-1}M_\odot$. Given the current state of the high $z$ clustering observations this model is difficult to completely rule out. However, like Model B, due to the lack of the flexibility in varying the lower mass cut-off this model to performs poorly in matching the DLA bias (Fig. 5.3). With these parameters fixed, one can match the observed HI density up to high redshifts by making the normalization redshift dependent. We find that the following form fits the data well:

$$A_h(z) = 3.5 \times 10^6 \, h^{-1} M_\odot \left(1 + \frac{1}{z}\right) \times (1+z)^3 \tag{5.8}$$

As can be seen from Fig. 5.5, despite having minimal redshift evolution in the parameters, this model qualitatively follows Model A and Model B in the distribution of HI as a function of halo masses. However unlike the other two models, we deliberately do not include any satellites to distribute HI inside an individual halo. This is to avoid having any 1-halo finger-of-god effects in the redshift space. Thus when compared with other models, this will serve to illustrate their impact over and above the redshift space distortions that are captured by the halo velocities themselves.

## 5.5 Validating Hidden Valley Simualtions

The amplitude of the 21-cm signal depends on the abundance and the clustering of the HI. In the previous section, we considered three different models for distributing HI in halos and measured its abundance. In this section, we look in detail at the clustering of HI. We will mostly show the results from our fiducial Model A and simply comment on similarities or differences with the prediction of other models, unless explicitly showing the differences is more insightful.

We will look only at the 2-point statistics of HI clustering. Even though it's not observable, we will begin with real space clustering of HI as a function of redshift since it helps elucidate its relation to the underlying dark matter clustering. Next we will discuss the clustering in redshift space where the signal will actually be observed. Lastly, we will discuss the baryon acoustic oscillations (BAO) in 21-cm signal since its one of the major goals of upcoming 21-cm surveys to detect BAO and measure distances to high redshifts with them.

In order to optimize what can be learned from the surveys mentioned above, theoretical predictions in the mildly and fully non-linear regimes are also needed. Previous work has suggested that perturbative models can accurately predict the clustering of biased tracers to a significant fraction of the nonlinear scale $k_{\rm nl} = \Sigma^{-1}$ at high $z$ [147, 39, 238, 90, 157], where $\Sigma$ is mean square one-dimensional displacement in the Zeldovich approximation given by

$$k_{\rm nl} = \Sigma^{-1} = \left[\frac{1}{6\pi^2}\int P_L(k)\ dk\right]^{-1/2} \quad . \tag{5.9}$$

with $P_L$ the linear theory power spectrum. For high redshift tracers such as HI, perturbative models with their sophisticated biasing schemes become more useful due to increasing complexity of bias and decreasing non-linearity of the matter field as we go further back in time [157]. While we leave a detailed study of modeling 21-cm signal with such models for future work, when more sophisticated models and more simulation volume could become available, here we will compare the clustering signal to the predictions of linear theory and 'Zeldovich

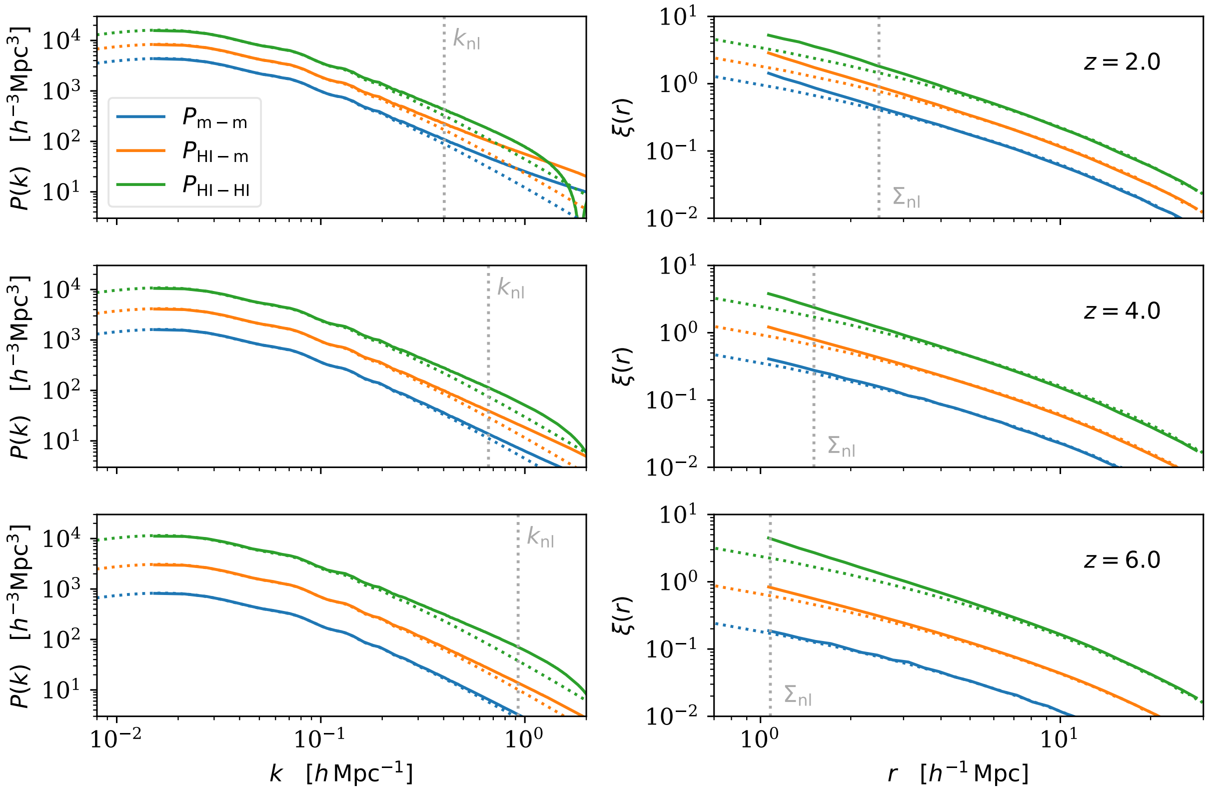


Figure 5.6: The real-space power spectrum (left) and cross correlation function (right) of the dark matter and HI in our fiducial model at $z = 2$, 4, and 6. Solid lines show the N-body results while dotted lines show linear theory with scale-independent bias (set by the amplitude of the cross-spectra at low $k$ or cross-correlation at large $r$). Blue, orange and green line show the matter clustering, matter-HI cross-clustering and the HI auto-clustering respectively. The downturn in the HI auto-spectrum (green) at high $k$ is due to our subtraction of a constant 'shot-noise' component (see text). The vertical grey lines mark $k_{\mathrm{nl}}$ and $\Sigma_{\mathrm{nl}}$ of Eq. (5.9).

effective field theory' (ZEFT [241]). ZEFT is a combination of lowest order Lagrangian perturbation theory (i.e. the Zeldovich approximation [261]) plus a counter-term going as $k^2$ (it can also be thought of as a $k^2$ component to the bias).

## Real-space clustering

We begin with a discussion of the real-space clustering of the HI as a function of redshift, and its relation to the underlying dark matter clustering and to linear theory. Fig. 5.6 shows the real-space power spectra on the left, and the two-point functions (i.e. correlation functions) as a function of separation, $r$, on the right at some selected redshifts. The blue, orange

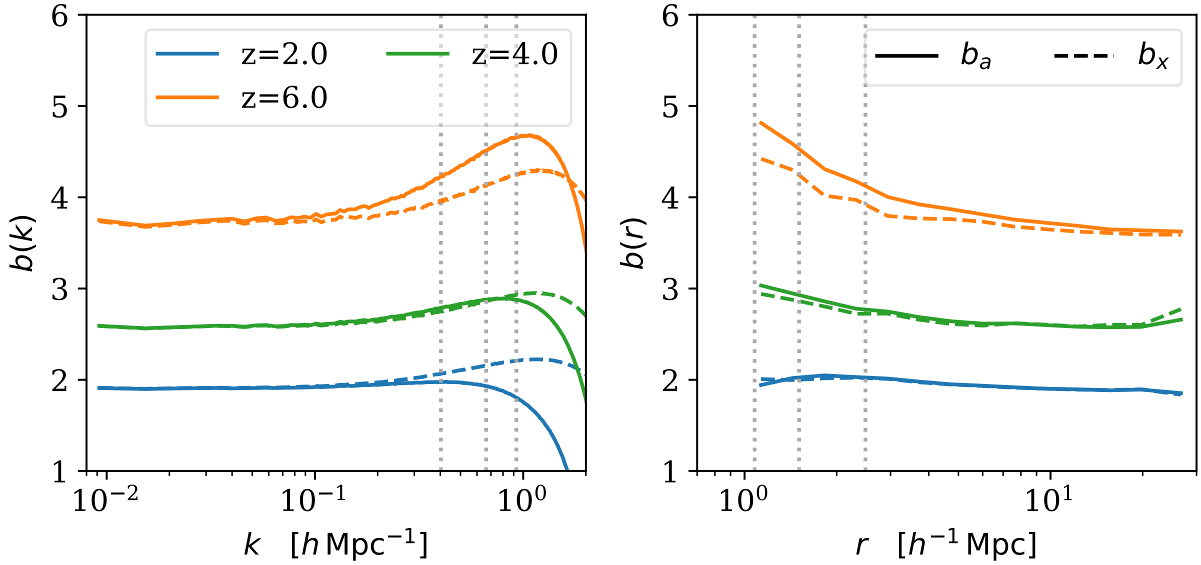


Figure 5.7: (Left) The HI bias, in real-space, measured from the cross- and auto-spectra: $b_a(k) \equiv \sqrt{P_{HI,HI}/P_{mm}}$ (solid) and $b_\times(k) \equiv P_{HI,m}/P_{mm}$ (dotted). As the bias becomes larger, it also becomes more scale-dependent and the difference between $b_a$ and $b_\times$ extends to lower $k$. (Right) The scale-dependent bias defined by the auto- and cross-correlations (solids and dashed, respectively) viz. $b_a(r) \equiv \sqrt{\xi_{HI,HI}/\xi_{mm}}$ and $b_\times(r) \equiv \xi_{HI,m}/\xi_{mm}$.

and green lines show matter auto-clustering (spectra + correlation), matter-HI clustering and the HI auto-clustering respectively, and we compare them to the predictions of linear theory with constant bias (i.e. $b^2 P_L(k)$ and $bP_L(k)$ respectively for power spectra) as dotted lines with $b$ matched to the amplitude of the matter-HI cross-spectra at low $k$ (we perform a simple unweighted average of points with $k < 0.06\,h\,\mathrm{Mpc}^{-1}$). The difference between the simulations and linear theory predictions, coming from a combination of non-linear clustering and scale-dependent bias, is clearly visible at all redshifts.

Fig. 5.7 shows the bias explicitly for both power spectra and correlation functions. The solid lines show the bias estimated from the auto-clustering $b_a(k) \equiv \sqrt{P_{HI,HI}/P_{mm}}$ (and corresponding ratios in configuration space) while the dashed lines are the cross-clustering biases $b_\times(k) \equiv P_{HI,m}/P_{mm}$. The difference between them indicates the degree to which the HI and matter fields are decorrelated. At larger scales, the two biases converge to same values showing that the HI provides a good tracer of the matter field and the cross-correlation coefficient is close to unity. The decorrelation occurs on the scales of a few Mpc and shifts to larger scales (lower $k$) with increasing bias as we go higher in redshift.

On large scales ($> 10\,h^{-1}$Mpc), the bias is scale-independent and our simulations are large enough that we can clearly see the 'flat' low $k$ plateau in the Fourier space. However we see the bias becoming scale dependent on small scales in both Fourier and configuration space, with the dependence extending to larger scales and lower $k$ for the more biased objects at higher redshifts. For this figure, we have defined the biases with respect to the non-linear matter spectra (correlation function) – the scale-dependence of the bias would be larger if we had used the linear theory spectrum in the definition. Note also that as the the bias of the HI in our fiducial model becomes larger and more scale dependent at higher redshifts, the non-linear scale shown in dotted gray lines $k_{\rm nl}/\Sigma_{\rm nl}$ simultaneously shifts to smaller scales. Thus scale-dependence of the bias thus becomes relevant before the non-linear clustering (a similar effect is seen for high-$z$ galaxies in ref. [157, 255]).

The trade-off between complex biasing and non-linearity makes modeling high redshift tracers an ideal application for perturbative models with sophisticated biasing models, such as those developed in Refs. [241, 238, 157] (see also ref. [237]). Fig. 5.8 shows real-space power spectrum at $z = 2$ and 6 compared to the predictions of ZEFT. We have fit all three spectra simultaneously, e.g. the same value of $b_2$ that fits the HI auto-spectrum fits the cross-spectrum. At high redshift the contribution of shear terms becomes suppressed so we have not included shear terms in our fit, though we do include a $b_{\nabla^2}$ contribution, leading to a total of 4 free parameters in our model. The agreement is very good up to about $\sim 0.75\,k_{\rm nl}$, as suggested by ref. [237] in a much smaller volume, and within the expected sample variance over the perturbative range. We expect theoretical models including higher-order effects would do even better. Over this range the N-body results can depart by order unity from the linear theory predictions.

One complication while fitting HI clustering with any model is to take into account the shot noise. Unlike galaxies, HI is not a discrete tracer of the underlying matter field, hence the Poisson approximation for noise is no longer true. This is also shown in ref. [237] who find that $P(k)$ does not asymptote to a constant at high $k$, likely due to the HI profile inside the halos on small scales. Thus if one knows the shape of 1$-$halo term, this can be fit for or subtracted while modeling the signal. In addition the 21-cm signal is dominated by low mass halos, $\sim 10^{10}h^{-1}M_\odot$, whose clustering has a complex shot noise form. While this needs to be investigated in the future, here we approximate the noise as Poisson, i.e. $P_{\rm SN} \sim \sum_h M_{\rm HI}^2/(\sum M_{\rm HI})^2$, where $M_{\rm HI}$ is the HI mass in a halo and the sum is over all the halos. This simplistic form ignores any scale dependence of the noise and ref. [237] show that this over-estimates the noise on small scales.

Lastly, we have shown the results only for HI distribution with Model A. The results in real space are qualitatively similar for the other models with the only difference being in the amplitude of the clustering i.e. Model B and Model C predict slightly higher bias on large scales at higher redshifts. This can be seen from the inset plot in Fig. 5.3. As expected, this also leads to greater scale dependence of bias and higher decorrelation with matter clustering on smaller scales.

## Redshift-space clustering: supercluster infall

Future experiments will measure the clustering signal in redshift space, not real space, thus it is useful to look at the impact of peculiar velocities on the signal. There are several effects

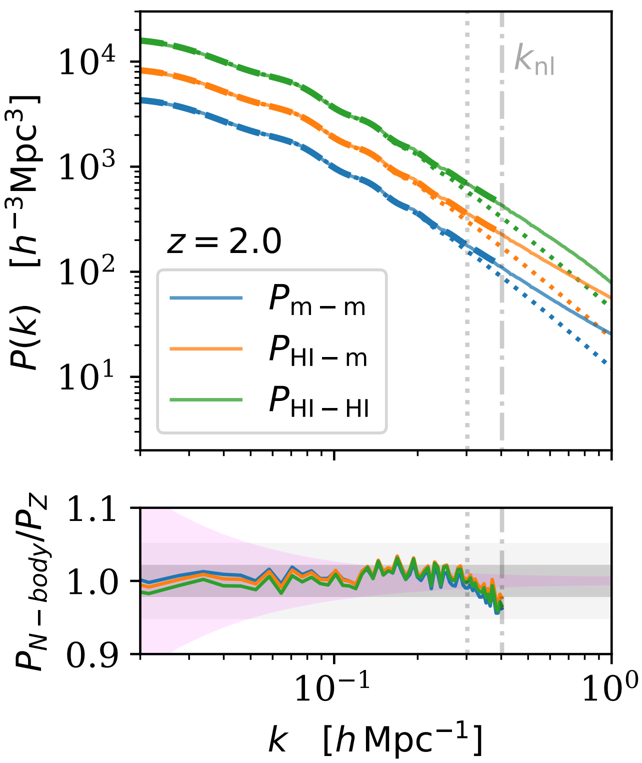


Figure 5.8: (Top) The real-space power spectrum of the dark matter and HI in our fiducial model at $z = 2$ and 6. Solid lines show the N-body results, dashed lines show the Zeldovich effective field theory calculation and dotted lines linear theory. Blue lines show the matter power spectrum, orange lines the matter-HI cross-spectrum and green lines the HI auto-spectrum. A single set of parameters fits all curves simultaneously. The dotted and dash-dot vertical grey lines mark $0.75k_{\rm nl}$ and $k_{\rm nl}$ of Eq. (5.9). (Bottom) The ratio of the the N-body results to Zeldovich fit. The dark and light grey shaded regions show $\pm 2\%$ and $\pm 5\%$. The shaded magenta region shows the sample variance error in our simulation volume (including shot noise).

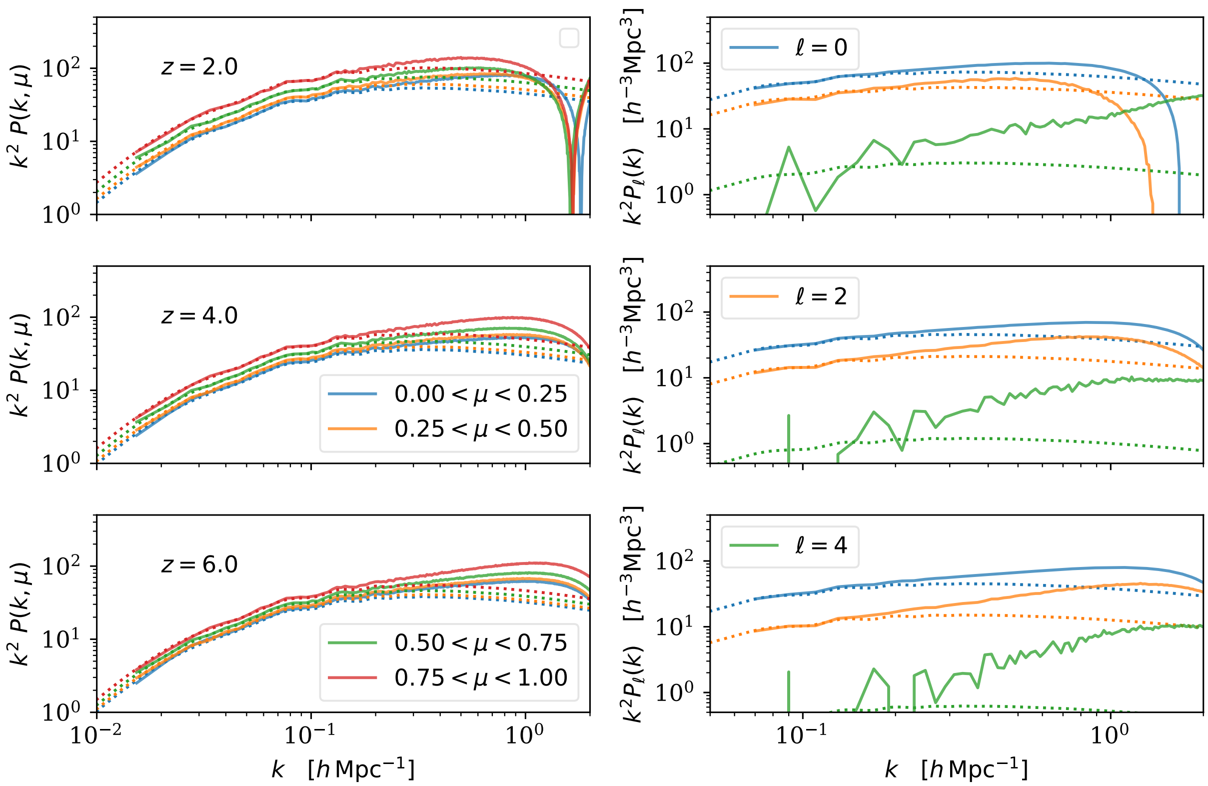


Figure 5.9: The redshift-space power spectrum of the HI in our fiducial model at $z = 2$, 4 and 6. (Left) The solid lines show the N-body result for $P(k, \mu)$ wedges while the dotted lines show linear theory prediction with scale-independent bias. (Right) The first three, even multipoles of the anisotropic redshift space power spectrum along with the linear theory, constant bias predictions (dotted).

which are of interest. First, the fact that only the line-of-sight peculiar velocity contributes to the measured redshift imprints an anisotropy in the clustering signal [121, 99]. In the distant observer limit[5] our power spectrum becomes a function of $k$ and $|\mu|$, with $\mu \equiv \hat{k} \cdot \hat{z}$ if $\hat{z}$ is the (common) line-of-sight direction. On large scales, supercluster infall enhances the signal, while on smaller scales inter- and intra-halo virial motions lead to anisotropic power suppression. The amount of suppression, also referred to as the finger-of-god (FOG) effect, is dependent upon the amount of HI that lives in satellites within massive halos and their virial motions. We focus here on the former and explore the FOG effect in the next section.

Fig. 5.9 shows the HI auto-spectrum in redshift space in two different forms and at various redshifts - on the left are the $P(k, \mu)$ wedges in 4 slices of $\mu$ while on the right are the first three

[5]Since the observations are at high $z$ we make the distant observer approximation throughout. From the analysis of Refs. [43, 45] we expect this introduces errors well below our other uncertainties.

multipoles generated by anisotropic clustering along the line of sight. We have multiplied the curves by $k^2$ to reduce the dynamic range in order to better separate the different curves. In addition, we have subtracted the shot noise with the same approximation of weighted means as for the real space clustering. In linear theory, the line-of-sight power is enhanced by supercluster infall [121] by a factor $(1 + [f/b]\mu^2)^2$, where $f = d\ln D/d\ln a \simeq \Omega_m^{0.55}(z) \approx 1$ is the growth rate. This prediction is shown in dotted lines for different wedges and multipoles and agrees well with the simulations on large scales.

To model intermediate scales, similar to real space clustering, we turn to perturbative models and compare the power spectrum multipoles with ZEFT prediction. This is shown in Fig. 5.10. There are numerous ways of computing the redshift-space power spectrum in the Zeldovich approximation [240], here we have performed a Hankel transform of the correlation function multipoles. The N-body multipole power spectra are noisier than their real-space counterparts, but the level of agreement is still quite good for such a simple model. Over the range shown the N-body results depart from linear theory by order unity, while the agreement with our Zeldovich model is always within sample variance. In addition, we also show the sample variance after including the thermal noise, which dominates on small scales, for a HIRAX-like and Stage II experiment and find that perturbation theory fits the model well within the errors for HIRAX-like experiment on these small scales as well. Higher order perturbation theory and a more sophisticated treatment of redshift-space distortions would almost certainly improve the agreement, however this preliminary investigation suggests that even low order perturbation theory is correctly predicting the signatures of non-linear evolution and complex bias in our simulations. Given the enormous uncertainties associated with the manner in which HI traces the matter field, this suggests the Zeldovich approximation can be used as an efficient and relatively accurate forecasting tool [44].

In Fig. 5.11, we also show the comparison for power spectrum wedges in redshift space. To be more realistic here, we have taken into account the "pessimistic" case of the foreground wedge as outlined in ref. [49] and split only the observable modes outside this into two equal wedges with respect to the line of sight. This allows us to see the impact of anisotropic thermal noise that is otherwise averaged over in case of multipoles. We clearly see that the thermal noise is larger perpendicular to the line of sight, but is however small in comparison to the sample variance for our $1\,h^{-1}$Gpc volume. To fit Zeldovich perturbation theory to the power spectrum wedges, we have used only first three multipoles and find that it is able to fit the simulations to within 5% up to non-linear scales. Despite being within sample variance, the fit on the large scales for $z = 2$ seems biased for the two wedges which is likely due to using only the first three, even multipoles to get the model power spectrum wedges.

## Redshift-space clustering: Fingers of God

Small-scale clustering in redshift space is suppressed due to FOG effects along the line of sight. This puts an upper limit on the modes which can be used to extract information and hence it is important to look at the amplitude of these effects. The simplest phenomological

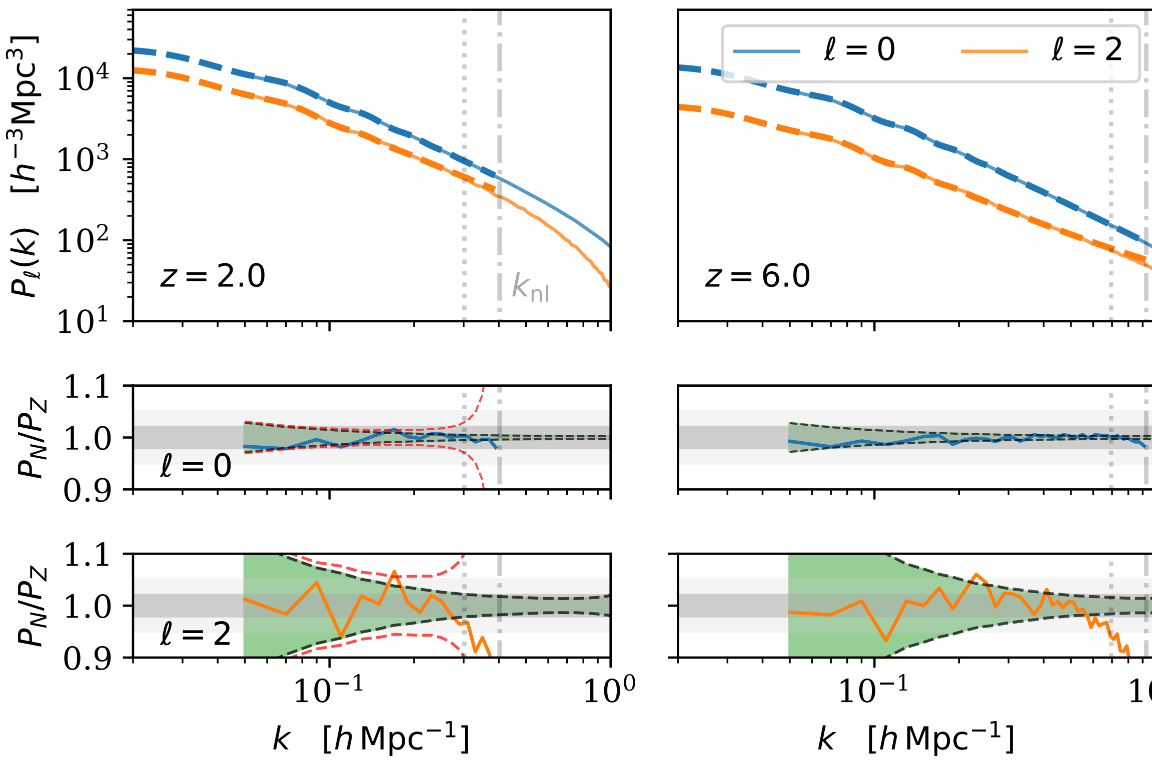


Figure 5.10: (Top) The redshift-space, HI power spectrum multipoles in our fiducial model at $z = 2$ and 6. Solid lines show the N-body results while dashed lines show the Zeldovich effective field theory calculation. Blue lines show the monopole ($\ell = 0$) while red lines show the quadrupole ($\ell = 2$). A single set of parameters fits both multipoles simultaneously. The dotted and dash-dot vertical grey lines mark $0.75k_{\rm nl}$ and $k_{\rm nl}$ of Eq. (5.9). (Bottom rows) The two rows show the ratio of the N-body results to the Zeldovich fit for monopole and quadrupole. The dark and light grey shaded regions show $\pm 2\%$ and $\pm 5\%$. The shaded green region shows the expected sample variance error in our simulation volume, including shot noise, though the actual error in our simulations is expected to be less due to our fixed amplitude construction of initial conditions. The dashed red and black lines show the sample variance error after including the thermal noise for HIRAX-like and Stage II experiment respectively.

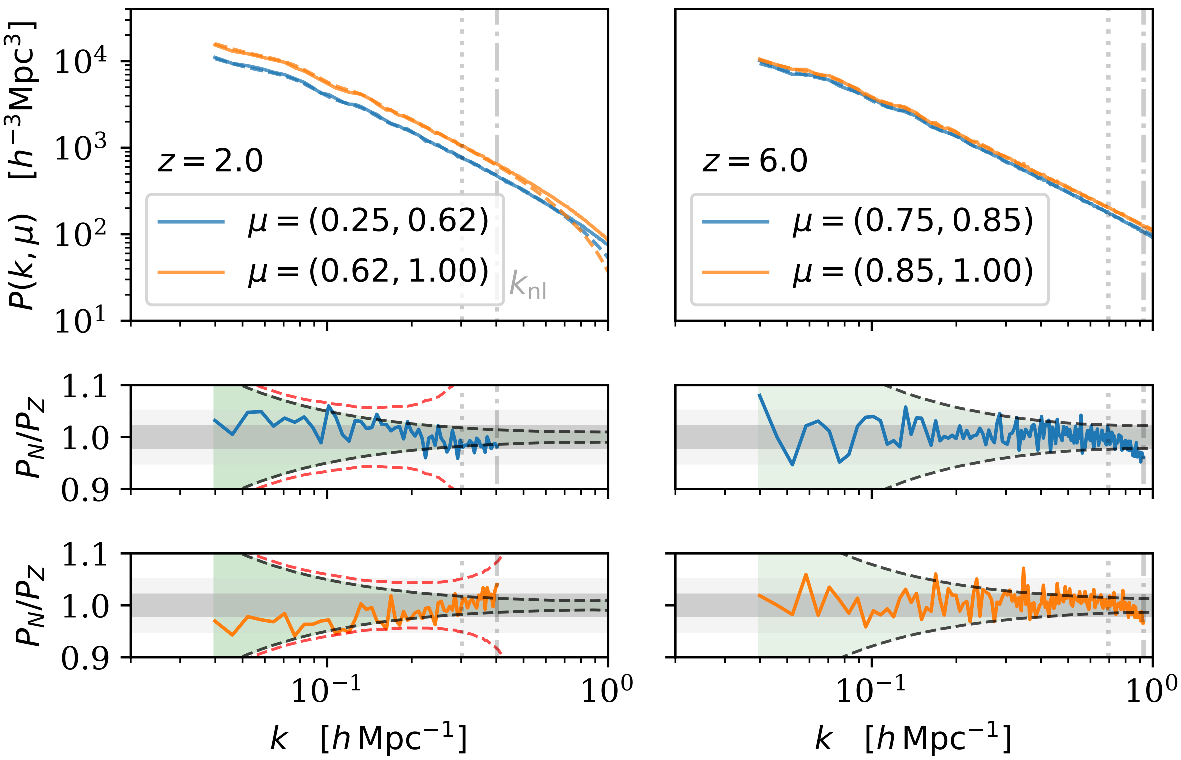


Figure 5.11: (Top) The redshift-space, HI power spectrum wedges for our fiducial model at $z = 2$ and 6. Solid lines show the N-body results while dashed lines show the Zeldovich effective field theory calculation. A single set of parameters fits both the wedges simultaneously. The dotted and dash-dot vertical grey lines mark $0.75k_{\rm nl}$ and $k_{\rm nl}$ of Eq. (5.9). (Bottom rows) The two rows show the ratio of the N-body results to the Zeldovich fit for the two wedges. The dark and light grey shaded regions show $\pm 2\%$ and $\pm 5\%$. The shaded green region shows the expected sample variance error in our simulation volume, including shot noise, though the actual error in our simulations is expected to be less due to our fixed amplitude construction of initial conditions. The dashed red and black lines show the sample variance error after including the thermal noise for HIRAX-like and Stage II experiment respectively.

expression to model the redshift space spectrum using FOG effects is:

$$P^s_{\rm HI}(k,\mu) = (1+[f/b]\mu^2)^2 b_L^2 P_{\rm L}(k)\mathcal{K}(k,\mu,\sigma_s) + N(k) \tag{5.10}$$

where $b_L$, $P_L$ are the linear bias and linear power spectrum, $N(k)$ is the additive component of shot noise and the kernel $\mathcal{K}(k,\mu,\sigma_s)$ contains both perturbative and non perturbative effects. Usually the FOG effect contribution to this kernel is modeled using a Gaussian or a Lorentzian. To quantitatively see where FOG lead to suppression of power and loss of information on small scales, we extract the kernel as

$$\mathcal{K}(k,\mu,\sigma_s) = \frac{1}{(1+[f/b]\mu^2)^2}\Big[\frac{P^s_{\rm HI}(k,\mu) - P^s_{\rm HI}(k,0)}{b_L^2 P_{\rm L}(k)} + 1\Big] \tag{5.11}$$

where we assumed that the shot noise $N(k)$ is $\mu$ independent and $\mathcal{K}(k,0,\sigma_s)=1$. This kernel is shown in Fig. 5.12 for different HI models. On large scales, where linear theory is valid, we find the kernel to be close to unity as per our expectations. On intermediate scales, the signal increases due to nonlinear redshift space distortions and biasing. At high-$k$ the FOG suppress the signal, and this suppression becomes smaller at high redshfit because the low mass halos we probe at high $z$ have low velocity dispersion. As seen in Fig. 5.5, since the amount of HI in satellites is higher in Model A, compared to the other two models, the FOG suppression is higher and at slightly larger scales. Interestingly, though Model C does not have satellites and hence does not strictly have 1-halo FOG effects caused due to velocity dispersion, it sees the same suppression as Model B at high redshifts. This suggests that this suppression is due to the combined effect of cluster-infall velocities of halos and the 1-halo contribution to clustering.

Given that FOG effect is subdominant in suppressing clustering at $k \leq k_{\rm NL}$, they will not set the limit to the scales along the line of sight from which we can extract cosmological information. This is one advantage of 21-cm surveys over other spectroscopic surveys which can be severely limited by FOG effects (and redshift measurement uncertainties [255]). Small FOG also mean that the radial resolution of the analysis will be set by the channel bandwidth or the frequency resolution. The channel bandpass can be approximated with a Gaussian which gives an effective beam in the parallel direction [36]

$$B_{\parallel}(k_{\parallel}) = \exp\left(-\frac{[r_\nu k_{\parallel}\ \delta\nu/\nu_{21}]^2}{16\ln 2}\right) \tag{5.12}$$

where $r_\nu = c(1+z)^2/H(z)$ and $\delta\nu$ is the channel bandwidth. Based on Fig. 5.12, if we expect to be able to model the signal up to $k = 0.6$, $0.8$ and $1\,h\,{\rm Mpc}^{-1}$ at $z = 2$, 3 and $z \geq 4$, and we require the beam suppression on these scales to not be greater than $e^{-1}$, then this sets the minimum bandwidth to $\delta\nu = 5$, 2, 1, 0.8 and $0.6\,$MHz respectively.

## Baryon acoustic oscillations

A major goal of high $z$, 21-cm cosmology is the measurement of distances using the baryon acoustic oscillation method [249]. In Fig. 5.13 we show this signal, in real and redshift

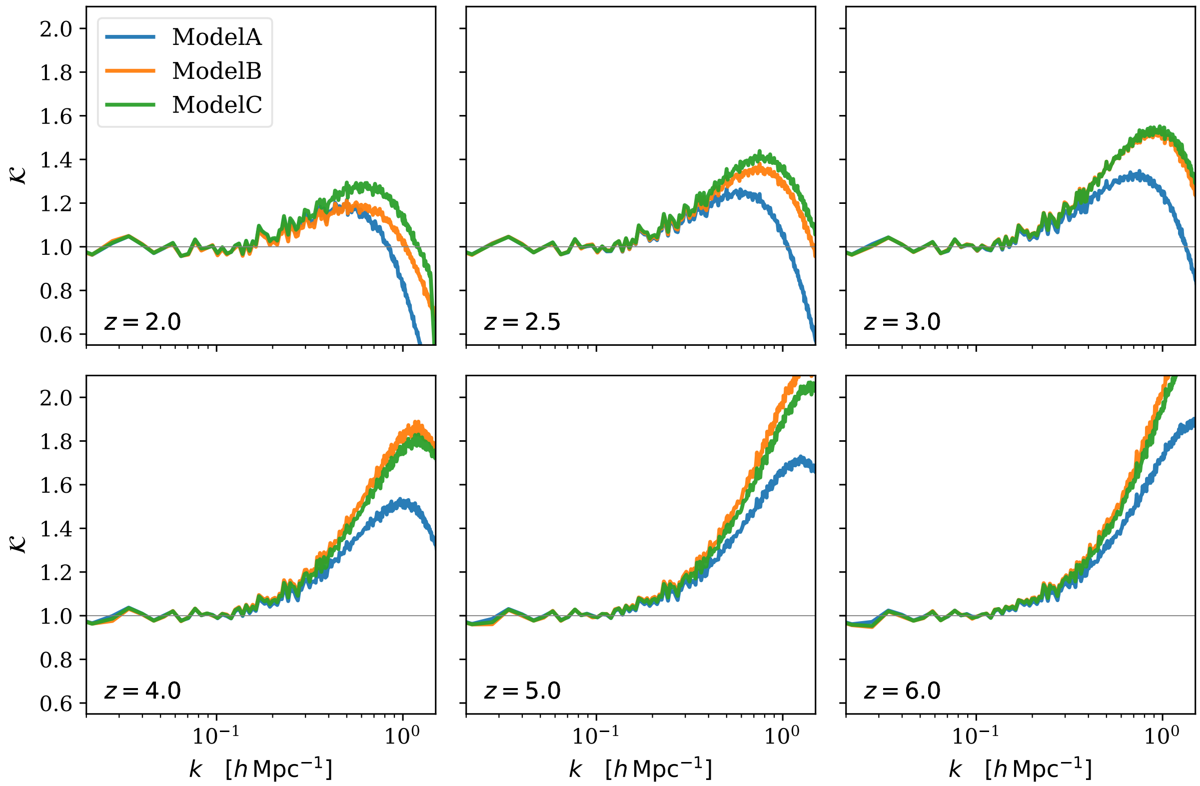


Figure 5.12: Fingers of god suppression in the form of the kernel defined in Eq. 5.11 for the three models of the distribution of HI for various redshifts.

space, as power spectrum and correlation function monopole and compare it against linear theory (dotted lines). We find that scale-dependent biasing, redshift-space distortions and non-linear evolution have only a small effect on the BAO signal, and this observation gets stronger as we go higher in redshift.

In Fourier space the BAO signal appears as a quasi-periodic sequence of damped oscillations superposed upon the smooth shape of the power spectrum. To enhance the visibility of peaks, we divide $P(k)$ in Fig. 5.13 by a "no-wiggle" template which is formed simply by smoothing the power spectrum with a Savitsky-Golay filter. This disentangles effects like scale-dependent bias which leads to only a smooth trend in $P(k)$ and are hence removed by the broad-band division. It is clear from Fig. 5.13 that the BAO peaks would be easily visible in the $k$-band probed by the upcoming 21-cm surveys. Non-linear structure formation damps the BAO peaks and reduces the signal-to-noise ratio for measuring the acoustic scale [28, 151, 72, 223, 58, 147, 215, 251, 250]. Since the non-linear scale shifts to smaller scales at high-redshifts, this damping is expected to be small. In Fig. 5.13 only the fourth BAO peak is slightly damped at $z = 2$ as compared to linear power spectrum and no damping is

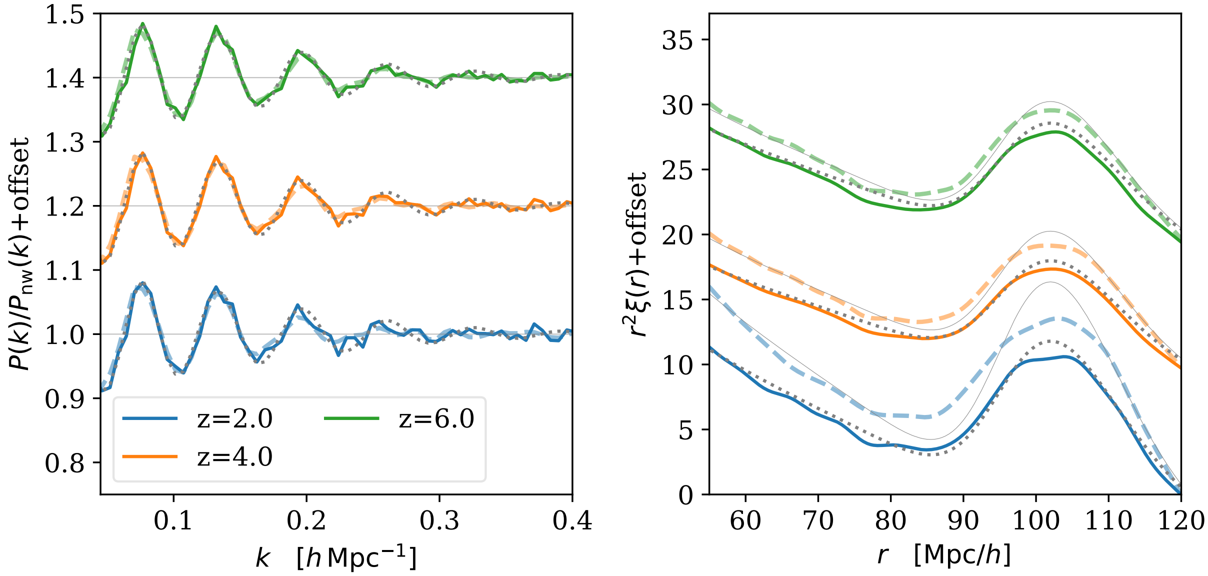


Figure 5.13: BAO signal in real (solid lines) and redshift space (monopole, dashed) at various redshift compared with the linear theory in real (gray dots) and redshift space (gray solid line): (Left) Ratio of power spectrum to the "no-wiggle" template which is formed by smoothing with a Savitsky-Golay filter. We have moved lines for different redshift vertically by 0.2 to enhance visibility. (Right) Correlation function estimated by Hankel transform of the power spectrum, compared with linear theory i.e. linear bias and Kaiser prediction in real and redshift space respectively. We have offset lines for different redshift together vertically by multiples of 10 to enhance visibility.

visible at $z = 6$, in accordance with the value of $k_{\rm NL}$ at these redshifts.

Since the amount of damping is small at high redshifts and therefore quite difficult to see in the power spectrum, we also show the correlation function where the BAO signal appears as a single, well-localized peak at the BAO scale $\sim 100\,h^{-1}$Mpc. Since our purpose here is to only visually assess the degree of peak broadening, we do not measure the correlation function on these scales via pair-counting in the simulations, but compute it from the power spectrum measurement via Hankel transform. For this purpose, we extrapolate the measurement on large scales with the linear power spectrum and linear bias, and on small scales with a power-law.

The peak broadening over the linear theory prediction is more clearly visible in correlation space, for both real and redshift space clustering, and it decreases significantly between redshift $z = 2$ and 4. While not shown here to maintain clarity of the figure, we find that the Zeldovich approximation provides a good fit to the peak damping in the correlation function at all redshifts. As an aside, we note that the real and redshift space signals at higher redshifts are closer than at low redshifts, illustrating the decreasing effects of redshift space distortions on the broadband due to the increasing bias. Thus though the peak damping is

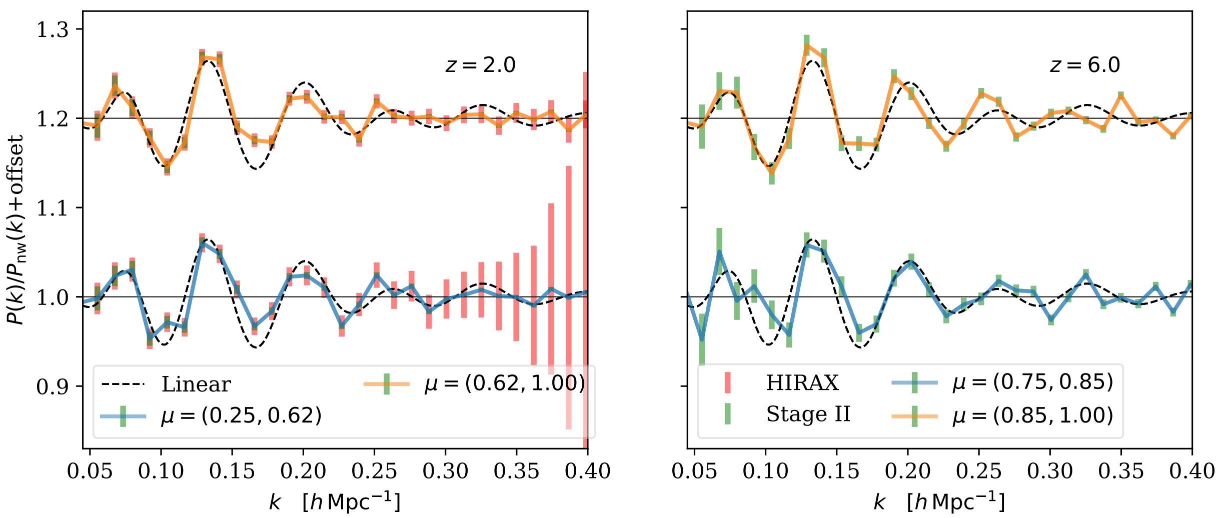


Figure 5.14: BAO signal for the power spectrum wedges for the same configuration as Figure 5.11 at redshifts $z = 2$ and 6, after taking the ratio of the power spectrum to the "no-wiggle" template which is formed by smoothing with a Savitsky-Golay filter. We have moved lines for different $\mu$-bins vertically by 0.2 to enhance visibility. The black dashed line is the linear theory prediction. We show error bars for the two experiments HIRAX-like (red) and Stage II (green). The error bars include the shot noise, thermal noise and sample variance for the volume corresponding to redshift slice of $\Delta z = 0.2$ around the the central redshift. We have assumed sky coverage of $15000\,\deg^2$ and $20000\,\deg^2$ for the two experiments respectively.

slightly larger in redshift space than in real space at $z = 2$, but this is no-longer (noticeably) the case at $z = 6$.

The BAO peak can be sharpened, or the high-$k$ oscillations partially restored, by a process known as 'reconstruction' [75]. Reconstruction is adversely affected by modes lost to foregrounds and instrument imperfections [213], but this can be partly overcome by combining 21-cm observations with other surveys [54]. Conveniently, the gains from reconstruction are largest at the lowest redshifts, where the overlap with other probes of large-scale structure is also the largest.

To assess the feasibility of detecting BAO signature in presence of foreground wedges, Fig. 5.14 shows BAO wiggles in the power spectrum wedges after removing the broadband. We consider the "pessimistic" foreground wedge as outlined in the previous section for Fig. 5.11 [49]. We estimate realistic error bars for two experimental setups: HIRAX-like with sky coverage of $15000\,\deg^2$ and Stage II covering $20000\,\deg^2$ in the sky. The errors include the shot noise, thermal noise and sample variance for the volume corresponding to redshift slice of $\Delta z = 0.2$ around the the central redshift. At redshift $z = 2$, both the experiments should be able to detect the BAO signature with equally high significance on all the scales that are not damped due to non-linear evolution. At redshift $z = 6$, Stage II is able to detect the signal with high significance despite having access to a very narrow wedge due to foregrounds. These results show that 21-cm interferometers are ideal instruments to measure BAO, in principle, and have clear advantages over single dish experiments [236], despite the fact that the latter are not affected by the foreground wedge.

## 5.6 Reconstruction of HI Field

Finally, we turn to the problem of reconstruction of lost modes in the foreground wedge in 21-cm surveys. We will make use of the 'Model A' of the Hidden Valley[6] simulations [158] at $z = 2$, 4 and $z = 6$. Thus our mock HI data lives in redshift space and captures the small scale non-linear redshift space distortion effects due to satellite motion. While our model is consistent with our best current knowledge, the particular values of various modeling parameters we have assumed may not be correct. However as long as this field can be modeled with a flexible bias framework and the scatter between the HI mass and halo mass (or underlying dark matter density) is similar to other tracers, such as stellar mass, we believe our qualitative results do not depend critically upon these details.

For our analysis, we will use two Cartesian meshes (discussed further in Section 5.6) with 256 and 512 cells along each dimension, which have resolutions of 4 and $2\,h^{-1}$Mpc respectively. To generate the HI data, we desposit the galaxies, weighted by their HI mass, on these meshes with a cloud-in-cloud (CIC) interpolation scheme and then estimate the HI overdensity field ($\delta_{\mathrm{H}I}$) in the usual way. Similarly, to generate the final, Eulerian matter field at the redshifts of interest, we use a 4% subsampled snapshot of the particle positions and paint them with the same CIC scheme (and equal weights per particle). The initial, Lagrangian field ($\delta_L$), is generated on the meshes using the same initial seed (hence same initial conditions) as the simulation itself.

Once we generate the 'clean HI data' on a mesh we need to simulate the foreground wedge and thermal noise to construct a mock observed data for the purpose of reconstruction. To include the foreground wedge, $w$, we simply omit from our calculations all of the modes that are within the wedge, i.e. below a certain cut-off $k_{\|}/k_{\perp}$, as shown in Fig. 5.1. We simulate thermal noise by drawing a zero-mean, Gaussian realization, $n(\mathbf{k})$, from the 2D thermal noise power spectrum, $P_{th}(k, \mu)$. Then, we corrupt the 'clean' data by adding this noise realization and use it as the 'observed' data for reconstruction

$$\delta^n_{\mathrm{H}I}(\mathbf{k}) = \delta_{\mathrm{H}I}(\mathbf{k}) + n(\mathbf{k}) \tag{5.13}$$

There have been many approaches to determining the density field from noisy or incomplete observations in cosmology, from early work like refs. [183, 26, 201, 171, 67] through ref. [163] and references therein. Our method to reconstruct the long-wavelength modes puts in practice the intuition developed in the introduction, that the non-linear evolution of matter under gravity propagates information from large scales in the initial conditions to

[6]http://cyril.astro.berkeley.edu/HiddenValley

the small scales in the final matter field. As developed in previous chapters, we reconstruct the initial density field by optimizing its posterior, conditioned on the observed data (HI density in $k$-space), assuming Gaussian initial conditions. Evolving this initial field allows us to reconstruct the observed data on all scales, thus reconstructing the sought-after long wavelength modes. In this first application of the method we will hold the cosmology fixed, though in future one could imagine jointly fitting the cosmology and the long wavelength modes. Varying cosmology and hence the prior power spectrum is especially important when quantifying uncertainities on the reconstructed fields but that is beyond the scope of this work and we defer it for future.

In this section, we begin by outlining our forward model with the focus on the bias model. Next, we use this forward model to setup the likelihood function for reconstruction and modify it to account for the additional noise and foreground wedge present in the observed data. Lastly, we also outline annealing schemes that we develop to assist convergence of our algorithm and hence improve our reconstructions.

## Forward Model at field level

To use the framework of refs. [211, 156], we require a forward model $[\mathcal{F}(\mathbf{s})]$ to connect the observed data ($\mathbf{d}$) with the Gaussian initial conditions (ICs; $\mathbf{s}$) in a differentiable manner at field level. As before, this forward model is typically composed of two parts - non-linear dynamics to evolve dark-matter field from the Gaussian ICs to the Eulerian space and a mapping from the underlying matter field to the observed tracers i.e. a bias model. We try two different models to shift the particles from Lagrangian space to their Eulerian space: a simple Zeldovich displacement [261] and full N-body evolution [86], albeit at relatively low resolution.

For the mapping from the matter field to the tracers we use bias model. As demonstrated in previous section, quadratic bias model with ZEFT works well upto intermediate scales and the FOG effect is subdominant for HI. While in previous section we used the bias model to match HI clustering, now we are instead interested in modeling the observations at the field level. Thus we use the approach of Lagrangian bias model at field level, as outlined in Chapter 2 Section 2.3, upto quadratic order with $\delta_L(\mathbf{q})$, $\delta_L^2(\mathbf{q})$ and $s_L^2(\mathbf{q}) \equiv \sum_{ij} s_{ij}^2(\mathbf{q})$. We use these fields from the ICs of the simulation itself (as described in Section 5.3), but evolved to $z = 0$ using linear theory. Again, since $\delta_L^2(\mathbf{q})$ and $s^2(\mathbf{q})$ are correlated, we define a new field $g_L^2(\mathbf{q}) = \delta_L^2(\mathbf{q}) - s^2(\mathbf{q})$ which does not correlate with $\delta_L^2(\mathbf{q})$ on large scales and use this instead of shear field. In addition, we subtract the zero-lag terms to make these fields have zero mean.

Then to generate our model field, each particle is 'shifted' to its Eulerian position, $\mathbf{x}$, with the non-linear dynamics of choice and then binned onto the grid with cloud-in-cloud (CIC) interpolation and weight

$$weight = 1 + b_1\delta_L(\mathbf{q}) + b_2(\delta_L^2(\mathbf{q}) - \langle\delta_L^2(\mathbf{q})\rangle) + b_g\left(g_L(\mathbf{q}) - \langle g_L(\mathbf{q})\rangle\right) \tag{5.14}$$

We use the $512^3$ particle mesh for these fields, with particle/mesh spacing $2\,h^{-1}$Mpc for our box of $1024\,h^{-1}$Mpc (and no further smoothing). The contributions of $\delta_L$, $\delta_L^2$ and $g_L^2$ assigned to each particle are based on its initial location ($\mathbf{q}$). Thus our modeled tracer field is:

$$\delta^b_{\rm HI}(\mathbf{x}) = \delta_{[1]}(\mathbf{x}) + b_1\delta_{[\delta_L]}(\mathbf{x}) + b_2\delta_{[\delta_L^2]}(\mathbf{x}) + b_g\delta_{[g_L]}(\mathbf{x}) \qquad . \tag{5.15}$$

where $\delta_{[W]}(\mathbf{x})$ refers to the field generated by shifting the particles weighted with '$W$' field.

To fit for the bias parameters, we minimize the mean square model error between the data and the model fields which is equivalent to minimizing the error power spectrum of the residuals, $\mathbf{r}(k) = \delta^b_{\rm HI}(\mathbf{k}) - \delta_{\rm HI}(\mathbf{k})$, in Fourier space:

$$P_{\rm err}(k) = \frac{1}{N_{\rm modes}(k)} \sum_{\mathbf{k},|\mathbf{k}|\sim k} \left|\delta^b_{\rm HI}(\mathbf{k}) - \delta_{\rm HI}(\mathbf{k})\right|^2 \tag{5.16}$$

where the sum is over half of the $\mathbf{k}$ plane since $\delta^\star(\mathbf{k}) = \delta(-\mathbf{k})$ for the Fourier transform of a real field, and the 'data' correspond to our 'clean' field with no noise at this stage.

We find that the best-fit parameters are scale independent to a very good degree (see below). Thus to minimize the number of fitted parameters we use scalar bias parameters and fit for them by minimizing the error power spectrum only on large scales, $k < 0.3\,h\,{\rm Mpc}^{-1}$. We will show below that the fit is quite insensitive to this $k$-range (chosen reasonably) used for fitting the bias parameters.

Traditionally, bias parameters are defined such that the bias model field matches the observations in real space. However the observations of 21-cm surveys are done in redshift space. To model these observations, we 'shift' the Lagrangian field directly into redshift space and minimize the error power spectrum (Eq. 5.16) directly in redshift space instead of real space.

Finally, we shall assume throughout that the cosmological parameters will be well known, and in fact use the values assumed in the simulation. In principle one could iterate over cosmological parameters, but the 21-cm data themselves (and external data) will provide us with extremely tight constraints on cosmological parameters even before reconstruction [55].

## Reconstruction

Once the bias parameters are fixed the procedure above provides a differentiable 'forward model', $\mathcal{F}(\mathbf{s})(= \delta^b_{\rm HI}(\mathbf{x}))$, from the Gaussian initial conditions ($\mathbf{s}(\mathbf{k})$) to the observations, $\mathbf{d}(\mathbf{k}) = \delta_{HI}(\mathbf{k})$. To reconstruct the initial conditions we need a likelihood model for the data. Since the error power spectrum was minimized to fit for the model bias parameters, it measures the remaining disagreement between the observations and our model and hence provides a natural likelihood function. When using this form of likelihood, we have made the assumption that the residuals in Fourier space between our model and data are drawn from a diagonal Gaussian in the Fourier space with variance given by error power spectrum. The diagonal assumption is valid due to the translational invariance of both the data and the model. The Gaussian assumption is motivated on large scales by the fact that the dynamics are linear, and on small scales by central limit theorem when averaged over large number of modes on these scales. Moreover, while this likelihood might not be completely accurate or optimal on all scales, it does provide us well motivated and simple (negative) loss function, maximizing which should reconstruct the data. This is sufficient for our purpose here, where we are only interested in a point estimate of the reconstructed field. Thus we can write down the negative log-likelihood:

$$\mathcal{L} = \frac{1}{2}\chi^2 = \sum_k \frac{1}{N_{\mathrm{modes}}(k)} \sum_{\mathbf{k},|\mathbf{k}|\sim k} \frac{|\delta^b_{\mathrm{H}I}(\mathbf{k}) - \delta_{\mathrm{H}I}(\mathbf{k})|^2}{P_{err}(k)} \tag{5.17}$$

where the sum is over half of the $\mathbf{k}$ plane since $\delta^\star(\mathbf{k}) = \delta(-\mathbf{k})$ for the Fourier transform of a real field. This is combined with the prior over the initial modes, which are assumed to be Gaussian and uncorrelated in the Fourier space. Hence the negative log-likelihood for the Gaussian prior can be combined with the negative log-likelihood of the data to get the posterior

$$\mathcal{P} = \sum_k \frac{1}{N_{\mathrm{modes}}(k)} \sum_{\mathbf{k},|\mathbf{k}|\sim k} \Big(\frac{|\delta^b_{\mathrm{H}I}(\mathbf{k}) - \delta_{\mathrm{H}I}(\mathbf{k})|^2}{P_{\mathrm{e}rr}(k)} + \frac{|\mathbf{s}(\mathbf{k}))|^2}{P_{\mathrm{s}}(k)}\Big) \tag{5.18}$$

where $P_{\mathrm{s}}$ is the initial prior power spectrum. To reconstruct the initial modes $\mathbf{s}$, we minimize this posterior with respect to them using L-BFGS[7] [169], as in refs. [211, 156], to get a maximum-a-posteriori (MAP) estimate.

We note that while, in principle, one would measure the (modeling) error power spectrum as an average of different simulations, due to the computational requirements inherent in simulating the HI field we are forced to use the same single simulation to fit for the bias parameters and measure error spectra, and then use it as mock data for reconstruction. This could potentially lead to overfitting, improving the reconstruction by underestimating the error spectra and ignoring cosmic variance. To check this, we estimate the error power spectra for modeling the halo mass field on a set of (cheaper) simulations with smaller boxes and poorer resolution, where the problem of cosmic variance if anything should be worse. We find that using the bias parameters fit for a one simulation and estimating the error spectra on other simulations, the error power spectrum varies. However its ratio with the error power spectrum for the 'fit' simulation is not consistently greater than 1, as one would have expected in case of overfitting but has a distribution around 1 on all scales of interest. Hence while one would need to quantify the distribution of this error spectra to get uncertainties on the reconstructed field, we do not find any evidence that using the same simulation as mock data and to estimate error spectra leads to any overfitting or an artificially good reconstruction.

## Noise

So far we have ignored the presence of noise and the foreground wedge in our data. While shot noise is included automatically if we use the HI realization in the simulations, we must

[7] https://en.wikipedia.org/wiki/Limited-memory_BFGS

handle foregrounds explicitly. Due to the foreground wedge, $w$, we loose all the information in the modes below a certain cut-off $k_\parallel/k_\perp$, as shown in Fig. 5.1. To take this into account in our reconstruction, we simply drop these modes from our likelihood term.

In addition to the wedge, 21-cm surveys also suffer from thermal noise that dominates on small scales and has angular dependence with respect to the line of sight. As outlined previously in Eq. 5.13, this is incorporated by drawing a Gaussian noise realization, $n(\mathbf{k})$, with zero mean and noise power spectrum, $P_{\rm th}(k,\mu)$ that is then used to added to our simulated data ($\delta_{\rm HI}$) to generate our mock data $\delta^n_{\rm HI}$. Including both effects our final posterior is :

$$\mathcal{P}_w = \sum_k \frac{1}{\mathrm{N}_{modes}(k)} \left( \sum_{\substack{\mathbf{k},|\mathbf{k}|\sim k,\\ \mathbf{k}\notin w}} \frac{|\delta^b_{\rm HI}(\mathbf{k}) - \delta^n_{\rm HI}(\mathbf{k})|^2}{P_{err}(k,\mu)} + \sum_{\mathbf{k},|\mathbf{k}|\sim k} \frac{|\mathbf{s}(\mathbf{k}))|^2}{P_{\rm s}(k)} \right) \tag{5.19}$$

The error power spectrum, $P_{err}$, is now a combination of the modeling error (as before) and the noise power spectrum. This changes the amplitude of $P_{err}$, especially on small scales, and also introduces an angular dependence. We have indicated this by the additional $\mu$ dependence in $P_{err}$ in the likelihood term of $\mathcal{P}_w$. Note the data automatically include shot-noise, since we have a single realization of the halo field in the simulation.

## Annealing

Reconstructing the initial modes by minimizing Eq. 5.18 is an optimization problem in a high dimensional space with both the number of underlying features (initial modes) and the number of data points (grid cells) being in millions. Despite using gradient and approximate Hessian information, it is a hard problem to solve. Since we are aware of the underlying physics driving our model, as well as its performance, we use our domain knowledge to assist the convergence of the optimizer by modifying the loss function over iterations rather than simply brute-forcing the optimization with the vanilla loss function. A more detailed discussion on these schemes is provided in refs. [211, 88, 156]. Here we briefly summarize the two annealing schemes that we use to improve our performance

- Residual smoothing : Both the dynamics and the bias model are more linear on large scales than smaller scales. Hence the posterior surface is more convex on these scales and convergence is easier. However since the number of modes scales as $k^3$, the large scale modes are a small fraction of the total and are harder for the optimizer to reconstruct in practice. To mitigate this we smooth the residual term of the loss function on small scales with a Gaussian kernel. Thus on these scales, the prior pulls down the small scale power to zero and we force the optimizer to get the large scales correct first.

- Upsampling: To minimize the cost of reconstruction, we begin our optimization on a low-resolution grid and reconstruct all the modes following the residual smoothing. Upon convergence, we upsample the converged initial field to a higher resolution grid and paint our HI data on this grid as well. Since the higher resolution has information to smaller scales, this allows us to leverage these scales to improve our reconstruction. Further, since the largest scales have already converged on the lower resolution, they remain mostly unchanged and we do not need to repeat the residual smoothing on all the scales for this higher resolution.

## 5.7 Results

We present the results for our reconstruction in the section. Our primary metrics to gauge the performance of our model as well as reconstruction are the cross correlation function, $r_{cc}(k)$, and transfer function, $T_f(k)$, defined as

$$r_{cc}(k) = \frac{P_{XY}(k)}{\sqrt{P_X(k)P_Y(k)}} \qquad , \qquad T_f(k) = \sqrt{\frac{P_Y(k)}{P_X(k)}} \quad , \tag{5.20}$$

and the error power spectrum, $P_{err}$, defined in Eq. 5.16. These metrics will always be defined between either the model or the reconstructed fields as $Y$ and the corresponding true field as $X$ unless explicitly specified otherwise.

To gain some intuition for these functions it may be helpful to recall the results for the linear case. For Gaussian signal, $\mathbf{s}$, with covariance S, and Gaussian noise, $\mathbf{n}$, with covariance N and a data vector $\mathbf{d} = \mathbf{s} + \mathbf{n}$, the posterior is given by $P(s|d) \propto P(d|s)P(s)$ which is the product of two Gaussians. The MAP solution is given by the well-known Wiener filter[8] [254]

$$\tilde{s} = \mathrm{S}\,(\mathrm{S} + \mathrm{N})^{-1}\,\mathbf{d} \equiv W\mathbf{d} \qquad . \tag{5.21}$$

For stationary problems both S and N are diagonal in Fourier space. In this simple case $r_{cc}(k) = T_f(k) = W^{1/2}$. In the limit of very small noise, $P_N/P_S \ll 1$, the measurements are a faithtful representation of the true field and $W^2 = r_{cc} = T_f \simeq 1$. In the limit of very large noise, $P_N/P_s \gg 1$, the filter becomes prior dominated and the most-likely value of $\mathbf{s}$ is zero. In this limit $W^2 = r_{cc} = T_f \to 0$.

In our case, there is a non-linear transformation at the heart of the model, i.e. $\mathbf{d} = \mathcal{F}(\mathbf{s}) + \mathbf{n}$. Therefore the Wiener filter is no longer the solution, but much of the same intuition applies. In particular $r_{cc}$ measures how faithfully the reconstructed map describes the input map, up to rescalings of the output map amplitude. The transfer function, on the other hand, tells us about the amplitude of the output map as a function of scale, with $r\,T_f = P_{XY}/P_X$.

### Bias model

We begin by evaluating the performance of our bias model using the known initial conditions in the simulation and the aforementioned three metrics, and compare the error power

[8] https://en.wikipedia.org/wiki/Wiener_filter

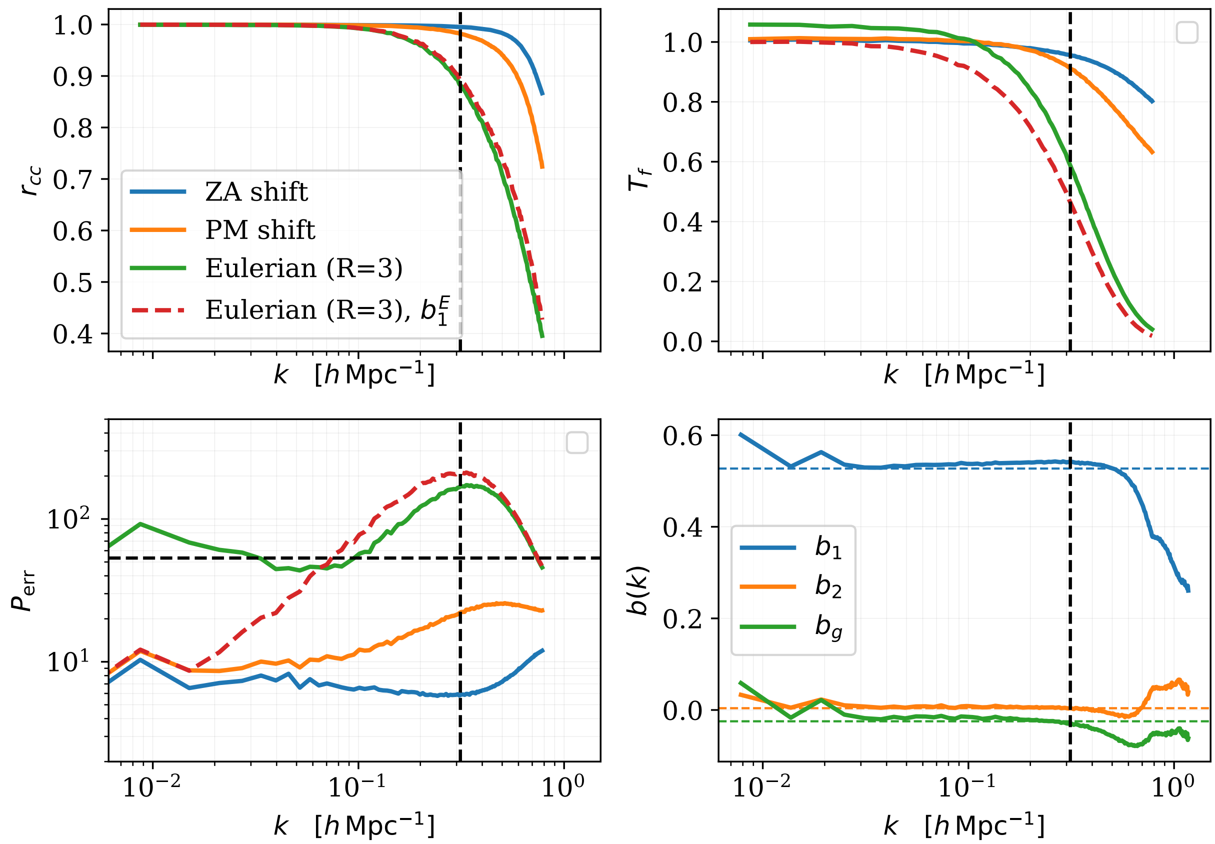


Figure 5.15: Comparison of different bias models through the real-space cross-correlation (top left) and transfer function (top right) at $z = 2$. Blue and orange lines correspond to the Lagrangian bias model with Zeldovich and N-body dynamics respectively. The green line corresponds to an Eulerian bias model through quadratic order, while the dashed red line is a simple linear bias model in Eulerian space. In both cases the Eulerian fields are smoothed with a Gaussian kernel of $3\,h^{-1}$Mpc. The vertical dashed-black line corresponds to the $k_{max}$ upto which the the error is minimized. (Bottom left) Comparison of different bias models at the level of the error power spectrum. The dashed black line is the 'Poisson' shot noise for the HI-mass-weighted field. (Bottom right) The scale dependence of the bias parameters for the Lagrangian bias model with Zeldovich dynamics. The dashed lines correspond to our default assumption: the scale-independent fits to $k < 0.3\,h\,\mathrm{Mpc}^{-1}$ data.

| | Model A | | | | Model B | | | |
|---|---|---|---|---|---|---|---|---|
| $z$ | $b_1$ | $b_2$ | $b_g$ | $T_f(k)$ | $b_1$ | $b_2$ | $b_g$ | $T_f(k)$ |
| 2 | 0.528 | 0.006 | -0.023 | $0.98 - 0.197\,k^2$ | 0.55 | -0.025 | -0.012 | $0.97 - 0.222\,k^2$ |
| 4 | 0.434 | 0.046 | -0.011 | $0.993 - 0.110\,k^2$ | 0.446 | 0.102 | -0.012 | $0.99 - 0.151\,k^2$ |
| 6 | 0.399 | 0.094 | -0.009 | $0.995 - 0.112\,k^2$ | 0.378 | 0.16 | -0.011 | $0.984 - 0.187\,k^2$ |

Table 5.3: The best-fit bias parameters (and transfer function) to the HiddenValley simulation HI fields for models A and B of ref. [158] at $z = 2$, 4 and 6. The bias parameters are defined on a $2\,h^{-1}$Mpc grid (see text).

spectrum with the HI-mass-weighted shot noise. The statistics for the best fit to the HI field at $z = 2$ are shown in Fig. 5.15. Though not shown in this figure, the results for $z = 4$ and 6 are very similar. Fig. 5.15 compares three different bias models: two Lagrangian bias models (as described in Section 5.6), with Zeldovich dynamics and PM dynamics[9] respectively, as well as an Eulerian bias model where the three bias parameters are defined with respect to the fields generated from the Eulerian matter field smoothed at $3\,h^{-1}$Mpc with a Gaussian smoothing kernel. In addition, we show the simple case of linear Eulerian bias ($b_1^E$) to contrast with our other biasing schemes.

Firstly, comparing the Eulerian and Lagrangian bias models, we find that Lagrangian bias outperforms Eulerian bias at the level of cross-correlation and transfer function on all scales. Lagrangian bias models also lead to quite scale independent error power spectra and much lower noise than the Poisson shot-noise level, while this is not the case for Eulerian models. This implies that we can do analysis with higher fidelity than one would expect from the simplest Poisson prediction and are able to access information to smaller scales. This is in general agreement with the findings of ref. [206] for halos at different number densities and weightings. Note that while the linear-Eulerian model is a subset of the quadratic-Eulerian model, it performs worse at the level of cross-correlation. This is because the metric for fitting bias parameters is minimizing the noise power spectrum up to $k \simeq 0.3\,h\,\mathrm{Mpc}^{-1}$ where the quadratic Eulerian model is better than the linear bias model.

Amongst Lagrangian bias models we find that the Zeldovich displacements perform better in terms of the cross correlation and the transfer function with our observed HI data field and resolution than the PM dynamics. One can increase the accuracy of the PM displacements by instead increasing the number of time steps or using force resolution $B = 2$ for the PM simulations and we find that this improves the model slightly over ZA but makes the modeling much more expensive. Moreover, the difference between the performance of the two dynamics also depends on the resolution of the meshes used to do simulations. Currently, we are modeling the data from a much higher resolution simulation ($20480^3$ force mesh) with a quite 'low' resolution ($256^3$ or $512^3$ mesh) PM or ZA dynamics so its not obvious how

[9] Here, our PM dynamics corresponds to a FastPM simulation on a $512^3$ grid with 5 time steps and force resolution $B = 1$, i.e. a $512^3$ mesh for the force computation. For comparison, the HI data was generated on a $10240^3$ grid with 40 steps to $z = 2$ and force resolution $B = 2$.

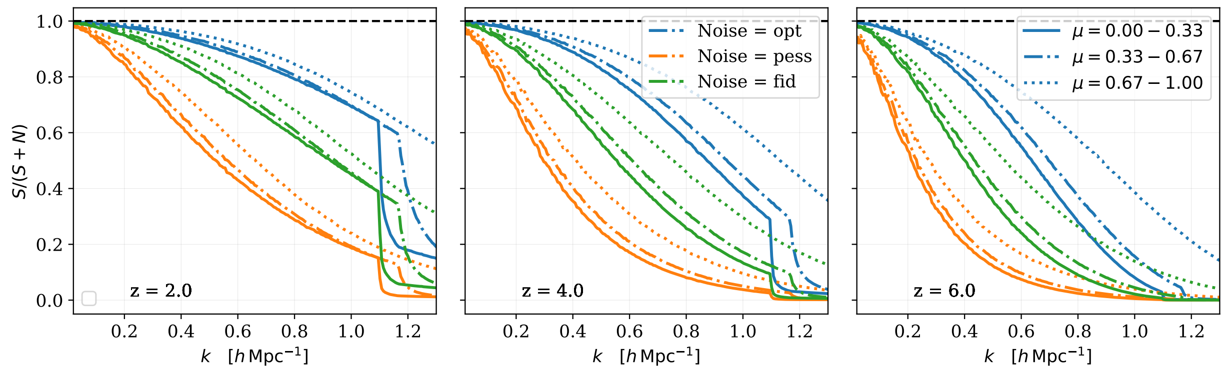


Figure 5.16: Ratio of signal to total signal and noise in our HI data at different redshifts as a function of scale and angle ($\mu$ bins) for the three different thermal noise cases considered for reconstruction. Here we have neglected any loss of modes due to foregrounds.

they should compare, but we do find the performance of PM improving as we increase the resolution of models as might be expected.

Another way to improve the bias model is to add a term corresponding to $b_\nabla^2$ which comes with $k^2$ dependence motivated by peaks bias as well as effective field theory counter-terms. We find that adding such a term does not change the two models at the level of cross-correlation, but significantly improves the PM model over ZA at the level of the transfer function. Going one step further, one can also make the bias parameters scale dependent and use them as transfer functions. To assess the scale dependence of the bias parameters, in the lower-right panel of Fig. 5.15 we also show the scale dependent bias parameters for the Zeldovich bias model which are fit for by minimizing the error power spectrum independently for every $k$-bin. The best-fit bias parameters still do not have any significant scale dependence up to intermediate scales. As mentioned in previous section, this explains why we find that the fit of bias parameters is quite insensitive to the $k-$range used for fitting the bias model, as long as we do not fit up to highly non-linear scales.

Given the differences in performance of ZA and PM dynamics, how scale-dependent the biases are on the small scales that begin to get increasingly noise dominated in the data and the cost of the ZA vs. PM forward models, we find the performance of a scale-independent bias model with ZA dynamics to be sufficient for reconstruction. Henceforth, we present results for the reconstruction with this model. However we suspect that it would be worth studying the performance of different bias models in more detail. Our comparison is also likely to change for different number densities and weightings (such as position, mass, HI mass etc.) of the biased tracers. We leave such a detailed study to future work.

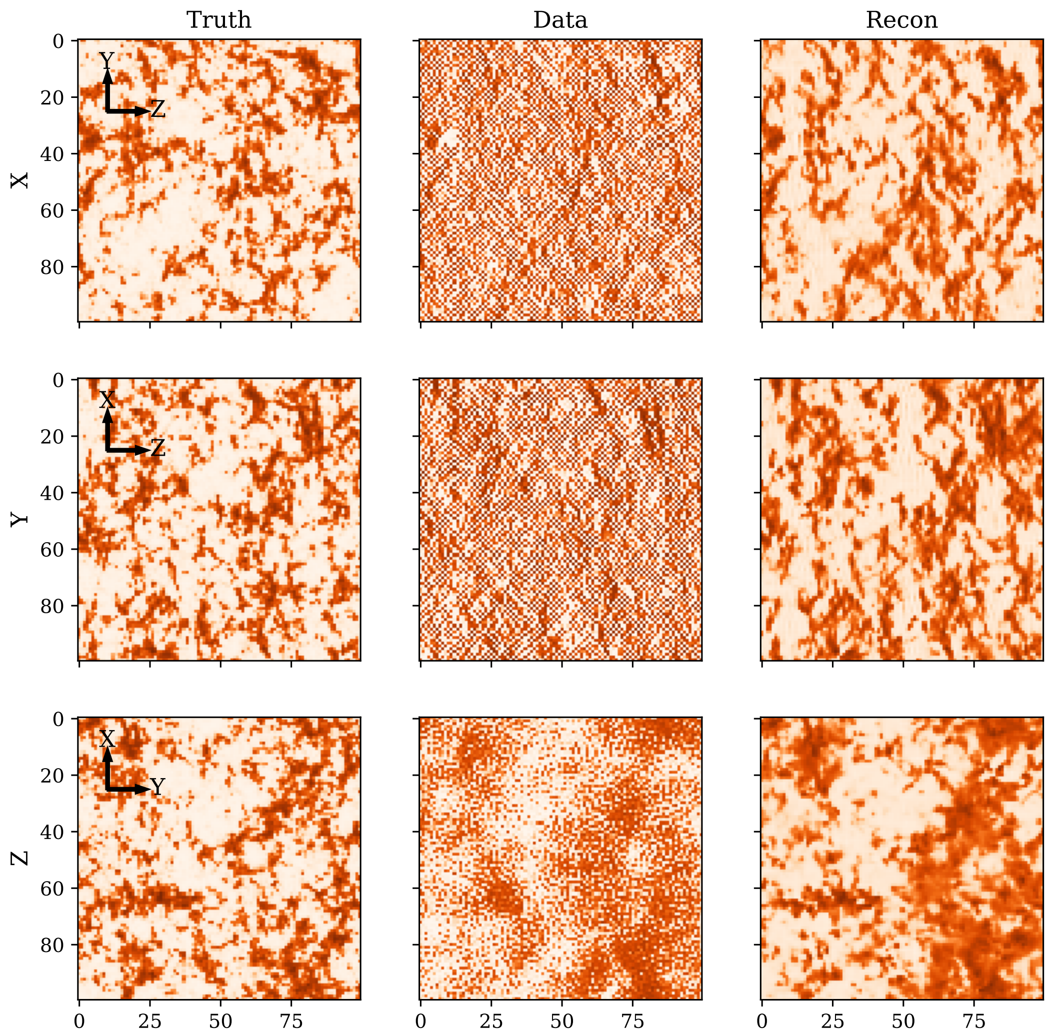


Figure 5.17: Different projections for the true HI field, data corrupted with thermal noise and a foreground wedge and our reconstructed HI field at redshift $z = 4$ for our fiducial thermal noise corresponding to 5 years of observing with a half-filled array but for a pessimistic wedge ($k_{\parallel} = 0.03\,h\,\mathrm{Mpc}^{-1}$, $\theta_w = 38°$). Different rows show $20\,h^{-1}$Mpc thick slices when projected along the axis specified by the $y$-axis label. The horizontal and vertical image dimensions correspond to $200\,h^{-1}$Mpc and correspond to direction specified by arrows on top left for every row. The line of sight of the data is along the $Z$ axis. We use a log-scale color scheme and the color-scale is same for all the panels in the same row.

## Reconstruction

### Configurations

In this section, we show the results for the reconstruction of the initial and HI field. We do reconstruction on our $1024\,h^{-1}$Mpc box at redshifts $z = 2$, 4 and 6. The line of sight is always assumed to be along the $z$-axis. Unless otherwise specified, we will show the reconstruction for our fiducial setup which is reconstruction in redshift space, with thermal noise corresponding to 5 years with a half-filled array, $k_{\parallel}^{min} = 0.03\,h\,\mathrm{Mpc}^{-1}$ and an optimistic foreground wedge ($\theta_w = 5°$, $15°$ and $26°$ at $z = 2$, 4 and 6). To gauge the impact of our assumptions regarding this fiducial setup, we will show comparisons with other setups which include a pessimistic foreground wedge (dashed) corresponding to $\theta_w = 15°$, $38°$ and $55°$ at $z = 2$, 4 and 6 respectively, and different thermal noise configurations corresponding to a full-filled array (optimistic case) and a quarter filled array (pessimistic case).

To gain some intuition about how these noise configurations compare with the signal, we also show the ratio of signal to signal plus noise in Fig. 5.16 as a function of scale and angle for different redshifts. Since the impact of the foreground wedge is binary with respect to scale and angle, we have ignored the loss of modes due to it in plotting Fig. 5.16. However to emphasize how severe the loss of information due to the wedge is, at redshift $z = 2$, 4 and 6 we completely loose 21(7)%, 60(21)% and 88(40)% of the modes due to the pessimistic (optimistic) foreground wedge. When we include the thermal noise, even in the fiducial case, a further 30(43)%, 24(51)% and 9(37)% of the modes outside the wedge become noise dominated. Thus we preface our results by re-iterating that reconstructing the large-scale modes is a non-trivial problem in these situations.

### Annealing: Implementation

To implement our annealing scheme we begin with a $256^3$ mesh and anneal by smoothing the loss-function at smoothing scales corresponding to 4, 2, 1, 0.5 and 0 cells. For the given resolution, this roughly corresponds to $k \sim 0.2$, 0.4, 0.8 and $1.6\,h\,\mathrm{Mpc}^{-1}$. Thus even in the case of largest smoothing, we still have enough small scale modes outside the wedge to inform reconstruction. We find that the statistics of interest stop changing roughly after $\sim$ 100 iterations, thus we do this many iterations for every step of annealing before declaring it 'converged'. After converging on this mesh, we upsample our reconstructed initial field to a $512^3$ grid and repeat our reconstruction exercise starting from this point while comparing to data now painted on this higher resolution grid. At this stage, we do residual smoothing only corresponding to 1 and 0 cells, 100 iterations each.

We have tried other annealing methods, such as different smoothing scales and other upsampling schemes. In addition, to study convergence, we have also let the optimizer run for longer, increasing the number of iterations. We find that none of these choices have a significant impact, and while running more iterations can improve results marginally, our aforementioned implementation provides a good balance between computational cost and performance for this work. Moreover, given the heuristic nature of our annealing scheme, its not obvious if we will converge to a unique solution. To study this, we run simulations with different initial conditions and find that the reconstructed fields are correlated well enough, and hence identical, on the scales of interest here.

### Reconstructed field : Visual

Before gauging our reconstruction quantitatively, we also first visually see the impact of noise and reconstruction at the level of the field to develop some intuition. Fig. 5.17 shows different projections of the true HI field, as well as the data which is now corrupted with thermal noise in addition to the foreground wedge and our reconstructed HI field for our fiducial thermal noise corresponding to 5 years of observing with a half-filled array but for a pessimistic wedge ($k_\parallel = 0.03\,h\,\mathrm{Mpc}^{-1}$, $\theta_w = 38°$) at $z = 4$. The line of sight direction is Z. As expected from Fig. 5.16, where the signal is close to zero on small scales, the data is heavily corrupted with small scale noise and the noise is higher when we take the sum over the transverse direction than when along the line of sight. In fact, visually, one can only faintly distinguish the biggest structure peaks in the corrupted data from noise and its impressive how well we are able to reconstruct smaller structures in the HI field despite this. Due to the foreground wedge, the structures seem to be stretched in the transverse direction in the data. This can also be seen by comparing first two rows with the last, where structures are more isotropic since the stretching is the same in both transverse directions. For the reconstructed field we have visibly reduced this stretching by reconstructing modes in the wedge. Overall the reconstructed field is smoother than the input data, since we do not fully reconstruct the small-scale modes.

### Reconstructed field : Two point function

Next, to quantitatively see how the foreground wedge and thermal noise combined affects our data, we estimate the cross-correlation and transfer function of this noisy input data with the true HI field. This is shown in Fig. 5.18 for $z = 2$, 4 and 6 as thin lines. In addition to our fiducial setup, we also consider other configurations for the wedge and thermal noise as outlined at the beginning of this section. This figure contrasts with Fig. 5.16 since there we neglected the loss of modes due to foreground wedge and only focused on thermal noise. For the combined noisy data, the transfer function with respect to the true HI field is zero on the largest scales ($k < 0.03\,h\,\mathrm{Mpc}^{-1}$) since these modes are completely lost to the foregrounds and we have no information on these scales. On intermediate scales, the cross correlation and transfer function increase but are still well below unity since some modes are still lost to the wedge in every $k-$bin, and as per our expectations, this loss is greater in the pessimistic wedge case. On the smallest scales, the transfer function exceeds one since these modes are dominated by thermal noise. However the cross-correlation on these scales drops rapidly since this noise is uncorrelated to the data and contains no information.

For comparison, we show as thick lines in Fig. 5.18 the cross-correlation and transfer function of the reconstructed HI field with true HI field. This highlights how our recon-

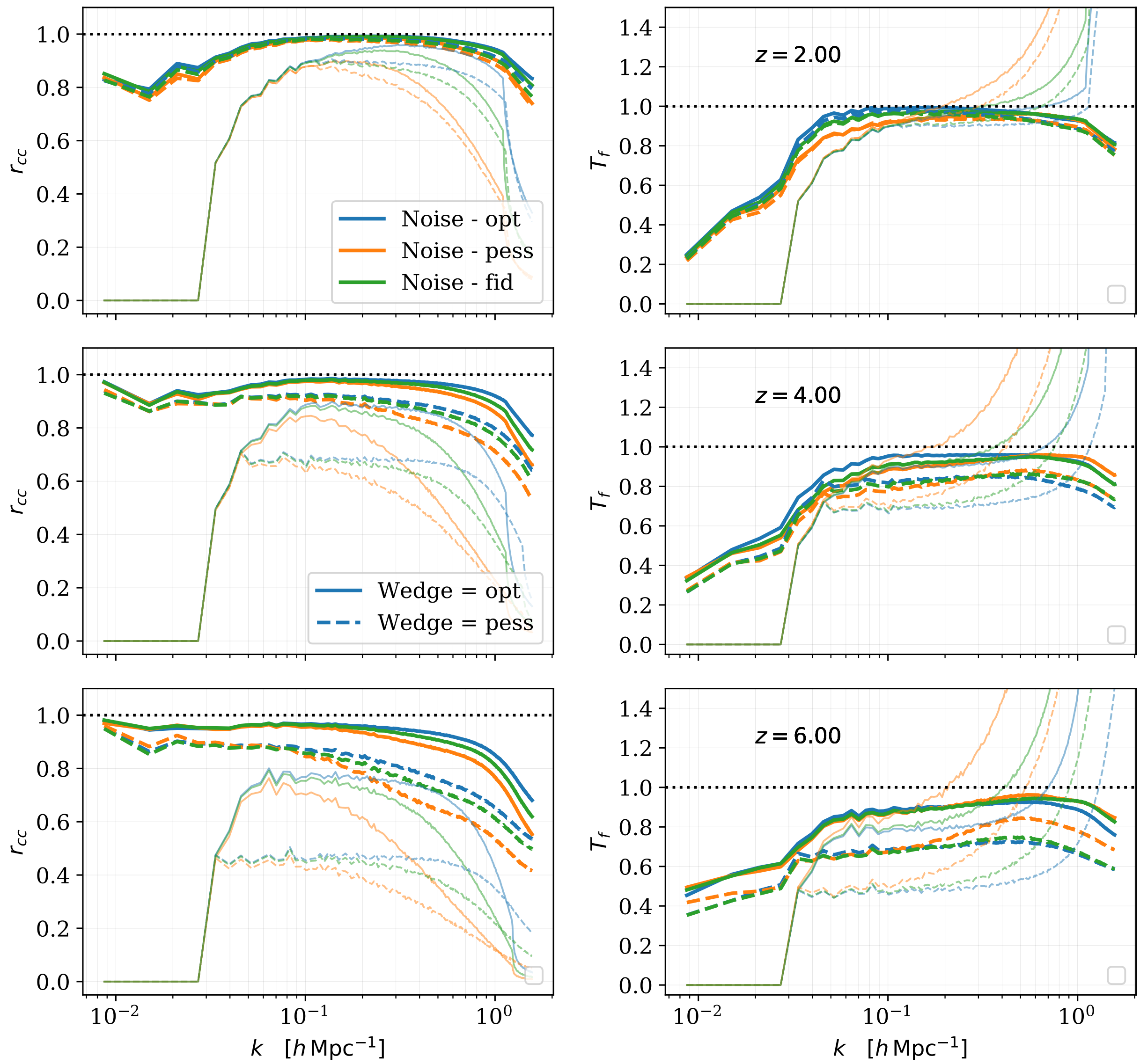


Figure 5.18: We show the cross-correlation (left) and transfer function (right) of the reconstructed HI field at $z = 2$, 4 and 6 for three different thermal noise levels as well as two wedge configurations (optimistic and pessimistic; see text for more details). For comparison, we also show these quantities for the noisy and masked data which was used as the input for reconstruction with light colors.

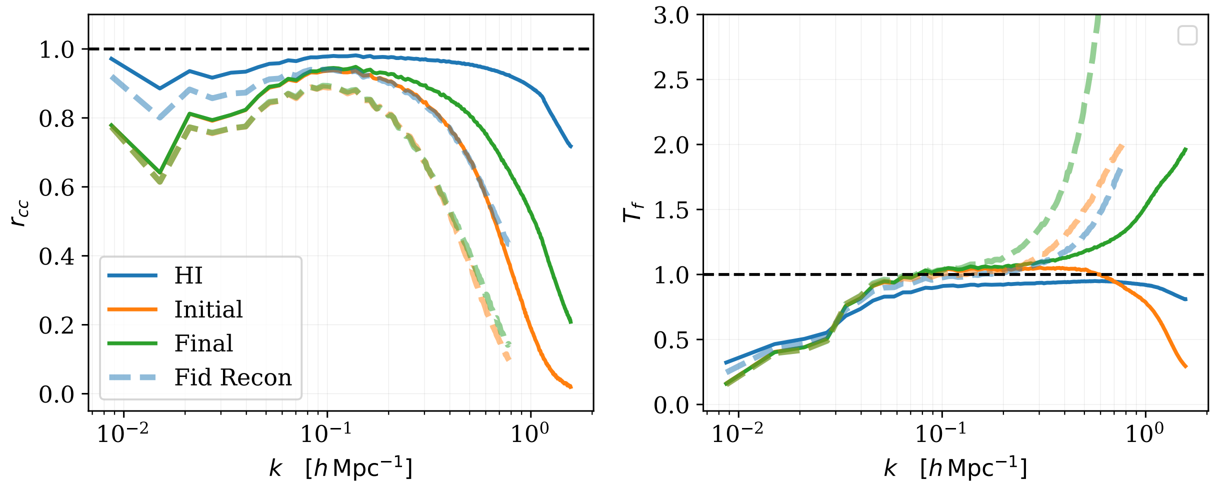


Figure 5.19: The cross-correlation (left) and transfer function (right) at $z = 4$ for the reconstructed initial matter, final matter and HI field with their corresponding true fields. We have assumed 5 years of observing with a half-filled array, $k_{\parallel}^{min} = 0.03\,h\,\mathrm{Mpc}^{-1}$ and $\theta_w = 15°$. The dashed lines are for reconstruction on the fiducial $256^3$ mesh while the solid lines are reconstruction after upsampling to a $512^3$ mesh, which leads to significant gains.

struction helps in recovering the information lost due to foregrounds and thermal noise. The gains in cross-correlation coefficient over noisy data are quite impressive, reaching $\sim 0.8$, 0.9, 0.96 for the optimistic wedge on the largest scales for $z = 2$, 4 and 6 respectively where we have access to no modes in the data. The modes in this regime are constructed only out of mode coupling due to no-linear evolution. On intermediate scales, where the data have the most information, the cross correlation reaches 1 for all redshifts while it drops again (to below 0.8) on the smallest scales which are thermal noise dominated. A similar trend is observed in the transfer function, where we recover $\sim 40$, 50 and 60% of the largest scales lost completely to the foregrounds for $z = 2$, 4 and 6 respectively. We recover more power as we move to smaller scales, with the transfer function reaching close to unity on intermediate scales $k \simeq 0.1\,h\,\mathrm{Mpc}^{-1}$ before starting to decrease at the smallest, noise dominated scales.

Reconstruction is slightly worse in the case of pessimistic wedge, with higher redshifts paying a higher penalty simply due to the larger difference in the two configurations. However the cross-correlation is still $\simeq 80\%$ at $z = 6$ on the largest scales, even in the most pessimistic setup. While the foreground wedge affects reconstruction on all scales, thermal noise does not affect reconstruction on the large scales. On small scales, reconstruction is slightly worse with increasing noise, again penalizing higher redshifts more than lower redshifts.

With our procedure, along with reconstructing the observed data, we also reconstruct the initial and final matter field. Its instructive to see how close are these to the true fields since they have different science applications. The initial (Lagrangian) field can be used to reconstruct Baryon Acoustic Oscillations (BAOs), while the final matter field across redshifts has applications in CMB and weak lensing science. Here we briefly look at the recovery of these fields. In Fig. 5.19, we show the cross-correlation and transfer function of the reconstructed initial matter, final matter and HI field for our fiducial setup at $z = 4$. As for the HI data field, the cross correlation and transfer function increases as we go from large to intermediate scales since the large scales are completely absent in the data due to foreground wedge. Since the information moves from larger scales to small scales during non-linear evolution, the cross correlation of the reconstructed final-matter and HI field are much better on smaller scales than the initial field. While the transfer function for initial and HI field drops on small scales due to thermal noise, that of final matter field increases over 1. This is simply because our dynamic model for reconstruction is the Zeldovich approximation while the true data was generated by particle-mesh simulations.

In Fig. 5.19 we also show how upsampling improves the performance of reconstruction. The dashed lines show the reconstruction on the fiducial $256^3$ grid, without any upsampling, while the solid lines show the results when continuing reconstruction after upsampling the reconstructed field to a $512^3$ mesh. Since the higher resolution allows us to push to smaller scales it increases the number of modes not dominated by thermal noise while also recovering some of the signal that was earlier lost due to grid-smoothing on these scales. We find large gains in our reconstruction for all three fields. While we have not pushed to even higher resolution due to CPU limitations, we suspect it would yield diminishing returns since the smaller scales are dominated by thermal noise.

#### Impact of $k_\parallel^{\mathrm{m}in}$

While changing the thermal noise and wedge configurations, we have so far kept the $k_\parallel^{\mathrm{m}in}$ fixed at $k_\parallel^{\mathrm{m}in} = 0.03\,h\,\mathrm{Mpc}^{-1}$. In Fig. 5.20, we show how the reconstruction performs for different values of $k_\parallel^{\mathrm{m}in}$, and compare it to the hypothetical case where we loose no modes to foregrounds. Again, we consider our fiducial setup at $z = 4$ with optimistic wedge ($\theta_w = 15°$) and thermal noise corresponding to 5 years of observing with a half-filled array without upsampling annealing. Reconstruction on all scales is slightly worse than the case when we loose no modes to the foregrounds, but not by much. We find that for a given wedge, small scales are quite insensitive to the $k_\parallel^{\mathrm{m}in}$ threshold. On large scales, reconstruction gets progressively worse to smaller $k$ as we increase $k_\parallel^{\mathrm{m}in}$. However even for the most pessimistic case, $k_\parallel^{\mathrm{m}in} = 0.05\,h\,\mathrm{Mpc}^{-1}$, the cross correlation is better than 0.8 on the largest scales. Furthermore upsampling annealing would improve the reconstruction on all scales.

#### Real vs. redshift space

Its also instructive to compare reconstruction in real and redshift space, since this gives us access to new signal (through the velocity field) but it is often the case that one loses power

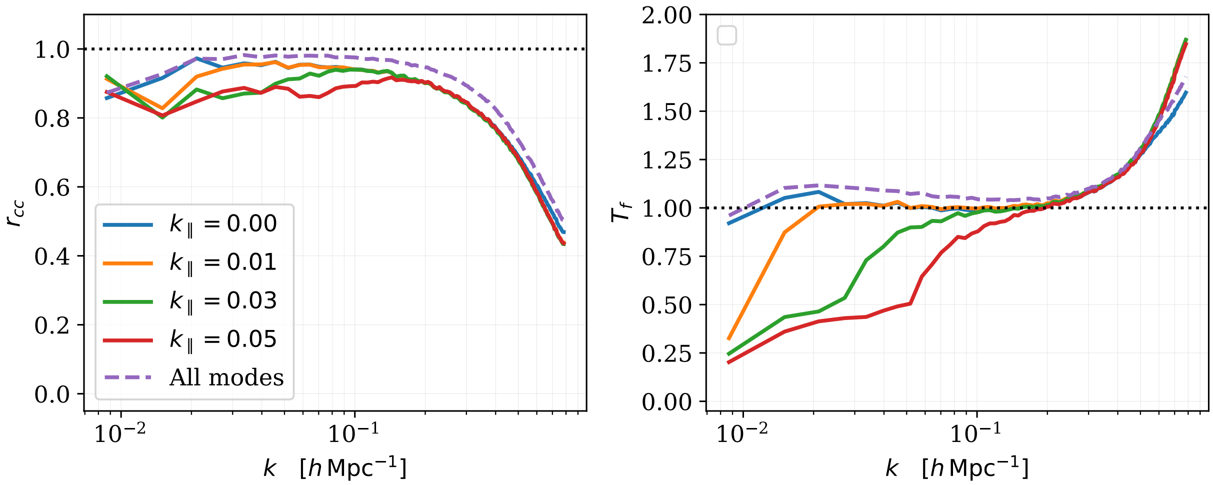


Figure 5.20: The cross-correlation (left) and transfer function (right) at $z = 4$ with an optimistic wedge ($\theta_w = 15°$) and fiducial thermal noise (corresponding to 5 years of observing with a half-filled array) for different $k_\parallel^{min}$ (in $h\,\mathrm{Mpc}^{-1}$), without upsampling. For comparison, we also show the case where we do not lose any modes to foregrounds (i.e. no wedge and $k_\parallel^{min} = 0$) but have the same fiducial thermal noise (dashed line). We have checked that as the thermal noise is reduced the cross correlation moves closer to 1 as expected.

in Fourier modes in the radial direction. However for the 21-cm signal finger-of-god effects are subdominant and most of the redshift space signal can be modeled with perturbation theory [237, 158]. As a result, we find that doing reconstruction from the redshift space data improves our results over real space data. We show this in Fig. 5.21 where we compare the statistics for reconstruction in real space (dashed) and redshift space (solid) for $z = 2$, 4 and 6. We model the redshift space data by moving the Lagrangian fields to Eulerian space with Zeldovich dynamics, as before, and then using the Zeldovich velocity component along the line of sight. The velocity field information residing in the anisotropic clustering provides additional information which improves our performance in redshift space over real space. The gains are largest at $z = 6$ and decrease with decreasing redshift. This is likely because we model only the linear dynamics while non-linear RSD, as well as the finger-of-god effects, increase at lower redshifts. Using higher order perturbation theory, or the particle mesh dynamics, should improve the performance at lower $z$.

### Angular cross-correlation

Given that the line of sight and transverse modes are differently affected by foreground wedge, thermal noise and redshift space distortions, we conclude this section by looking at the cross-correlation coefficient for the reconstructed data as a function of $\mu$. This is shown

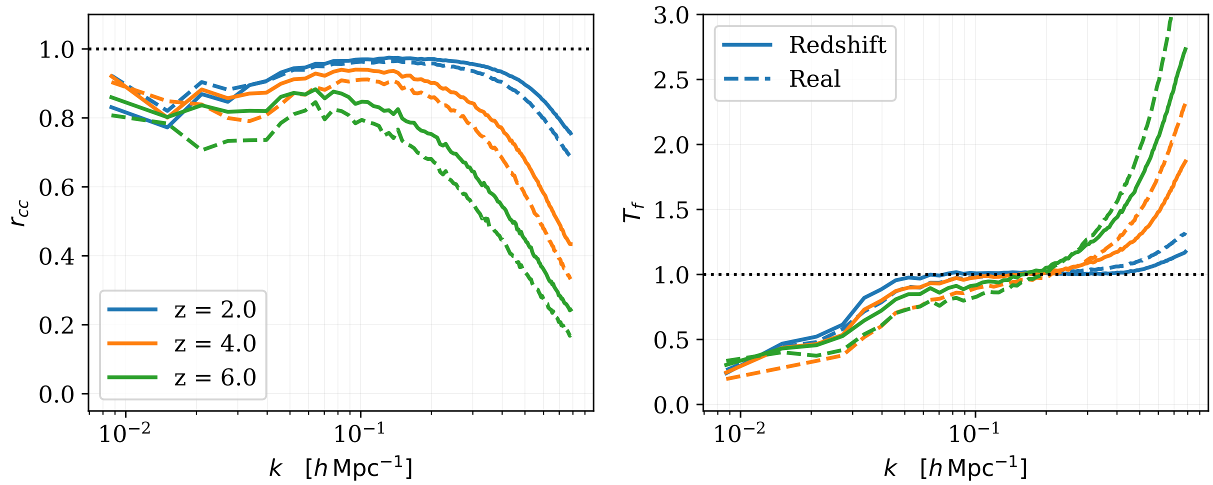


Figure 5.21: We show the cross-correlation (left) and transfer function (right) of the reconstructed HI field at $z = 2$, 4 and 6 for the fiducial noise setup and optimisitic wedge in real and redshift space. The additional information available in the redshift-space field enhances the recovery of the signal.

in Fig. 5.22 for our fiducial thermal noise model (after annealing). We recover the largest scales almost perfectly, even though we do not have any modes along the line of sight in the data. On the other hand small scale modes along the line of sight are significantly better reconstructed than the transverse modes. We find that the reconstruction of line-of-sight modes is less sensitive to the loss of modes in the foreground wedge than transverse modes. However in all cases the better foregrounds are controlled, and the smaller the wedge can be made, the better reconstruction proceeds.

## 5.8 Implications

Our ability to reconstruct long wavelength modes of the HI field has several implications, and we explore some of them here. The first two subsections discuss cross-correlation opportunities afforded by reconstruction while the last describes the improvement in BAO distance measures.

The utility of large 21-cm intensity mapping arrays is the highest in the high redshift regime, where there is a lot of cosmic volume to be explored and which is the most difficult to be accessed using other methods. While there are some fields that will cross-correlate straight-forwardly with the 21-cm data, notably the Lyman-$\alpha$ forest and sparse galaxy and quasars samples which entail true three-dimensional correlations, any field that is projected in radial direction occupies the region of the Fourier space that is the most contaminated

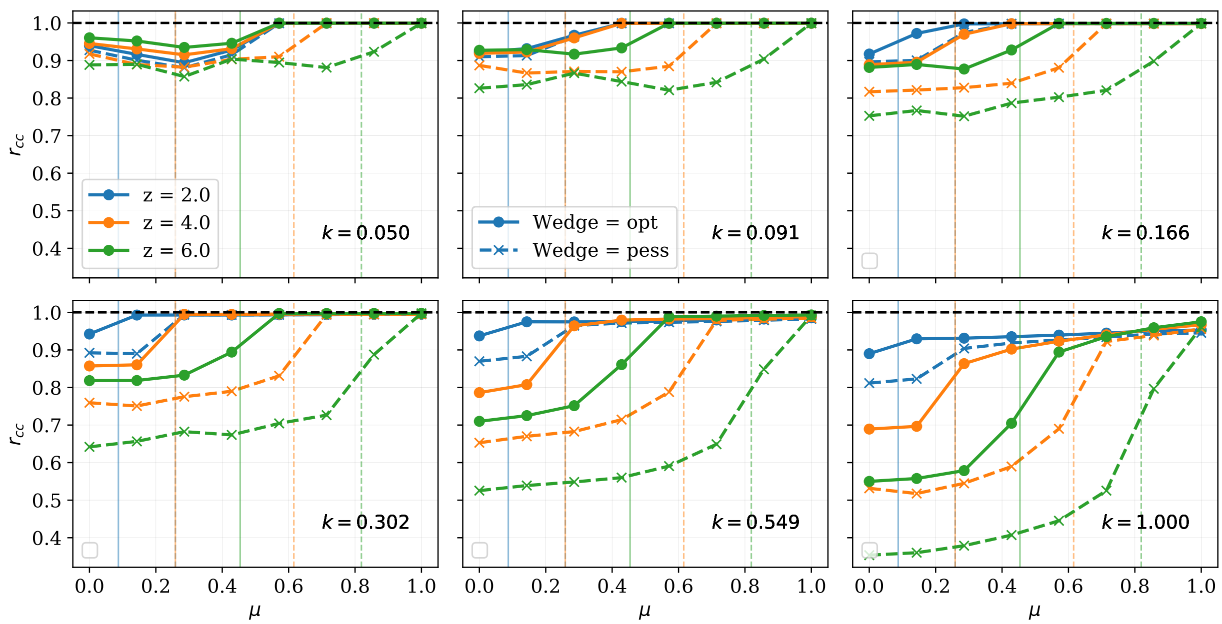


Figure 5.22: We show the cross-correlation of the reconstructed HI field with the corresponding true field as a function of the angle $\mu$ with the line of sight in different $k$ bins for fiducial thermal noise and two wedge configurations (with corresponding $\mu_{\mathrm{wedge}}$ shown as thin vertical lines) at $z = 2$, 4 and 6. All the modes are reconstructed well along the line of sight, while the large scales are reconstructed better than small scales in the transverse direction.

with the foregrounds. This technique allows us to re-enable these cross-correlations and thus significantly broadens the appeal of high-redshift 21-cm experimentation. We discuss two important examples below.

The first question that needs to addressed is whether it is preferable to cross-correlate with the reconstructed HI field or the evolved matter field or even the linear field. While there are some arguments against, we opted to use the reconstructed HI field, which we refer to simply as the "reconstructed" field. Most importantly, on scales where data are available, this field will resemble the measured data regardless of modeling imperfections. In particular, Figure 5.20 show that the HI field has a higher cross-correlation coefficient than the initial field, indicating that the modeling is imperfect but nevertheless sufficiently flexible to account for these deficiencies.

Finally we note that low-$k$ modes are extremely important in the quest for Primordial Non Gaussianities (PNG), with constraints on PNG from 21 cm survey severely hampered by the loss of long wavelength modes due to foregrounds [55]. PNG of the local-type would benefit enormously from reconstruction, which appears to be most robust way to recover the true signal at large scales free of residual foregrounds [21, 227]. The equilateral and squeezed triangle configurations could potentially also benefit, because their sensitivity is normally limited by non-linear gravitational evolution that produces similarly shaped bispectra. We intend to return to this specific case in future work.

## Redshift distribution reconstruction

A common problem facing future photometric surveys is to determine the redshift distribution of the objects, many of which may be too faint or too numerous to obtain redshifts of directly [167]. One approach is to use 'clustering redshifts', wherein the photometric sample is cross-correlated with a spectroscopic sample in order to determine $dN/dz$ of the former [110, 166, 79, 152, 149].

One difficulty with this approach for intensity mapping surveys is that, for broad $dN/dz$, the photometric sample only probes $k_\parallel \approx 0$. In linear theory the cross-correlation between a high-pass filtered 21-cm field and the photometric sample is highly suppressed. Translating a redshift uncertainty of $\delta z$ into a comoving distance uncertainty of $\sigma_\chi = c\,\delta z/H(z)$, to probe $k_\parallel = 0.03\,h\,\mathrm{Mpc}^{-1}$ requires $\delta z/(1+z) < 0.01 - 0.015$ at $z = 2-6$. Such photo-$z$ precision is in principle achievable, given enough filters, but primarily at lower redshift and for brighter galaxies [94, 132]. The more common assumption of $\delta z/(1+z) = 0.05$ corresponds to

$$\sigma_\chi \simeq 120\,h^{-1}\mathrm{Mpc}\left(\frac{1+z}{5}\right)^{-1/2} \tag{5.22}$$

for $2 \le z \le 6$. Modes with $k_\parallel = 0.03\,h\,\mathrm{Mpc}^{-1}$ are almost entirely unconstrained by such measurements.

To be more quantitative we note that such a photometric redshift uncertainty would smooth the galaxy field in the redshift direction. At very low $k$, and for the purposes of exploration, we can assume scale-independent linear bias so that on large scales we have

$$\delta_{\rm photo}(k,\mu) = \left(b_p + f\mu^2\right)\mathcal{D}\,\delta_m(\vec{k}) + \text{noise} \quad , \quad \mathcal{D}(k,\mu) \equiv \exp[-k^2\mu^2\sigma_\chi^2/2] \tag{5.23}$$

where $\delta_m(\vec{k})$ is the matter overdensity and $\mathcal{D}$ encompasses the effect of photometric redshift uncertainty which we have approximated as Gaussian. Similarly, for the true HI field, assuming scale independent bias on these scales,

$$\delta_{\mathrm{H}I}(k,\mu) = \left(b_{\rm HI} + f\mu^2\right)\,\delta_m(\vec{k}) + \text{noise} \tag{5.24}$$

Using Eq. 5.20 the cross-power spectrum with $\delta_{\rm rec}$ is then given by

$$P_\times(k,\mu) \equiv \langle\delta_{\rm rec}\delta_{\rm photo}\rangle = \frac{b_p + f\mu^2}{b_{\rm HI} + f\mu^2}\,\mathcal{D}(k,\mu)\ r(k,\mu)T_f(k,\mu)\ P_{HI}(k,\mu) \tag{5.25}$$

At high redshift both the galaxies and HI are highly biased and we are interested in $\mu \approx 0$ modes so the first factor becomes $b_p/b_{HI}$ which simply rescales the amplitude of $T_f$. Eq. 5.25

shows why we need to reconstruct the low $k$ modes in order to achieve a significant signal in cross-correlation: $\mathcal{D}$ highly damps the signal at high $k_\parallel$ and without reconstruction $rT_f \to 0$ at low $k_\parallel$.

For Gaussian fields the variance of the cross-correlation is $\mathrm{V}ar\left[\delta P_\times\right] = N_{\mathrm{m}odes}^{-1}\left(P_\times^2 + P_{\mathrm{p}hoto}P_{\mathrm{rec}}\right)$ where $N_{\mathrm{m}odes}$ is the number of independent modes in the bin and $P_{\mathrm{rec}} = T_f^2 P_{HI}$ is the reconstructed auto-spectra of HI field along with the reconstruction noise. Additionally, the auto-spectrum $P_{\mathrm{p}hoto}$ includes a contribution from the noise auto-spectrum, which we assume to be shot-noise: $\bar{n}^{-1}$. In this limit

$$P_{\mathrm{p}hoto} = \left(b_p + f\mu^2\right)^2 \mathcal{D}^2 P_m + \frac{1}{\bar{n}} \tag{5.26}$$

where $P_m$ is the matter power spectra. Thus,

$$\frac{\mathrm{V}ar[P_\times]}{P_\times^2} \simeq N_{\mathrm{m}odes}^{-1}\left(1 + \rho^{-2}\right) \tag{5.27}$$

where

$$\rho^2 = \frac{P_\times^2}{P_{\mathrm{photo}}P_{\mathrm{rec}}} = r^2 \frac{b_p^2 \mathcal{D}^2\, \bar{n} P_m}{1 + b_p^2 \mathcal{D}^2\, \bar{n} P_m} \tag{5.28}$$

quantifies the effective signal and plays the role of the more familiar $\bar{n}P$ that frequently appears in power spectrum errors [82]. An important caveat here is that to estimate $\rho$ as a function of $\mu$, the correct way is to integrate over the $\mu$-bin, and not simply to estimate it at the bin-center. Since the photometric damping kernel scales as $\mu^2$, estimating at the bin center causes over damping and the impact is especially severe for the smallest $\mu$ bin as modes with $\mu \to 0$ should effectively be undamped.

For clustering redshifts with dense spectroscopic samples most of the weight comes from transverse modes near the non-linear scale. For example, the optimal quadratic estimator for $dN/dz$ ([149]; § 5.1) weights $P_\times(k_\perp, k_\parallel \approx 0)$ with $P_{\mathrm{photo}}^{-1}(k_\perp, 0)$ which typically peaks at several Mpc scales. Similarly the estimator of ref. [152] has weights proportional to $J_0(kr)$ integrated between $r_{\mathrm{m}in}$ and $r_{\mathrm{m}ax}$. Taking $r_{\mathrm{m}in}$ to be large enough that 1-halo terms are small leads to similar scales being important. As shown in Fig. 5.22 the transverse modes at intermediate scales are quite well reconstructed by our procedure, suggesting that 21-cm experiments would provide highly constraining clustering redshifts even for very high $z$ populations.

As an example to show how well we are able to cross-correlate photometric surveys with the reconstructed HI field, we consider a strawman survey at redshift $z \approx 4$, as outlined in ref. [255], that detects Lyman break galaxies (LBG) with the $g$-band dropout technique. Based on Table 5 of ref. [255] we take $\bar{n} \simeq 10^{-2.5}(\,h\,\mathrm{Mpc}^{-1})^3$ and $b \simeq 3.2$. Given these numbers, we show how the $\rho^2$ as well as noise-to-signal ratiofrom for the cross-spectra as function of scales and angles in Fig. 5.23. The solid lines are the estimates from the simulations while the dashed lines are the 'theoretical' predictions. To generate the photometric data in the simulation, we simply select the heaviest halos up to the given number density. To implement photometric uncertainties, we smooth the data with the Gaussian kernel of Eq. 5.23.

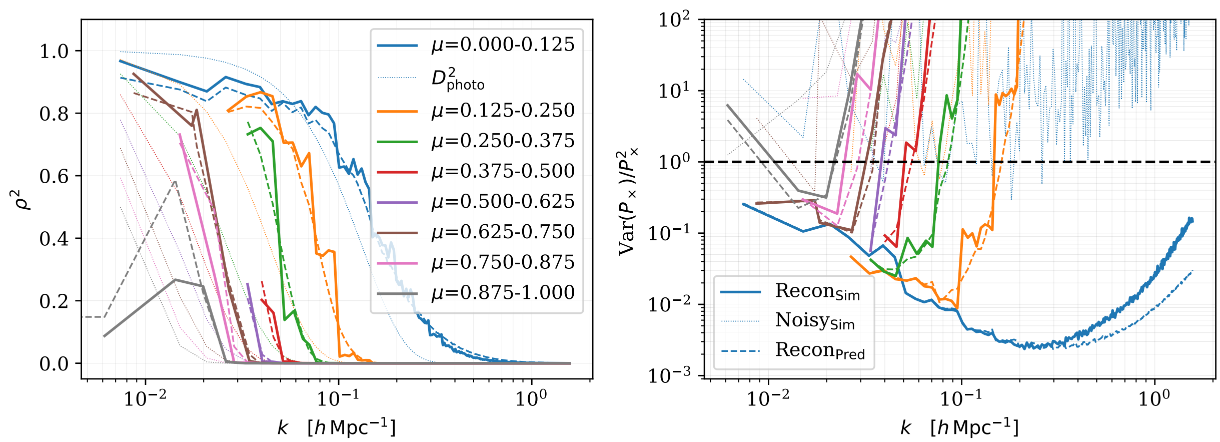


Figure 5.23: We show the effective cross-correlation ($\rho^2$, left) as well as the variance of the cross-spectra (right) of the reconstructed HI field (fiducial setup) with the photometric field at $z = 4$ and number density $\bar{n} \simeq 10^{-2.5}(\,h\,\mathrm{Mpc}^{-1})^3$, for different $\mu$-bins. The solid lines show the measurement from the simulations while the dashed lines are theoretical predicition based on Eq. 5.28. The dotted lines on the left show the photometric damping kernel of Eq. 5.23 while on the right they show the variance for the input HI data with thermal noise and wedge (see text for discussion).

An alternate way to implement photometric redshifts would be to scatter the positions of halos along the line of sight with standard deviation given by Eq. 5.22, and we find that this leads to similar results for scales where $\mathrm{V}ar[P_\times]/P_\times^2 < 1$, but becomes noisier on smaller scales. Thus here, we stick with the smoothing implementation. Given a photometric field, we then estimate its auto-spectra (with shot-noise ) and cross-spectra with the reconstructed HI field in $\mu$-bins and use Eq. 5.28 to estimate $\rho$ and correspondingly the variance. Similarly, to get the 'theoretical' prediction, we linearly interpolate the estimated $r_c$ for every $k$-bin as function of $\mu$ and then integrate the last term of Eq. 5.28 in every $\mu$-bin.

For the reconstructed HI field, we find in Fig. 5.23 that the signal to noise in both, the predicted and measured cross-spectra for the smallest $\mu$-bin is of the order 10 on all scales while reaching $\sim 100$ on the intermediate scales that are reconstructed the best. For higher $\mu$-bins, the signal to noise is still of the order $\sim 10$ on the largest scales but it deteriorates rapidly due to the photometric damping kernel. For comparison, we also the show as dotted lines the signal to noise for the cross-spectra with the input noisy HI data (with the wedge and the thermal noise) and see that it does not achieve 1 on any scales. This clearly demonstrates the gains made by using reconstructed HI field for estimating photometric redshifts by measuring clustering.

## Cross-correlation with CMB weak lensing

In CMB lensing we are attempting to cross-correlate our HI with the reconstructed convergence field, $\kappa$, given by

$$\kappa(\theta) = \int_0^{\chi_s} d\chi \; W_\kappa(\chi)\delta_m(\chi,\theta) \quad with \quad W_\kappa = \frac{3\Omega_m(1+z)}{2}\left(\frac{H_0}{c}\right)^2 \frac{\chi(z)(\chi_s-\chi)}{\chi_s} \quad . \tag{5.29}$$

with $\chi_s \simeq \chi(z=1150)$. Lensing kernel varies very slowly in radial direction and hence it will be insensitive to parallel wavenumbers larger than $k_\parallel \sim 10^{-3} h\,\mathrm{M}pc^{-1}$. Therefore, the suppression is even more strong than in the case of photometric redshifts and cross-correlation is completely hopeless unless one recovers the $k_\parallel \approx 0$ modes.

When cross-correlating with a tomograpic bin of reconstructed 21-cm density, the angular cross power spectrum is given by

$$C_\ell^\times = \int_{z_{\min}}^{z_{\max}} \frac{c\,dz}{\chi^2(z)H(z)} W_\kappa(z)\; r(z,k_\perp(z),k_\parallel=0)T_f(z,k_\perp(z),k_\parallel=0)b_{\mathrm{HI}}(z)P_{mm}(k_\perp(z),z) \tag{5.30}$$

where transverse wavenumber is evaluated at $k_\perp = \ell/\chi(z)$ and we have neglected any magnification bias. For slices that are thin $\Delta\chi \ll \chi$ (but thick enough so that the Limber approximation is valid) this simplifies to

$$C_\ell^\times = W_\kappa \; b\; rT_f \frac{c\,\Delta z}{\chi^2 H(z)} P_{mm} \tag{5.31}$$

Similarly, the HI auto power is given by

$$C_\ell^{HI} = b^2 T_f^2 \frac{c\,\Delta z}{\chi^2 H(z)} P_{mm} \tag{5.32}$$

while the $\kappa$ autospectrum remains an integral over the line of sight. As before, the noise $\mathrm{V}ar[C_\ell^\times] = N_{\mathrm{modes}}^{-1}((C_\ell^\times)^2 + C_\ell^{\kappa\kappa}C_\ell^{\mathrm{HI}}) \propto r^2$ assuming the second term dominates. The amount of signal-to-noise available for extraction is thus proportional to $r$. Our method thus allows us to reconstruct over 80% of all signal available (at a fixed noise of CMB map) compared to none in case of using the pure foreground cleaned 21-cm signal.

## BAO reconstruction

A major goal of high $z$, 21-cm cosmology is the measurement of distances using the baryon acoustic oscillation (BAO) method [249]. In ref. [158] we found that future interferometers would be able to make high-precision measurements of the BAO scale out to $z \simeq 6$ with scale-dependent biasing and redshift-space distortions having only a small effect on the signal. Non-linear structure formation damps the BAO peaks and reduces the signal-to-noise ratio for measuring the acoustic scale [28, 151, 72, 223, 58, 146, 215, 251, 250]. Since the non-linear scale shifts to smaller scales at high-redshifts, this damping is modest. We find that only the fourth BAO peak is slightly damped (compared to linear theory) at $z = 2$ and no damping is visible at $z = 6$.

Galaxy surveys which measure BAO typically apply a process known as reconstruction [75, 173] to their data in order to restore some of the signal lost to non-linear evolution (e.g. see refs. [7, 41, 22] and references therein). It is known that the absence of low $k_\parallel$ modes and the presence of the foreground wedge make reconstruction much less effective [213], though some of the lost signal can be recovered with other surveys [54]. Our approach provides another route to BAO reconstruction [156], so it is interesting to ask how the performance of the algorithm compares to standard reconstruction and how it is impacted by loss of data due to foregrounds. For standard reconstruction, we will follow the algorithm outlined in ref. [213]. This differs slightly from the traditional reconstruction using galaxies in that one removes the modes lost in the wedge to estimate Zeldovich displacements and instead of point objects like galaxies, one shifts the HI fields using this displacement. Since BAO reconstruction is most effective at $z = 2$, we focus our attention on this case – which is also the epoch at which our knowledge of the manner in which HI inhabits halos is most secure. At this redshift an instrument like PUMA is shot-noise limited.

To gauge how well are we able to recover the BAO signal we closely follow the previous chapter [156] which in turn builds upon refs. [215, 213]. The information lost due to the non-linear evolution and recovered with reconstruction can be quantified by measuring the linear information in the reconstructed field, $\delta_r$. This is done by estimating its projection onto the linear field, $\delta_{\rm l\mathit{in}}$ in the form of the 'propagator' as in Eq. 4.15 which results in the total signal to noise for the linear information (Eq. 4.17):

$$\frac{S}{N} = \frac{b^2 G^2 P_{\rm l\mathit{in}}}{\langle \delta_r \delta_r \rangle} = r_c^2 \tag{5.33}$$

We compare the performance of the two methods in Fig. 5.24 where we show the cross-correlation of the two reconstructed fields with the true linear field for different redshifts and wedge configurations. Since the comparison for other noise levels is qualitatively similar, we show only the case of fiducial setup corresponding to 5 years of observation with half-filled array. Overall, our method outperforms standard reconstruction significantly, with higher cross-correlation on all scales and extending to smaller scales. More importantly, as shown in the second column of Fig. 5.24, standard reconstruction fails to reconstruct modes inside the foreground region while our method is able to do so. These modes provide complementary information to the line of sight modes, constraining the angular diameter distance while line of sight modes constrain $H(z)$. Thus, unlike the standard method, our reconstruction should be able to constrain the angular diameter distance as well as improve measures of the Hubble parameter.

To be more quantitative, we can use the Fisher formalism to estimate the error on $s_0$ as outlined in eq. 4.19 (for a derivation, see refs. [215, 213]). While the nature of this calculation is rather crude, our aim here is to not do any accurate Fisher forecast for measuring BAO, but simply to broadly compare our reconstruction with the standard reconstruction under a sensible metric and to that end this procedure should suffice. To be

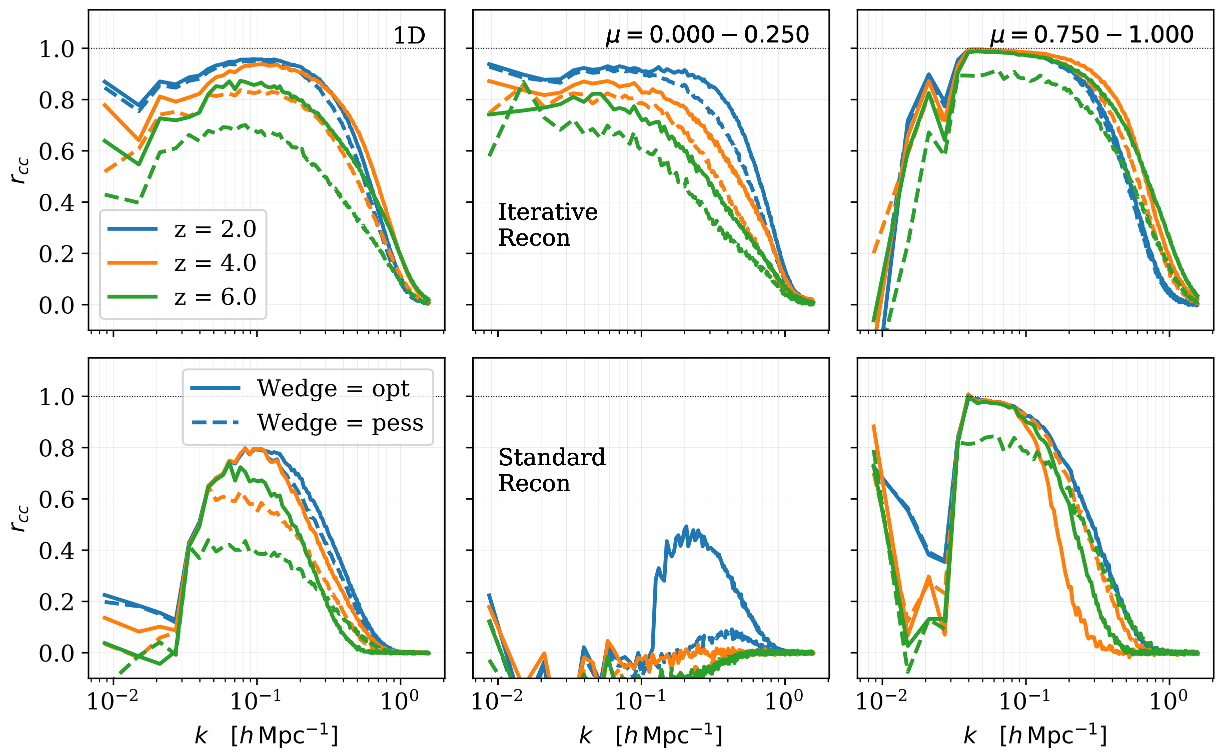


Figure 5.24: We show the cross-correlation of the reconstructed initial/linear field with the true Lagrangian field for our method of reconstruction (iterative, top row) and standard reconstruction (bottom row) for the three redshifts and two wedge configurations (solid and dashed) and fiducial thermal noise setup corresponding to 5 years with half-filled array. The first column is the cross correlation monopole while the second and third column show the cross correlation in bins nearly perpendicular to and along the line of sight respectively.

more yet conservative, instead of quoting the relative Fisher errors individually, we estimate the ratio of predicted errors for the two methods. We find that for the BAO peak, $s_0$, under the fiducial thermal noise setup, our reconstruction reduces errors over the standard method by a factor of $\sim 2$ (2) and $\sim 2.8$ (3.5) for optimistic (pessimistic) wedge at $z = 2$ and 6. The conclusions remain relatively unchanged for other thermal noise configurations. While this is for angular averaged BAO, as mentioned previously, we expect gains to be comparable for Hubble parameter and larger for angular diameter distance. We leave a more accurate calculation for future work.

## 5.9 Conclusions

Intensity mapping techniques have emerged as a promising tool to efficiently probe the dark matter distribution at high redshifts, and a number of upcoming surveys plan to use the 21-cm emission signal from neutral hydrogen to probe this largely unexplored territory. The major challenge in accurately simulating 21-cm signal at these redshifts and on cosmological scales is simultaneously achieving high enough mass resolution to properly resolve the 21-cm emission while simultaneously covering a large enough volume to make precise statements about the clustering of the HI.

In this chapter, we have discussed two challenges in doing 21-cm cosmology. We begin with the challenges in simulating HI observations and present the HiddenValley simulations, a set of $10240^3$ particle N-body simulations of a $1\,(h^{-1}\mathrm{Gpc})^3$ volume. We have focused on the study of 21-cm fluctuations between redshifts 2 and 6 to demonstrate how the scales and resolution of these simulation allow us to address several modeling issues with higher fidelity than before.

We used three different prescriptions from the literature to model the cosmological distribution of neutral hydrogen (Section 5.4). Our first model is (sub)halo-based, where each halo contains some amount of HI which is then distributed between central and satellites galaxies. The second assumes HI traces the stellar mass of galaxies. The third is a simple halo-only model with constant parameters across the redshift range, primarily as a contrast to the other two models. We find that while the Model A and C are able to match the abundance of neutral hydrogen at all redshifts of interest (Fig. 5.3), Model B has a different evolution with the redshift due to constrained evolution directed only by stellar mass evolution. Despite having very different mechanism for HI distribution, all three models predict that majority of HI occupies halos in the mass range $10^{10} - 10^{11.5}\,h^{-1}M_{\odot}$ (Fig. 5.5).

These models also predict similar clustering in the real and redshift space, in both Fourier and configuration space. None of the models predict any significant from finger of god effects on the redshift space clustering for the range of scales relevant for proposed 21-cm instruments (Fig. 5.12). In common with earlier work we find the bias of HI increases from near 2 at $z = 2$ to 4 at $z = 6$, becoming more scale dependent at high $z$ (Fig. 5.7). As a preliminary step towards theoretical modeling of observed 21-cm clustering, we fit these signals with 'Zeldovich effective field theory' (ZEFT [241]) which is a simple, tree-level, Lagrangian perturbation theory model. We find that the model is simultaneously able to fit the matter auto-spectra, HI-matter cross spectra and the HI auto-spectra in real space at these redshifts, thus capturing the scale-dependence of the bias and the decorrelation with the matter field (Fig. 5.8). Though the redshift space spectra are noisier in our simulations, the simple model is still able to fit both the multipoles (Fig. 5.10) and the wedges (Fig. 5.11) within sample variance to beyond half $k_{\mathrm{nl}}$. The scale of our simulations also allows us to extract the baryon acoustic oscillations in the 21-cm clustering and we find that the damping of BAO signal decreases and is negligible at $z = 6$ (Fig. 5.13). Moreover, the damping along the line of sight due to redshift space distortions also decreases significantly by $z = 6$. In addition, we estimate uncertainties assuming a "pessimistic" wedge and realistic thermal noise to show that a HIRAX-like experiment is able to detect the BAO signal at $z = 2$ in power spectrum wedges, and a Stage II experiment can detect the same at $z = 6$ with high significance (Fig. 5.14).

We then apply recently developed field reconstruction methods to the case of future 21-cm cosmology experiments. In many respects this is an optimal target for such methods. First, we are dealing with continuous fields which are naturally more suited for these methods, since the problem of the non-analytical object creation does not apply. In galaxy clustering, while its possible to circumvent the discreteness of the data by averaging in pixels that are sufficiently big that the galaxy counts in cells become effectively continuous, it leads to information loss. However, for 21-cm intensity mapping experiment, the finite resolution of the experiment naturally leads to a continuous version of the problem. We simply do not have information of scales that are small enough to even contemplate separating individual objects, even though the signal is dominated by them.

Second, the 21-cm intensity field is dominated by numerous contributions from relatively low mass dark matter halos [42, 237, 158], which are well described by a low-order bias expansion to relatively high wavenumbers. This allows us to start from the underlying dark matter field and model the observed data at the field level more simply and accurately than for discrete and more biased tracers such as galaxies. Third, we are missing some regions of $k$-space ($\sim 20(7) - 80(40)\%$ of the modes for our pessimistic (optimistic) case) but, on the other hand, measuring a very large number of modes over other regions of $k$-space. As we have demonstrated, the measured modes and the couplings introduced by non-linear evolution more than make up for the missing ones.

Our method proceeds by maximizing the posterior for the initial conditions, which is constructed by combining a Gaussian prior on the initial field with the likelihood of a forward model matching the observations. We find that, similar to modeling the clustering of HI, the forward model consisting of simple Zeldovich dynamics and a quadratic, Lagrangian bias scheme model do a good job of fitting our mock data at the field level, with errors well below the shot noise level in the field (Fig. 5.15).

For $2 < z < 6$ we are able to recover modes down to $k \simeq 10^{-2}\,h\,\mathrm{Mpc}^{-1}$ with cross-correlation coefficients larger than 0.8 for both optimistic and pessimistic assumptions about foreground contamination (Fig. 5.18). Our reconstruction is relatively insensitive to loss of line-of-sight modes, up to $k_{\parallel}^{min} = 0.05\,h\,\mathrm{Mpc}^{-1}$, but more sensitive to missing modes in the 'wedge' (Section 5.2) as shown in Fig. 5.20. For our fiducial thermal noise assumptions we recover the $k \simeq 10^{-2}\,h\,\mathrm{Mpc}^{-1}$ modes with cross-correlation coeffecient greater than 0.9 in all directions and the line of sight modes almost perfectly, even though we do not have any of these modes in the data. On the other hand small scale modes along the line of sight are significantly better reconstructed than the transverse modes. Thus as shown in Fig. 5.22, we find that the reconstruction of line-of-sight modes is less sensitive to the loss of modes in the foreground wedge than transverse modes. However in all cases the better foregrounds are controlled, and the smaller the wedge can be made, the better reconstruction proceeds. At $z \simeq 2$ our reconstructions are relatively insensitive to thermal noise over the range we have tested. However at higher $z$ increasingly noisy data leads to steadily lower cross-correlation coefficient, as shown in Fig. 5.18.

Our method also provides a technique for density field reconstruction for baryon acoustic oscillations (BAO) [156]. It is known that the absence of low $k_{\parallel}$ modes and the presence of the foreground wedge make reconstruction much less effective [213], though some of the lost signal can be recovered with other surveys [54]. By constraining the reconstructed initial field, as well as the evolved HI field, we can use the measured modes to 'undo' some of the non-linear evolution and increase the signal-to-noise ratio on the acoustic peaks (see Section 5.8). In particular, we find that while the standard methods of reconstruction recover almost no modes in the foreground wedge, our method reconstructs modes with cross correlation better than 80%. This can lead to improvements of a factor of 2-3 in isotropic BAO analysis and more in transverse directions. We note that these gains over standard methods are significantly larger than in the case of galaxy surveys since the standard reconstructions is already quite efficient for the latter [213, 207, 156].

We have focused primarily on the reconstruction technique in this paper, but the ability to reconstruct low $k$ modes opens up many scientific opportunities. We described (Section 5.8) how 21-cm fluctuations could provide superb clustering redshift estimation at high $z$, where it is otherwise extremely difficult to obtain dense spectroscopic samples (Fig. 5.23). This could be extremely important for high $z$ samples coming from LSST, Euclid and WFIRST. The recovery of low $k_{\parallel}$ modes also opens up a wealth of cross-correlation opportunities with projected fields (e.g. lensing) which are restricted to modes transverse to the line of sight. The measurement of long wavelength fluctuations should also enhance the mapping of the cosmic web at these redshifts, helping to find protoclusters or voids for example [252].

In this work we have assumed that we measure the 21-cm field in an unperturbed redshift-space field. In practice, what we observe is the field that has been displaced on large scales by the effect of weak gravitational lensing by the intervening matter along the line of sight. It is clear that the two effects must be degenerate at some level. A location of a given halo in observed redshift-space is obtained by adding the effect of the Lagrangian displacement from the proto-halo region and the effect of weak-lensing by the lower-redshift structures. The latter can be replaced, at least approximately, by a distribution of matter whose Lagrangian displacement absorbs both effects. However, the degeneracy is not perfect. In particular, weak lensing effect is almost exclusively limited to moving the structures in transverse direction by a displacement field that changes slowly with distance. These issues have been studied in the context of traditional lensing estimators in ref. [91], which find encouraging results. Similar lessons should apply to our method, which should, if anything, perform better since it naturally extracts more signal. We leave this for future investigation.

For the purpose of reconstruction, we have assumed a fixed cosmology and fixed bias parameters. Ideally, one would like to estimate the model and cosmological parameters at the same time as reconstructing linear field. The impact of keeping these parameters fixed at their fiducial values varies with the science objective, for instance it will differently affect BAO reconstruction vs. photometric redshift estimation. In some cases, since the non-linear dynamics of our forward model are quite cheap, one can imagine doing this reconstruction recursively, updating model parameters if they vary significantly. A detailed analysis of this is beyond the scope of current work and we leave this for the future. For completeness, we point out that some recent papers (e.g. ref. [78]) have explored ways of taking into account the model and cosmology parameters simultaneously for other biased tracers.

We have also made simplifying assumptions to generate our observed mock data to test the reconstruction algorithm. Since HI assignment to halos is still poorly understood, we have assumed a simple semi-analytic model. We have neglected any effect of UV background fluctuations [234, 158] or assembly bias [237] on HI distribution in halos and galaxies. However a flexible bias model, and our forward modeling framework, should be able to include these. In the same vein, it's worth exploring the impact of stochasticity (scatter) between HI mass and dark matter mass on reconstruction since it adds noise on all scales. However we leave it for future work when the required observations can calibrate the amplitude of the effect.

## Acknowledgments

We would like to thank the Cosmic Visions 21-cm Collaboration for stimulating discussion on the challenges for 21-cm surveys. C.M. would also like to thank Marcel Schmittfull for useful discussions. M.W. is supported by the U.S. Department of Energy and by NSF grant number 1713791. This research used resources of the National Energy Research Scientific Computing Center (NERSC), a U.S. Department of Energy Office of Science User Facility operated under Contract No. DE-AC02-05CH11231. This work made extensive use of the NASA Astrophysics Data System and of the `astro-ph` preprint archive at `arXiv.org`.

# Chapter 6

# FlowPM: Distributed TensorFlow Implementation of the FastPM Cosmological N-body Solver

The contents of this chapter will be published as

> FlowPM: Distributed TensorFlow Implementation of the FastPM Cosmological N-body Solver
> *Modi C., Lanusse F., Seljak U.* under-prep

In the previous chapters, we have developed and implemented forward modeling framework for reconstruction of cosmological fields to different cosmological probes. In these models, the first step is to begin with the initial dark matter distribution and evolve dark matter particles under gravitational force to generate the non-linear dark matter field at late times. To make this step fast and efficient, in this chapter we present FlowPM - a cosmological N-body code implemented in Mesh-TensorFlow for GPU-accelerated, distributed, and differentiable simulations. We demonstrate how this novel tool can be used for efficiently solving large scale cosmological inference problems, in particular the reconstruction of cosmological fields with hybrid PM and neural network forward model. We implement and validate the accuracy of a novel multi-grid PM scheme based on image pyramids to compute large scale forces efficiently. We also explore the scaling of the simulation on large scale supercomputers and compare it with corresponding python based PM code, finding on an average 10x speed-up in terms of wallclock time. We provide skeleton code for these examples and the entire code is publicly available at https://github.com/modichirag/flowpm.

## 6.1 Introduction

N-Body simulations evolving billions of dark matter particles under gravitational forces have become essential tool for modern day cosmology data analysis and interpretation. They are required for accurate predictions of the large scale structure (LSS) of the Universe, probed by tracers such as galaxies, quasars, gas, weak gravitational lensing etc. While the full N-body simulations can provide very precise predictions, they are extremely slow and computationally expensive. As a result they are usually complemented by fast approximated numerical schemes such as Particle-Mesh (PM) solvers [153, 229, 251, 83, 115]. In these approaches, the gravitational forces experienced by dark matter particles in the simulation volume are computed by Fast Fourier Transforms on a 3D grid. This makes PM simulations very computationally efficient and scalable, at the cost of approximating the interactions on small scales close to the resolution of the grid and ignoring the force calculation on sub-resolution scales.

The next generation of cosmological surveys such as Dark Energy Spectroscopic Instrument (DESI) [68], Large Synoptic Survey Telescope (LSST) [138] and others will probe LSS with multiple tracers over unprecedented scales and dynamic range. This will make both the modeling and the analysis challenging even with the current PM simulations. To improve the modeling in terms of dynamic range and speed, many recent works have proposed regressive and generative models to learn these simulations using deep convolution networks [107, 130].

At the same time, there has been a considerable interest in exploring novel techniques to push to increasingly smaller and non-Gaussian regimes for cosmological analysis. Recent work has demonstrated that one of the most promising approaches to do this is with forward modeling frameworks and using techniques like simulations based inference or reconstruction of cosmological fields for analysis [211, 9, 56]. However given the highly non-linear forward dynamics and multi-million dimensionality of the cosmological simulations, such approaches are only tractable if one has access to differentiable forward simulations [120, 246, 211, 156].

To address both of these challenges, in this work we present FlowPM, a TensorFlow implementation of N-Body PM solver. Written entirely in TensorFlow, these simulations are GPU-accelerated and hence faster than CPU-based PM simulations, while also being entirely differentiable end-to-end. At the same time, they encode the exact underlying dynamics for gravitational evolution (within a PM scheme), while still leaving room for natural synthesis with machine learning components to develop hybrid simulations, which can complement by learning the sub-grid and non-gravitational dynamics not included in PM gravity solver cosmological simulations.

With evolving billions of particles to simulate today's cosmological surveys, N-Body simulations are quite memory intensive and necessarily require distributed computing. In FlowPM, we develop such distributed computation with a novel model parallelism framework - Mesh-Tensorflow [219]. This allows us to control distribution strategies and split tensors and computational graphs over multiple processors.

The primary bottleneck for large scale distributed PM simulations are distributed 3D-FFTs, which make up for more than half the wall-clock time [158]. One way to overcome these is with multi-grid scheme for computing gravitational forces [225, 153, 105]. In these schemes, large scale forces are estimated on a coarse distributed grid and then stitched together with small scale force estimated locally. We also propose a novel multi-grid scheme based on Image Pyramids [37, 11], that does not require any fine-tuned stitching of scales, and benefits from highly optimized 3-D convolutions of TensorFlow.

In this first work, we have implemented the FastPM scheme of [83] for PM evolution with force resolution $B = 1$. Different PM schemes, as well as other approximate simulations like Lagrangian perturbation theory fields [229, 127, 224], are built upon the same underlying components, with interpolations to-and-from PM grid and efficient FFTs to estimate gravitational forces being the key elements. Thus modifying FlowPM to include other PM schemes is a matter of implementation rather than methodology development. Therefore in this work, we will focus in detail on these underlying components while only giving the outline of the full algorithm. For further technical details on the choices and accuracy of the implemented FastPM scheme, we refer the reader to the original chapter of [83].

The structure of this chapter is as follows - in Section 6.2 we outline the basic FastPM algorithm and discuss multi-grid scheme for force estimation in Section 6.3. Then in Section 6.4, we introduce Mesh-TensorFlow. In Section 6.5, we build upon these and introduce FlowPM. We compare the scaling and accuracy pf FlowPM with python FastPM code in Section 6.6. At last, in Section 6.7, we demonstrate the efficacy of FlowPM with a toy example by combining it with neural network forward models and reconstructing the initial conditions of the Universe. We end with discussion in Section 6.8.

Throughout the chapter, we use "grid" to refer to the particle-mesh grid and "mesh" to refer to the computational mesh of Mesh-TF. Unless explicitly specified, every FFT referred throughout the chapter is a 3D FFT.

## 6.2 The FastPM particle mesh N-body solver

Schematically, FastPM implements a symplectic series of Kick-Drift-Kick operations [193] to do the time integration for gravitational evolution, starting from the Gaussian initial conditions of the Universe to the observed large scale structures at the final time-step. In the *Kick* stage, we estimate the gravitational force on every particle and update their momentum $p$. Next, in the staggered *Drift* stage, we displace the particle to update their position ($x$) with the current velocity estimate. Thus, we can write the drift and kick operators as [193] -

$$x(t_1) = x(t_0) + p(t_r)\mathcal{D}_{\rm PM} \tag{6.1}$$

$$p(t_1) = p(t_0) + f(t_r)\mathcal{K}_{\rm PM}, \tag{6.2}$$

where $\mathcal{D}_{\rm PM}$ and $\mathcal{K}_{\rm PM}$ are scalar drift and kick factors and $f(t_r)$ is the gravitational force.

Estimating the gravitational force is the most computationally intensive part of the simulation. In a PM solver, the gravitational force is calculated via 3D Fourier transforms. First, the particles are interpolated to a spatially uniform grid with a kernel $W(r)$ to estimate the mass and corresponding overdensity field at every point in space. The most common choice for the kernel, and the one we implement, is a linear window of unity size corresponding to the cloud-in-cell interpolation scheme [111]. We then apply a Fourier transform to obtain the over-density field $\delta_k$ in Fourier space. This field is related to the force field via a transfer function ($\nabla\nabla^{-2}$).

$$f(\mathbf{k}) = \nabla\nabla^{-2}\delta(\mathbf{k}) \tag{6.3}$$

Once the force field is estimated on the spatial grid, it's interpolated back to the position of every particle with the same kernel as was used to generate the density field in the first place.

There are various ways to write down the transfer function in a discrete Fourier space, as explored in detail in [111]. The simplest way of doing this is with a naive Green's function kernels ($\nabla^{-2} = k^{-2}$) and differentiation kernels ($\nabla = i\mathbf{k}$). In FlowPM however, we implement a finite differentiation kernel as used in FastPM with

$$\nabla^{-2} = \left(\sum_{d=x,y,z}\left(x_0\omega_0 sinc\frac{\omega_d}{2}\right)^2\right)^{-1} \tag{6.4}$$

$$\nabla = D_1(\omega) = \frac{1}{6}\Big(8sin\omega - sin2\omega\Big) \tag{6.5}$$

where $x_0$ is the grid size and $\omega = kx_0$ is the circular frequency that goes from $(-\pi, \pi]$.

## 6.3 Multi-grid PM Scheme

Every step in PM evolution requires one forward 3D FFT to estimate the overdensity field in Fourier space, and three inverse FFTs to estimate the force component in each direction. The simplest way to implement 3D FFTs is as 3 individual 1D Fourier transforms in each direction [186]. However in a distributed implementation, where the tensor is distributed on different processes, it involves transpose operations and expensive all-to-all communications in order to get the dimension being transformed on the same process. This makes these FFTs the most time-intensive step in the simulation [158]. There are several ways to make this force estimation more efficient, such as fast multipole methods [95] and multi-grid schemes [153, 105]. In FlowPM, we implement a novel version of the latter.

The basic idea of a multi-grid scheme is to use grids at different resolutions, with each of them estimating force on different scales which are then stitched together. Here we discuss this approach for a 2 level multi-grid scheme, since that is implemented in FlowPM and the extension to more levels is similar. The long range (large-scale) forces are computed on a global coarse grid that is distributed across processes. On the other hand, the small scale forces are computed on a fine, higher resolution grid that is local, i.e. it estimates short range forces on smaller independent sections that are hosted locally by individual processes. Thus, the distributed 3D FFTs are computed only on the coarse mesh while the higher resolution mesh computes highly efficient local FFTs.

This force splitting massively reduces the communication data-volume but at the cost of increasing the total number of operations performed. Thus while it scales better for large grids and highly distributed meshes, it can be an over-kill for small simulations. Therefore in FlowPM we implement both, a multi-grid scheme for large simulations, and the usual single-grid force scheme for small grid sizes, with the user having the freedom to choose between the two.

## Image Pyramids

In this section we briefly discuss image pyramids that will later form the basis our multi-grid implementation for force estimation. As used in image processing and signal processing communities, image pyramids refer to multi-scale representations of signals and image built through recursive reduction operations on the original image [37, 11]. The reduction operation is a combination of - i) smoothing operation, often implemented by convolving the original image with a low-pass filter ($\mathcal{G}$) to avoid aliasing effects by reducing the minimum frequency of the signal features, and ii) subsampling or downsampling operation ($\mathcal{S}$), usually by a factor of 2 along each dimensions, to compress the data. This operation can be repeatedly applied at every 'level' to generate a 'pyramid' structure of the low-pass filtered copies of the original image. Given a level $g_l$ of original image $g_0$, the pyramid next level is generated by

$$g_{l+1} = \mathrm{R}EDUCE(g_l) = \mathcal{S}[\mathcal{G} \star g_l] \tag{6.6}$$

where $\star$ represents convolution. If the filter $w$ used is a Gaussian filter, the pyramid is called a Gaussian pyramid.

However, in our multi-grid force estimation, we are interested in decoupling the large and small scale forces. This can be achieved by constructing something akin to 'Laplacian' pyramid from our which is a set of band-pass filtered copies of the signal[1]. In this case, one reverse the reduce operation by - i) Upsampling ($\mathcal{U}$) the image at level $g_{l+1}$, generally by inserting zeros between pixels and then ii) interpolating the missing values by convolving it with the same filter $\mathcal{G}$ to create the expanded low-pass image $g'_l$

$$g'_l = \mathrm{E}XPAND(g_{l+1}) = \mathcal{G} \star \mathcal{U}[g_{l+1}] \tag{6.7}$$

A Laplacian representation at any level can then be constructed by taking the difference of the original and expanded low-pass filtered image at that level

$$L_l = g_l - g'_l \tag{6.8}$$

In Fig. 6.1, we show the Guassian and Laplacian pyramid constructed for an example image, along with the flow-chart for these operations.

Lastly, given the image at the highest level of the pyramid ($g_N$) and the Laplacian representation at every level ($L_0...L_{N-1}$), we can exactly recover the original image by recursively

[1]Since we will not use the Gaussian kernel for smoothing, our pyramid structure is not a Laplacian pyramid in the strictest sense, but the underlying idea is the same.

[2]Image taken from http://graphics.cs.cmu.edu/courses/15-463/2012_fall/hw/proj2g-eulerian/

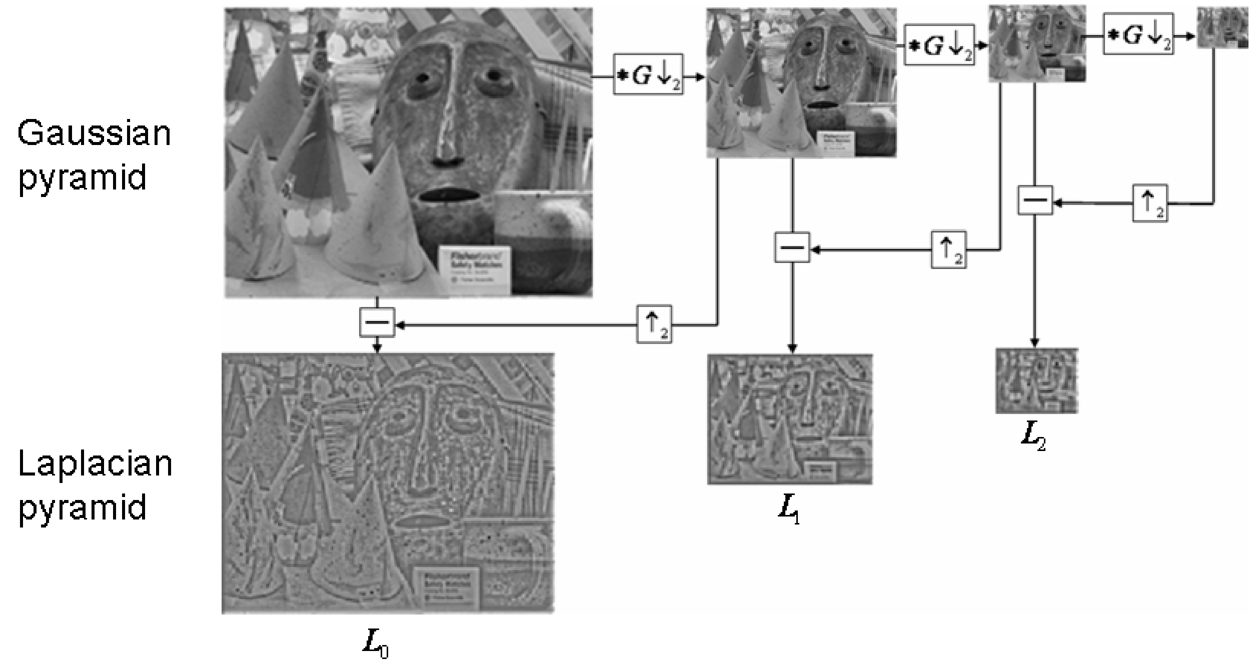


Figure 6.1: An example of Gaussian image pyramid and the corresponding Laplacian pyramid. The arrows and small boxes mark the operations involved[2].

doing the series of following inverse transform-

$$g_l = L_l + EXPAND(g_{l+1}) \quad \forall l \in [N-1...0] \tag{6.9}$$

We will apply these operations in Section 6.5 to estimate forces on a two-level grid.

## 6.4 Mesh-TensorFlow

The last ingredient we need to build FlowPM is a model parallelism framework that is capable of distributing the N-body simulation over multiple processes . To this end, we adopt Mesh-TensorFlow [219] as the framework to implement our PM solver. Mesh-TF is a language for distributed deep learning capable of specifying a general class of distributed tensor computations. In that spirit, it goes beyond the simple batch splitting of data parallelism and generalizes to be able to split any tensor and associated computations across any dimension on a mesh of processors.

We only summarize the key component elements of Mesh-TensorFlow here and refer the reader to [219] [3] for more details. These are -

- a *mesh*, which is a $n$-dimensional array of processors with *named* dimensions.

[3] https://github.com/tensorflow/mesh

- the dimensions of every tensor are also *named* and depending on it, its either distributed/split across or replicated on all processors in a mesh. Hence every processor holds a *slice* of every tensor. The dimensions can thus be seen as 'logical' dimensions which will be split in the same manner for all tensors and operations.

- a user specified *computational layout* to map which tensor dimension is split along which mesh dimension. The unspecified tensor dimensions are replicated on all processes. While the layout does not affect the results, it can affect the performance of the code.

The user builds a Mesh-TensorFlow graph of computations in python and this graph is then *lowered* to generate the TensorFlow graphs. It is at this stage the defined tensor dimensions and operations are split amongst different processes on the mesh based on the computational layout. Multi-CPU/GPU meshes are implemented with *PlacementMeshImpl*, i.e. a separate TensorFlow operations is placed on the different devices, all in one big TensorFlow graph. In this case, the TensorFlow graph will grow with the number of processes. On the other hand, TPU meshes are implemented in with *SimdMeshImpl* wherein TensorFlow operations (and communication collectives) are emitted from the perspective of one core, and this same program runs on every core, relying on the fact that each core actually performs the same operations. Due to Placement Mesh Implementation, time for lowering also increases as the number of processes are increased. Returning to Mesh-TF computations, lastly, the tensors to be evaluated are *exported* to TF tensors in which case they are gathered on the single process.

```python
import mesh_tensorflow as mtf
nc = 128 #specify grid size
#Setup mesh implementation for GPU
graph = mtf.Graph()
mesh = mtf.Mesh(graph, "my_mesh")
devices = ["device:GPU:%d"%(i) for i in range(8)]
mesh_shape = [("row", 4), ("col", 2)]
layout_rules = [("nx", "row"), ("ny", "col")]
mesh_impl = mtf.placement_mesh_impl.PlacementMeshImpl(mesh_shape,
    layout_rules, devices)
#Name dimensions and define operation
x_dim, y_dim , z_dim = mtf.Dimension("nx", nc), mtf.Dimension("ny", nc),
    mtf.Dimension("nz", nc)
batch_dim = mtf.Dimension("batch", 1)
shape = [batch_dim, x_dim, y_dim , z_dim]
field = mtf.RandomOperation(mesh, shape, tf.random.normal).outputs[0]
#Lower and export to evaluate
lowering = mtf.Lowering(graph, {mesh:mesh_impl})
tf_field = lowering.export_to_tf_tensor(field)
with tf.Session as sess: sess.run(tf_field)
```

Listing 6.1: Sample code to generate random normal field of grid size 128 on a 2D computational mesh of 8 GPUs with x and y directions split across 4 and 2 processors respectively

Listing 6.1 shows an example code to illustrate these operations which form the starting elements of any Mesh-TensorFlow. The code also sets up context for FlowPM, naming the three directions of the PM simulation grid and explicitly specifying which direction is split along which mesh-dimension. Note that for a batch of simulations, computationally the most efficient splitting will almost always maximize the splits along the batch dimension. While FlowPM supports that splitting, we will henceforth fix the batch size to 1 since our focus is on model parallelism of large scale simulations.

## 6.5 FlowPM: FastPM implementation in Mesh-Tensorflow

Finally, in this section, we introduce FlowPM and discuss technical details about its implemetation in Mesh-TensorFlow. We will not discuss the underlying algorithm of a PM simulation since it is similar in spirit to any PM code, and is exactly the same as FastPM [83]. Rather we will focus on domain decomposition and the multi-grid scheme for force estimation which are novel to FlowPM.

### Domain decomposition and Halo Exchange

In Mesh-Tensorflow, every process has a slice of every tensor. Thus for our PM grid, where we split the underlying grid spatially along different dimensions, every process will hold only the physical region and the particles corresponding to that physical region. However at every PM step, there is a possibility of particles moving in-and-out of any given slice of the physical region. At the same time, convolution operations on any slice need access to the field outside the slice when operating on the boundary regions. Th strategy for communication between neighboring slices to facilitate this is called halo-exchange. We implement this exchange by padding every slice with buffer regions of *halo size* ($h$) that are shared between the slices on adjacent processes. The choice of *halo size* depends on several factors[4]. Firstly, in its current implementation, the halo size has to be larger than the maximum displacement of the particle over the simulation. For cosmological simulations of reasonable volumes and resolutions, this corresponds to $\sim 20$ Mpc/h in physical size. The halo size also should be large enough that the smoothing operations implemented in the pyramid scheme reduce the force close to zero on these scales and avoid aliasing during subsampling.

Our algorithm to do halo-exchange is outlined in Algorithm 1 and illustrated for a 1-dimension grid in Fig. 6.2. It is primarily motivated by the fact that Mesh-TensorFlow allows to implement independent, local operations simply and efficiently as *slicewise* operations along the dimensions that are not distributed. Thus we can implement all of the operations - convolutions, CIC interpolations, position and velocity updates for particles and local FFTs -

[4]In case of the pyramid scheme, the halo size is defined on the high resolution grid and we reduce it by the corresponding downsampling factor for the coarse grid.

on these un-split dimensions as one would for a typical single-process implementation without worrying about distributed strategies. To take advantage of this, we begin by reshaping our tensors from 3 dimensions (excluding batch dimension) to 6 dimensions such that the first three indices split the tensor according the computational layout and the last three indices are not split, but replicated across all the processes and correspond to the local slice of the grid on each process. This is shown in Fig. 6.2, where an original 1-D tensor of size $N = 12$ in split over $nx = 2$ processes. In the second panel, this is re-shaped to a 2-D tensor with the first dimension $nx = 2$ split over processes and $s_x$ is the un-split dimension. The un-split dimension is then zero-padded with *halo size* resulting in the size along the un-split dimension to be $s_x = N//n_x + 2h$. This is followed by an exchange with the neighboring slices over the physical volume common to the two adjacent processes.

After the slicewise operation updates the local slices, the same steps are followed in reverse. The padded halo regions are exchanged again to combine updates in the overlapping volume from adjacent processes. Then the padded regions are dropped and the tensor is reshaped to the original shape.

## Multi-grid Scheme with Image Pyramids

To implement the multi-grid scheme with image pyramids, we need a smoothing and a subsampling operation. While traditionally smoothing operations are performed in Fourier space in cosmology, here we are restricted to these operations in local, pixel space. However local operations in pixel space have a spread in the Fourier domain, and this can lead to issues with aliasing given that we wish to estimate forces with FFT on the subsampled coarse grid as well as local FFT on the non-periodic local slices of the high resolution grid. Therefore, we require a large kernel size for the smoothing operation in the pixel space and a trade-off needs to be made with the increased computational and memory cost of halo-exchange to be performed at the boundaries.

In our experiments, we find that a 3-D bspline kernel of order 6 balances these trade-offs well and allows us to achieve sub-percent accuracy, as we show later. Furthermore In FlowPM, we take the advantage of highly efficient TensorFlow ops and implement both, the smoothing and subsampling operations together by constructing a 3D convolution filter with this bspline kernel and convolving the underlying field with stride 2 convolutions. In default implementation, we repeat these operations twice and our global mesh is 4x coarser than the higher resolution mesh. The full algorithm for this REDUCE operation is outlined in Algorithm 2. Based on the discussion in Section 6.3, we also outline the reverse operation with EXPAND method.

Finally we are in the position to outline the multi-grid scheme for force computation. This is outlined in Algorithm 3. Schematically, we begin by reducing the high resolution grid to generate the coarse grid. Then we estimate the force components in all three directions on both the grids, with the key difference that the coarse grid performs distributed FFT on a global mesh while for the high resolution grid, every process performs local FFTs in parallel on the locally available grids. To recover the correct total force, we need to combine these

**Algorithm 1** Halo Exchange

```
global variables
    N - size of the global grid
    h - halo size, to be padded
    nx, ny, nz - #splits along three directions
    sx, sy, sz - size of local slice after split
    nx, ny, nz - Name of dimension along nx, ny, nz
    sx, sy, sz - Name of dimension along sx, sy, sz
end global variables

procedure RESHAPE_EXPAND(G)
    ASSERT(G.shape == (N, N, N))
    G ⇐ G.reshape(nx, ny, nz, sx, sy, sz)
    for axis ∈ sx, sy, sz do
        G ⇐ ZEROPAD(G, size = h, axis = axis)
    end for
    return G
end procedure

procedure RESHAPE_REDUCE(G)
    ASSERT(G.shape == (nx, ny, nz, sx + 2h, xy + 2h, sz + 2h))
    for axis ∈ sx, sy, sz do
        G ⇐ REMOVEPAD(G, size = h, axis = axis)
    end for
    G ⇐ G.reshape(N, N, N)
    return G
end procedure

procedure EXCHANGE(G)
                    ▷ Add updates in overlapping padded regions from neighboring processes
end procedure

procedure HALOEXCHANGEOP(G, SlicewiseOp)
                    ▷ Strategy for operating slicewise op with halo exchange
    ASSERT(G.shape == (N, N, N))
    G ⇐ RESHAPE_EXPAND(G)
    G ⇐ EXCHANGE(G)
    G ⇐ SLICEWISEOP(G)
    G ⇐ EXCHANGE(G)
    G ⇐ RESHAPE_REDUCE(G)
    return G
end procedure
```

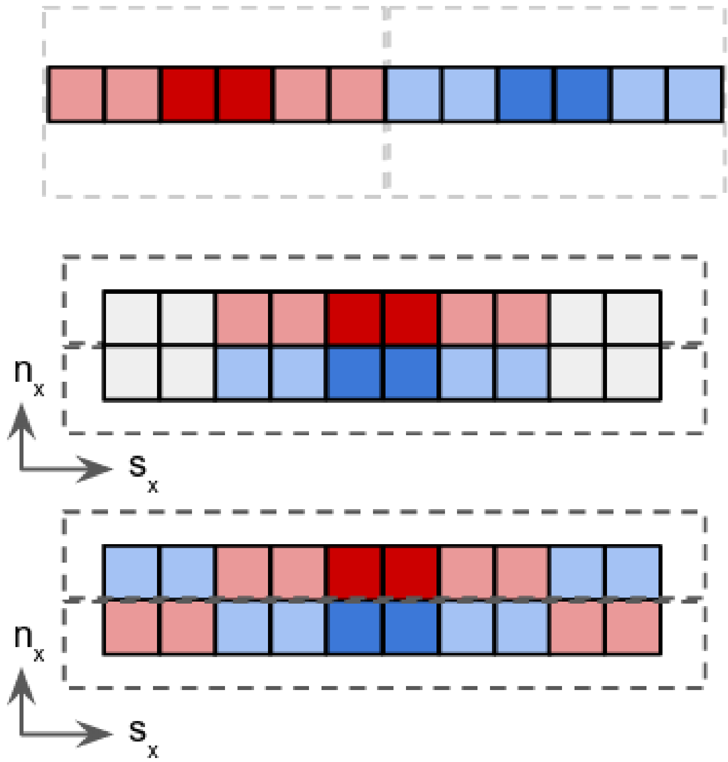


Figure 6.2: An illustration of the halo exchange strategy as outlined in Algorithm 1 for a simple 1-D tensor of size $N = 12$ and *halo size* $h = 2$, specifically R*eshape_Expand* operation. The red and blue regions are to be split on two process, with light regions indicating the overlapping volume that will be exchanged. In the second panel, the tensor is reshaped with the split along the first, $nx$ dimension and the second un-split $s_x$ that is zero-padded. In the third panel, the regions are exchanged (here under the assumption of periodic boundary conditions).

long and the short range forces together. For this, we expand the long-range force grid back to the high resolution. At the same time, we remove the long-range component from the high-resolution grid with a reduce and expand operation, similar to the band-pass level generated in the Laplacian pyramid in Section 6.3. In the end, we combine these long and short range forces to recover the original force.

Note that in implementing a multi-grid scheme for PM evolution, only the force calculation in the kick step is modified, while the rest of the PM scheme remains the same and operates on the origial high-resolution grid.

**Algorithm 2** Methods for pyramid scheme

**procedure** REDUCE($H,\ f=2,\ n=6,\ S=2$)
  ▷ Downsample field $H$ by convolving with a bspline kernel of order $n$ consecutively $f$ times with stride $S$
  $K \Leftarrow$ BSpline(n)
  $D \Leftarrow H$
  **for** $i \in 0 \dots f$ **do**
    $D \Leftarrow$ Conv3D($D, K, S$)
  **end for**
  **return** $D$
**end procedure**

**procedure** EXPAND($D,\ f=2,\ n=6,\ S=2$)
▷ Upsample field $D$ by convolving with a bspline kernel of order $n$ consecutively $f$ times with stride $S$
  $K \Leftarrow$ BSpline(n) $x$ 8
  $H \Leftarrow D$
  **for** $i \in 0 \dots f$ **do**
    $H \Leftarrow$ TransposedConv3D($H, K, S$)
  **end for**
  **return** $H$
**end procedure**

## 6.6 Scaling and Numerical Accuracy

In the section, we will discuss the numerical accuracy and scaling of these simulations. Since the novel aspects of FlowPM are a differentiable Mesh-Tensorflow implementation and multigrid PM scheme, and our discussion will center around comparison with the corresponding differentiable python implementation of FastPM which shares the same underlying PM scheme. We do not discuss the accuracy with respect to high resolution N-Body simulations with correct dynamics, and refer the reader to [83] for details on such a comparison. Our tests are performed primarily on GPU nodes on Cori supercomputer at NERSC, with each node hosting 8 NVIDIA V100 ('Volta') GPUs each with with 16 GB HBM2 memory and connected with NVLink interconnect. To compare things with python version, we run the FastPM+vmad code on Cori-Haswell nodes.

### Accuracy of the simulations

We begin by establishing the accuracy of FlowPM for both, mesh and the pyramid scheme with the corresponding FastPM simulation. We run both the simulations in a 400 Mpc/h box on $128^3$ grid for 10 steps from $z=9$ to $z=0$ with force-resolution of 1. The initial conditions

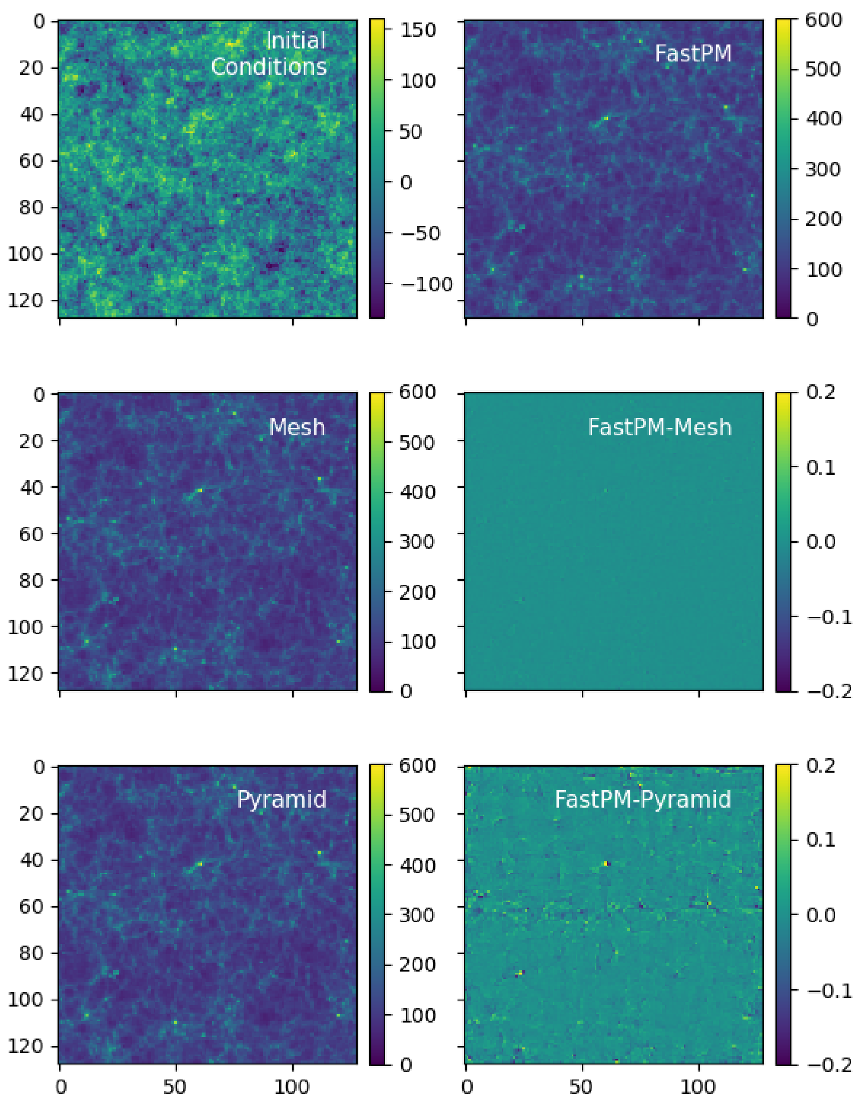


Figure 6.3: Compare the accuracy of FlowPM simulation for Mesh (second left) and Pyramid (third left) scheme with FastPM simulation (top right) for the same initial conditions at the level of fields. The residuals are shown in second and third right image. Configuration is 10 step simulation with $128^3$ grid and 400 Mpc/h in size. FastPM simulation is run on single process while FlowPM simulations are run on 4 process with nx=2 and ny=2, the splits in x and y direction. Third axis is summed over the box for the projections.

**Algorithm 3** Force computation in Muti-grid pyramid method

**procedure** FORCEGRIDS($G$, mode)
▷ Estimate the component force grids with 3D FFT
  $\tilde{G} \Leftarrow \mathrm{F}FT3D(G, mode)$
  **for** $i \in x, y, x$ **do**
    $F_i \Leftarrow \mathrm{i}FFT3D(\nabla_i \nabla^{-2} \tilde{G}, mode)$
  **end for**
  **return** $[F_x, F_y, F_z]$
**end procedure**

**procedure** FORCE($H,\ f = 2,\ n = 6,\ S = 2$)
▷ Pyramid scheme to estimate force meshes
  $D \Leftarrow \mathrm{REDUCE}(H,\ f,\ n,\ S)$
  $F_L \Leftarrow$ FORCEGRIDS$(D, mode = distributed)$
  $F_S \Leftarrow$ FORCEGRIDS$(H, mode = local)$
  **for** $i \in x, y, x$ **do**
    $F_{i,L} \Leftarrow \mathrm{EXPAND}(F_{i,L},\ f,\ n,\ S)$
    $F_{i,l} \Leftarrow \mathrm{REDUCE}(F_{i,S},\ f,\ n,\ S)$
    $F_{i,l} \Leftarrow \mathrm{EXPAND}(F_{i,l},\ f,\ n,\ S)$
    $F_{i,S} \Leftarrow F_{i,S} - F_{i,l}$
    $F_i \Leftarrow F_{i,L} + F_{i,S}$
  **end for**
  **return** $[F_x, F_y, F_z]$
**end procedure**

are generated at the 1st order in LPT. The FastPM simulation is run on a single process while the FlowPM simulations are run on different mesh-splits to validate both the multi-process implementations. We use halo size of 16 grids cells for all configurations and find that increasing the halo size increases the accuracy marginally for all configurations. Moreover, given the more stringent memory constraints of GPU, we run the FastPM simulation with a 64-bit precision while the FlowPM simulations are run with 32-bit precision.

Fig. 6.3 compares the two simulations at the level of the fields. For the FlowPM simulations, we show the configuration run on 4 GPUs, with the grid split in 2 along the x and y direction each. The pyramid implementation shows higher residuals than the single mesh implementation, but they are sub-percent in either case.

In Fig. 6.4 where we compare the two simulations more quantitatively by measuring their clustering. To compare their 2-point functions, we measure the transfer function which is the ratio of the power spectra ($P(k)$) of two fields

$$T_f(k) = \sqrt{\frac{P_a(k)}{P_b(k)}} \tag{6.10}$$

and their cross correlation which compares the phases and hence is a measure of higher order clustering

$$r_c(k) = \frac{P_{ab}(k)}{\sqrt{P_a(k) \times P_b(k)}} \tag{6.11}$$

with $P_{ab}$ being the cross power spectra of the two fields.

Both the transfer function and cross correlation are within 0.01% across all scales, with the latter starting to deviate marginally on small scales. Thus the choices made in terms of convolution filters for up-down sampling, halo size and other parameters in multi-grid scheme, though not extensively explored, are adequate to reach the requisite accuracy. We anticipate this to be a grid resolution dependent statement, and the resolution we have chosen is fairly typical of cosmological simulations that will be run for the analysis of future cosmological surveys and the analytic methods that will most likely use these differentiable simulations.

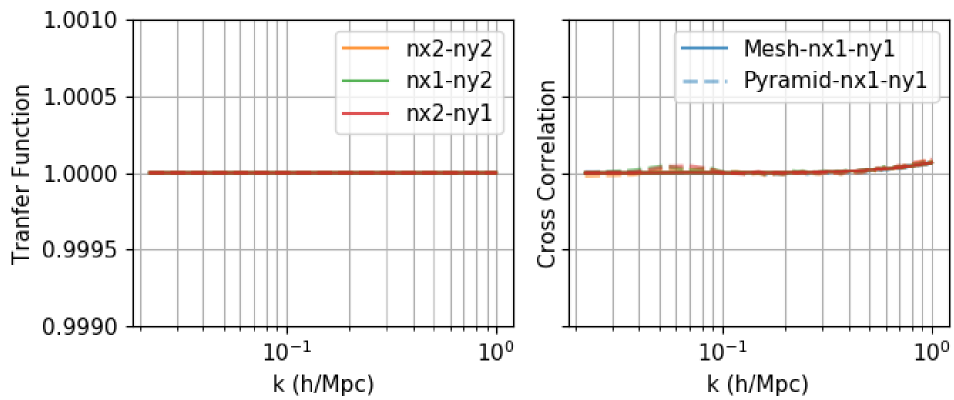


Figure 6.4: Compare the accuracy of FlowPM simulation for Mesh (solid) and Pyramid (dashed) scheme with FastPM simulation at the level of 2 point functions, cross-correlation (left) and transfer-function (right). Configuration is 10 step simulation with $128^3$ grid and 400 Mpc/h in size. FastPM simulation is run on single process while FlowPM simulations are run on different number of processes with nx and ny as splits in x and y direction respectively, as indicated in the legends.

## Scaling on Cori GPU

We perform the scaling tests on the Cori GPUs for varying grid and mesh sizes, and compare it against the scaling of the python implementation of FastPM. As mentioned previously, though the accuracy of the simulation is independent of the mesh layout, the performance can be dependent on it. Thus for the FlowPM implementation, we will look at the timing for different layouts of our mesh.

Since 3D FFTs are typically the most computationally expensive part of any cosmological simulation, we begin with their time-scaling. For the Mesh-TF implementation, where we

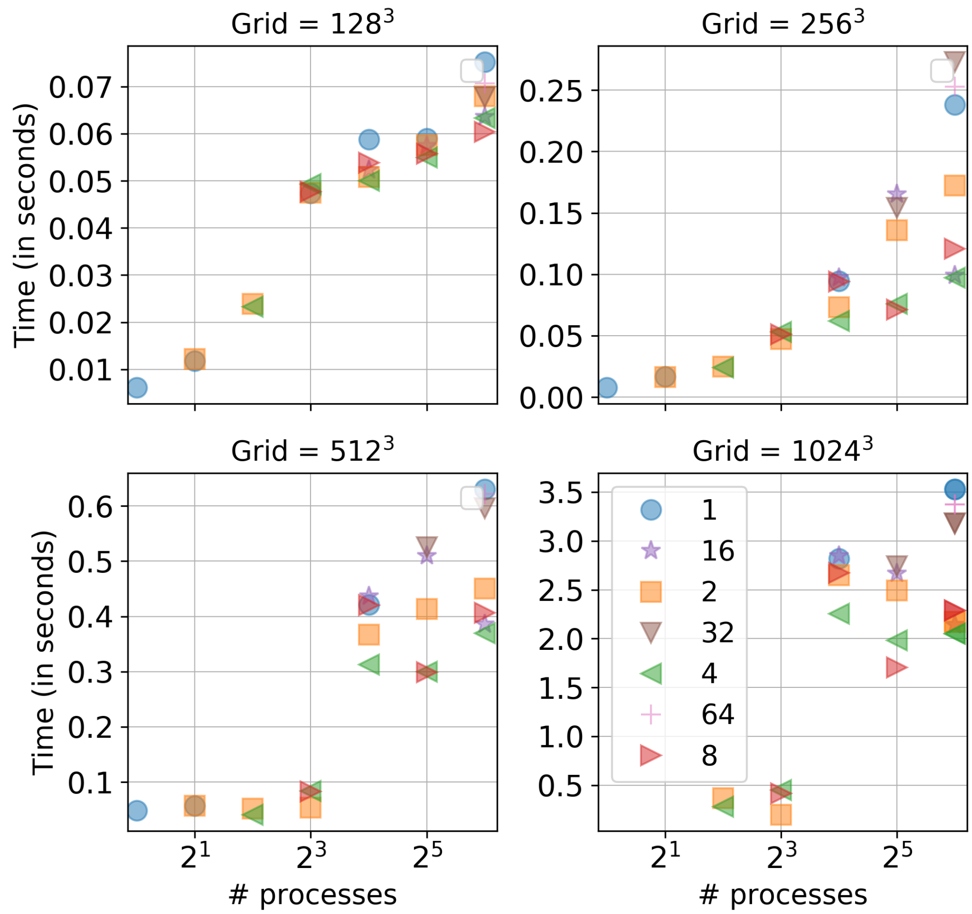


Figure 6.5: Scaling for a single forward+backward 3D FFT implemented in FlowPM in Mesh-Tensorflow for different grid sizes and number of process. Different symbols indicate different layout for computational mesh, with legends indicating the number of splits along x-direction.

have implemented these operations as low-level Mesh-Tensorflow operators, the time scaling is shown in Fig. 6.5. For small grids, the timing for FFT is almost completely dominated by the time spent in all-to-all communications for transpose operations. As a result, the scaling is poor with the timing increasing as we increase the number of processes. However for very large grids, i.e. $N \geq 512$, the compute cost approaches communication cost for small number of process and we see a slight dip upto 8 processes, which is the number of GPUs on a single node. However after that, further increase in number of processes leads to a significant increase in time due to inter-node communications. At the same time, as can be seen from different symbols, unbalanced splits in mesh layout in $x$ and $y$ directions leads to worse performance than a balanced split, with the difference becoming noticeable for large grid sizes.

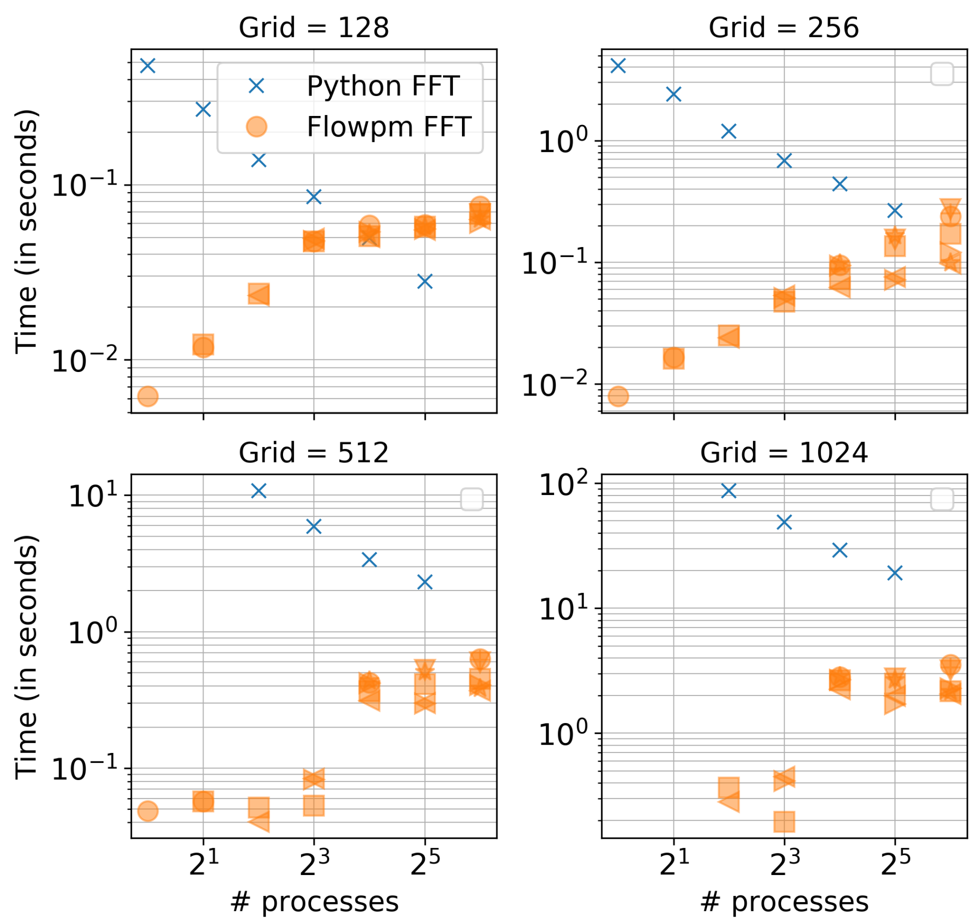


Figure 6.6: Compare the timings of a single forward+backward 3D FFT in FlowPM in Mesh-Tensorflow with PFFT implementation in python-FastPM. Different layouts for Mesh-TF implementation follow the legend of Fig. 6.5.

In Fig. 6.6, we compare the timing of FFT with that implemented in FastPM which implements the PFFT algorithm for 3D FFTs [186]. The scaling for PFFT is close to linear with the increasing number of processes. However due to GPU accelerators, the Mesh-TF FFTs are still order of magnitudes faster in most cases, with only getting comparable for small grid sizes and large mesh sizes.

While the scaling of FFTs is sub-optimal, what is more relevant for us is the scaling of 1 PM step that involves other operations in addition to FFTs. Thus, next we turn to the scaling of generating initial conditions (ICs) for the cosmological simulation. Our ICs are generated as first-order LPT displacements (Zeldovich displacements) [261]. Schematically, the operations involved in this are outlined in Algorithm 4. It provides a natural test since this step involves all the operations that enter a single PM step i.e. kick, drift, force evaluation and interpolation.

**Algorithm 4** Generating IC

**procedure** Gen-IC($N, pk$)
  $g \Leftarrow$ sample 3D normal random field of size $N$
  $\delta_L \Leftarrow$ Scale $g$ by power spectrum $pk$
  $F \Leftarrow$ Estimate force at grid-points from $\delta_L$ i.e. Force
  $d \Leftarrow$ Scale $F$ to obtain displacement
  $X \Leftarrow$ Displace particles with $d$, i.e. Drift
  $V \Leftarrow$ Scale to obtain velocity of particles i.e. Kick
  $\delta \Leftarrow$ Interpolate particles at X to obtain density
  **return** $\delta$
**end procedure**

We establish the scaling for this step in Fig. 6.7 for both the implementations in FlowPM, the single mesh as well as pyramid scheme. Firstly, note that since this step combines computationally intensive operations (like interpolation) with communication intensive operations (like FFT), the scaling for a PM step generally has the desirable slope with the timings improving as we increase the number of processes. There is, however, still a communication overhead as we move from GPUs on a single node to multi-nodes (see for grid size of 128). Secondly, as expected, given the increase in number of operations for the pyramid scheme as compared to single-mesh implementation the single-mesh implementation is more efficient for small grids. However its scaling is poorer than the pyramid scheme which is $\sim 20\%$ faster for grid size of $N = 1024$.

In Fig. 6.8, we compare this implementation with the python implementation. We find that FlowPM is alteast 10x faster than FastPM for the same number of processes, across all sizes (except the combination of smallest grid and largest mesh size). Moreover, since the both FlowPM and FastPM benefit with increasing the number of processes, we expect that it will be hard to beat the performance of FlowPM with simply increasing the number of processes in FastPM.

## 6.7 Example application: Reconstruction of initial conditions

With the turn of the decade, the next generation of cosmological surveys will probe increasingly smaller scales, over the largest volumes, with different cosmological probes. As a result, there is a renewed interest in developing forward modeling approaches and simulations based inference techniques to optimally extract and combine information from these

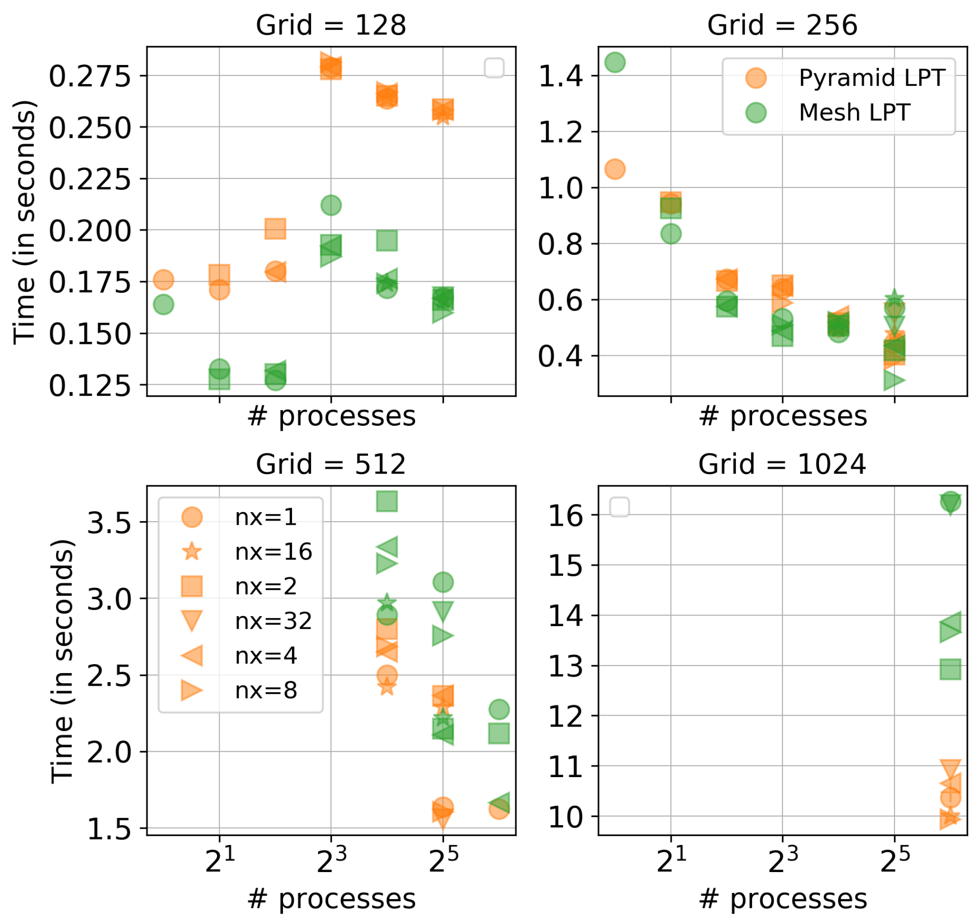


Figure 6.7: Scaling for generating initial conditions with 2nd order LPT in Mesh-Tensorflow for different grid sizes and number of process. Different symbols indicate different layout for computational mesh, with legends indicating the number of splits along x-direction. The scaling of pyramid scheme is shown in orange and a single mesh implementation is shown in green.

surveys. Differentiable simulators such as FlowPM will make these approaches tractable in high-dimensional data spaces of cosmology and hence play an important role in the analysis of these future surveys. One such approach that we have discussed in the previous chapters is reconstructing the initial conditions of the Universe ($\mathbf{s}$) from the late-time observations ($\mathbf{d}$) [247, 120, 211, 156, 206] and here we demonstrate the efficacy of FlowPM in doing so.

To review the approach in brief, we approach this reconstruction in a forward model Bayesian framework [211, 156, 159]. We forward model ($\mathcal{F}$) the observations of interest from the initial conditions of the Universe ($\mathbf{s}$) and compare them with the observed data ($\mathbf{d}$) under a likelihood model - $\mathcal{L}(\mathbf{d}|\mathbf{s})$. This can be combined with the Gaussian prior on the initial

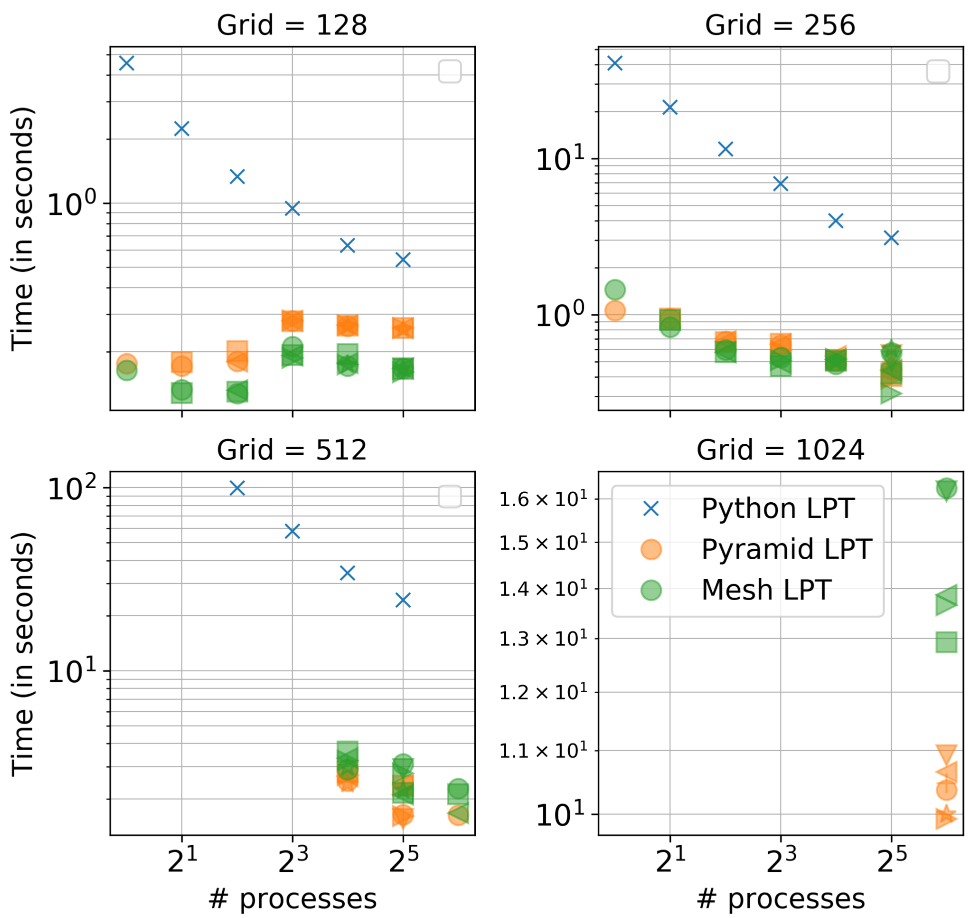


Figure 6.8: Compare the LPT timings for FlowPM in Mesh-Tensorflow and python-FastPM. Different layouts and schemes for Mesh-TF implementation follow the legend of Fig. 6.7.

modes to write the corresponding posterior - $\mathcal{P}(\mathbf{s}|\mathbf{d})$. This posterior is either optimized to get a maximum-a-posteriori (MAP) estimate of the initial conditions, or alternatively it can be explored with sampling methods as in [120]. However in either approach, given the multi-million dimensionality of the observations, it is necessary to use gradient based approaches for optimization and sampling and hence a differentiable forward model is necessary. Particle mesh simulations evolving the initial conditions to the final matter field will form the first part of these forward models for most cosmological observables of interest. With the two examples used in Chapter 3 and Chapter 4, here we demonstrate how the inbuilt differentiability and interfacing of FlowPM with TensorFlow makes developing such approaches natural.

## Reconstruction from Dark Matter

In the first toy problem, consider the reconstruction of the initial matter density field ($\mathbf{s}$) from the final Eulerian dark matter density field ($\mathbf{d} = \delta_e$) as an observable. While the 3D Eulerian dark matter field is not observed directly in any survey, and weak lensing surveys only allow us probe the projected matter density field, this problem is illustrative in that the forward model is only the PM simulation i.e. $\mathcal{F} = \mathrm{F}lowPM$ with the modeled density field $\delta_m = \mathcal{F}(\mathbf{s})$. We will include more realistic observation and complex modeling in the next example.

We assume a Gaussian uncorrelated data noise with constant variance $\sigma^2$ in configuration space. Then, the negative log-posterior of the initial conditions is:

$$\mathcal{P} = \frac{(\delta_e - \delta_m)^2}{2\sigma^2} + \frac{1}{2}\mathbf{s}^\dagger \mathbf{S}^{-1}\mathbf{s} \tag{6.12}$$

where the first term is the negative Gaussian log-likelihood and the second term is the negative Gaussian log-prior on the initial conditions with the variance (power spectrum) $\mathbf{S}$ in the Fourier space.

To reconstruct the initial conditions, we need to minimize the negative log-posterior Eq. 6.12. The snippet of Mesh-TensorFlow code for such a reconstruction using TF Estimator API [51] is outlined in Listing 6.2. In the interest of brevity, we have skipped variable names and dimension declarations, data I/O and other *setup code* and included only the logic directly relevant to reconstruction. Using Estimators allows us to naturally reuse the entire machinery of TensorFlow including but not limited to monitoring optimization, choosing from various inbuilt optimization algorithms, restarting optimization from checkpoints and others. As with other Estimator APIs, the reconstruction code can be split into three components with minimal functions as -

- recon_model : this generates the graph for the forward model using FlowPM from variable linear field (initial conditions) and metrics to optimize for reconstruction
- model_fn : this creates the train and predict specs for the TF Estimator API, with the train function performing the gradient based updates
- main : this calls the estimator to perform and evaluate reconstruction

```
def recon_model(mesh, data, x0):
    ... setup code ...
    #Define initial conditions as variable
    var=mtf.get_variable(mesh,'linear', shape, tf.constant_initializer(x0))
    #Forward model here with FlowPM
    model=FLOWPM(var, ...)
    #Define metrics for loss
    chisq=mtf.reduce_sum(((model-data)/sigma)^2)
    prior=mtf.reduce_sum(r2c(var)^2/power)
```

```
    loss =chisq + prior
    return var, model, loss

def model_fn(x0, data, mode, params):
    ... setup code ...
    var, model, loss=recon_model(mesh, data, x0)
    #Construct optimizer for reconstruction
    if mode == tf.estimator.ModeKeys.TRAIN:
        var_grads=mtf.gradients([loss],[v.outputs
        for v in graph.trainable_variables])
        optimizer=mtf.optimize.AdamOptimizer(0.1)
        update_ops=optimizer.apply_grads( var_grads, graph.trainable_variables)
    #Lower mesh tensorflow variables and ops
    lowering=mtf.Lowering(graph,{mesh:mesh_impl})
    tf_init=lowering.export_to_tf_tensor(var)
    tf_model=lowering.export_to_tf_tensor(model)
    tf_loss=lowering.export_to_tf_tensor(loss)
    #If predict, return current reconstruction
    if mode == tf.estimator.ModeKeys.PREDICT:
        tf.summary.scalar("loss", tf_loss)
        predictions={"ic":tf_init,"data":tf_data}
        return tf.estimator.EstimatorSpec(mode=tf.estimator.ModeKeys.PREDICT,predictions=predictions)
    #If train, optimize for reconstruction
    if mode == tf.estimator.ModeKeys.TRAIN:
        tf_up_op=[lowering.lowered_operation(op) for op in update_ops]
        train_op=tf.group(tf_up_op)
        ...checkpoint hooks...
        return tf.estimator.EstimatorSpec(tf.estimator.ModeKeys.TRAIN, loss=tf_loss, train_op=train_op)

def main():
    ... setup code ...
    #Define estimator for reconstruction
    def input_fn():
        return x0, datafea
    recon_estimator = tf.estimator.Estimator(model_fn=model_fn,model_dir=./tmp/)
    # Train (Reconstruct)
    recon_estimator.train(input_fn=input_fn, max_steps=100)
    #and evaluate model.
    eval_results = recon_estimator.predict(input_fn=input_fn)["ic"]
```

Listing 6.2: Code to reconstruct the initial conditions from the observed matter density field with FlowPM and TensorFlow Estimator API

We show the results of this reconstruction in Fig. 6.9 and 6.10. Here, the forward model is a 5-step PM simulation in a 400 Mpc/h box on $128^3$ grid with force resolution of 1. In addition to gradient based optimization outlined in Listing 6.2, we implement adiabatic methods as described in [88, 156, 159] to assist reconstruction of large scales. We skip those details here in the code for the sake of simplicity, but they are included straightforwardly in this API as a part of recon_model and training spec.

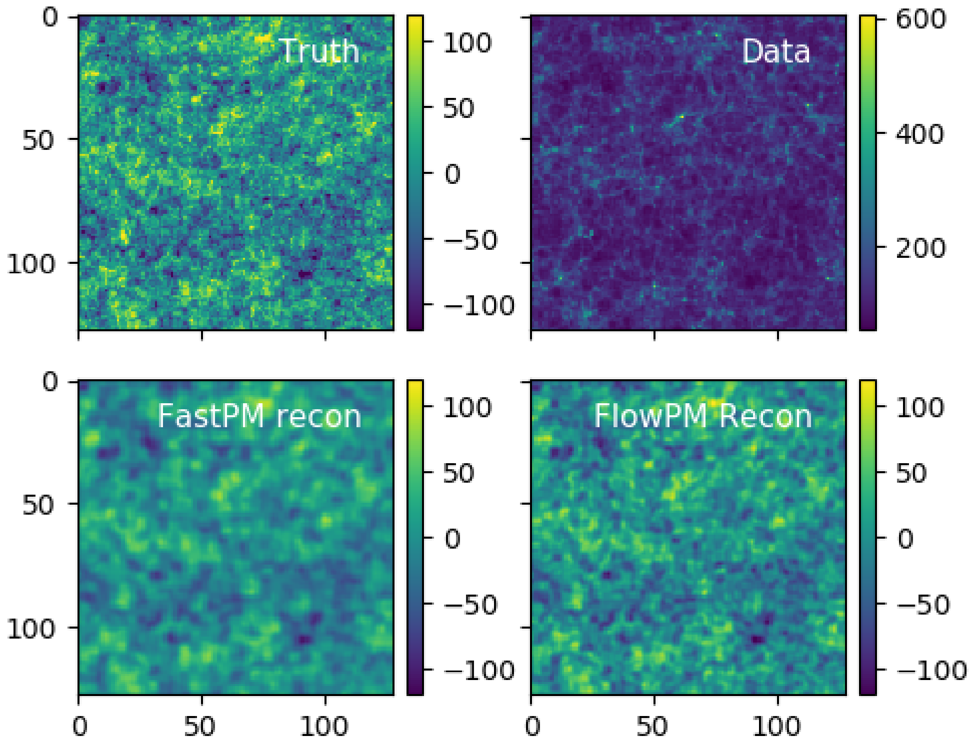


Figure 6.9: Compare the LPT timings for FlowPM in Mesh-Tensorflow and python-FastPM. Different layouts and schemes for Mesh-TF implementation follow the legend of Fig. 6.7.

We compare our results with the previous reconstruction code in python based on FastPM, vmad[5] and abopt[6] (henceforth referred to as FastPM reconstruction). Both the reconstructions follow same adiabatic optimization scheduled to converge large scales as described in [156, 88]. FastPM reconstruction (blue in Fig. 6.10) uses gradient descent algorithm with single step line-search. Every iteration (including gradient evaluation and linesearch) taking roughly $\sim$ 4.6 seconds on 4 nodes i.e. 128 cores on Cori Haswell at NERSC. We reconstructed for 500 steps, uptil the large scales converged, in total wall-clock time of $\sim$ 2300 seconds. In comparison, for FlowPM reconstruction (orange curves in Fig. 6.10) we take advantage of different algorithms in-built in TensorFlow and use Adam [126] optimization with initial learning rate of 0.01, without any early stopping or tolerance. Every adiabatic

[5] https://github.com/rainwoodman/vmad
[6] https://github.com/bccp/abopt

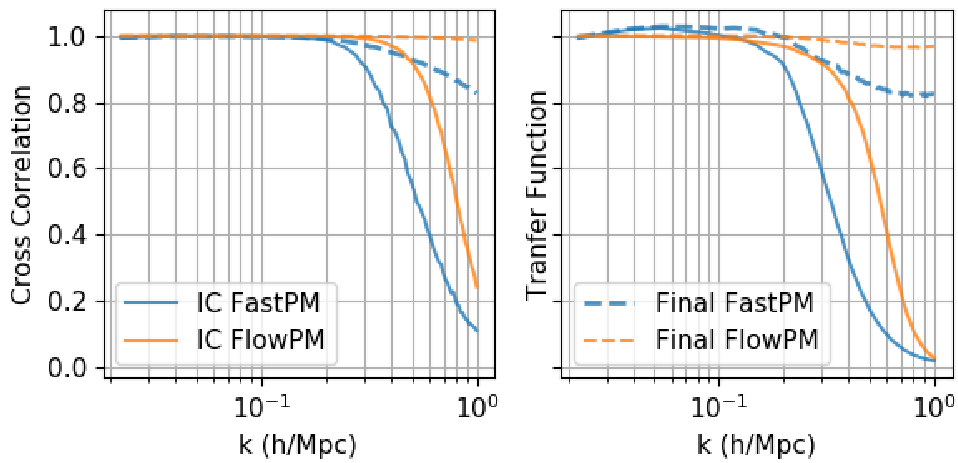


Figure 6.10: Compare the LPT timings for FlowPM in Mesh-Tensorflow and python-FastPM. Different layouts and schemes for Mesh-TF implementation follow the legend of Fig. 6.7.

optimization step run for 100 iterations. With every iteration taking $\sim$ 1.1 seconds on a single Cori GPU and 500 iterations for total optimization clocked in at $\sim$ 550 seconds in wallclock time. These numbers, except time per iteration, will likely change with a different learning rate and optimization algorithm and we have not explored these in detail for this toy example.

In Fig. 6.9, we show the true initial and data field along with the reconstructed initial field by both codes. In Fig 6.10, we show the cross correlation and transfer function between the reconstructed and true initial fields (solids) as well as the final data field (dashed). While it appears as FlowPM reconstructs initial field better than FastPM, this is primarily due to poor convergence of gradient descent. FastPM reconstruction can be improved and made comparable to FlowPM if we instead use L-BFGS algorithm with little increase in wall clock of time, up to 4.8 seconds per iteration.

## Reconstruction from Halos with a Neural Network model

In the next example, we consider a realistic case of reconstruction of the initial conditions from dark matter halos under a more complex forward model. Dark matter halos and their masses are not observed themselves. However they are a good proxy for galaxies which are the primary tracers observed in large scale structure surveys, since they capture the challenges posed by galaxies as a discrete, sparse and biased tracer of the underlying matter field. Traditionally, halos are modeled as a biased version of the Eulerian or Lagrangian matter and associated density field [221, 148, 206]. To better capture the discrete nature of the observables at the field level, [156] proposed using neural networks to model the halo masses and positions from the Eulerian matter density field. Here we replicate their formalism and reconstruct the initial conditions from the halo mass field as observable.

As outlined in Chapter 4 [156], the output of PM simulation is supplemented with two pre-trained fully connected networks, NNp and NNm, to predict a mask of halo positions and estimates of halo masses at every grid point. These are then combined to predict a halo-mass field ($\mathrm{M_{NN}}$) that is compared with the observed halo-mass field ($\mathrm{M}_d$) upto a pre-chosen number density. The heuristic likelihood for the data inspired from the log-normal scatter of halo masses with respect to observed stellar luminosity and validated against simulations in 4.14

$$\mathcal{L} = \frac{\mu + \log(M_d^R + M_0) - \log(M_{NN}^R + M_0))}{2\sigma^2} \tag{6.13}$$

where $\mathrm{M}_0$ is a constant varied over iterations to assist with optimization, $\mathrm{M}^R$ are mass-fields smoothed with a Gaussian of scale $R$ and $\mu$ and $\sigma$ are mass-dependent mean and standard deviations of the log-normal error model estimated from simulations.

The code snippet in Listing 6.3 modifies the code in 6.2 by including these pre-trained neural networks NNp and NNm in the forward model to supplement FlowPM. It also demonstrates how to include associated variables like $\mathrm{M}_0$ in the recon_model function that can be updated with ease over iterations to modify the model and optimization.

```

def recon_model(mesh, data, x0, M0):
    ... setup code and load pre-trained variables of NN ...
    #Define initial conditions as variable
    var=mtf.get_variable(mesh,'linear', shape, tf.constant_initializer(x0)
        )
    #Forward model here with FlowPM
    final_field=FLOWPM(var, ...)
    #Supplement FlowPM with NN models
    position= NNp(field_field)
    mass= NNm(final_field)
    model=position*mass
    #Define metrics for loss
    chisq=mtf.reduce_sum(((mu + mtf.log(model+M0)-mtf.log(data+M0))/sigma)
        ^2)
    prior=mtf.reduce_sum(r2c(var)^2/power)
    loss =chisq + prior
    return var, model, loss

def model_fn(ft, data, mode, params):
    ... setup code ...
    var, model, loss=recon_model(mesh, data, ft['x0'], ft['M0'])
    ... same as Listing 6.2 from here ...

def main():
    ... setup code ...
    #Estimator with dict input
```

```
    def input_fn():
        ft={'x0':x0, 'M0':M0}
        return ft, data
    ...  same as Listing 6.2 from here  ...
    recon_estimator = tf.estimator.Estimator(model_fn=model_fn,model_dir
        =./tmp/)
    # Train (Reconstruct)
    recon_estimator.train(input_fn=input_fn, max_steps=100)
    #and evaluate model.
    eval_results = recon_estimator.predict(input_fn=input_fn)["ic"]
```

Listing 6.3: Update Listing 6.2 to include neural networks in the forward model and associated variables to be changed over iterations of reconstruction

We again compare the results for FastPM and FlowPM reconstruction with the same configuration as before in Fig. 6.11 and 6.12. Here, the data is halo mass field with number density $10^{-3}$ on a $128^3$ grid for a 400 Mpc/h box. At this resolution and number density, only 17.5% of grid points are non-zero, indicating the sparsity of our data. The forward model is a 5 step FastPM simulation followed by two layer fully connected networks with total 5000 and 600 weights respectively (see [156] for details). The position network takes in non-local features as a flattened array that can also be implemented as a convolution kernel of size 3 in TensorFlow. Both the codes reconstruct the initial conditions equally well at the level of cross-correlation. However the transfer functions for both the reconstruction is quite different. [211, 156, 112] discuss simulation based methods to correct the reconstructed transfer function, but we do not discuss them here since it is beyond the scope and not the main point of this work.

In addition to the ease of implementing reconstruction in FlowPM, the most significant gain of FlowPM is in terms of the speed of iteration. The time taken for 1 FlowPM iteration is $\sim 1.7$ second while time taken for 1 iteration in FastPM reconstruction in $\sim 15$ seconds. The huge increase in time for FastPM iterations as compared to FlowPM is due to the python implementation of single convolution kernel and its gradients as required by the neural network bias model, which is very efficiently implemented in TensorFlow. Due to increased complexity of forward model, gradient descent with line search does not converge at all. Thus we use LBFGS optimization for FastPM reconstruction and it takes roughly 450 iterations. FlowPM implementation, with Adam algorithm as before, does 100 iterations at every step and totals to 1500 iterations since we do not include early stopping. As a result, FlowPM implementation takes roughly 30 minutes on a single GPU while FastPM reconstruction takes roughly 2 hours on 128 processes.

## 6.8 Conclusion

In this work, we present FlowPM - a cosmological N-body code implemented in Mesh-TensorFlow for GPU-accelerated, distributed, and differentiable simulations to tackle the

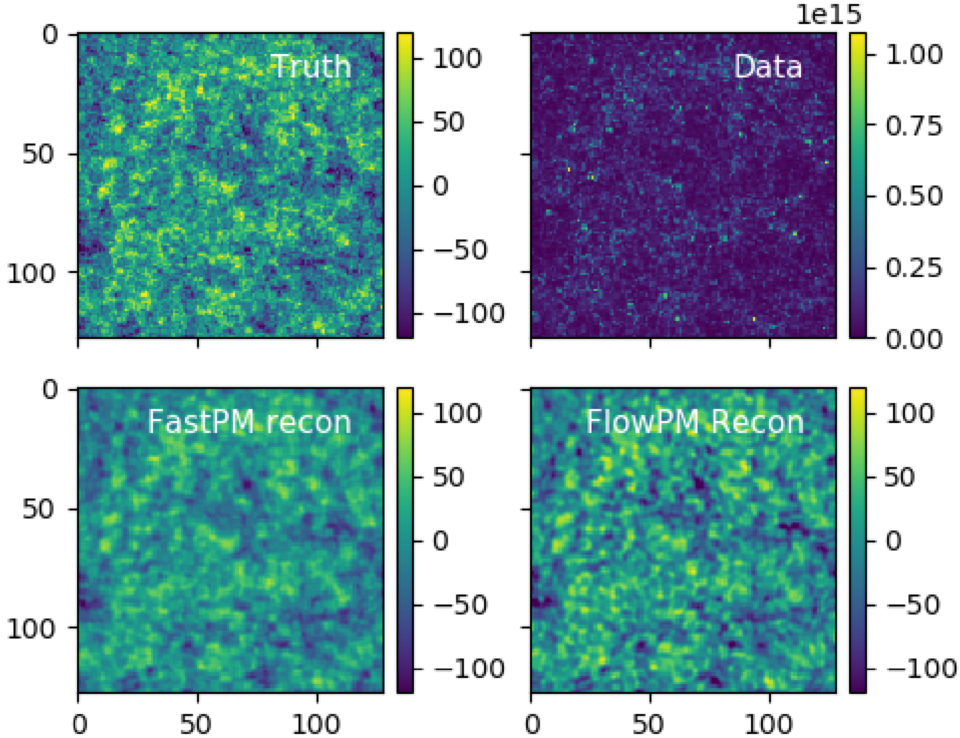


Figure 6.11: Compare the LPT timings for FlowPM in Mesh-Tensorflow and python-FastPM. Different layouts and schemes for Mesh-TF implementation follow the legend of Fig. 6.7.

unprecedented modeling and analytic challenges posed by the next generation of cosmological surveys.

FlowPM implements FastPM scheme as the underlying particle-mesh gravity solver, with gravitational force estimated with 3D Fourier transforms. For distributed computation, we use Mesh-TensorFlow as our model parallelism framework which gives us full flexibility in determining the computational layout and distribution of our simulation. To overcome the bottleneck of large scale distributed 3D FFTs, we propose and implement a novel multi-grid force computation scheme based on image pyramids. We demonstrate that without any fine tuning, this method is able to achieve sub-percent accuracy while reducing the communication data-volume by a factor of 64x. At the same time, given the GPU accelerations, FlowPM is 4-20x faster than the corresponding python FastPM simulation depending on the resolution and compute distribution.

However the main advantage of FlowPM is the differentiability of the simulation and natural interfacing with deep learning frameworks. Built entirely in TensorFlow, the simulations are differentiable with respect to every component. This allows for development of novel analytic methods such as simulations based inference and reconstruction of cosmological fields,

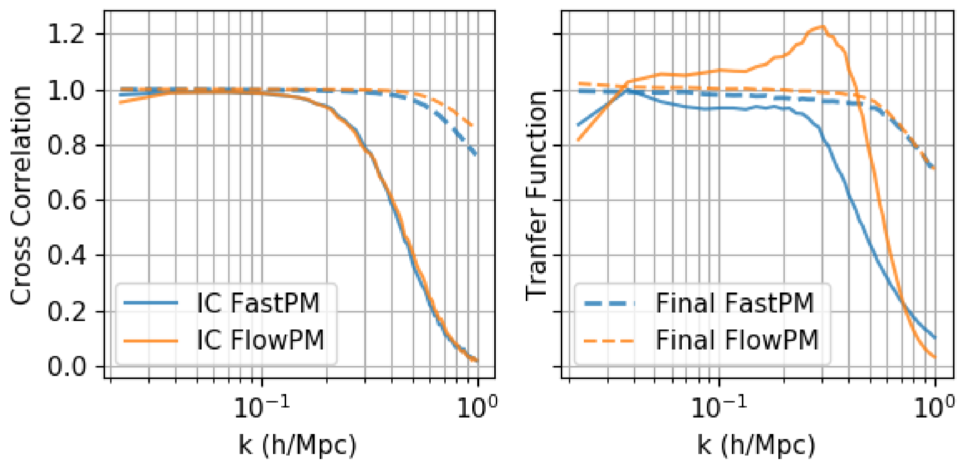


Figure 6.12: Compare the LPT timings for FlowPM in Mesh-Tensorflow and python-FastPM. Different layouts and schemes for Mesh-TF implementation follow the legend of Fig. 6.7.

that were hitherto intractable due to the multi-million dimensionality of these problems. We demonstrate with two examples, providing the logical code-snippets, how FlowPM makes the latter straightforward by using TensorFlow Estimator API to do optimization in $128^3$ dimensional space. It is also able to naturally interface with machine learning frameworks as a part of the forward model in this reconstruction. Lastly, due to its speed, it is able to achieve comparable accuracy to FastPM based reconstruction in 5 times lower wall-clock time, and 640 times lower computing time.

FlowPM is open-source and we have made it publicly available on our Github repo at https://github.com/modichirag/flowpm. We provide example code to do forward PM evolution with single-grid and multi-grid force computation. We also provide code for the reconstruction with both the examples demonstrated in the chapter. We hope that this will encourage the community to use this novel tool and develop scientific methods to tackle the next generation of cosmological surveys.

# Acknowledgements

This material is based upon work supported by the National Science Foundation under Grant Numbers 1814370 and NSF 1839217, and by NASA under Grant Number 80NSSC18K1274. This research used resources of the National Energy Research Scientific Computing Center (NERSC), a U.S. Department of Energy Office of Science User Facility operated under Contract No. DE-AC02-05CH11231.

# Chapter 7

# Conclusions

In the upcoming decade, the 3D density field of our cosmos will be mapped with the largest imaging surveys, making large scale structures of the Universe a leading probe of cosmology. To realize their potential, we need to develop analytic and computational methods that will maximize the information extracted from all scales probed by these surveys. This requires tackling the challenges of large amounts of data and ability to systematically combine multiple probes while correctly accounting for the non-linearities and non-Gaussianities of the signal.

In this thesis, we have developed a formalism to maximize the cosmological information extracted from the nonlinear regime by reconstructing cosmological fields in a forward model framework. We focus on forward modeling since they are the most promising ways to jointly model different cosmological observations from the same initial conditions of the Universe, including their individual systematic biases and noise. While this approach can be computationally expensive, we are assisted in this by computational and algorithmic advances of the past decade as well as development in machine learning techniques.

A necessary ingredient for our approach is the differentiability of the forward model and we develop them for different cosmological probes in Chapter 2. We show that particle mesh simulations which evolve dark matter under gravitational interaction and form the first step of any LSS model are differentiable. Most LSS surveys observe biased tracers of the dark matter field and for them, we develop a Lagrangian bias model at the field level that reduces stochasticity over other Eulerian and Lagrangian bias models. Primary observable for imaging surveys are galaxies, which are not only biased but discrete and hence inherently non-differentiable. Thus we propose a new neural network framework to model halo properties such as position and mass. It takes in dark matter properties as the input and outputs quantities such as the probability of finding a halo at a given position and the halo mass, outperforming traditional bias model.

We lay out our new approach for the analysis of LSS in Chapter 3. We reconstruct the initial density field of the Universe by maximizing their posterior, given the likelihood of the observed data under the forward model. However this reconstructed map typically has millions of data points and contains too much information to be useful on its own. To circumvent this, we also construct a power spectrum estimator for the map which is the summary statistic containing all the information for a field of Gaussian initial modes. In chapter 4, we combine this approach with neural network model to reconstruct the initial density field from dark matter halos. We show that for upcoming surveys such as DESI, our formalism reconstructs Baryon Acoustic Oscillations better than standard reconstruction methods by over 20% in real space, and a factor of few in redshift space.

Forward modeling makes our approach quite versatile and allows us to go beyond simply reconstructing initial field and overcome the challenges posed by non-linearity and non-Gaussianity of the observables. With neutral hydrogen intensity mapping in Chapter 5 , we show how this can also be used to recover lost information in the observed data. We reconstruct the large scale modes lost in the 21-cm maps due to orders of magnitude brighter foregrounds. This reconstructed field allows us to achieve otherwise infeasible science goals such as cross-correlation analysis with CMB lensing and photometric surveys like LSST and realize the potential of 21-cm intensity mapping to probe the high redshift Universe.

Ultimately, with the necessity to jointly model multiple cosmological probes and push to increasingly non-linear scales for upcoming LSS surveys, we expect the methods developed here to superseed the traditional data analysis methods in cosmology. However developing fast, efficient differentiable simulations to model the unprecedented scales and dynamic range of these surveys is still challenging. We take first steps in this direction in Chapter 6 by developing FlowPM - a TensorFlow implementation of distributed N-Body PM solver. Written entirely in TensorFlow, these simulations are GPU-accelerated and hence faster than CPU-based PM simulations. A bottleneck for large scale distributed PM simulations is distributed 3D FFTs for estimating force in PM simulations. We overcome this by developing a novel multi-grid scheme for force estimation. The key advantage of FlowPM is its end-to-end differentiability. This allows for development of novel analytic methods such as simulations based inference and reconstruction of cosmological fields. At the same time, they encode the exact underlying dynamics for gravitational evolution (within a PM scheme), while still leaving room for natural synthesis with cutting edge machine learning components to develop hybrid simulations, which can complement by learning the sub-grid and non-gravitational dynamics not included in PM gravity solver cosmological simulations.

We thus hope that the methodological, algorithmic and computational tools developed in this thesis will assist the community in realizing the full potential of the next generation of cosmological surveys.

# Bibliography


[1] M. Abadi et al. "TensorFlow: Large-Scale Machine Learning on Heterogeneous Distributed Systems". In: *ArXiv e-prints* (Mar. 2016). arXiv: 1603.04467 [cs.DC].

[2] Kevork N. Abazajian et al. "CMB-S4 Science Book, First Edition". In: *arXiv e-prints*, arXiv:1610.02743 (Oct. 2016), arXiv:1610.02743. arXiv: 1610.02743 [astro-ph.CO].

[3] Des Collaboration T. M. C. Abbott et al. "Dark Energy Survey year 1 results: Cosmological constraints from galaxy clustering and weak lensing". In: *Physical Review D* 98 (2018), p. 043526.

[4] F. B. Abdalla et al. "Cosmology from HI galaxy surveys with the SKA". In: *Advancing Astrophysics with the Square Kilometre Array (AASKA14)*, 17 (Apr. 2015), p. 17. arXiv: 1501.04035.

[5] Muntazir Abidi and Tobias Baldauf. "Cubic halo bias in Eulerian and Lagrangian space". In: *Journal of Cosmology and Astroparticle Physics* 2018 (2018), pp. 029–029.

[6] Planck Collaboration Y. Akrami et al. "Planck 2018 results. I. Overview and the cosmological legacy of Planck". In: *Astronomy and Astrophysics* (2018).

[7] S. Alam et al. "The clustering of galaxies in the completed SDSS-III Baryon Oscillation Spectroscopic Survey: cosmological analysis of the DR12 galaxy sample". In: *Mon. Not. R. Astron. Soc.* 470 (Sept. 2017), pp. 2617–2652. DOI: 10.1093/mnras/stx721. arXiv: 1607.03155.

[8] David Alonso et al. "Calibrating photometric redshifts with intensity mapping observations". In: *Phys. Rev. D* 96.4, 043515 (Aug. 2017), p. 043515. DOI: 10.1103/PhysRevD.96.043515. arXiv: 1704.01941 [astro-ph.CO].

[9] Justin Alsing, Benjamin Wandelt, and Stephen Feeney. "Massive optimal data compression and density estimation for scalable, likelihood-free inference in cosmology". In: *Mon. Not. R. Astron. Soc.* 477.3 (July 2018), pp. 2874–2885. DOI: 10.1093/mnras/sty819. arXiv: 1801.01497 [astro-ph.CO].

[10] L. Amendola et al. "Cosmology and fundamental physics with the Euclid satellite". In: *Living Reviews in Relativity* 21, 2 (Apr. 2018), p. 2. DOI: 10.1007/s41114-017-0010-3. arXiv: 1606.00180.

[11] C. H. Anderson et al. *Pyramid Methods in Image Processing*. 1984.

[12] C. J. Anderson et al. "Low-amplitude clustering in low-redshift 21-cm intensity maps cross-correlated with 2dF galaxy densities". In: *Mon. Not. R. Astron. Soc.* 476 (May 2018), pp. 3382–3392. DOI: 10.1093/mnras/sty346. arXiv: 1710.00424.

[13] R. E. Angulo and A. Pontzen. "Cosmological N-body simulations with suppressed variance". In: *Mon. Not. R. Astron. Soc.* 462 (Oct. 2016), pp. L1–L5. DOI: 10.1093/mnrasl/slw098. arXiv: 1603.05253.

[14] R. E. Angulo et al. "The fate of substructures in cold dark matter haloes". In: *Mon. Not. R. Astron. Soc.* 399 (Oct. 2009), pp. 983–995. DOI: 10.1111/j.1365-2966.2009.15333.x. arXiv: 0810.2177.

[15] Grigor Aslanyan. "Cosmo++: An Object-Oriented C++ Library for Cosmology". In: *Comput. Phys. Commun.* 185 (2014), pp. 3215–3227. DOI: 10.1016/j.cpc.2014.08.021. arXiv: 1312.4961 [astro-ph.IM].

[16] T. Baldauf et al. "Evidence for quadratic tidal tensor bias from the halo bispectrum". In: *Phys. Rev. D* 86.8, 083540 (Oct. 2012), p. 083540. DOI: 10.1103/PhysRevD.86.083540. arXiv: 1201.4827 [astro-ph.CO].

[17] T. Baldauf et al. "Halo stochasticity from exclusion and nonlinear clustering". In: *Phys. Rev. D* 88.8, 083507 (Oct. 2013), p. 083507. DOI: 10.1103/PhysRevD.88.083507. arXiv: 1305.2917 [astro-ph.CO].

[18] Tobias Baldauf, Vincent Desjacques, and Uroš Seljak. "Velocity bias in the distribution of dark matter halos". In: *Physical Review D* 92.12 (2015), p. 123507.

[19] K. Bandura et al. "Canadian Hydrogen Intensity Mapping Experiment (CHIME) pathfinder". In: *Ground-based and Airborne Telescopes V*. Vol. 9145. Proc. SPIE. July 2014, p. 914522. DOI: 10.1117/12.2054950. arXiv: 1406.2288 [astro-ph.IM].

[20] Josh Barnes and Piet Hut. "A hierarchical O(N log N) force-calculation algorithm". In: *Nature* 324.6096 (Dec. 1986), pp. 446–449. DOI: 10.1038/324446a0.

[21] N. Bartolo et al. "Non-Gaussianity from inflation: theory and observations". In: Phys. Rep. 402.3-4 (Nov. 2004), pp. 103–266. DOI: 10.1016/j.physrep.2004.08.022. arXiv: astro-ph/0406398 [astro-ph].

[22] Julian E. Bautista et al. "The SDSS-IV Extended Baryon Oscillation Spectroscopic Survey: Baryon Acoustic Oscillations at Redshift of 0.72 with the DR14 Luminous Red Galaxy Sample". In: *Astrophys. J.* 863.1, 110 (Aug. 2018), p. 110. DOI: 10.3847/1538-4357/aacea5. arXiv: 1712.08064 [astro-ph.CO].

[23] Peter Behroozi et al. "UniverseMachine: The Correlation between Galaxy Growth and Dark Matter Halo Assembly from z=0-10". In: *arXiv e-prints*, arXiv:1806.07893 (June 2018), arXiv:1806.07893. arXiv: 1806.07893 [astro-ph.GA].

[24] Andreas A. Berlind and David H. Weinberg. "The Halo Occupation Distribution: Toward an Empirical Determination of the Relation between Galaxies and Mass". In: *The Astrophysical Journal* 575.2 (2002), p. 587. URL: http://stacks.iop.org/0004-637X/575/i=2/a=587.

[25] F. Bernardeau et al. "Large scale structure of the universe and cosmological perturbation theory". In: *Phys. Rept.* 367 (2002), pp. 1–248. DOI: 10.1016/S0370-1573(02)00135-7. arXiv: astro-ph/0112551.

[26] Edmund Bertschinger and Avishai Dekel. "Recovering the Full Velocity and Density Fields from Large-Scale Redshift-Distance Samples". In: *Astrophys. J.* 336 (Jan. 1989), p. L5. DOI: 10.1086/185348.

[27] F. Beutler et al. "The clustering of galaxies in the completed SDSS-III Baryon Oscillation Spectroscopic Survey: Anisotropic galaxy clustering in Fourier-space". In: *ArXiv e-prints* (July 2016). arXiv: 1607.03150.

[28] S. Bharadwaj. "Perturbative Growth of Cosmological Clustering. II. The Two-Point Correlation". In: *Astrophys. J.* 460 (Mar. 1996), p. 28. DOI: 10.1086/176950. eprint: astro-ph/9511085.

[29] Matteo Biagetti et al. "Measuring non-local Lagrangian peak bias". In: *Monthly Notices of the Royal Astronomical Society* 441.2 (2014), pp. 1457–1467.

[30] Jack Birkin et al. "Reconstructing the baryon acoustic oscillations using biased tracers". In: *Mon. Not. R. Astron. Soc.* 483.4 (Mar. 2019), pp. 5267–5280. DOI: 10.1093/mnras/sty3365. arXiv: 1809.08135 [astro-ph.CO].

[31] Michael R. Blanton et al. "Sloan Digital Sky Survey IV: Mapping the Milky Way, Nearby Galaxies, and the Distant Universe". In: *AJ* 154.1, 28 (July 2017), p. 28. DOI: 10.3847/1538-3881/aa7567. arXiv: 1703.00052 [astro-ph.GA].

[32] Diego Blas, Julien Lesgourgues, and Thomas Tram. "The Cosmic Linear Anisotropy Solving System (CLASS). Part II: Approximation schemes". In: *Journal of Cosmology and Astro-Particle Physics* 2011.7, 034 (July 2011), p. 034. DOI: 10.1088/1475-7516/2011/07/034. arXiv: 1104.2933 [astro-ph.CO].

[33] J. R. Bond, A. H. Jaffe, and L. Knox. "Estimating the power spectrum of the cosmic microwave background". In: *Phys. Rev. D* 57 (Feb. 1998), pp. 2117–2137.

[34] J. R. Bond et al. "Excursion set mass functions for hierarchical Gaussian fluctuations". In: *Astrophys. J.* 379 (Oct. 1991), pp. 440–460. DOI: 10.1086/170520.

[35] C. B. Brook et al. "The Stellar-to-halo Mass Relation for Local Group Galaxies". In: *Astrophys. J. Lett.* 784, L14 (Mar. 2014), p. L14. DOI: 10.1088/2041-8205/784/1/L14. arXiv: 1311.5492.

[36] P. Bull et al. "Late-time Cosmology with 21 cm Intensity Mapping Experiments". In: *Astrophys. J.* 803, 21 (Apr. 2015), p. 21. DOI: 10.1088/0004-637X/803/1/21. arXiv: 1405.1452.

[37] P. Burt and E. Adelson. "The Laplacian Pyramid as a Compact Image Code". In: *IEEE Transactions on Communications* 31.4 (1983), pp. 532–540.

[38] Ruby Byrne et al. "Fundamental Limitations on the Calibration of Redundant 21 cm Cosmology Instruments and Implications for HERA and the SKA". In: *Astrophys. J.* 875.1, 70 (Apr. 2019), p. 70. DOI: 10.3847/1538-4357/ab107d. arXiv: 1811.01378 [astro-ph.IM].

[39] J. Carlson, B. Reid, and M. White. "Convolution Lagrangian perturbation theory for biased tracers". In: *Mon. Not. R. Astron. Soc.* 429 (Feb. 2013), pp. 1674–1685. DOI: 10.1093/mnras/sts457. arXiv: 1209.0780.

[40] J. Carlson, B. Reid, and M. White. "Convolution Lagrangian perturbation theory for biased tracers". In: *Mon. Not. R. Astron. Soc.* 429 (Feb. 2013), pp. 1674–1685. DOI: 10.1093/mnras/sts457. arXiv: 1209.0780.

[41] P. Carter et al. "Low redshift baryon acoustic oscillation measurement from the reconstructed 6-degree field galaxy survey". In: *Mon. Not. R. Astron. Soc.* 481 (Dec. 2018), pp. 2371–2383. DOI: 10.1093/mnras/sty2405. arXiv: 1803.01746.

[42] E. Castorina and F. Villaescusa-Navarro. "On the spatial distribution of neutral hydrogen in the Universe: bias and shot-noise of the H I power spectrum". In: *Mon. Not. R. Astron. Soc.* 471 (Oct. 2017), pp. 1788–1796. DOI: 10.1093/mnras/stx1599. arXiv: 1609.05157.

[43] E. Castorina and M. White. "Beyond the plane-parallel approximation for redshift surveys". In: *Mon. Not. R. Astron. Soc.* 476 (June 2018), pp. 4403–4417. DOI: 10.1093/mnras/sty410. arXiv: 1709.09730.

[44] E. Castorina and M. White. "Measuring the growth of structure with intensity mapping surveys". In: *arXiv e-prints* (Feb. 2019). arXiv: 1902.07147.

[45] E. Castorina and M. White. "The Zeldovich approximation and wide-angle redshift-space distortions". In: *Mon. Not. R. Astron. Soc.* 479 (Sept. 2018), pp. 741–752. DOI: 10.1093/mnras/sty1437. arXiv: 1803.08185.

[46] E. Castorina et al. "Excursion set peaks: the role of shear". In: *ArXiv e-prints* (Nov. 2016). arXiv: 1611.03619.

[47] M. C. Cautun and R. van de Weygaert. *The DTFE public software: The Delaunay Tessellation Field Estimator code*. Astrophysics Source Code Library. May 2011. arXiv: 1105.0370 [astro-ph.IM].

[48] K. C. Chan, R. Scoccimarro, and R. K. Sheth. "Gravity and large-scale nonlocal bias". In: *Phys. Rev. D* 85.8, 083509 (Apr. 2012), p. 083509. DOI: 10.1103/PhysRevD.85.083509. arXiv: 1201.3614 [astro-ph.CO].

[49] S.-F. Chen et al. "Synergies between radio, optical and microwave observations at high redshift". In: *ArXiv e-prints* (Oct. 2018). arXiv: 1810.00911.

[50] X. Chen. “The Tianlai Project: a 21CM Cosmology Experiment”. In: *International Journal of Modern Physics Conference Series*. Vol. 12. International Journal of Modern Physics Conference Series. Mar. 2012, pp. 256–263. DOI: 10.1142/S2010194512006459. arXiv: 1212.6278 [astro-ph.IM].

[51] Heng-Tze Cheng et al. “TensorFlow Estimators: Managing Simplicity vs. Flexibility in High-Level Machine Learning Frameworks”. In: *arXiv e-prints*, arXiv:1708.02637 (Aug. 2017), arXiv:1708.02637. arXiv: 1708.02637 [cs.DC].

[52] François Chollet et al. *Keras*. https://github.com/fchollet/keras. 2015.

[53] Chia-Hsun Chuang et al. “UNIT project: Universe \$N\$-body simulations for the Investigation of Theoretical models from galaxy surveys”. In: *arXiv e-prints*, arXiv:1811.02111 (Nov. 2018), arXiv:1811.02111. arXiv: 1811.02111 [astro-ph.CO].

[54] J. D. Cohn et al. “Combining galaxy and 21-cm surveys”. In: *Mon. Not. R. Astron. Soc.* 457 (Apr. 2016), pp. 2068–2077. DOI: 10.1093/mnras/stw108. arXiv: 1511.07377.

[55] Cosmic Visions 21 cm Collaboration et al. “Inflation and Early Dark Energy with a Stage II Hydrogen Intensity Mapping experiment”. In: *ArXiv e-prints* (Oct. 2018). arXiv: 1810.09572.

[56] Kyle Cranmer, Johann Brehmer, and Gilles Louppe. “The frontier of simulation-based inference”. In: *arXiv e-prints*, arXiv:1911.01429 (Nov. 2019), arXiv:1911.01429. arXiv: 1911.01429 [stat.ML].

[57] N. H. M. Crighton et al. “The neutral hydrogen cosmological mass density at z = 5”. In: *Mon. Not. R. Astron. Soc.* 452 (Sept. 2015), pp. 217–234. DOI: 10.1093/mnras/stv1182. arXiv: 1506.02037.

[58] M. Crocce and R. Scoccimarro. “Nonlinear evolution of baryon acoustic oscillations”. In: *Phys. Rev. D* 77.2, 023533 (Jan. 2008), p. 023533. DOI: 10.1103/PhysRevD.77.023533. arXiv: 0704.2783.

[59] Rupert A. C. Croft et al. “The Power Spectrum of Mass Fluctuations Measured from the Ly$\alpha$ Forest at Redshift z = 2.5”. In: *Astrophys. J.* 520.1 (July 1999), pp. 1–23. DOI: 10.1086/307438. arXiv: astro-ph/9809401 [astro-ph].

[60] Carolina Cuesta-Lazaro et al. “Towards a non-Gaussian model of redshift space distortions”. In: *arXiv e-prints*, arXiv:2002.02683 (Feb. 2020), arXiv:2002.02683. arXiv: 2002.02683 [astro-ph.CO].

[61] Dark Energy Survey Collaboration et al. “The Dark Energy Survey: more than dark energy - an overview”. In: *Mon. Not. R. Astron. Soc.* 460.2 (Aug. 2016), pp. 1270–1299. DOI: 10.1093/mnras/stw641. arXiv: 1601.00329 [astro-ph.CO].

[62] A. Datta, J. D. Bowman, and C. L. Carilli. “Bright Source Subtraction Requirements for Redshifted 21 cm Measurements”. In: *Astrophys. J.* 724 (Nov. 2010), pp. 526–538. DOI: 10.1088/0004-637X/724/1/526. arXiv: 1005.4071.

[63] Yann Dauphin et al. "Identifying and attacking the saddle point problem in high-dimensional non-convex optimization". In: *CoRR* abs/1406.2572 (2014). URL: http://arxiv.org/abs/1406.2572.

[64] R. Davé et al. "The neutral hydrogen content of galaxies in cosmological hydrodynamic simulations". In: *Mon. Not. R. Astron. Soc.* 434 (Sept. 2013), pp. 2645–2663. DOI: 10.1093/mnras/stt1274. arXiv: 1302.3631.

[65] Romeel Dave' et al. "Voigt-Profile Analysis of the Ly Forest in a Cold Dark Matter Universe". In: *The Astrophysical Journal* 477 (1996), pp. 21–26.

[66] M. Davis et al. "The evolution of large-scale structure in a universe dominated by cold dark matter". In: *Astrophys. J.* 292 (May 1985), pp. 371–394. DOI: 10.1086/163168.

[67] Avishai Dekel. "Dynamics of Cosmic Flows". In: *Ann. Rev. Astron. & Astrophys.* 32 (Jan. 1994), pp. 371–418. DOI: 10.1146/annurev.aa.32.090194.002103. arXiv: astro-ph/9401022 [astro-ph].

[68] DESI Collaboration et al. "The DESI Experiment Part I: Science,Targeting, and Survey Design". In: *ArXiv e-prints* (Oct. 2016). arXiv: 1611.00036 [astro-ph.IM].

[69] V. Desjacques et al. "Modeling scale-dependent bias on the baryonic acoustic scale with the statistics of peaks of Gaussian random fields". In: *Phys. Rev. D* 82.10, 103529 (Nov. 2010), p. 103529. DOI: 10.1103/PhysRevD.82.103529. arXiv: 1009.3449 [astro-ph.CO].

[70] O. Doré et al. "WFIRST Science Investigation Team "Cosmology with the High Latitude Survey" Annual Report 2017". In: *ArXiv e-prints* (Apr. 2018). arXiv: 1804.03628.

[71] G. Efstathiou. "Myths and truths concerning estimation of power spectra: the case for a hybrid estimator". In: *Mon. Not. R. Astron. Soc.* 349 (Apr. 2004), pp. 603–626. DOI: 10.1111/j.1365-2966.2004.07530.x. eprint: astro-ph/0307515.

[72] D. J. Eisenstein, H.-J. Seo, and M. White. "On the Robustness of the Acoustic Scale in the Low-Redshift Clustering of Matter". In: *Astrophys. J.* 664 (Aug. 2007), pp. 660–674. DOI: 10.1086/518755. eprint: astro-ph/0604361.

[73] D. J. Eisenstein et al. "Improving Cosmological Distance Measurements by Reconstruction of the Baryon Acoustic Peak". In: *Astrophys. J.* 664 (Aug. 2007), pp. 675–679. DOI: 10.1086/518712. eprint: astro-ph/0604362.

[74] D. J. Eisenstein et al. "Improving Cosmological Distance Measurements by Reconstruction of the Baryon Acoustic Peak". In: *Astrophys. J.* 664 (Aug. 2007), pp. 675–679. DOI: 10.1086/518712. eprint: arXiv:astro-ph/0604362.

[75] D. J. Eisenstein et al. "Improving Cosmological Distance Measurements by Reconstruction of the Baryon Acoustic Peak". In: *Astrophys. J.* 664 (Aug. 2007), pp. 675–679. DOI: 10.1086/518712. eprint: astro-ph/0604362.

[76] Daniel J. Eisenstein and Wayne Hu. "Baryonic Features in the Matter Transfer Function". In: *Astrophys. J.* 496.2 (Mar. 1998), pp. 605–614. DOI: 10.1086/305424. arXiv: astro-ph/9709112 [astro-ph].

[77] F. Elsner and B. D. Wandelt. "Efficient Wiener filtering without preconditioning". In: *Astron. Astrophys.* 549, A111 (Jan. 2013), A111. DOI: 10.1051/0004-6361/201220586. arXiv: 1210.4931 [astro-ph.CO].

[78] Franz Elsner et al. "Cosmology Inference from Biased Tracers using the EFT-based Likelihood". In: *arXiv e-prints*, arXiv:1906.07143 (June 2019), arXiv:1906.07143. arXiv: 1906.07143 [astro-ph.CO].

[79] T. Erben et al. "CARS: the CFHTLS-Archive-Research Survey. I. Five-band multi-colour data from 37 sq. deg. CFHTLS-wide observations". In: *Astron. Astrophys.* 493.3 (Jan. 2009), pp. 1197–1222. DOI: 10.1051/0004-6361:200810426. arXiv: 0811.2239 [astro-ph].

[80] A. E. Evrard et al. "Virial Scaling of Massive Dark Matter Halos: Why Clusters Prefer a High Normalization Cosmology". In: *Astrophys. J.* 672 (Jan. 2008), pp. 122–137. DOI: 10.1086/521616. eprint: astro-ph/0702241.

[81] H. A. Feldman, N. Kaiser, and J. A. Peacock. "Power-spectrum analysis of three-dimensional redshift surveys". In: *Astrophys. J.* 426 (May 1994), pp. 23–37. DOI: 10.1086/174036. eprint: arXiv:astro-ph/9304022.

[82] H. A. Feldman, N. Kaiser, and J. A. Peacock. "Power-spectrum analysis of three-dimensional redshift surveys". In: *Astrophys. J.* 426 (May 1994), pp. 23–37. DOI: 10.1086/174036. eprint: astro-ph/9304022.

[83] Y. Feng, M.-Y. Chu, and U. Seljak. "FastPM: a new scheme for fast simulations of dark matter and halos". In: *ArXiv e-prints* (Mar. 2016). arXiv: 1603.00476. URL: http://adsabs.harvard.edu/abs/2016arXiv160300476F.

[84] Y. Feng and C. Modi. "A fast algorithm for identifying Friends-of-Friends halos". In: *ArXiv e-prints* (July 2016). arXiv: 1607.03224 [astro-ph.IM].

[85] Y. Feng, U. Seljak, and M. Zaldarriaga. "Exploring the posterior surface of the large scale structure reconstruction". In: *In preparation* ().

[86] Y. Feng et al. "FASTPM: a new scheme for fast simulations of dark matter and haloes". In: *Mon. Not. R. Astron. Soc.* 463 (Dec. 2016), pp. 2273–2286. DOI: 10.1093/mnras/stw2123. arXiv: 1603.00476.

[87] Y. Feng et al. "FASTPM: a new scheme for fast simulations of dark matter and halos". In: *Mon. Not. R. Astron. Soc.* 463 (Dec. 2016), pp. 2273–2286. DOI: 10.1093/mnras/stw2123. arXiv: 1603.00476.

[88] Yu Feng, Uroš Seljak, and Matias Zaldarriaga. "Exploring the posterior surface of the large scale structure reconstruction". In: *Journal of Cosmology and Astro-Particle Physics* 2018.7, 043 (July 2018), p. 043. DOI: 10.1088/1475-7516/2018/07/043. arXiv: 1804.09687 [astro-ph.CO].

[89] Andreu Font-Ribera, Patrick McDonald, and Anvze Slosar. "How to estimate the 3D power spectrum of the Lyman- forest". In: *Journal of Cosmology and Astroparticle Physics* 2018 (2018), pp. 003–003.

[90] S. Foreman, H. Perrier, and L. Senatore. "Precision comparison of the power spectrum in the EFTofLSS with simulations". In: *Journal of Cosmology and Astro-Particle Physics* 5, 027 (May 2016), p. 027. DOI: 10.1088/1475-7516/2016/05/027. arXiv: 1507.05326.

[91] Simon Foreman et al. "Lensing reconstruction from line intensity maps: the impact of gravitational nonlinearity". In: *Journal of Cosmology and Astro-Particle Physics* 2018.7, 046 (July 2018), p. 046. DOI: 10.1088/1475-7516/2018/07/046. arXiv: 1803.04975 [astro-ph.CO].

[92] James N Fry and Enrique Gaztanaga. "Biasing and hierarchical statistics in large-scale structure". In: *The Astrophysical Journal* 413 (1993), pp. 447–452.

[93] S. R. Furlanetto, S. P. Oh, and F. H. Briggs. "Cosmology at low frequencies: The 21 cm transition and the high-redshift Universe". In: Phys. Rep. 433 (Oct. 2006), pp. 181–301. DOI: 10.1016/j.physrep.2006.08.002. eprint: astro-ph/0608032.

[94] A. Gorecki et al. "A new method to improve photometric redshift reconstruction. Applications to the Large Synoptic Survey Telescope". In: *Astron. Astrophys.* 561, A128 (Jan. 2014), A128. DOI: 10.1051/0004-6361/201321102. arXiv: 1301.3010.

[95] L. Greengard and V. Rokhlin. "A Fast Algorithm for Particle Simulations". In: *Journal of Computational Physics* 73.2 (Dec. 1987), pp. 325–348. DOI: 10.1016/0021-9991(87)90140-9.

[96] J. E. Gunn and J. R. Gott III. "On the Infall of Matter Into Clusters of Galaxies and Some Effects on Their Evolution". In: *Astrophys. J.* 176 (Aug. 1972), p. 1. DOI: 10.1086/151605.

[97] James E. Gunn and Bruce A. Peterson. "On the Density of Neutral Hydrogen in Intergalactic Space." In: *Astrophys. J.* 142 (Nov. 1965), pp. 1633–1636. DOI: 10.1086/148444.

[98] Nico Hamaus et al. "Minimizing the stochasticity of halos in large-scale structure surveys". In: *Physical Review D* 82.4 (2010), p. 043515.

[99] A. J. S. Hamilton. "Linear Redshift Distortions: a Review". In: *The Evolving Universe.* Ed. by D. Hamilton. Vol. 231. Astrophysics and Space Science Library. 1998, p. 185. DOI: 10.1007/978-94-011-4960-0_17. eprint: astro-ph/9708102.

[100] A. J. S. Hamilton. "Towards optimal measurement of power spectra - I. Minimum variance pair weighting and the Fisher matrix". In: *Mon. Not. R. Astron. Soc.* 289 (Aug. 1997), pp. 285–294.

[101] A. J. S. Hamilton. "Towards optimal measurement of power spectra - II. A basis of positive, compact, statistically orthogonal kernels". In: *Mon. Not. R. Astron. Soc.* 289 (Aug. 1997), pp. 295–304.

[102] Andrew James Hamilton. "Linear redshift distortions: A Review". In: 1998.

[103] J. Han et al. "The multidimensional dependence of halo bias in the eye of a machine: a tale of halo structure, assembly and environment". In: *ArXiv e-prints* (Feb. 2018). arXiv: 1802.09177.

[104] N. Hand et al. "nbodykit: an open-source, massively parallel toolkit for large-scale structure". In: *ArXiv e-prints* (Dec. 2017). arXiv: 1712.05834 [astro-ph.IM].

[105] Joachim Harnois-Déraps et al. "High-performance $P^3M$ N-body code: CUBE$P^3M$". In: *Mon. Not. R. Astron. Soc.* 436.1 (Nov. 2013), pp. 540–559. DOI: 10.1093/mnras/stt1591. arXiv: 1208.5098 [astro-ph.CO].

[106] Haibo He and Edwardo A. Garcia. "Learning from Imbalanced Data". In: *IEEE Trans. on Knowl. and Data Eng.* 21.9 (Sept. 2009), pp. 1263–1284. ISSN: 1041-4347. DOI: 10.1109/TKDE.2008.239. URL: http://dx.doi.org/10.1109/TKDE.2008.239.

[107] Siyu He et al. "Learning to predict the cosmological structure formation". In: *Proceedings of the National Academy of Science* 116.28 (July 2019), pp. 13825–13832. DOI: 10.1073/pnas.1821458116. arXiv: 1811.06533 [astro-ph.CO].

[108] H. Hildebrandt et al. "KiDS-450: cosmological parameter constraints from tomographic weak gravitational lensing". In: *Mon. Not. R. Astron. Soc.* 465.2 (Feb. 2017), pp. 1454–1498. DOI: 10.1093/mnras/stw2805. arXiv: 1606.05338 [astro-ph.CO].

[109] C. M. Hirata and U. Seljak. "Reconstruction of lensing from the cosmic microwave background polarization". In: *Phys. Rev. D* 68 (Oct. 2003), pp. 83002–+.

[110] Shirley Ho et al. "Correlation of CMB with large-scale structure. I. Integrated Sachs-Wolfe tomography and cosmological implications". In: *Phys. Rev. D* 78.4, 043519 (Aug. 2008), p. 043519. DOI: 10.1103/PhysRevD.78.043519. arXiv: 0801.0642 [astro-ph].

[111] R. W. Hockney and J. W. Eastwood. *Computer Simulation Using Particles*. Bristol, PA, USA: Taylor & Francis, Inc., 1988. ISBN: 0-85274-392-0.

[112] B. Horowitz, U. Seljak, and G. Aslanyan. "Efficient optimal reconstruction of linear fields and band-powers from cosmological data". In: *Journal of Cosmology and Astro-Particle Physics* 2019.10, 035 (Oct. 2019), p. 035. DOI: 10.1088/1475-7516/2019/10/035. arXiv: 1810.00503 [astro-ph.CO].

[113] Wayne Hu. "Power Spectrum Tomography with Weak Lensing". In: 1999.

[114] Vid Irvsivc et al. "New Constraints on the free-streaming of warm dark matter from intermediate and small scale Lyman-\$$\alpha$\$*forestdata*". In: *Physical Review D* 96 (2017), p. 023522.

[115] Albert Izard, Martin Crocce, and Pablo Fosalba. "ICE-COLA: towards fast and accurate synthetic galaxy catalogues optimizing a quasi-N-body method". In: *Mon. Not. R. Astron. Soc.* 459.3 (July 2016), pp. 2327–2341. DOI: 10.1093/mnras/stw797. arXiv: 1509.04685 [astro-ph.CO].

[116] J.C. Jackson. "Fingers of God: A critique of Rees' theory of primoridal gravitational radiation". In: *Mon. Not. Roy. Astron. Soc.* 156 (1972), 1P–5P. DOI: 10.1093/mnras/156.1.1P. arXiv: 0810.3908 [astro-ph].

[117] J. Jasche and F. S. Kitaura. "Fast Hamiltonian sampling for large-scale structure inference". In: *Mon. Not. R. Astron. Soc.* 407 (Sept. 2010), pp. 29–42. DOI: 10.1111/j.1365-2966.2010.16897.x. arXiv: 0911.2496.

[118] J. Jasche, F. Leclercq, and B. D. Wandelt. "Past and present cosmic structure in the SDSS DR7 main sample". In: *Journal of Cosmology and Astro-Particle Physics* 1, 036 (Jan. 2015), p. 036. DOI: 10.1088/1475-7516/2015/01/036. arXiv: 1409.6308.

[119] J. Jasche and B. D. Wandelt. "Bayesian physical reconstruction of initial conditions from large-scale structure surveys". In: *Mon. Not. R. Astron. Soc.* 432 (June 2013), pp. 894–913. DOI: 10.1093/mnras/stt449. arXiv: 1203.3639.

[120] Jens Jasche and Benjamin D. Wandelt. "Bayesian physical reconstruction of initial conditions from large-scale structure surveys". In: *Mon. Not. R. Astron. Soc.* 432.2 (June 2013), pp. 894–913. DOI: 10.1093/mnras/stt449. arXiv: 1203.3639 [astro-ph.CO].

[121] N. Kaiser. "Clustering in real space and in redshift space". In: *Mon. Not. R. Astron. Soc.* 227 (July 1987), pp. 1–21. DOI: 10.1093/mnras/227.1.1.

[122] N. Kaiser. "On the spatial correlations of Abell clusters". In: *Astrophys. J. Lett.* 284 (Sept. 1984), pp. L9–L12. DOI: 10.1086/184341.

[123] N. Kaiser and S. Cole. "Galaxy formation and biased clustering". In: *NATO Advanced Science Institutes (ASI) Series C*. Ed. by C. S. Frenk et al. Vol. 264. NATO Advanced Science Institutes (ASI) Series C. 1989, p. 243.

[124] Nick Kaiser. "Clustering in real space and in redshift space". In: *Mon. Not. R. Astron. Soc.* 227 (July 1987), pp. 1–21. DOI: 10.1093/mnras/227.1.1.

[125] Martin Kilbinger. "Cosmology with cosmic shear observations: a review". In: *Reports on Progress in Physics* 78.8 (July 2015), p. 086901. DOI: 10.1088/0034-4885/78/8/086901. URL: https://doi.org/10.1088%2F0034-4885%2F78%2F8%2F086901.

[126] D. P. Kingma and J. Ba. "Adam: A Method for Stochastic Optimization". In: *ArXiv e-prints* (Dec. 2014). arXiv: 1412.6980 [cs.LG].

[127] F. -S. Kitaura, G. Yepes, and F. Prada. "Modelling baryon acoustic oscillations with perturbation theory and stochastic halo biasing." In: *Mon. Not. R. Astron. Soc.* 439 (Mar. 2014), pp. L21–L25. DOI: 10.1093/mnrasl/slt172. arXiv: 1307.3285 [astro-ph.CO].

[128] F.-S. Kitaura. "The initial conditions of the Universe from constrained simulations". In: *Mon. Not. R. Astron. Soc.* 429 (Feb. 2013), pp. L84–L88. DOI: 10.1093/mnrasl/sls029. arXiv: 1203.4184.

[129] Alexander Knebe et al. "Structure finding in cosmological simulations: the state of affairs". In: *Mon. Not. R. Astron. Soc.* 435.2 (Oct. 2013), pp. 1618–1658. DOI: 10.1093/mnras/stt1403. arXiv: 1304.0585 [astro-ph.CO].

[130] Doogesh Kodi Ramanah et al. "Super-resolution emulator of cosmological simulations using deep physical models". In: *arXiv e-prints*, arXiv:2001.05519 (Jan. 2020), arXiv:2001.05519. arXiv: 2001.05519 [astro-ph.CO].

[131] Andrey V. Kravtsov et al. "The Dark Side of the Halo Occupation Distribution". In: *The Astrophysical Journal* 609 (2004), pp. 35–49.

[132] C. Laigle et al. "The COSMOS2015 Catalog: Exploring the $1 < z < 6$ Universe with Half a Million Galaxies". In: *Astrophys. J. Suppl.* 224, 24 (June 2016), p. 24. DOI: 10.3847/0067-0049/224/2/24. arXiv: 1604.02350.

[133] T. Lazeyras, M. Musso, and V. Desjacques. "Lagrangian bias of generic large-scale structure tracers". In: *Phys. Rev. D* 93.6, 063007 (Mar. 2016), p. 063007. DOI: 10.1103/PhysRevD.93.063007. arXiv: 1512.05283.

[134] K. Lee et al. "First Data Release of the COSMOS Ly Mapping and Tomography Observations: 3D Ly Forest Tomography at 2.05 ¡ z ¡ 2.55". In: *Astrophysical Journal Supplement Series* 237 (2018), pp. 31–31.

[135] Antony Lewis, Anthony Challinor, and Anthony Lasenby. "Efficient computation of CMB anisotropies in closed FRW models". In: *Astrophys. J.* 538 (2000), pp. 473–476. DOI: 10.1086/309179. arXiv: astro-ph/9911177 [astro-ph].

[136] A. Liu, A. R. Parsons, and C. M. Trott. "Epoch of reionization window. II. Statistical methods for foreground wedge reduction". In: *Phys. Rev. D* 90.2, 023019 (July 2014), p. 023019. DOI: 10.1103/PhysRevD.90.023019. arXiv: 1404.4372.

[137] David G. Lowe. "Distinctive Image Features from Scale-Invariant Keypoints". In: *International Journal of Computer Vision* 60.2 (Nov. 2004), pp. 91–110. ISSN: 1573-1405. DOI: 10.1023/B:VISI.0000029664.99615.94. URL: https://doi.org/10.1023/B:VISI.0000029664.99615.94.

[138] LSST Science Collaboration et al. "LSST Science Book, Version 2.0". In: *ArXiv e-prints* (Dec. 2009). arXiv: 0912.0201 [astro-ph.IM].

[139] L. Lucie-Smith et al. "Machine learning cosmological structure formation". In: *ArXiv e-prints* (Feb. 2018). arXiv: 1802.04271.

[140] R. Mandelbaum et al. “Galaxy halo masses and satellite fractions from galaxy-galaxy lensing in the Sloan Digital Sky Survey: stellar mass, luminosity, morphology and environment dependencies”. In: *Mon. Not. R. Astron. Soc.* 368 (May 2006), pp. 715–731. DOI: 10.1111/j.1365-2966.2006.10156.x. eprint: astro-ph/0511164.

[141] Rachel Mandelbaum. “Weak Lensing for Precision Cosmology”. In: *Annual Review of Astronomy and Astrophysics* 56 (2018), pp. 393–433.

[142] Y.-Y. Mao, A. R. Zentner, and R. H. Wechsler. “Beyond assembly bias: exploring secondary halo biases for cluster-size haloes”. In: *Mon. Not. R. Astron. Soc.* 474 (Mar. 2018), pp. 5143–5157. DOI: 10.1093/mnras/stx3111. arXiv: 1705.03888.

[143] Yao-Yuan Mao, Andrew R Zentner, and Risa H Wechsler. “Beyond assembly bias: exploring secondary halo biases for cluster-size haloes”. In: *Monthly Notices of the Royal Astronomical Society* 474.4 (Dec. 2017), pp. 5143–5157. ISSN: 0035-8711. DOI: 10.1093/mnras/stx3111. eprint: https://academic.oup.com/mnras/article-pdf/474/4/5143/23126779/stx3111.pdf. URL: https://doi.org/10.1093/mnras/stx3111.

[144] K. W. Masui et al. “Measurement of 21 cm Brightness Fluctuations at $z \sim 0.8$ in Cross-correlation”. In: *Astrophys. J. Lett.* 763, L20 (Jan. 2013), p. L20. DOI: 10.1088/2041-8205/763/1/L20. arXiv: 1208.0331 [astro-ph.CO].

[145] T. Matsubara. “Nonlinear perturbation theory with halo bias and redshift-space distortions via the Lagrangian picture”. In: *Phys. Rev. D* 78.8, 083519 (Oct. 2008), p. 083519. DOI: 10.1103/PhysRevD.78.083519. arXiv: 0807.1733.

[146] T. Matsubara. “Resumming cosmological perturbations via the Lagrangian picture: One-loop results in real space and in redshift space”. In: *Phys. Rev. D* 77.6, 063530 (Mar. 2008), p. 063530. DOI: 10.1103/PhysRevD.77.063530. arXiv: 0711.2521.

[147] T. Matsubara. “Resumming cosmological perturbations via the Lagrangian picture: One-loop results in real space and in redshift space”. In: *Phys. Rev. D* 77.6, 063530 (Mar. 2008), p. 063530. DOI: 10.1103/PhysRevD.77.063530. arXiv: 0711.2521.

[148] Takahiko Matsubara. “Nonlinear perturbation theory with halo bias and redshift-space distortions via the Lagrangian picture”. In: *Phys. Rev. D* 78.8, 083519 (Oct. 2008), p. 083519. DOI: 10.1103/PhysRevD.78.083519. arXiv: 0807.1733 [astro-ph].

[149] M. McQuinn and M. White. “On using angular cross-correlations to determine source redshift distributions”. In: *Mon. Not. R. Astron. Soc.* 433 (Aug. 2013), pp. 2857–2883. DOI: 10.1093/mnras/stt914. arXiv: 1302.0857.

[150] M. McQuinn et al. “Cosmological Parameter Estimation Using 21 cm Radiation from the Epoch of Reionization”. In: *Astrophys. J.* 653 (Dec. 2006), pp. 815–834. DOI: 10.1086/505167. eprint: astro-ph/0512263.

[151] A. Meiksin, M. White, and J. A. Peacock. “Baryonic signatures in large-scale structure”. In: *Mon. Not. R. Astron. Soc.* 304 (Apr. 1999), pp. 851–864. DOI: 10.1046/j.1365-8711.1999.02369.x. eprint: astro-ph/9812214.

[152] Brice Ménard et al. "Clustering-based redshift estimation: method and application to data". In: *arXiv e-prints*, arXiv:1303.4722 (Mar. 2013), arXiv:1303.4722. arXiv: 1303.4722 [astro-ph.CO].

[153] Hugh Merz, Ue-Li Pen, and Hy Trac. "Towards optimal parallel PM N-body codes: PMFAST". In: *New Astronomy* 10.5 (Apr. 2005), pp. 393–407. DOI: 10.1016/j.newast.2005.02.001. arXiv: astro-ph/0402443 [astro-ph].

[154] HJ Mo and Simon DM White. "An analytic model for the spatial clustering of dark matter haloes". In: *Monthly Notices of the Royal Astronomical Society* 282.2 (1996), pp. 347–361.

[155] C. Modi, E. Castorina, and U. Seljak. "Halo bias in Lagrangian space: estimators and theoretical predictions". In: *Mon. Not. R. Astron. Soc.* 472 (Dec. 2017), pp. 3959–3970. DOI: 10.1093/mnras/stx2148. arXiv: 1612.01621.

[156] C. Modi, Y. Feng, and U. Seljak. "Cosmological reconstruction from galaxy light: neural network based light-matter connection". In: *Journal of Cosmology and Astro-Particle Physics* 10 (Oct. 2018), p. 028. DOI: 10.1088/1475-7516/2018/10/028. arXiv: 1805.02247.

[157] C. Modi, M. White, and Z. Vlah. "Modeling CMB lensing cross correlations with CLEFT". In: *Journal of Cosmology and Astro-Particle Physics* 8, 009 (Aug. 2017), p. 009. DOI: 10.1088/1475-7516/2017/08/009. arXiv: 1706.03173.

[158] C. Modi et al. "Intensity mapping with neutral hydrogen and the Hidden Valley simulations". In: *arXiv e-prints*, arXiv:1904.11923 (Apr. 2019), arXiv:1904.11923. arXiv: 1904.11923 [astro-ph.CO].

[159] C. Modi et al. "Reconstructing large-scale structure with neutral hydrogen surveys". In: *arXiv e-prints*, arXiv:1907.02330 (July 2019), arXiv:1907.02330. arXiv: 1907.02330 [astro-ph.CO].

[160] M. F. Morales et al. "Four Fundamental Foreground Power Spectrum Shapes for 21 cm Cosmology Observations". In: *Astrophys. J.* 752, 137 (June 2012), p. 137. DOI: 10.1088/0004-637X/752/2/137. arXiv: 1202.3830 [astro-ph.IM].

[161] B. P. Moster, T. Naab, and S. D. M. White. "Galactic star formation and accretion histories from matching galaxies to dark matter haloes". In: *Mon. Not. R. Astron. Soc.* 428 (Feb. 2013), pp. 3121–3138. DOI: 10.1093/mnras/sts261. arXiv: 1205.5807.

[162] M. Musso, A. Paranjape, and R. K. Sheth. "Scale-dependent halo bias in the excursion set approach". In: *Mon. Not. R. Astron. Soc.* 427 (Dec. 2012), pp. 3145–3158. DOI: 10.1111/j.1365-2966.2012.21903.x. arXiv: 1205.3401.

[163] Vijay K. Narayanan and Rupert A. C. Croft. "Recovering the Primordial Density Fluctuations: A Comparison of Methods". In: *Astrophys. J.* 515.2 (Apr. 1999), pp. 471–486. DOI: 10.1086/307040. arXiv: astro-ph/9806255 [astro-ph].

[164] J. F. Navarro, C. S. Frenk, and S. D. M. White. “A Universal Density Profile from Hierarchical Clustering”. In: *Astrophys. J.* 490 (Dec. 1997), pp. 493–508. DOI: 10.1086/304888. eprint: astro-ph/9611107.

[165] L. B. Newburgh et al. “HIRAX: a probe of dark energy and radio transients”. In: *Ground-based and Airborne Telescopes VI*. Vol. 9906. Proc. SPIE. Aug. 2016, p. 99065X. DOI: 10.1117/12.2234286. arXiv: 1607.02059 [astro-ph.IM].

[166] Jeffrey A. Newman. “Calibrating Redshift Distributions beyond Spectroscopic Limits with Cross-Correlations”. In: *Astrophys. J.* 684.1 (Sept. 2008), pp. 88–101. DOI: 10.1086/589982. arXiv: 0805.1409 [astro-ph].

[167] Jeffrey A. Newman et al. “Spectroscopic needs for imaging dark energy experiments”. In: *Astroparticle Physics* 63 (Mar. 2015), pp. 81–100. DOI: 10.1016/j.astropartphys.2014.06.007. arXiv: 1309.5384 [astro-ph.CO].

[168] J. Nocedal and S. J. Wright. *Numerical Optimization*. 2nd. New York: Springer, 2006.

[169] Jorge Nocedal and Stephen J. Wright. *Numerical Optimization*. second. New York, NY, USA: Springer, 2006.

[170] Y. Noh, M. White, and N. Padmanabhan. “Reconstructing baryon oscillations”. In: *Phys. Rev. D* 80.12, 123501 (Dec. 2009), p. 123501. DOI: 10.1103/PhysRevD.80.123501. arXiv: 0909.1802.

[171] Adi Nusser and Avishai Dekel. “Tracing Large-Scale Fluctuations Back in Time”. In: *Astrophys. J.* 391 (June 1992), p. 443. DOI: 10.1086/171360.

[172] A. Obuljen et al. “High-redshift post-reionization cosmology with 21cm intensity mapping”. In: *Journal of Cosmology and Astro-Particle Physics* 5, 004 (May 2018), p. 004. DOI: 10.1088/1475-7516/2018/05/004. arXiv: 1709.07893.

[173] Andrej Obuljen et al. “Baryon Acoustic Oscillations reconstruction with pixels”. In: *Journal of Cosmology and Astro-Particle Physics* 2017.9, 012 (Sept. 2017), p. 012. DOI: 10.1088/1475-7516/2017/09/012. arXiv: 1610.05768 [astro-ph.CO].

[174] Andrej Obuljen et al. “The H I content of dark matter haloes at $z \approx 0$ from ALFALFA”. In: *Mon. Not. R. Astron. Soc.* 486.4 (July 2019), pp. 5124–5138. DOI: 10.1093/mnras/stz1118. arXiv: 1805.00934 [astro-ph.CO].

[175] Teppei Okumura et al. “Reconstruction of halo power spectrum from redshift-space galaxy distribution: cylinder-grouping method and halo exclusion effect”. In: *Monthly Notices of the Royal Astronomical Society* 469 (2017), pp. 459–475.

[176] H. Padmanabhan, T. R. Choudhury, and A. Refregier. “Theoretical and observational constraints on the H I intensity power spectrum”. In: *Mon. Not. R. Astron. Soc.* 447 (Mar. 2015), pp. 3745–3755. DOI: 10.1093/mnras/stu2702. arXiv: 1407.6366.

[177] H. Padmanabhan, A. Refregier, and A. Amara. “A halo model for cosmological neutral hydrogen : abundances and clustering”. In: *Mon. Not. R. Astron. Soc.* 469 (Aug. 2017), pp. 2323–2334. DOI: 10.1093/mnras/stx979. arXiv: 1611.06235.

[178] N. Padmanabhan, U. Seljak, and U. L. Pen. “Mining weak lensing surveys.” In: *New Astronomy* 8 (2003), pp. 581–603.

[179] N. Padmanabhan et al. “A 2 per cent distance to z = 0.35 by reconstructing baryon acoustic oscillations - I. Methods and application to the Sloan Digital Sky Survey”. In: 2012.

[180] Aseem Paranjape, Ravi K Sheth, and Vincent Desjacques. “Excursion set peaks: a self-consistent model of dark halo abundances and clustering”. In: *Monthly Notices of the Royal Astronomical Society* (2013), stt267.

[181] A. R. Parsons et al. “A Per-baseline, Delay-spectrum Technique for Accessing the 21 cm Cosmic Reionization Signature”. In: *Astrophys. J.* 756, 165 (Sept. 2012), p. 165. DOI: 10.1088/0004-637X/756/2/165. arXiv: 1204.4749 [astro-ph.IM].

[182] P. J. E. Peebles. “Statistical Analysis of Catalogs of Extragalactic Objects. I. Theory”. In: *Astrophys. J.* 185 (Oct. 1973), pp. 413–440. DOI: 10.1086/152431.

[183] P. J. E. Peebles. “Tracing Galaxy Orbits Back in Time”. In: *Astrophys. J.* 344 (Sept. 1989), p. L53. DOI: 10.1086/185529.

[184] I. Pérez-Ràfols et al. “The SDSS-DR12 large-scale cross-correlation of damped Lyman alpha systems with the Lyman alpha forest”. In: *Mon. Not. R. Astron. Soc.* 473 (Jan. 2018), pp. 3019–3038. DOI: 10.1093/mnras/stx2525. arXiv: 1709.00889.

[185] S. Perlmutter et al. “Measurements of Ω and Λ from 42 High-Redshift Supernovae”. In: *Astrophys. J.* 517.2 (June 1999), pp. 565–586. DOI: 10.1086/307221. arXiv: astro-ph/9812133 [astro-ph].

[186] Michael Pippig. “PFFT - An extension of FFTW to massively parallel architectures”. In: *SIAM Journal on Scientific Computing* 35 (May 2013), pp. C213–C236. DOI: 10.1137/120885887.

[187] Planck Collaboration and N. Aghanim. “Planck 2018 results. VI. Cosmological parameters”. In: *arXiv e-prints*, arXiv:1807.06209 (July 2018), arXiv:1807.06209. arXiv: 1807.06209 [astro-ph.CO].

[188] J. C. Pober. “The impact of foregrounds on redshift space distortion measurements with the highly redshifted 21-cm line”. In: *Mon. Not. R. Astron. Soc.* 447 (Feb. 2015), pp. 1705–1712. DOI: 10.1093/mnras/stu2575. arXiv: 1411.2050.

[189] J. Prat et al. “Dark Energy Survey year 1 results: Galaxy-galaxy lensing”. In: *Phys. Rev. D* 98.4, 042005 (Aug. 2018), p. 042005. DOI: 10.1103/PhysRevD.98.042005. arXiv: 1708.01537 [astro-ph.CO].

[190] W. H. Press and P. Schechter. “Formation of Galaxies and Clusters of Galaxies by Self-Similar Gravitational Condensation”. In: *Astrophys. J.* 187 (Feb. 1974), pp. 425–438. DOI: 10.1086/152650.

[191] W. H. Press et al. *Numerical recipes in C. The art of scientific computing.* Cambridge: University Press, —c1992, 2nd ed., 1992.

[192] William H. Press and Paul Schechter. "Formation of galaxies and clusters of galaxies by selfsimilar gravitational condensation". In: *Astrophys. J.* 187 (1974), pp. 425–438. DOI: 10.1086/152650.

[193] Thomas Quinn et al. "Time stepping N-body simulations". In: *arXiv e-prints*, astro-ph/9710043 (Oct. 1997), astro–ph/9710043. arXiv: astro-ph/9710043 [astro-ph].

[194] A. Rahmati et al. "The distribution of neutral hydrogen around high-redshift galaxies and quasars in the EAGLE simulation". In: *Mon. Not. R. Astron. Soc.* 452 (Sept. 2015), pp. 2034–2056. DOI: 10.1093/mnras/stv1414. arXiv: 1503.05553.

[195] D. Reed et al. "Dark matter subhaloes in numerical simulations". In: *Mon. Not. R. Astron. Soc.* 359 (June 2005), pp. 1537–1548. DOI: 10.1111/j.1365-2966.2005.09020.x. eprint: astro-ph/0406034.

[196] Adam G. Riess et al. "Large Magellanic Cloud Cepheid Standards Provide a 1% Foundation for the Determination of the Hubble Constant and Stronger Evidence for Physics beyond ΛCDM". In: *Astrophys. J.* 876.1, 85 (May 2019), p. 85. DOI: 10.3847/1538-4357/ab1422. arXiv: 1903.07603 [astro-ph.CO].

[197] Adam G. Riess et al. "Observational Evidence from Supernovae for an Accelerating Universe and a Cosmological Constant". In: *AJ* 116.3 (Sept. 1998), pp. 1009–1038. DOI: 10.1086/300499. arXiv: astro-ph/9805201 [astro-ph].

[198] S. A. Rodrıguez-Torres et al. "The clustering of galaxies in the SDSS-III Baryon Oscillation Spectroscopic Survey: modelling the clustering and halo occupation distribution of BOSS CMASS galaxies in the Final Data Release". In: *Mon. Not. R. Astron. Soc.* 460 (Aug. 2016), pp. 1173–1187. DOI: 10.1093/mnras/stw1014. arXiv: 1509.06404.

[199] Ashley J. Ross et al. "The clustering of galaxies in the completed SDSS-III Baryon Oscillation Spectroscopic Survey: observational systematics and baryon acoustic oscillations in the correlation function". In: *Mon. Not. R. Astron. Soc.* 464.1 (Jan. 2017), pp. 1168–1191. DOI: 10.1093/mnras/stw2372. arXiv: 1607.03145 [astro-ph.CO].

[200] G. B. Rybicki and W. H. Press. "Interpolation, realization, and reconstruction of noisy, irregularly sampled data". In: *Astrophys. J.* 398 (Oct. 1992), pp. 169–176.

[201] George B. Rybicki and William H. Press. "Interpolation, Realization, and Reconstruction of Noisy, Irregularly Sampled Data". In: *Astrophys. J.* 398 (Oct. 1992), p. 169. DOI: 10.1086/171845.

[202] Shun Saito et al. "Understanding higher-order nonlocal halo bias at large scales by combining the power spectrum with the bispectrum". In: *Physical Review D* 90.12 (2014), p. 123522.

[203] Fabian Schmidt et al. "A rigorous EFT-based forward model for large-scale structure". In: *Journal of Cosmology and Astro-Particle Physics* 2019.1, 042 (Jan. 2019), p. 042. DOI: 10.1088/1475-7516/2019/01/042. arXiv: 1808.02002 [astro-ph.CO].

[204] M. Schmittfull, T. Baldauf, and M. Zaldarriaga. "Iterative initial condition reconstruction". In: *ArXiv e-prints* (Apr. 2017). arXiv: 1704.06634.

[205] M. Schmittfull, T. Baldauf, and M. Zaldarriaga. "Iterative initial condition reconstruction". In: *Phys. Rev. D* 96.2, 023505 (July 2017), p. 023505. DOI: 10.1103/PhysRevD.96.023505. arXiv: 1704.06634.

[206] M. Schmittfull et al. "Modeling Biased Tracers at the Field Level". In: *arXiv e-prints* (Nov. 2018). arXiv: 1811.10640.

[207] Marcel Schmittfull, Tobias Baldauf, and Matias Zaldarriaga. "Iterative initial condition reconstruction". In: *Phys. Rev. D* 96.2, 023505 (July 2017), p. 023505. DOI: 10.1103/PhysRevD.96.023505. arXiv: 1704.06634 [astro-ph.CO].

[208] U. Seljak. "Cosmography and Power Spectrum Estimation: A Unified Approach". In: *Astrophys. J.* 503 (Aug. 1998), pp. 492–+.

[209] U. Seljak, N. Hamaus, and V. Desjacques. "How to Suppress the Shot Noise in Galaxy Surveys". In: *Physical Review Letters* 103.9 (Aug. 2009), pp. 091303–+. DOI: 10.1103/PhysRevLett.103.091303. arXiv: 0904.2963.

[210] U. Seljak and M. S. Warren. "Large-scale bias and stochasticity of haloes and dark matter". In: *Mon. Not. R. Astron. Soc.* 355 (Nov. 2004), pp. 129–136. DOI: 10.1111/j.1365-2966.2004.08297.x. eprint: astro-ph/0403698.

[211] U. Seljak et al. "Towards optimal extraction of cosmological information from nonlinear data". In: *Journal of Cosmology and Astro-Particle Physics* 12, 009 (Dec. 2017), p. 009. DOI: 10.1088/1475-7516/2017/12/009. arXiv: 1706.06645.

[212] H.-J. Seo and D. J. Eisenstein. "Improved Forecasts for the Baryon Acoustic Oscillations and Cosmological Distance Scale". In: *Astrophys. J.* 665 (Aug. 2007), pp. 14–24. DOI: 10.1086/519549. eprint: astro-ph/0701079.

[213] H.-J. Seo and C. M. Hirata. "The foreground wedge and 21-cm BAO surveys". In: *Mon. Not. R. Astron. Soc.* 456 (Mar. 2016), pp. 3142–3156. DOI: 10.1093/mnras/stv2806. arXiv: 1508.06503.

[214] H.-J. Seo et al. "Modeling the reconstructed BAO in Fourier space". In: *Mon. Not. R. Astron. Soc.* 460 (Aug. 2016), pp. 2453–2471. DOI: 10.1093/mnras/stw1138. arXiv: 1511.00663.

[215] H.-J. Seo et al. "Nonlinear Structure Formation and the Acoustic Scale". In: *Astrophys. J.* 686 (Oct. 2008), pp. 13–24. DOI: 10.1086/589921. arXiv: 0805.0117.

[216] Hee-Jong Seo et al. "High-precision Predictions for the Acoustic Scale in the Nonlinear Regime". In: *The Astrophysical Journal* 720.2 (2010), p. 1650. URL: http://stacks.iop.org/0004-637X/720/i=2/a=1650.

[217] J. R. Shaw et al. "All-sky Interferometry with Spherical Harmonic Transit Telescopes". In: *Astrophys. J.* 781, 57 (Feb. 2014), p. 57. DOI: 10.1088/0004-637X/781/2/57. arXiv: 1302.0327 [astro-ph.CO].

[218] J. R. Shaw et al. “Coaxing cosmic 21 cm fluctuations from the polarized sky using m -mode analysis”. In: *Phys. Rev. D* 91.8, 083514 (Apr. 2015), p. 083514. DOI: 10.1103/PhysRevD.91.083514. arXiv: 1401.2095.

[219] Noam Shazeer et al. “Mesh-TensorFlow: Deep Learning for Supercomputers”. In: *CoRR* abs/1811.02084 (2018). arXiv: 1811.02084. URL: http://arxiv.org/abs/1811.02084.

[220] R. K. Sheth, H. J. Mo, and G. Tormen. “Ellipsoidal collapse and an improved model for the number and spatial distribution of dark matter haloes”. In: *Mon. Not. R. Astron. Soc.* 323 (May 2001), pp. 1–12. DOI: 10.1046/j.1365-8711.2001.04006.x. eprint: astro-ph/9907024.

[221] R. K. Sheth and G. Tormen. “Large-scale bias and the peak background split”. In: *Mon. Not. R. Astron. Soc.* 308 (Sept. 1999), pp. 119–126. DOI: 10.1046/j.1365-8711.1999.02692.x. eprint: astro-ph/9901122.

[222] Ravi K Sheth and Giuseppe Tormen. “Large-scale bias and the peak background split”. In: *Monthly Notices of the Royal Astronomical Society* 308.1 (1999), pp. 119–126.

[223] R. E. Smith, R. Scoccimarro, and R. K. Sheth. “Motion of the acoustic peak in the correlation function”. In: *Phys. Rev. D* 77.4, 043525 (Feb. 2008), p. 043525. DOI: 10.1103/PhysRevD.77.043525. eprint: astro-ph/0703620.

[224] George Stein, Marcelo A. Alvarez, and J. Richard Bond. “The mass-Peak Patch algorithm for fast generation of deep all-sky dark matter halo catalogues and its N-body validation”. In: *Mon. Not. R. Astron. Soc.* 483.2 (Feb. 2019), pp. 2236–2250. DOI: 10.1093/mnras/sty3226. arXiv: 1810.07727 [astro-ph.CO].

[225] I. Suisalu and E. Saar. “An adaptive multigrid solver for high-resolution cosmological simulations”. In: *Mon. Not. R. Astron. Soc.* 274.1 (May 1995), pp. 287–299. DOI: 10.1093/mnras/274.1.287. arXiv: astro-ph/9412043 [astro-ph].

[226] E. R. Switzer et al. “Determination of $z \sim 0.8$ neutral hydrogen fluctuations using the 21 cm intensity mapping autocorrelation”. In: *Mon. Not. R. Astron. Soc.* 434 (July 2013), pp. L46–L50. DOI: 10.1093/mnrasl/slt074. eprint: 1304.3712 (astro-ph.CO).

[227] T. Takahashi. “Primordial non-Gaussianity and the inflationary Universe”. In: *Progress of Theoretical and Experimental Physics* 2014.6, 06B105 (June 2014), 06B105. DOI: 10.1093/ptep/ptu060.

[228] S. Tassev and M. Zaldarriaga. “Estimating CDM particle trajectories in the mildly non-linear regime of structure formation. Implications for the density field in real and redshift space”. In: *Journal of Cosmology and Astro-Particle Physics* 12, 011 (Dec. 2012), p. 011. DOI: 10.1088/1475-7516/2012/12/011. arXiv: 1203.5785.

[229] Svetlin Tassev, Matias Zaldarriaga, and Daniel J. Eisenstein. "Solving large scale structure in ten easy steps with COLA". In: *Journal of Cosmology and Astro-Particle Physics* 2013.6, 036 (June 2013), p. 036. DOI: 10.1088/1475-7516/2013/06/036. arXiv: 1301.0322 [astro-ph.CO].

[230] M. Tegmark. "How to measure CMB power spectra without losing information". In: *Phys. Rev. D* 55 (May 1997), pp. 5895–5907.

[231] M. Tegmark et al. "Measuring the Galaxy Power Spectrum with Future Redshift Surveys". In: *Astrophys. J.* 499 (May 1998), pp. 555–576. DOI: 10.1086/305663. eprint: astro-ph/9708020.

[232] Max Tegmark. "Measuring Cosmological Parameters with Galaxy Surveys". In: *Phys. Rev. Lett.* 79 (20 Nov. 1997), pp. 3806–3809. DOI: 10.1103/PhysRevLett.79.3806. URL: https://link.aps.org/doi/10.1103/PhysRevLett.79.3806.

[233] A. R. Thompson, J. M. Moran, and G. W. Swenson Jr. *Interferometry and Synthesis in Radio Astronomy, 3rd Edition.* 2017.

[234] P. Upton Sanderbeck et al. "Estimates for the impact of Ultraviolet Background fluctuations on galaxy clustering measurements". In: *arXiv e-prints* (Oct. 2018). arXiv: 1810.12321.

[235] A. Vale and J. P. Ostriker. "Linking halo mass to galaxy luminosity". In: *Mon. Not. R. Astron. Soc.* 353.1 (Sept. 2004), pp. 189–200. DOI: 10.1111/j.1365-2966.2004.08059.x. arXiv: astro-ph/0402500 [astro-ph].

[236] F. Villaescusa-Navarro, D. Alonso, and M. Viel. "Baryonic acoustic oscillations from 21 cm intensity mapping: the Square Kilometre Array case". In: *Mon. Not. R. Astron. Soc.* 466 (Apr. 2017), pp. 2736–2751. DOI: 10.1093/mnras/stw3224. arXiv: 1609.00019.

[237] F. Villaescusa-Navarro et al. "Ingredients for 21cm intensity mapping". In: *ArXiv e-prints* (Apr. 2018). arXiv: 1804.09180.

[238] Z. Vlah, E. Castorina, and M. White. "The Gaussian streaming model and convolution Lagrangian effective field theory". In: *Journal of Cosmology and Astro-Particle Physics* 12, 007 (Dec. 2016), p. 007. DOI: 10.1088/1475-7516/2016/12/007. arXiv: 1609.02908.

[239] Z. Vlah, E. Castorina, and M. White. "The Gaussian streaming model and Lagrangian effective field theory". In: *ArXiv e-prints* (Sept. 2016). arXiv: 1609.02908.

[240] Z. Vlah and M. White. "Exploring redshift-space distortions in large-scale structure". In: *arXiv e-prints* (Dec. 2018). arXiv: 1812.02775.

[241] Z. Vlah, M. White, and A. Aviles. "A Lagrangian effective field theory". In: *Journal of Cosmology and Astro-Particle Physics* 9, 014 (Sept. 2015), p. 014. DOI: 10.1088/1475-7516/2015/09/014. arXiv: 1506.05264.

[242] Zvonimir Vlah, Urovs Seljak, and Tobias Baldauf. "Lagrangian perturbation theory at one loop order: successes, failures, and improvements". In: *Physical Review D* 91 (2015), p. 023508.

[243] B. D. Wandelt, E. Hivon, and K. M. Górski. "Cosmic microwave background anisotropy power spectrum statistics for high precision cosmology". In: *Phys. Rev. D* 64.8, 083003 (Oct. 2001), p. 083003. DOI: 10.1103/PhysRevD.64.083003. eprint: astro-ph/0008111.

[244] Benjamin D. Wandelt, David L. Larson, and Arun Lakshminarayanan. "Global, Exact Cosmic Microwave Background Data Analysis Using Gibbs Sampling". In: *Phys. Rev.* D70 (2004), p. 083511. eprint: astro-ph/0310080.

[245] H. Wang et al. "Reconstructing the cosmic density field with the distribution of dark matter haloes". In: *Mon. Not. R. Astron. Soc.* 394 (Mar. 2009), pp. 398–414. DOI: 10.1111/j.1365-2966.2008.14301.x. arXiv: 0803.1213.

[246] H. Wang et al. "Reconstructing the Initial Density Field of the Local Universe: Methods and Tests with Mock Catalogs". In: *Astrophys. J.* 772, 63 (July 2013), p. 63. DOI: 10.1088/0004-637X/772/1/63. arXiv: 1301.1348.

[247] L. Wang, B. Reid, and M. White. "An analytic model for redshift-space distortions". In: *Mon. Not. R. Astron. Soc.* 437 (Jan. 2014), pp. 588–599. DOI: 10.1093/mnras/stt1916. arXiv: 1306.1804.

[248] Risa H. Wechsler and Jeremy L. Tinker. "The Connection Between Galaxies and Their Dark Matter Halos". In: *Ann. Rev. Astron. & Astrophys.* 56 (Sept. 2018), pp. 435–487. DOI: 10.1146/annurev-astro-081817-051756. arXiv: 1804.03097 [astro-ph.GA].

[249] D. H. Weinberg et al. "Observational probes of cosmic acceleration". In: Phys. Rep. 530 (Sept. 2013), pp. 87–255. DOI: 10.1016/j.physrep.2013.05.001. arXiv: 1201.2434.

[250] M. White. "Reconstruction within the Zeldovich approximation". In: *Mon. Not. R. Astron. Soc.* 450 (July 2015), pp. 3822–3828. DOI: 10.1093/mnras/stv842. arXiv: 1504.03677.

[251] M. White. "The Zel'dovich approximation". In: *Mon. Not. R. Astron. Soc.* 439 (Apr. 2014), pp. 3630–3640. DOI: 10.1093/mnras/stu209. arXiv: 1401.5466.

[252] M. White and N. Padmanabhan. "Matched filtering with interferometric 21 cm experiments". In: *Mon. Not. R. Astron. Soc.* 471 (Oct. 2017), pp. 1167–1180. DOI: 10.1093/mnras/stx1682. arXiv: 1705.09669.

[253] M. White et al. "Tests of redshift-space distortions models in configuration space for the analysis of the BOSS final data release". In: *Mon. Not. R. Astron. Soc.* 447 (Feb. 2015), pp. 234–245. DOI: 10.1093/mnras/stu2460. arXiv: 1408.5435.

[254] N. Wiener. *Extrapolation, Interpolation, and Smoothing of Stationary Time Series: With Engineering Applications*. Technology Press books in science and engineering. Technology Press of the Massachusetts Institute of Technology, 1964. URL: https://books.google.com/books?id=A6QgAAAAMAAJ.

[255] Michael J. Wilson and Martin White. "Cosmology with dropout selection: Straw-man surveys and CMB lensing". In: *arXiv e-prints*, arXiv:1904.13378 (Apr. 2019), arXiv:1904.13378. arXiv: 1904.13378 [astro-ph.CO].

[256] L. Wolz, C. Blake, and J. S. B. Wyithe. "Determining the H I content of galaxies via intensity mapping cross-correlations". In: *Mon. Not. R. Astron. Soc.* 470.3 (Sept. 2017), pp. 3220–3226. DOI: 10.1093/mnras/stx1388. arXiv: 1703.08268 [astro-ph.GA].

[257] Xiaohu Yang, H. J. Mo, and Frank C. van den Bosch. "Constraining galaxy formation and cosmology with the conditional luminosity function of galaxies". In: *Monthly Notices of the Royal Astronomical Society* 339.4 (Mar. 2003), pp. 1057–1080. ISSN: 0035-8711. DOI: 10.1046/j.1365-8711.2003.06254.x. eprint: https://academic.oup.com/mnras/article-pdf/339/4/1057/18191789/339-4-1057.pdf. URL: https://doi.org/10.1046/j.1365-8711.2003.06254.x.

[258] J. Yoo and U. Seljak. "Joint analysis of gravitational lensing, clustering, and abundance: Toward the unification of large-scale structure analysis". In: *Phys. Rev. D* 86.8, 083504 (Oct. 2012), p. 083504. DOI: 10.1103/PhysRevD.86.083504. arXiv: 1207.2471.

[259] Y. Yu, H.-M. Zhu, and U.-L. Pen. "Halo Nonlinear Reconstruction". In: *Astrophys. J.* 847, 110 (Oct. 2017), p. 110. DOI: 10.3847/1538-4357/aa89e7. arXiv: 1703.08301.

[260] M. Zaldarriaga, S. R. Furlanetto, and L. Hernquist. "21 Centimeter Fluctuations from Cosmic Gas at High Redshifts". In: *Astrophys. J.* 608 (June 2004), pp. 622–635. DOI: 10.1086/386327. eprint: astro-ph/0311514.

[261] Y. B. Zel'dovich. "Gravitational instability: An approximate theory for large density perturbations." In: *Astron. Astrophys.* 5 (Mar. 1970), pp. 84–89.

[262] P. Zhang et al. "Probing Gravity at Cosmological Scales by Measurements which Test the Relationship between Gravitational Lensing and Matter Overdensity". In: *Physical Review Letters* 99.14, 141302 (Oct. 2007), p. 141302. DOI: 10.1103/PhysRevLett.99.141302. arXiv: 0704.1932.

[263] H.-M. Zhu et al. "Nonlinear reconstruction". In: *Phys. Rev. D* 96.12, 123502 (Dec. 2017), p. 123502. DOI: 10.1103/PhysRevD.96.123502. arXiv: 1611.09638.